

NASA-CR-183942

MTI 88TR39

Final Report

INTERNAL ROTOR FRICTION INSTABILITY

Prepared for:
National Aeronautics and Space Administration
George C. Marshall Space Flight Center
Marshall Space Flight Center

Prepared under:
Contract No. NAS8-35601

February 1990

(NASA-CR-183942) INTERNAL ROTOR FRICTION
INSTABILITY Final Report, Nov. 1983 - Oct.
1987 (Mechanical Technology) 169 pCSCL 131

NPO-21395

Unclas
63/37 0278784

MTI 88TR39

Final Report

INTERNAL ROTOR FRICTION INSTABILITY

Prepared for:
National Aeronautics and Space Administration
George C. Marshall Space Flight Center
Marshall Space Flight Center
Alabama, 35812

Prepared under:
Contract No. NAS8-35601

Prepared by:
J. Walton, A. Artiles, J. Lund, J. Dill, and E. Zorzi
Mechanical Technology Incorporated
968 Albany-Shaker Road
Latham, New York 12110

February 1990

ABSTRACT

This report documents the analytical developments and experimental investigations performed in assessing the affect of internal friction on rotor systems dynamic performance. Analytical component models for axial splines, Curvic™ splines, and interference fit joints commonly found in modern high-speed turbomachinery were developed. Rotor systems operating above a bending critical speed were shown to exhibit unstable subsynchronous vibrations at the first natural frequency. The effect of speed, bearing stiffness, joint stiffness, external damping, torque, and coefficient of friction, was evaluated.

Testing included material coefficient of friction evaluations, component joint quantity and form of damping determinations, and rotordynamic stability assessments. Under conditions similar to those in the SSME turbopumps, material interfaces exhibited a coefficient of friction of approximately 0.2 for lubricated and 0.8 for unlubricated conditions. The damping observed in the component joints displayed nearly linear behavior with increasing amplitude. Thus, the measured damping, as a function of amplitude, is not represented by either linear or Coulomb friction damper models. Rotordynamic testing of an axial spline joint under 5000 in.-lb of static torque, demonstrated the presence of an extremely severe instability when the rotor was operated above its first flexible natural frequency. The presence of this instability was predicted by nonlinear rotordynamic time-transient analysis using the nonlinear component model developed under this program. Corresponding rotordynamic testing of a shaft with an interference fit joint demonstrated the presence of subsynchronous vibrations at the first natural frequency. While subsynchronous vibrations were observed, they were bounded and significantly lower in amplitude than the synchronous vibrations.

FOREWORD

This Final Technical Report was prepared by the Advanced Technology Operation of Mechanical Technology Incorporated, Latham, New York, for NASA George C. Marshall Space Flight Center under Contract Number NAS8-35601. The work described was performed during the period November 1983 through October 1987. Mr. George von Pragenau was the NASA project manager responsible for this program. This report describes the analysis developed and tests performed during the course of the program.

MTI program management was accomplished by Dr. E. S. Zorzi and Mr. J. Walton. Analytic development and evaluations were conducted by Drs. J. Lund, A. Artiles, C. Lee, J. Walowit, J. Dill, Mr. J. Walton, and Ms. F. Gillham. Experimental investigations were conducted by Messrs. J. Walton, M. Martin, R. Hamm, P. Quantock and Dr. J. Dill.

TABLE OF CONTENTS

SECTION	PAGE
ABSTRACT	iii
FOREWORD	v
LIST OF FIGURES	ix
LIST OF TABLES	xiii
1.0 INTRODUCTION	1-1
1.1 Rotor Destabilization Due to Friction Effects	1-2
1.2 Analytic Considerations and Basic Shaft Hysteresis Models	1-3
1.2.1 Viscous Damping	1-5
1.2.2 Hysteretic Damping	1-7
1.2.3 Coloumb Damping	1-9
1.3 Spline Friction Instability	1-10
2.0 PROPULSION HARDWARE REVIEW	2-1
3.0 INTERNAL ROTOR FRICTION ANALYSIS	3-1
3.1 Component Analysis	3-1
3.1.1 Axial Spline Joint	3-1
3.1.2 Interference Fit Joint	3-15
3.1.3 Curvic Coupling	3-21
3.2 Integrated Analysis and Parametric Evaluations	3-29
3.2.1 Numerical Approach	3-30
3.2.2 Rotor Model and Initial Conditions	3-33
3.2.3 Numerical Results	3-37
3.2.4 Conclusions	3-55
3.3 Analysis of SSME High Pressure Oxidizer Turbopump	3-57
3.3.1 Turbopump Rotordynamic Model and Linear Analysis	3-57
3.3.2 HPOTP Rotordynamic Time Transient Simulations	3-63
3.3.3 Conclusions	3-69
4.0 TRACTION TESTING	4-1
4.1 Test Rig and Specimen Description	4-1

TABLE OF CONTENTS (Continued)

SECTION	PAGE
4.2 Method of Test	4-4
4.3 Results	4-5
5.0 COMPONENT TESTING	5-1
5.1 Test Item Description	5-1
5.2 Method of Test	5-7
5.3 Component Test Results and Data Reduction	5-9
5.3.1 Data Reduction Algorithm	5-11
5.3.2 Axial Spline Data Reduction Results	5-12
5.3.3 Interference Fit Data Reduction Results	5-12
5.3.4 Curvic Spline Data Reduction Results	5-14
5.3.4 Dependence of Damping on Amplitude	5-14
6.0 ROTORDYNAMIC TESTING	6-1
6.1 Test Item Description	6-1
6.2 Method of Test	6-4
6.3 Rotordynamics Test Rig Analysis	6-4
6.3.1 Dynamic Test Rig Model	6-4
6.3.2 Results of Test Rig Transient Analysis	6-8
6.4 Experimental Rotordynamic Test Results	6-11
6.4.1 Axial Spline Rotordynamic Testing	6-12
6.4.2 Interference Fit Rotordynamic Testing	6-21
7.0 CONCLUSIONS AND RECOMMENDATIONS	7-1
7.1 Conclusions	7-1
7.2 Recommendations	7-4
8.0 REFERENCES	8-1
APPENDIX A: ANALYSIS OF A SLEEVE SHRUNK ON A SHAFT UNDER BENDING PRIOR TO SLIP	A-1
APPENDIX B: RELIEVED SHRUNK-ON SLEEVE	B-1

LIST OF FIGURES

NUMBER	PAGE
1-1 Friction-Producing Joints in SSME HPOTP	1-1
1-2 Simple Rotor Model	1-4
1-3 Rotor Whirl Orbit	1-8
2-1 High-Pressure Fuel Turbopump Friction Joints	2-2
3-1 Axial Spline Teeth in Contact	3-2
3-2 Components of Tooth Flexibility	3-3
3-3 Tooth Geometry and Coordinate System Fixed on the Rotor	3-7
3-4 Transformation from Rotating to Fixed Coordinate Systems	3-12
3-5 Parts of the Rotor Interconnected by the the Spline Coupling Model	3-14
3-6 Hysteresis Loop in the Plane of Transmitted Moment vs Relative Deflection across the Spline for a Circular Orbit	3-15
3-7 Microslip under an Interference Fit	3-17
3-8 Zones of Microslip on Interference Surface	3-18
3-9 Interference Fit Schematic	3-18
3-10 Lap Joint Geometry	3-22
3-11 Force Distribution along Length of Lap Joint Interface (Upper Member)	3-27
3-12 Force Distribution along Length of Lap Joint Interface (Lower Member)).....	3-27
3-13 Plot of Force versus Displacement Hysteresis Loop for Lap Joint	3-28
3-14 Plot of Tooth Force versus Circumferential Position and Applied Moments ...	3-28
3-15 Moment across Spline versus Time near Sticking Conditions	3-32
3-16 Rotor Model Used to Study Spline Friction Joint	3-34
3-17 Mode Shape Corresponding to First Natural Frequency of Model without Friction	3-36
3-18 Transient Response to Different Initial Conditions ($0 < t < 0.1$ sec)	3-39
3-19 Transient Response to Different Initial Conditions ($0.1 < t < 1.0$ sec)	3-39
3-20 Dependence of Limit Cycle on Damping	3-40
3-21 Dependence of Limit Cycle on Friction-Torque Product	3-41
3-22 Limit Cycle Orbits for Different Combinations of Imbalance and Friction-Torque Product	3-41
3-23 Comparison FFT of Lateral Motion for Different Combinations of Imbalance and Friction-Torque Product	3-42
3-24 FFT of Lateral Motion for Different Amounts of Imbalance	3-43
3-25 Effect of Imbalance on Limits of Orbit Annulus	3-44

LIST OF FIGURES (Continued)

NUMBER	PAGE
3-26 Comparison of Orbitally Stable (Larger) and Unstable (Smaller) Limit Cycles at Different Side Loads	3-46
3-29 Transient Orbit for Small Initial Conditions Showing Decay to Stable Mode ...	3-48
3-30 Transient Orbit for Large Initial Conditions Showing Approach to Stable Limit Cycle	3-48
3-31 Envelopes of Lateral Motion vs Time for Different Initial Conditions at 100-lb Side Load	3-50
3-32 Envelopes of Lateral Motion vs Time for Different Initial Conditions at 200-lb Side Load	3-50
3-33 Envelopes of Lateral Motion vs Time for Different Initial Conditions at 300-lb Side Load	3-51
3-34 Envelopes of Lateral Motion vs Time for Different Initial Conditions at 400-lb Side Load	3-51
3-35 Comparison of Envelopes of Lateral Motion vs Time for Different Initial Conditions and Side Loads	3-52
3-36 Effect of Side Load on Limit Cycle	3-53
3-37 Transient Orbit for Six Different Side Loads and Larger (1 lb-sec/in.) External Damping	3-53
3-38 Limit Cycle Orbits at Different Degrees of Bearing Asymmetry	3-54
3-39 Limit Cycle Ellipse Size vs K_{yy} Stiffness Coefficient	3-54
3-40 HPOTP Cross Section Showing Bearing and Shaft Interconnections	3-41
3-41 HPOTP Three-Level Geometry Model Plot	3-58
3-42 HPOTP Mode Shape Plots	3-62
3-43 Time Transient Simulation of HPOTP at 30,000 rpm	3-64
3-44 Effect of Main Impeller Imbalance on HPOTP Vibrations at the Preburner	3-65
3-45 Effect of Main Impeller Imbalance on HPOTP Orbit at Preburner Spline	3-66
3-46 Normalized FFT Plots for Preburner Vibration under Various Imbalance Forces	3-67
3-47 Effect of Turbine Bearing and Interstage Seal Damping on HPOTP Orbit at Preburner Spline	3-68
4-1 Coefficient of Friction Test Configuration	4-2
4-2 Traction Test Rig with Chill Cap	4-2
4-3 Friction Force Wave Form	4-6
4-4 Friction Coefficient for Unlubricated Inconel vs Waspaloy at 70°F, Two Normal Loads, and Three Frequencies	4-8
4-5 Steel vs Steel Friction Coefficient at 70°F under Lubricated and Unlubricated Conditions	4-8

LIST OF FIGURES (Continued)

NUMBER	PAGE
4-6 Waspaloy vs Waspaloy Friction Coefficient at 70 and 1000°F Temperatures under Lubricated and Unlubricated Conditions	4-9
4-7 Inconel vs Waspaloy Friction Coefficient at 70 and 300°F Temperatures under Lubricated and Unlubricated Conditions	4-9
4-8 Inconel vs Inconel Friction Coefficient at 70 and 300°F Temperatures under Lubricated and Unlubricated Conditions	4-10
4-9 Titanium Friction Coefficient at 70 and 320°F Temperatures under Lubricated and Unlubricated Conditions	4-10
5-1 Component Test Specimens As Fabricated	5-2
5-2 Interference Fit and Axial Spline Sleeves As Manufactured	5-3
5-3 Moment Transmitted across 2.15-in. Diameter Joint before Slip As a Function of Interference (100-lb Excitation)	5-5
5-4 Moment Transmitted across 2.15-in. Diameter Joint before Slip As a Function of Interference (200-lb Excitation)	5-5
5-5 Moment Transmitted across 1.65-in. Diameter Joint before Slip As a Function of Interference (100-lb Excitation)	5-6
5-6 Moment Transmitted across 1.65-in. Diameter Joint before Slip As a Function of Interference (200-lb Excitation)	5-6
5-7 Solid Shaft Impact Testing Setup	5-7
5-8 Component Damping Test Setup and Instrumentation	5-8
5-9 Curvic Test Joint Swept Sine Test Data	5-10
5-10 Spline Component Data: Transfer Function versus Frequency	5-13
5-11 Interference Fit Component Data: Transfer Function versus Frequency	5-13
5-12 Curvic Component Data (3130 lb Bolt Force): Transfer Function versus Frequency	5-15
5-13 Curvic Component Data (2000 lb Bolt Force): Transfer Function versus Frequency	5-15
5-14 Component Data: Damping Ratio versus Amplitude	5-18
6-1 Rotordynamic Test Rig	6-2
6-2 Close-up for Rotordynamic Test Rig	6-3
6-3 Rotordynamic Test Rig Model with Spline Sleeve	6-6
6-4 Rotordynamic Test Rig Model with Spline Sleeve As Simplified for Time Transient Analysis	6-6
6-5 Rotordynamic Test Rig First Mode Shape with Spline Sleeve	6-7
6-6 Rotordynamic Test Rig Predicted Time-Transient Response	6-10
6-7 FFT Plot of Rotordynamic Rig Analytic Predictions	6-11

LIST OF FIGURES (Continued)

NUMBER	PAGE
6-8 FFT Plots Showing Sub and Supercritical Operation of Rotordynamic Test Rig with Axial Spline	6-12
6-9 FFT Plot of Axial Spline Subsynchronous Instability	6-13
6-10 FFT Waterfall Plot Showing Loss of Spline Friction Instability	6-13
6-11 FFT Plot of Experimentally Observed Interference Fit Induced Subsynchronous Vibration	6-14
6-12 FFT Waterfall Plot Showing Time Varying Nature of Interference Fit Induced Subsynchronous Vibrations	6-14
6-13 FFT Plot for Interference Fit Joint with 5-gram Change in Imbalance at Sleeve	6-15
6-14 FFT Plot Showing Instability for Shaft with Both Interference Fit and Axial Spline Joints	6-15
6-15 Experimentally Observed Internal Friction-Induced Instability for Combined Interference Fit and Spline Joints	6-16
6-16 FFT Plot Showing Subsynchronous Instability for 20-lb Side Load at Axial Splint Joint	6-16
6-17 FFT Plot Showing Instability for 70-lb Side Load at Axial Spline	6-17

LIST OF TABLES

NUMBER		PAGE
2-1	SSME Interface Materials	2-2
2-2	Axial Spline Contact Pressures	2-2
3-1	Rotordynamic Model for Parametric Study	3-35
3-2	Five Lowest Natural Frequencies of the Linear Model	3-35
3-3	HPOTP Three-Level Rotordynamic Model	3-59
3-4	Bearing and Joint Stiffness	3-60
3-5	SSME Turbopump Spline Coupling Parameters	3-60
3-6	SSME HPOTP Critical Speeds	3-61
4-1	Traction Test Matrix	4-4
4-2	Coefficient of Friction (Unlubricated)	4-11
4-3	Coefficient of Friction (Lubricated)	4-11
5-1	Component Test Shaft with Interference Sleeve	5-4
5-2	Results of Component Test Data Reduction	5-12
6-1	Damped Natural Frequencies of Rotordynamic Test Rig with Spline	6-7

1.0 INTRODUCTION

Internal friction as a problem in rotor-bearing systems was first recognized in the mid-1920s when manufacturers began shrinking disks onto supercritical rotors. The violent whirling that resulted spurred the analyses and tests that gave the first real understanding of this cause-effect relationship. Internal rotor friction appears as a persistent problem on high-speed rotors because all shafts and components dissipate vibrational energy to some extent. The rotor instability resulting from this vibrational energy is usually cured by hardware fixes — special dampers, redesigning rotor fits or modifying bearings — which do not allow a true understanding of the mechanisms to be developed. While material hysteresis is one of the most commonly studied destabilizing mechanisms, other internal rotor destabilizing mechanisms exist, such as friction either in joints or under shrunk-on disks. These destabilizing mechanisms have received virtually no attention and little, if any, experimental confirmation.

Today, internal friction is seen to be a potential source of problems in advanced, high-pressure O_2/H_2 propulsion equipment. Turbopumps such as the Space Shuttle Main Engine (SSME) High Pressure Oxidizer Turbopump (HPOTP) are of built-up design with many joints, fits, and areas for friction-induced excitation if slippage takes place, as shown in Figure 1-1. These rotors operate above flexible bending critical speeds, have light external damping, and are very small, yet run at high speeds and high output power levels. Hence, the forces on the rotors are very large, which tends to encourage joint slippage and friction force generation.

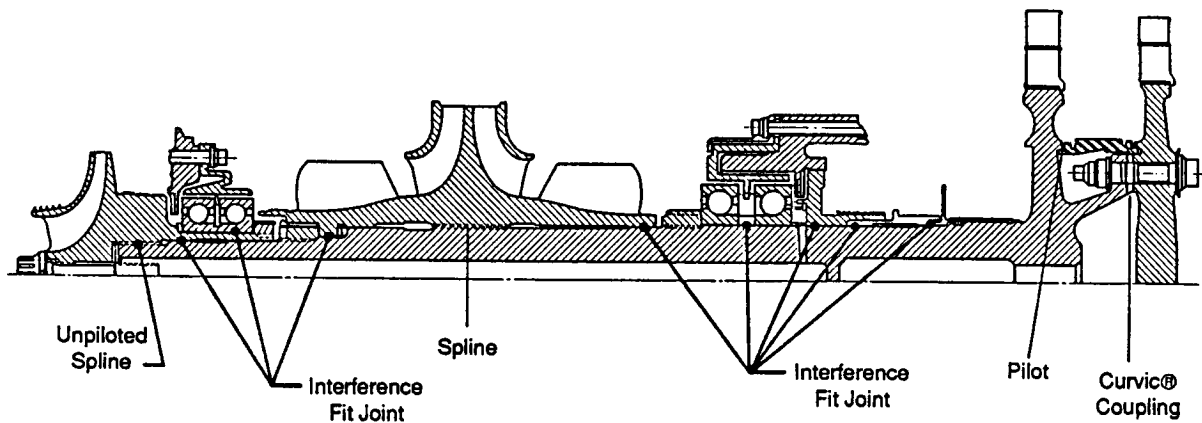


Figure 1-1. Friction-Producing Joints in SSME HPOTP

90560

Under this NASA-sponsored program, Mechanical Technology Incorporated (MTI) has begun a systematic evaluation of internal rotor-friction-caused instabilities. The completed three-phase program incorporated technologies such as rotordynamics, frictional behavior of materials, and structural analysis and is described as follows:

- **Phase I - Internal Friction Review and Analysis.** Review SSME propulsion hardware and relevant literature. Analyze friction-producing components and design basic traction and component test rigs.
- **Phase II - Component Test and Evaluation.** Fabricate and test traction and component rigs. Develop the interface to a rotordynamic analysis tool that incorporates component models and then design a rotordynamic simulator that emphasizes basic phenomena.
- **Phase III - Rotordynamic Evaluation.** Fabricate and test the rotor simulator and evaluate SSME hardware for instability potential. Prepare final report.

1.1 Rotor Destabilization Due to Friction Effects

Engineers involved with stability assessment of high-speed rotating equipment have long been aware of the destabilizing influence of material damping on rotating machinery operation. This phenomenon was postulated as early as 1924 by A. L. Kimball [1],* who suspected that internal damping contributed to destabilization of rotating systems when critical speeds are traversed. Robertson [2] extended this to reflect upon rotor whirl induced by material hysteresis. In the 1950s through the 1960s, numerous contributors such as Timoshenko [3], Dimentberg [4], Tondl [5], Gunter [6], Ehrich [7,8], Black [9], and Bolotin [10] provided additional insight into the effects of material damping on high-speed rotor performance. Subsequent research by Childs [11], Black [12], and Williams and Trent [13] has included material dissipation to evaluate phenomena such as spline-induced loading on rotor stability. Further, Lund [14], Dimarogonas [15], and Zorzi [16] offered contributions that include linear material hysteresis in computational rotor assessments.

A review of the above-referenced material leaves the researcher with a sense of confusion regarding how to account for material or interface damping mechanisms. Specifically, much of the design work performed by the turbomachinery industry applies linear damping models (viscous, etc.), if any, to account for material hysteresis. Some of the activities reported in the open literature, such as Williams et al. [13], include

*Numbers in brackets indicate references, which are located in Section 8.0.

nonlinear forms of damping (Coloumb damping, etc.) rather than linear models to address component interface dissipation effects. This disparity is primarily due to design versus analytic needs and capabilities. To place this into perspective, a design tool (such as a transfer matrix rotor stability code) may be heavily exercised to evaluate numerous alternatives. As such, this design analysis routinely uses linearized bearing and seal dynamic parameters (stiffness and damping) and linear material damping models. Specialized analytic capabilities that deal with more complex forms of damping [13] are more often restricted to simplified rotor geometries to permit detailed examination of component damping (such as spline friction effects).

A review of publications, such as those by Lazan [17] or Pisarenko [18,19], illustrates a key aspect of this program and quickly demonstrates the limitation of providing acceptable phenomenological models that describe real material behavior.

Pisarenko's contributions focus on nonlinear models using the Davidenkov [20] hypothesis for dissipation in elastic systems subjected to oscillations. Using the method offered by academicians N. M. Krylov and N. N. Bogolyubov [21], useful results and asymptomatic expansion of the governing equation were implemented by Lazan [17]. Certainly, an equally detailed treatment of component damping for splines, Curvic®* couplings interference fits, as well as shaft hysteresis, could span many careers. What this review has shown is that little (if any) experimental confirmation exists to date.

1.2 Analytic Considerations and Basic Shaft Hysteresis Models

Since the mechanism of internal damping and friction in rotors is uncertain, several friction models may be used. To review the subject briefly, three different models will be discussed: viscous, hysteretic, and Coloumb. For purposes of this discussion, a simple rotor model will be employed (see Figure 1-2). This model consists of a heavy disk mounted on a flexible shaft and supported by flexible bearings.

As shown on Figure 1-2, the angular speed of rotation equals Ω , and the whirl motion is described by the coordinates of the disk center, x and y , measured in a stationary frame. If the motion is harmonic with a whirl frequency, ω (rad/sec), the motion equation can be written as

*A registered trademark of Gleason Works, Inc.

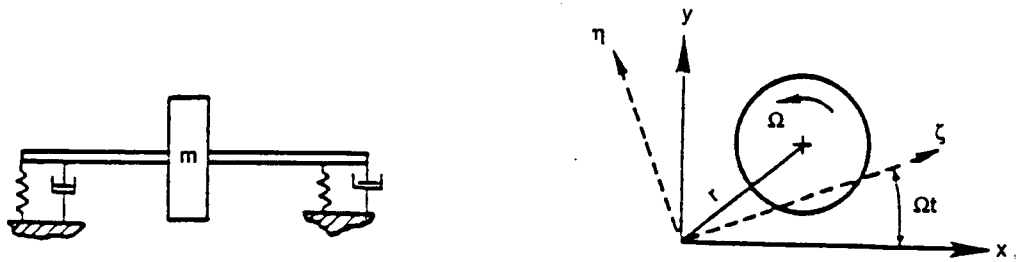


Figure 1-2. Simple Rotor Model

90561

$$x = x_C \cos(\omega t) - x_S \sin(\omega t) = \text{Re}[(x_C + ix_S)e^{j\omega t}] \quad (1.1a)$$

$$y = y_C \cos(\omega t) - y_S \sin(\omega t) = \text{Re}[(y_C + iy_S)e^{j\omega t}] \quad (1.1b)$$

In general, this equation describes an elliptical whirl orbit with major-semiaxis, a , and minor semiaxis, b , where

$$a = |x_P| + |x_R| \quad (1.2a)$$

$$b = |x_P| - |x_R| \quad (1.2b)$$

$$x_P = 1/2(x + iy) = 1/2[x_C - y_S + i(x_S + y_C)]; \quad (1.2c)$$

$$|x_P| = 1/2 [(x_C - y_S)^2 + (x_S + y_C)^2]^{1/2}$$

$$x_R = 1/2(x - iy) = 1/2[x_C + y_S + i(x_S - y_C)]; \quad (1.2d)$$

$$|x_R| = 1/2 [(x_C + y_S)^2 + (x_S - y_C)^2]^{1/2}$$

and where

$$x = x_C + ix_S \quad (1.3a)$$

$$y = y_C + iy_S \quad (1.3b)$$

from which

$$a^2 + b^2 = 2(|x_p|^2 + |x_r|^2) = (x_C^2 + x_S^2 + y_C^2 + y_S^2) \quad (1.4)$$

and

$$ab = |x_p|^2 - |x_r|^2 = x_S y_S - x_C y_C \quad (1.5)$$

For the above equations, the value of a is always positive, but the value of b may be negative, in which case the motion is backward (retrograde) whirl. For a circular whirl orbit, it is found that, for forward whirl,

$$y_C = x_S; y_S = -x_C \text{ or } y = -ix; \text{ i.e. } a = b = [(x_C^2 + x_S^2)]^{1/2} \quad (1.6a)$$

and, for backward whirl,

$$y_C = -x_S; y_S = x_C \text{ or } y = ix; \text{ i.e. } a = -b = [(x_C^2 + x_S^2)]^{1/2} \quad (1.6b)$$

1.2.1 Viscous Damping

In setting up the equations of motion, it proves convenient to introduce a rotating $\zeta - \eta$ coordinate system (Figure 1-2) where

$$\zeta = x \cos \Omega t + y \sin \Omega t \quad (1.7a)$$

$$\eta = -x \sin \Omega t + y \cos \Omega t \quad (1.7b)$$

In this coordinate system, the dissipation can be expressed simply as $c\zeta'$ or $c\eta'$ where c equals the coefficient of internal viscous damping. The equations are readily transformed back into stationary coordinates. If it is further assumed that the shaft and bearing stiffnesses are not isotropic, they may be labeled k_x and k_y , respectively. Furthermore, it is assumed that the bearings contribute damping, represented by a damping coefficient, B . These equations are

$$m\ddot{x} + c(\dot{x} + \Omega y) + B\dot{x} + k_x x = 0 \quad (1.8a)$$

$$m\ddot{y} + c(\dot{y} - \Omega x) + B\dot{y} + k_y y = 0 \quad (1.8b)$$

The solution at the threshold of instability will be in the form

$$\begin{bmatrix} [k_x - m\omega^2 + i\omega(c + B)] & \Omega c \\ -\Omega c & [k_y - m\omega^2 + i\omega(c + B)] \end{bmatrix} \begin{Bmatrix} x \\ y \end{Bmatrix} = 0 \quad (1.9)$$

For a solution to exist, the determinant must be zero, which results in

$$\omega = \{[1/2(k_x + k_y)]/m\}^{1/2} \quad (1.10a)$$

$$\Omega^2 = \omega^2(1 + B/c)^2 + [(k_x - k_y)^2/4c^2] \quad (1.10b)$$

Instability sets in when the speed reaches the value given by Equation 1.10b and the whirl frequency equals the resonant frequency (the critical speed). In the absence of external damping ($B = 0$) and for isotropic bearings ($k_x = k_y$), the rotor becomes unstable upon reaching the critical speed. The rotor can be stabilized either by providing external damping, B , or by making the supports anisotropic. This will raise the threshold speed but will not eliminate the instability.

The energy dissipated per whirl cycle by the internal rotor damping is computed as

$$E = c \int_0^{\tau=2\pi/\omega} [(\dot{x} + \Omega y)\dot{x} + (\dot{y} - \Omega x)\dot{y}] dt \quad (1.11a)$$

or

$$E = 2\pi c[\omega(a^2 + b^2)/2 - \Omega ab] \quad (1.11b)$$

The dissipated energy will be negative when

$$\Omega > [(a^2 + b^2)/ab]\omega/2 \quad (1.12)$$

The internal damping will act as negative damping (destabilizing) above this speed and as positive damping below this speed. For circular whirl orbit ($a = b$), the threshold speed becomes $\Omega = \omega$. For elliptical whirl orbits ($b < a$ and b positive, or forward whirl), the threshold speed will be raised as seen from Equation 1.10b ($k_x = k_y$ assumes unchanged ω).

In general, the dissipated energy can be addressed as

$$E_{dis} = \delta E |e|^2 \quad (1.13)$$

where E_{dis} is the dissipated energy, E is the modulus of elasticity, and δ is the logarithmic decrement and is defined as a damped, free vibration that can be written as

$$x = |x| e^{\lambda t} \cos(\omega t + \phi) \quad (1.14)$$

Where λ equals the damping exponent (negative for a stable system) and the logarithmic decrement, δ , is defined as

$$\delta = -\log[x(t + \tau)/x(t)] \quad (1.15)$$

where $\tau = 2\pi/\omega$ is the period such that δ measures the relative amplitude decay per cycle. Therefore, it is seen that

$$\delta = -\lambda \tau = -2\pi\lambda/\omega \quad (1.16)$$

1.2.2 Hysteretic Damping

To demonstrate how hysteretic damping affects the whirl motion of a rotor, consider the rotor shown in Figure 1-2 and assume the bearings to be isotropic such that the whirl orbit is circular with radius r .

As shown in Figure 1-3 (left), the neutral strain axis ($\epsilon = 0$) is perpendicular to the displacement vector, r . When the rotational speed, Ω , is larger than the whirl frequency, ω , a shaft fiber will travel in the same direction relative to the neutral strain axis. Since the strain lags the stress by an angle α , the neutral stress axis ($\sigma = 0$) must be ahead of the neutral strain axis. Thus, the elastic force from the shaft, kr , which is perpendicular to the neutral stress axis, forms the angle α with the amplitude direction such that it has

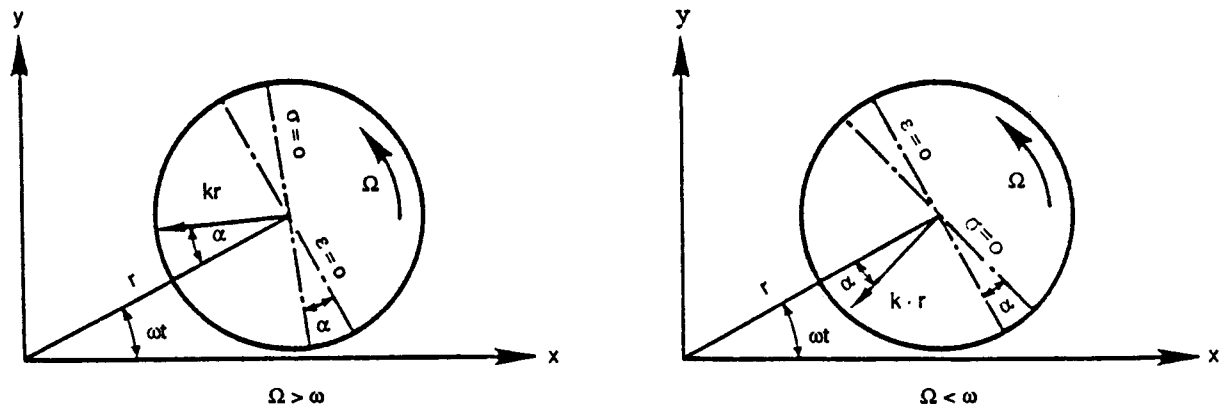


Figure 1-3. Rotor Whirl Orbit

83766

the component $kr(\cos\alpha)$. This component is the elastic restoring force, and the tangential component is $kr(\sin\alpha)$ at right angles to the amplitude direction. The latter component is tangential to the whirl orbit and in the direction of whirl such that it puts energy into the whirl motion, causing the rotor to be unstable. The exception to this is if ω is negative (backward whirl), the tangential force opposes the whirl and acts to stabilize the rotor.

In the case where the rotational speed, Ω , is less than the whirl frequency, ω , (Figure 1-3, right), a shaft fiber will travel in the opposite direction of Ω , relative to the neutral strain axis, and the position of the neutral stress axis must reverse. Therefore, the tangential force component will oppose the whirl motion and take energy out of the whirl motion (i.e., act as positive damping). This is a stable condition.

The above two situations can be covered by the convention

$$\begin{aligned} \gamma &= + \sin\alpha \quad \text{when } \Omega > \omega \text{ (and whenever } \omega \text{ is negative)} \\ \gamma &= - \sin\alpha \quad \text{when } \Omega < \omega \end{aligned} \tag{1.17}$$

The equations of motion for the rotor become

$$\begin{aligned} m\ddot{x} + B\dot{x} + K_R x + \gamma K_R y &= 0 \\ m\ddot{y} + B\dot{y} - \gamma K_R x + K_R y &= 0 \end{aligned} \tag{1.18}$$

At the threshold of instability, the solution is in the form similar to that for viscous damping, Equation 1.9, and the condition that the determinant be zero yields

$$\begin{aligned}\omega &= (K/m)^{1/2} \\ \omega B/K_T &= \gamma\end{aligned}\tag{1.19}$$

When the whirl frequency equals the resonant frequency (critical speed) of the rotor, the rotor is potentially unstable when γ is positive, which means when the speed exceeds the critical speed. If, however, the bearings provide sufficient damping such that $\omega B/K_T > \gamma$, the rotor will be stable at all speeds.

The instability whirl mode is found to be a circular whirl orbit with forward whirl. When the bearings are anisotropic, the whirl orbit becomes an ellipse with the instantaneous whirl frequency, ω_t , which is found to be

$$\omega_t = \omega ab / (x^2 + y^2)\tag{1.20}$$

The energy dissipated per whirl cycle is

$$E_{dis} = -K_T ab \int_0^{2\pi} \gamma \cdot d(\omega t)\tag{1.21}$$

If $\omega t < \Omega$ during the whirl cycle, then the dissipated ellipse is negative, corresponding to negative damping (or energy added to the rotor), and the rotor is unstable.

1.2.3 Coulomb Damping

In Coulomb damping (dry friction), the friction force is constant in magnitude and is always opposed to the direction of the relative sliding velocity. It is usually expressed as μN where N equals the normal force (contact force) and μ equals the friction coefficient.

The dry friction force has the components

$$F_x = [(-\dot{x} + \Omega y) / v] \mu N\tag{1.22}$$

$$F_y = [(-\dot{y} - \Omega x) / v] \mu N$$

where

$$v = [(\dot{x} + \Omega y)^2 + (\dot{y} - \Omega x)^2]^{1/2}$$

and the energy dissipated per cycle is

$$E_{dis} = \mu N \int_0^T \{ [(\dot{x} + \Omega y)/v] \dot{x} + [(\dot{y} - \Omega x)/v] \dot{y} \} dt \quad (1.23)$$

If the whirl orbit is circular with radius r , the energy dissipated per cycle is given by:

$$E_{dis} = 2\pi [(\Omega - \omega) / |\Omega - \omega|] r \mu N \quad (1.24)$$

Hence, the rotor becomes unstable upon reaching the critical speed.

1.3 Spline Friction Instability

An Army-funded activity [22] was completed at MTI that developed a mathematical model for predicting spline-coupling-induced nonsynchronous rotor vibrations. Predictions were compared with data from a rotordynamic test rig. A special feature of this spline model was the characterization of the friction forces that are produced at the mating spline teeth surfaces and the subsequent calculation of the internal damping coefficients. The spline internal damping and the resulting rotor instabilities were predicted for different spline configurations, and the results were correlated with measured data from a gas turbine rotor simulator test rig.

In this analysis, the spline coupling was modeled as a section of the shaft system having internal damping. This model was incorporated as one portion of a rotor-bearing system model. The system stability was then studied by computing the complex eigenvalues or damped natural frequencies of the system. Each damped natural frequency is a complex number wherein the imaginary part represents a frequency of system oscillation and the real part indicates stability. Positive or negative values for a real part indicate that the system will be unstable or stable, respectively, in that mode. A stability map (plot of real part against some parameter such as speed) or a Nyquist plot (real against imaginary part for various conditions) could then be drawn up covering the modes and operating conditions of interest. An overall picture of the system stability was thus generated.

The major assumptions involved in this analysis were

- The material on which the teeth were mounted was rigid, except for a small localized area about the base of each tooth. This implied that the deflection of the coupling resulted entirely from deflection of the teeth in rigid supports.
- All deflections were very small and all deflecting parts behaved elastically.
- Where a given stiffness was nonlinear (nonproportional to deflection), it was linearized about its value under steady-state operating conditions.
- Errors in tooth location and profile were small. Each tooth was in line contact with its mate and all carried about the same load.
- The forces on the coupling teeth were due predominantly to the transmitted torque and forces arising from the misalignment itself (such as elastic restoring forces). Other forces, such as those resulting from friction-induced moments were small.
- The spline friction damping was represented by equivalent viscous damping coefficients.
- Sources of rotor damping other than the spline friction were neglected.

The nonsynchronous rig configuration consisted of a damped thrust bearing simulator rig, which included a turbine shaft supported on two bearings. The rear end of the shaft was supported on a duplex-pair ball bearing and a squeeze-film damper through a flexible bearing support. The front of the shaft was modified to accommodate the interchangeable test splines that were supported by a separate set of duplex ball bearings.

Under nominal operating conditions, the test rig was predicted to be marginally unstable if very low damping was present at the bearing supports. The experimental results showed that the rotor was slightly unstable with the unlubricated side-fit spline. However, by reducing the spline friction forces with lubricating oil, the instability was suppressed. Further, as predicted with the rotor stability model, squeeze-film damping at the rig's thrust bearing eliminated the nonsynchronous whirl. Overall, there was close agreement between the predicted and measured response of the nonsynchronous whirl rig.

2.0 PROPULSION HARDWARE REVIEW

In this section the results of the hardware review of the SSME hardware are presented. The objective of this effort was to identify the types of rotor joints, interfaces, and materials as well as the environment under which destabilizing internal rotor friction forces may be encountered in both the HPOTP and the High-Pressure Fuel Turbopump (HPFTP) (see Figures 1-1 and 2-1). Information from this effort was then used in the definition of test parameters for the traction and component testing described in subsequent sections.

To accomplish this task, a set of the HPOTP and HPFTP design drawings were obtained from NASA and reviewed to characterize rotor joints with respect to their dimensions, fits, materials, and environmental operating conditions. The relevant material interfaces for the HPOTP and HPFTP are shown in Table 2-1.

To assess the material interface conditions and establish test conditions, published HPOTP and HPFTP specifications and NASA-supplied data were used. For example, the torque levels transmitted through the HPOTP preburner, Curvic coupling, and main impeller spline were 4,227, 32,017, and 59,806 in.-lb, respectively. These values were determined based on an assumed power level of 31,800 hp at 31,300 rpm. The HPFTP torque levels were determined similarly. For a power rating of 69,874 hp at 34,930 rpm, HPFTP transmitted torque levels ranged from 37,808 to 126,028 in.-lb between the three impeller and two turbine stages. This information was then used to characterize the contact pressures experienced in the spline joints. The simplifying assumptions used in identifying test conditions were as follows:

- All torque was transmitted by the spline teeth
- The pressure angle remained constant
- Load sharing between teeth was even
- All load was applied at the pitch diameter
- The spline teeth were rigid (i.e., no deformation)

Based on these assumptions, expected contact pressures were determined, as shown in Table 2-2. Although the basic full tooth contact pressures ranged from 12,700 to 42,000 psi, Rocketdyne manufacturing specifications require that a minimum of 75% theoretical contact area be maintained. Therefore, contact pressures for the friction testing were modified to reflect an assumed reduction in the contact area, as also shown in Table 2-2.

Table 2-1. SSME Interface Materials

Pump	Materials	Temperature Range
HPOTP	Inconel/Waspaloy Waspaloy/Waspaloy	Cold (-300°F) Wide (-300 to 1090°F)
HPFTP	Inconel/Waspaloy Waspaloy/Waspaloy Titanium/Inconel Titanium/Titanium	Cold (-423°F) Wide (-423 to 1340°F) Cold (-423°F) Cold (-423°F)

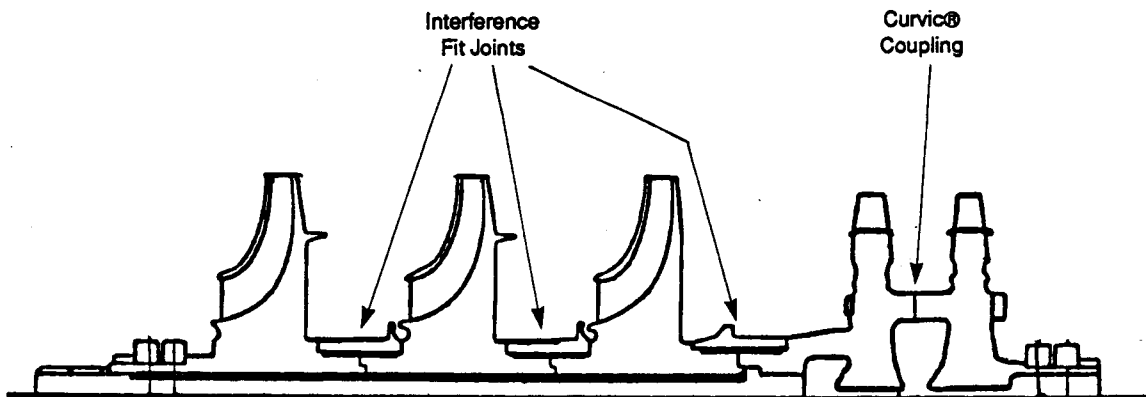


Figure 2-1. High-Pressure Fuel Turbopump Friction Joints

90582

Table 2-2. Axial Spline Contact Pressures

Spline Location	Full Contact Area Load (psi)	75% Contact Area Load (psi)
HPOTP Preburner	12,700	16,900
HPOTP Main Impeller	18,000	23,900
HPFTP Impeller 1-2	18,200	24,300
HPFTP Impeller 2-3	35,300	47,100
HPFTP Impeller/Turbine	42,000	56,000

In a similar fashion, the loads from the Curvic coupling between the HPOTP and HPFTP turbine stages were evaluated. The assumptions used for this analysis were as follows:

- All torque was transmitted by the Curvic teeth
- The pressure angle remained constant
- Load sharing between teeth and tooth rows was even
- Load was applied at the pitch diameter
- The teeth were rigid (no deformation)
- A minimum of 75% of the possible area was in contact

With these assumptions, the normal pressures in the Curvic coupling ranged from 17,800 to 28,100 psi for the HPOTP and from 19,500 to 55,400 psi for the HPFTP.

Contact pressures under interference fit joints were also estimated. In estimating the interference fit pressures, chilled operating fits as listed on SSME assembly drawings were used. Further, it was assumed that for each joint the following conditions applied:

- Interference fit joints can be modeled as two simple concentric cylinders
- No gross geometry changes occurred with speed
- The load was evenly distributed circumferentially

Based on these assumptions, the interference fit contact pressures ranged from 1,000 to 13,100 psi, with most of the pressures falling in the 3,000 to 7,800 psi range.

A rough order of magnitude for interference fit and spline joint motions was also prepared to assist in establishing test amplitudes. To determine order of magnitude motions between the HPOTP main impeller interference fits and the shaft, it was assumed that the main impeller is rigid and that the shaft bends inside it. This resulted in maximum interference fit motions on the order of 1 μ in./mil of shaft deflection. Similarly, maximum expected axial spline motions were estimated and were found to be in the range of 0.6 mil/mil of motion at the preburner pump bearings.

The results of the SSME propulsion hardware review were factored into all three phases of testing conducted under this program. Contact pressures, motions, and sizes were simulated as closely as possible during the testing in an effort to make the results and conclusions of this study as directly related to the actual SSME hardware as possible.

3.0 INTERNAL ROTOR FRICTION ANALYSIS

In this section the analysis developed to assess internal rotor friction effects on rotor system performance is presented. The objective of the analytical development was to establish models of three friction-producing joints, which could then be integrated into nonlinear, time-transient, rotordynamics analysis tools. The approach that was selected to analyze the stability of rotor-bearing systems containing internal friction components was to separate the nonlinearities of the joints from the linear elements of a rotor system so that the nonlinear forcing functions reside on the right-hand side of the equations of motion. Once formulated, a numerical integration of the governing nonlinear equations of motion versus time, using readily available methods, may be accomplished.

3.1 Component Analysis

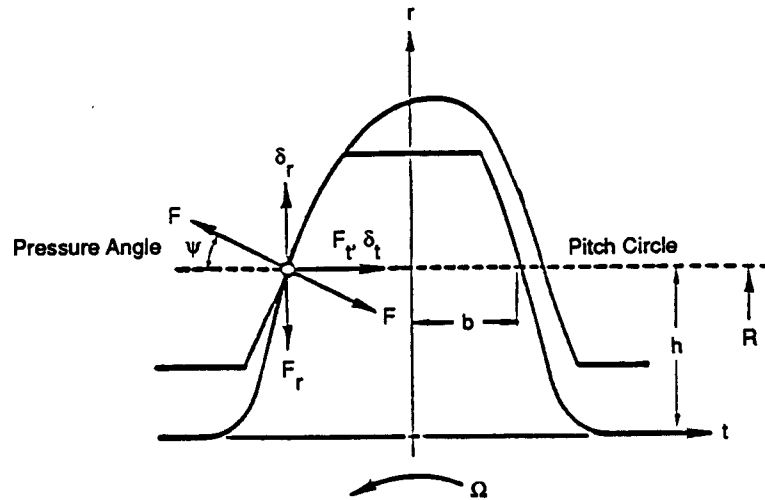
This section contains the analysis describing the nonlinear internal friction models. The three components treated are an axial spline joint, an interference fit joint, and a Curvic coupling. In the following three sections, the analysis developed for each of these components is described.

3.1.1 Axial Spline Joint

To evaluate the forces and moments transmitted across a spline coupling, the lateral and angular stiffnesses without friction are considered and presented. In this development, the stiffness of two teeth in contact is addressed first, followed by the extension to a complete spline coupling. Once the analysis for predicting spline coupling stiffness is established, the spline coupling frictional contributions are developed and added to the force and moment relationships describing the complete spline joint.

3.1.1.1 Spline Stiffness. To evaluate the overall stiffness of a spline coupling, the stiffness of two teeth in contact (shown in Figure 3-1) is considered first. The loading on a tooth is represented by the force, F , acting at the pitch circle under the pressure angle, ψ . This force has tangential and radial components given by

$$F_t = F \cos\psi, \quad F_r = F \sin\psi \quad (3.1)$$



90563

Figure 3-1. Axial Spline Teeth in Contact

The resulting deflection has the components δ_t and δ_r such that the deflection in the load direction becomes

$$\delta = \delta_t \cos\psi - \delta_r \sin\psi \quad (3.2)$$

Each tooth may be treated as a cantilever beam, mounted in a flexible base as shown in Figure 3-2. The tooth deflection is obtained as the sum of (a) bending of the tooth, (b) rotation of the base, and (c) radial compression of the tooth.

First, there is the bending of the tooth as a cantilever beam with a rigid base. The bending moment at the distance r from the base is equal to $F_t(h-r) - F_r b$ where b is half the width of the tooth at the pitch circle and h is the tooth height at the pitch circle. With a cross-sectional area moment of inertia (I), a cross-sectional area (A), an elasticity modulus (E), and an effective shear modulus (G), the slope of the bent tooth is

$$\frac{\partial \delta_t}{\partial r} = \int_0^r \frac{1}{EI} [F_t(h-r') - F_r b] dr' \quad (3.3)$$

and the deflection at the pitch circle ($r = h$) becomes

$$\delta_t = \int_0^h \int_0^r \frac{1}{EI} [F_t(h-r') - F_r b] dr' dr + \int_0^h \frac{F_t}{GA} dr \quad (3.4)$$

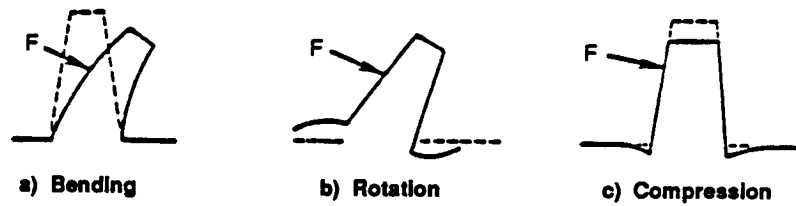
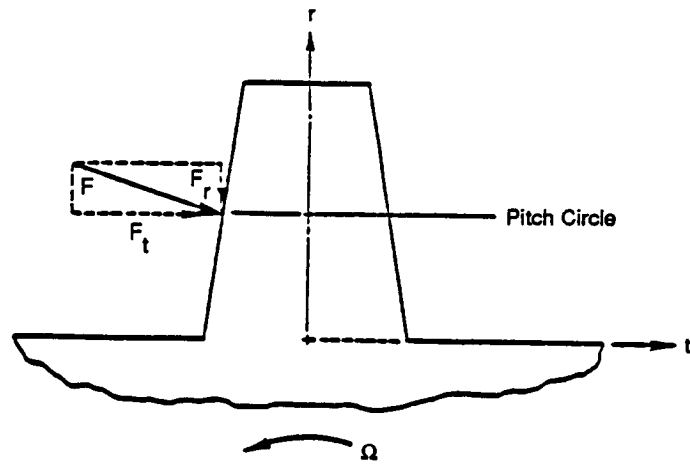


Figure 3-2. Components of Tooth Flexibility

90564

where the last integral is the contribution from shear deformation. The slope causes a radial displacement at the pitch circle, given by

$$\delta_r = b \left(\frac{\partial \delta_t}{\partial r} \right)_{r=h} = b \int_0^h \frac{1}{EI} [F_t(h-r) - F_r b] dr \quad (3.5)$$

Equations 3.4 and 3.5 shall be written as

$$\delta_t = \delta_{1t} F_t - \delta_{3t} F_r \quad (3.6)$$

$$\delta_r = \delta_{1r} F_t - \delta_{3r} F_r$$

where

$$\delta_{1t} = \int_0^h \frac{(h-r)^2}{EI} dr + \int_0^h \frac{1}{GA} dr \quad (3.7)$$

$$\delta_{3t} = \delta_{1r} = b \int_0^h \frac{(h-r)}{EI} dr \quad (3.8)$$

$$\delta_{3r} = b^2 \int_0^h \frac{1}{EI} dr \quad (3.9)$$

For a beam with constant cross section, $\delta_{1t} = (h^3/3EI + h/GA)$ and $\delta_{3t} = \delta_{1r} = bh^2/2EI$ and $\delta_{3r} = b^2h/EI$. For a tooth, however, the cross-section varies and integration is required to evaluate Equations 3.7, 3.8, and 3.9. A numerical procedure can be found in Reference 24.

Next, there is the bending of the base, which will be represented by a moment stiffness, k_M . In Reference 24, page 77, a suggested value is

$$k_M = EA_0B_0/5.3 \quad (3.10)$$

where A_0 is the cross-sectional area at the base of the tooth, B_0 is the width at the base ($A_0 = B_0L$, where L is the length of the tooth), and E is the modulus of elasticity.

The deflections at the pitch circle become

$$\delta_t = \frac{h}{k_M} (F_t h - F_r b) \quad (3.11)$$

$$\delta_r = \frac{b}{k_M} (F_t h - F_r b)$$

These equations shall be written as

$$\delta_t = \delta_{2t} F_t - \delta_{4t} F_r \quad (3.12)$$

$$\delta_r = \delta_{2r} F_t - \delta_{4r} F_r$$

where

$$\delta_{2t} = h^2/k_M \quad (3.13)$$

$$\delta_{2r} = \delta_{4t} = hb/k_M \quad (3.14)$$

$$\delta_{4r} = b^2/k_M \quad (3.15)$$

Finally, there is a radial compression of the tooth:

$$\delta_r = \delta_{5r} F_r \quad (3.16)$$

where

$$\delta_{5r} = \frac{1}{k_C} + \int_0^h \frac{dr}{EA} \quad (3.17)$$

and k_C is the radial stiffness of the base. The total deflection is the sum of the separate contributions. By adding Equations 3.6, 3.12, and 3.16, it is found that

$$\delta_t = (\delta_{1t} + \delta_{2t}) F_t - (\delta_{1r} + \delta_{2r}) F_r \quad (3.18)$$

$$\delta_r = (\delta_{1r} + \delta_{2r}) F_t - (\delta_{3r} + \delta_{4r} + \delta_{5r}) F_r$$

The flexibility coefficients δ_{1t} to δ_{5r} include the contributions from both of the teeth.

The deflection in the load direction is determined from Equation 3.2 with substitution from Equations 3.1 and 3.18:

$$\begin{aligned} \delta = & [(\delta_{1t} + \delta_{2t}) \cos^2 \psi + (\delta_{3r} + \delta_{4r} + \delta_{5r}) \sin^2 \psi \\ & - (\delta_{1r} + \delta_{2r}) \sin 2\psi] F \end{aligned} \quad (3.19)$$

Hence, the stiffness of two teeth in contact is

$$\begin{aligned} K_\psi = & F/\delta \\ = & 1/ [(\delta_{1t} + \delta_{2t}) \cos^2 \psi + (\delta_{3r} + \delta_{4r} + \delta_{5r}) \sin^2 \psi \\ & - (\delta_{1r} + \delta_{2r}) \sin 2\psi] \end{aligned} \quad (3.20)$$

Let the number of teeth be n and introduce a ξ - η - z coordinate system with the z -axis coinciding with the rotor axis, as shown in Figure 3-3a. Tooth j is located at the angle γ_j from the ξ -axis. If the relative lateral displacements between the two coupling parts are $\Delta\xi$ and $\Delta\eta$, the displacement in the load direction becomes

$$\delta_j = -\Delta\xi \sin(\gamma_j - \psi) + \Delta\eta \cos(\gamma_j - \psi) \quad (3.21)$$

The corresponding contact force is $F_j = K\psi\delta_j$. When projected into the two axes and summed over all n teeth, the result is

$$\begin{aligned} -F_\eta &= \sum_{j=1}^n -F_j \sin(\gamma_j - \psi) \\ &= K\psi \sum_{j=1}^n [\Delta\xi \sin^2(\gamma_j - \psi) - \Delta\eta \cos(\gamma_j - \psi) \sin(\gamma_j - \psi)] \end{aligned} \quad (3.22)$$

$$\begin{aligned} -F_\xi &= \sum_{j=1}^n -F_j \cos(\gamma_j - \psi) \\ &= K\psi \sum_{j=1}^n [\Delta\eta \cos^2(\gamma_j - \psi) - \Delta\xi \cos(\gamma_j - \psi) \sin(\gamma_j - \psi)] \end{aligned}$$

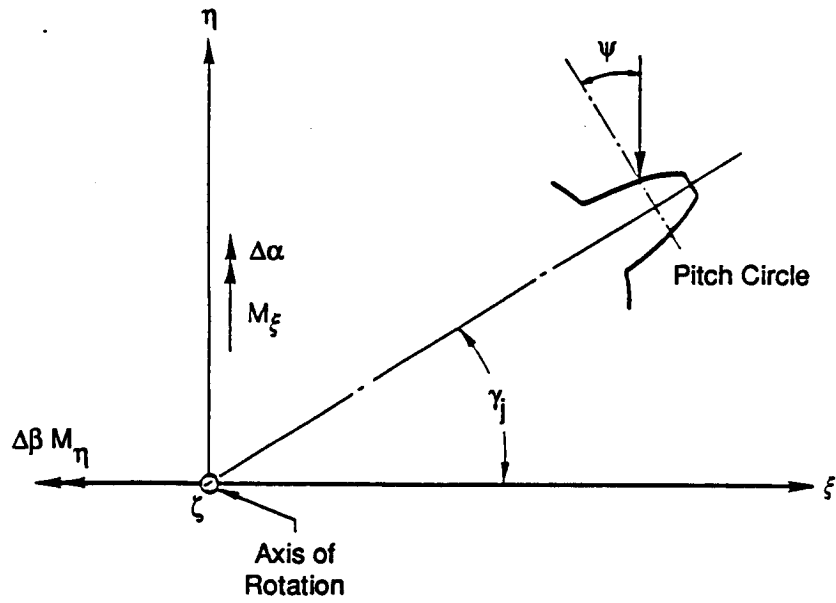
For evenly spaced teeth and $n > 3$, the following identities apply

$$\sum_{j=1}^n \cos^2 \gamma_j = \sum \sin^2 \gamma_j = n/2 \quad (3.23)$$

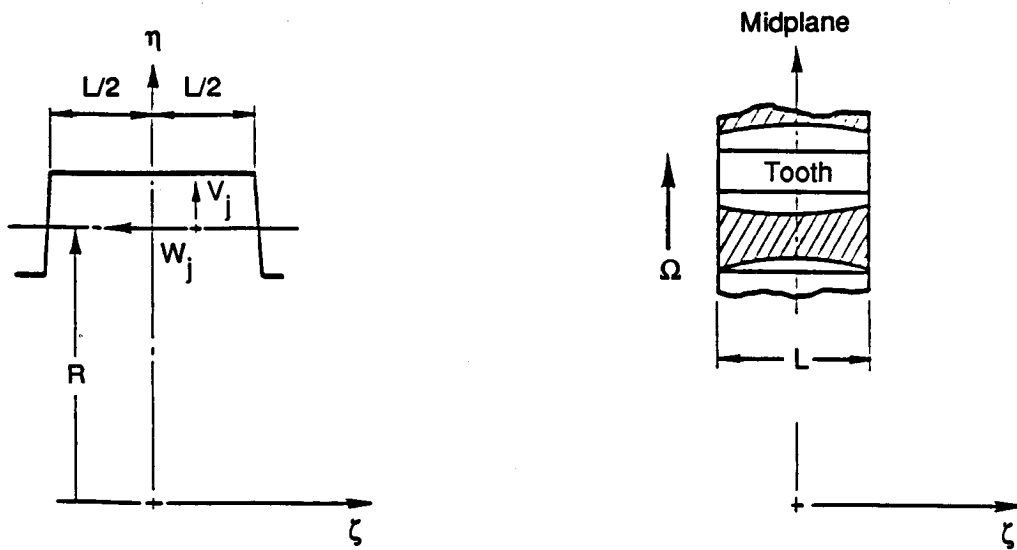
$$\sum_{j=1}^n \cos^2 \gamma_j \sin^2 \gamma_j = 0$$

Thereby Equation 3.22 can be written as

$$F_\xi = -K_L \Delta\xi, \quad F_\eta = -K_L \Delta\eta \quad (3.24)$$



a) Cross-Sectional View



b) Side View

c) Top View

86420

Figure 3-3. Tooth Geometry and Coordinate System Fixed on the Rotor

where the lateral stiffness is given by

$$K_L = nK_\psi/2 \quad (3.25)$$

To determine the angular stiffness of the spline coupling, the tooth stiffness per unit length shall be set equal to K_ψ/L where L is the axial length of the teeth. The relative angular displacements between the two coupling parts are $\Delta\alpha$ and $\Delta\beta$, assigned at the center plane of the coupling (α and β represent the local slopes of the deformed rotor axis such that $\alpha \sim d\xi/dz$ and $\beta \sim d\eta/dz$). At the distance z from the center plane, the displacement in the tooth load direction is

$$\delta_j = z [-\Delta\alpha \sin(\gamma_j - \psi) + \Delta\beta \cos(\gamma_j - \psi)] \quad (3.26)$$

The corresponding contact force, acting over an infinitesimal length dz , is

$$dF_j = \delta_j (K_\psi/L) dz$$

The associated bending moment at the center plane is $z dF_j$ and integrated over the length of the tooth, the resulting bending moment becomes

$$\int_{-L/2}^{L/2} z dF_j = \frac{1}{12} L^2 K_\psi [-\Delta\alpha \sin(\gamma_j - \psi) + \Delta\beta \cos(\gamma_j - \psi)] \quad (3.27)$$

By summing over all teeth, the two components of the bending moment along the axes become

$$-M_\xi = \sum_{j=1}^n \frac{L^2 K_\psi}{12} [\Delta\alpha \sin(\gamma_j - \psi) - \Delta\beta \cos(\gamma_j - \psi)] \sin(\gamma_j - \psi) \quad (3.28)$$

$$-M_\eta = \sum_{j=1}^n \frac{L^2 K_\psi}{12} [-\Delta\alpha \sin(\gamma_j - \psi) + \Delta\beta \cos(\gamma_j - \psi)] \cos(\gamma_j - \psi)$$

By making use of Equation 3.23, the equations reduce to

$$M_\xi = - K_A \Delta\alpha \quad (3.29)$$

$$M_\eta = - K_A \Delta\beta$$

where the angular stiffness is given by

$$K_A = L^2 n K_\psi / 24 = L^2 K_L / 12 \quad (3.30)$$

It should be emphasized that this derivation, as also the one for the lateral stiffness, tacitly assumes that all teeth are in contact and stay in contact during the motion. The assumption implies that the prestress caused by the steady torque is never completely relieved by the dynamic stresses or, in other words, that the dynamic contact force, F_j , never exceeds the steady contact force. This is the equivalent of the assumption of no backlash in a torsional vibration analysis.

In practice, tolerance effects will prevent equal sharing of the load among the teeth even to the point where some teeth may not be engaged at all. For this reason, the number of teeth, n , which is used to compute the stiffnesses, should be replaced by some effective number, based on tests and experience.

3.1.1.2 Spline Friction. In addition to stiffness, the spline coupling will also have friction. In the preceding analysis, the tooth contact offers no resistance to motion tangent to the surface and here sliding may take place. Under idealized conditions, where the teeth share the load equally, the normal force equals $T/nR\cos\psi$ where T is the steady transmitted torque, R is the radius of the pitch circle, n is the number of teeth, and ψ is the pressure angle. Hence, the friction force per unit length is $\mu T/nRL\cos\psi$ where μ is the coefficient of friction. It is directed opposite the local sliding velocity.

From Figure 3-3, the velocity tangent to the tooth profile is

$$v_j = (\Delta\dot{\xi} + \zeta\Delta\dot{\alpha})\cos(\gamma_j - \psi) + (\Delta\dot{\eta} + \zeta\Delta\dot{\beta})\sin(\gamma_j - \psi) \quad (3.31)$$

The velocity in the axial direction at the pitch circle is

$$w_j = R (\Delta\dot{\alpha} \cos\gamma_j + \Delta\dot{\beta} \sin\gamma_j) \quad (3.32)$$

where "dot" means time derivative. A side view of the tooth flank depicts the situation in Figure 3-3b. The friction force from the infinitesimal length $d\zeta$ has radial and axial components given by

$$dF_{vj} = \frac{\mu T}{nRL \cos \psi} \frac{v_j}{(v_j^2 + w_j^2)^{1/2}} d\zeta$$

$$dF_{wj} = \frac{\mu T}{nRL \cos \psi} \frac{w_j}{(v_j^2 + w_j^2)^{1/2}} d\zeta$$
(3.33)

Integrating dF_{vj} over the length, projecting it onto the ξ and η axes, and finally, summing over all teeth gives the F_ξ and F_η components of the friction force. Similarly, by integrating $\zeta dF_{vj} + R dF_{wj}$ over the length, projecting onto the axes, and summing over all teeth gives the M_ξ and M_η components of the friction moment.

The procedure as such is straightforward and is readily implemented in a time step integration of the motion. It is, however, cumbersome and results in a nonlinear coupling of the lateral and angular motions through the term $(V_j^2 + W_j^2)^{1/2}$. This appears to be an unwarranted complication considering the uncertainties and approximations inherent in the idealized physical model. Instead, a simplified model shall be adopted in which V_j is ignored such that all the friction is taken up in the bending moment while the shear force is unaffected. The principal justification is that the bending moment plays a bigger role in the deformation of the rotor than the shear force. Furthermore, in some spline coupling designs, the lateral motion may be restricted by pilots. With V_j equal to zero, dF_{wj} in Equation 3.33 is readily integrated to give:

$$F_{wj} = \text{sgn}(w_j) \frac{\mu T}{2\pi R \cos \psi} \Delta\gamma$$
(3.34)

where $\Delta\gamma = 2\pi/n$. The corresponding components of the bending moment are

$$-M_\xi = \sum_j^n F_{wj} R \cos \gamma_j$$

$$-M_\eta = \sum_j^n F_{wj} R \sin \gamma_j$$
(3.35)

When the number of teeth, n , is sufficiently large, $\Delta\gamma$ in Equation 3.34 can be replaced by $d\gamma$, and the summations in Equation 3.35 replaced by integrations over γ , such that

$$\begin{aligned}
-M_{\xi} &= \frac{\mu T}{2\pi \cos \psi} \int_0^{2\pi} \operatorname{sgn}(w) \cos \gamma \, d\gamma \\
-M_{\eta} &= \frac{\mu T}{2\pi \cos \psi} \int_0^{2\pi} \operatorname{sgn}(w) \sin \gamma \, d\gamma
\end{aligned} \tag{3.36}$$

where

$$\operatorname{sgn}(w) = \begin{cases} +1 & \text{when } w > 0 \\ -1 & \text{when } w < 0 \end{cases} \tag{3.37}$$

w is given by Equation 3.32 as

$$\begin{aligned}
w &= R (\Delta \dot{\alpha} \cos \gamma + \Delta \dot{\beta} \sin \gamma) \\
&= R [(\Delta \dot{\alpha}^2 + \Delta \dot{\beta}^2) \cos(\gamma - \lambda)]^{1/2}
\end{aligned} \tag{3.38}$$

where

$$\begin{aligned}
\cos(\lambda) &= \Delta \dot{\alpha} / (\Delta \dot{\alpha}^2 + \Delta \dot{\beta}^2)^{1/2} \\
\sin(\lambda) &= \Delta \dot{\beta} / (\Delta \dot{\alpha}^2 + \Delta \dot{\beta}^2)^{1/2}
\end{aligned} \tag{3.39}$$

Thereby it is seen that

$$\operatorname{sgn}(w) = \begin{cases} +1 & \text{when } \lambda - \pi/2 < \gamma < \lambda + \pi/2 \\ -1 & \text{when } \lambda + \pi/2 < \gamma < \lambda + 3\pi/2 \end{cases} \tag{3.40}$$

The integrals in Equation 3.36 are then computed as

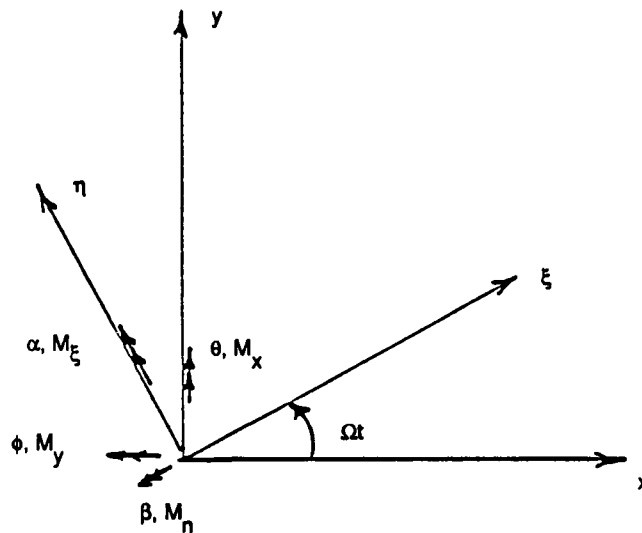
$$\begin{aligned}
\int_0^{2\pi} \operatorname{sgn}(w) \cos(\gamma) \, d\gamma &= 4 \cos \lambda \\
\int_0^{2\pi} \operatorname{sgn}(w) \sin(\gamma) \, d\gamma &= 4 \sin \lambda
\end{aligned} \tag{3.41}$$

and Equation 3.36 reduces to

$$\begin{aligned}
 -M_{\xi} &= \frac{2\mu T}{\pi \cos \psi} \frac{\Delta \dot{\alpha}}{(\Delta \dot{\alpha}^2 + \Delta \dot{\beta}^2)^{1/2}} \\
 -M_{\eta} &= \frac{2\mu T}{\pi \cos \psi} \frac{\Delta \dot{\beta}}{(\Delta \dot{\alpha}^2 + \Delta \dot{\beta}^2)^{1/2}}
 \end{aligned}
 \tag{3.42}$$

These should be added to Equation 3.29 to obtain the total bending moment. They apply in a coordinate system that is fixed in the spline coupling and, therefore, is rotating with the angular speed, Ω , of the rotor.

3.1.1.3 Transformation to a Fixed Reference Frame. To convert into fixed coordinates, an x-y-z-coordinate system, fixed on the ground, is introduced, with the z-axis along the rotor axis (coinciding with the ζ -axis). The relative lateral displacements between the two coupling parts are Δx and Δy , and the relative angular displacements are $\Delta \theta$ and $\Delta \phi$ (they give the slope of the deflected rotor axis such that $\theta \sim dx/dz$ and $\phi \sim dy/dz$). The corresponding shear forces are V_x and V_y , and the bending moments are M_x and M_y . The transformations between the two coordinate systems (see Figure 3-4) are



90565A

Figure 3-4. Transformation from Rotating to Fixed Coordinate Systems

$$\begin{aligned}\Delta\theta &= \Delta\alpha \cos\Omega t - \Delta\beta \sin\Omega t \\ \Delta\phi &= \Delta\alpha \sin\Omega t + \Delta\beta \cos\Omega t\end{aligned}\quad (3.43)$$

$$\begin{aligned}\Delta\dot{\theta} + \Omega\Delta\phi &= \Delta\dot{\alpha} \cos\Omega t - \Delta\dot{\beta} \sin\Omega t \\ \Delta\dot{\phi} - \Omega\Delta\theta &= \Delta\dot{\alpha} \sin\Omega t + \Delta\dot{\beta} \cos\Omega t\end{aligned}\quad (3.44)$$

$$\begin{aligned}M_x &= M_\xi \cos\Omega t - M_\eta \sin\Omega t \\ M_y &= M_\xi \sin\Omega t + M_\eta \cos\Omega t\end{aligned}\quad (3.45)$$

By substituting Equations 3.29 and Equation 3.42 into Equation 3.45 and by making use of Equations 3.43 and 3.44, it is found that

$$\begin{aligned}-M_x &= K_A\Delta\theta + \frac{2\mu T}{\pi\cos\psi} (\Delta\dot{\theta} + \Omega\Delta\phi) / (\Delta\dot{\alpha}^2 + \Delta\dot{\beta}^2)^{1/2} \\ -M_y &= K_A\Delta\phi + \frac{2\mu T}{\pi\cos\psi} (\Delta\dot{\phi} - \Omega\Delta\theta) / (\Delta\dot{\alpha}^2 + \Delta\dot{\beta}^2)^{1/2}\end{aligned}\quad (3.46)$$

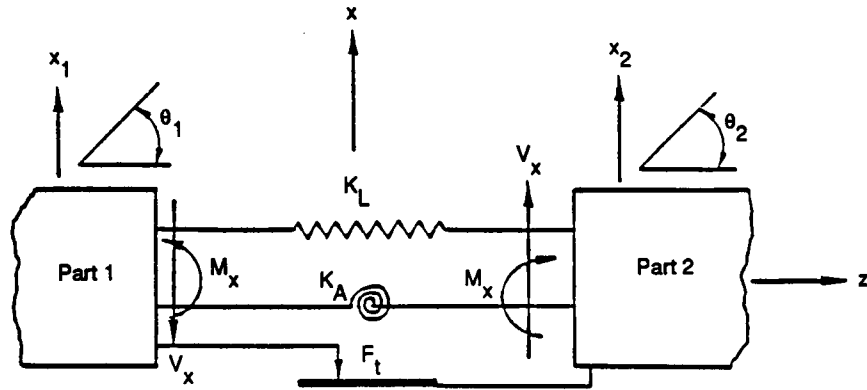
where

$$\Delta\dot{\alpha}^2 + \Delta\dot{\beta}^2 = (\Delta\dot{\theta} + \Omega\Delta\phi)^2 + (\Delta\dot{\phi} - \Omega\Delta\theta)^2\quad (3.47)$$

Similarly, the shear forces become

$$\begin{aligned}V_x &= -K_L \Delta x \\ V_y &= -K_L \Delta y\end{aligned}\quad (3.48)$$

The omission of a minus sign in Equations 3.46 is due to the adopted sign convention as shown in Figure 3-5. In the rotor model, the two parts of the spline coupling are



90565B

Figure 3-5. Parts of the Rotor Interconnected by the Spline Coupling Model

represented by two lumped mass stations, connected by the contacting teeth. The relative displacements across the coupling are

$$\begin{aligned} \Delta x &= x_2 - x_1, & \Delta y &= y_2 - y_1 \\ \Delta \theta &= \theta_2 - \theta_1, & \Delta \phi &= \phi_2 - \phi_1 \end{aligned} \quad (3.49)$$

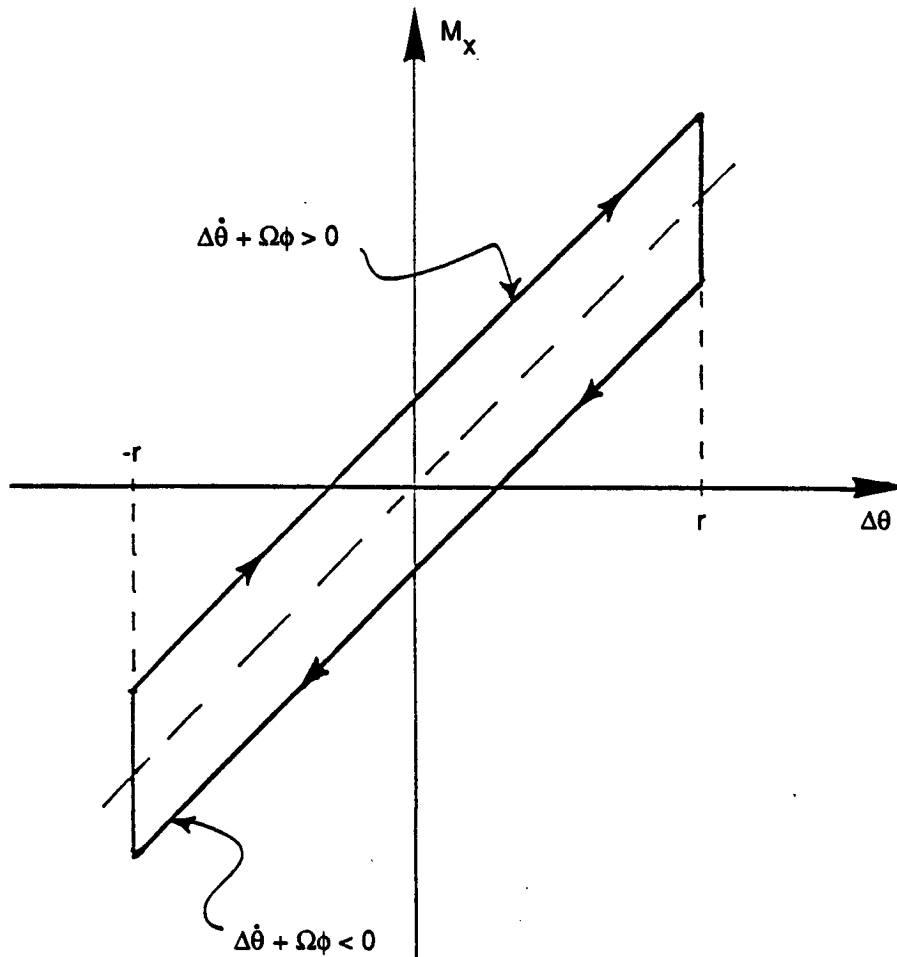
With these definitions, Equations 3.46 and 3.48 can be used directly in a rotor dynamics calculation. In the general case, numerical integration of the equations of motion is required.

In the special case of a rotor in isotropic bearings, the whirl orbit will be circular and Equation 3.46 gives rise to a closed hysteresis loop depicted in Figure 3-6. The circular motion is given by

$$\Delta \theta = r \cos \omega t \quad \Delta \phi = r \sin \omega t \quad (3.50)$$

where ω is a resonant frequency of the rotor and r is the "radius" in the orbit. The energy dissipated over one cycle is

$$U = \int_0^{2\pi/\omega} (M_x \dot{\Delta \theta} + M_y \dot{\Delta \phi}) dt = \operatorname{sgn}(\omega - \Omega) \frac{4\mu T}{\cos \psi} r \quad (3.51)$$



90566

Figure 3-6. Hysteresis Loop in the Plane of Transmitted Moment vs Relative Deflection across the Spline for a Circular Orbit

When $\Omega > \omega$, the energy becomes negative and the dry friction acts to destabilize the rotor. The whirl motion given by Equation (50) is forward whirl. For a backward whirl (change sign of $\Delta\phi$) the dissipated energy will always be positive. In the general case, the whirl orbit is elliptical, containing both a forward and a backward whirl component, and the hysteresis loop will not necessarily close.

3.1.2 Interference Fit Joint

Extensive research went into studying the phenomenon of microslip as it occurred in an interference fit joint in a rotor under transient conditions. This is a very complex nonlinear three dimensional elasticity problem to solve analytically. Most researchers use numerical methods (i.e., finite element method with nonlinear "gap" elements) to

obtain results, and this is usually in two dimensions under static loading. No closed-form solution is known, even for the linear problem of a sleeve transmitting a bending moment to the shaft to which it is welded at the interface, as shown schematically in Figure 3-7.

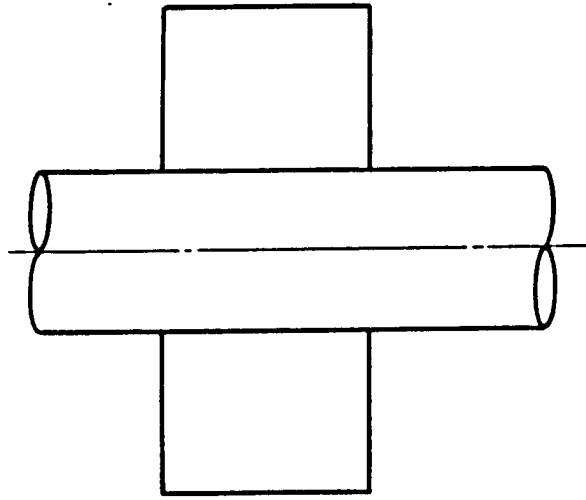
This problem was examined with a three dimensional finite element model in order to understand the incipience of interfacial slip (see Appendix A). Figure 3-8 is a plot of the growing slip zones on the contact surface as the transmitted bending moment is increased. By studying the ratio of the shear stress transmitted across the interface to the product of the coefficient of friction and the normal stress there, it is found that slip first begins to occur at the edge of the sleeve, at Point A on the circumference where the contact pressure decreases most rapidly with transmitted bending moment (see Figure 3-7). As the moment increases, this slip region grows both axially and circumferentially from its point of origin. Point B, which is diametrically opposed to Point A and near the middle of the interference fit region, is the site of another developing slip region in which the two surfaces are separating and the interface is traction free (unless the interference pressure is very large).

Under transient conditions, it is expected that a new slip region will develop from the first (and perhaps later the second) of the above-mentioned locations every time there is a reversal in the sign of the relative angular velocity across the joint, analogous to what occurs in the one dimensional lap joint problem discussed in Section 3.1.3.

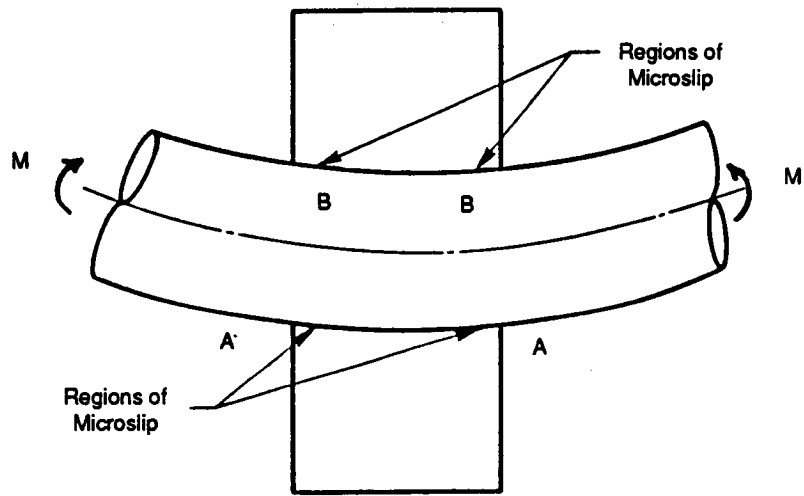
In order to implement a tractable interference fit joint model in the rotordynamic analysis, a macroslip joint model was developed. This model is essentially an elastic angular connection that transmits a moment up to a maximum value beyond which it slips. The first macroslip model consisted of a massless sleeve that was relieved in the center. (The details of this analysis are given in Appendix B.) Finally, a macroslip joint model was developed in order to achieve the interconnections between any two levels of the rotor model. The analysis is described below.

Figure 3-9 is a schematic of an interference fit between a shaft and a section of sleeve. The bending moment transmitted from one of these members to the other across the interface, due to a difference in slope in the axial centerlines of the members, is due to

- Forces normal to the interface (pressure)
- Forces tangent to the interface (frictional forces).



Undeformed Rotor



Rotor Undergoing
Stress-Reversals
During Whirl

90567

Figure 3-7. Microslip under an Interference Fit

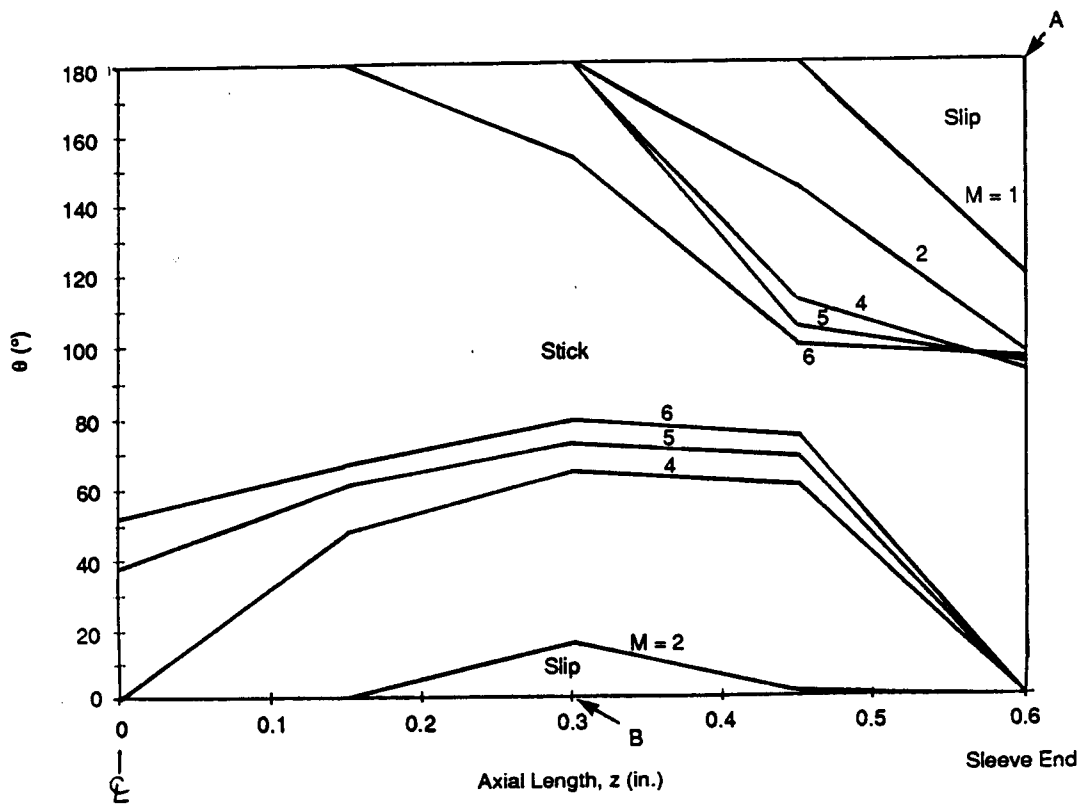


Figure 3-8. Zones of Microslip on Interference Surface

90568

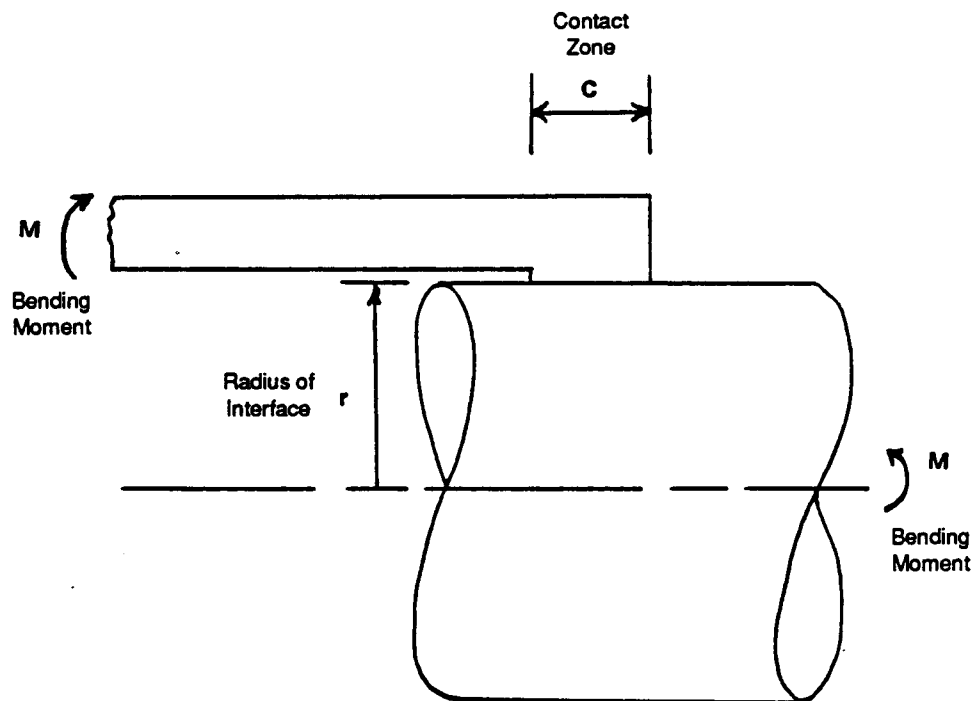


Figure 3-9. Interference Fit Schematic

90569

If the interference pressure is large enough and the length of the contact zone (c) is small compared to the radius, the first of these contributions is small and can be neglected compared to the second. The transmitted moment is then due only to the tangential stress at the interface, the magnitude of which is equal to μp where slip has occurred and zero where it has not. The maximum moment that can be transmitted to the sleeve before gross slip occurs can be calculated by integrating the product of the maximum shear stress and the moment arm over the surface of the interface:

$$M_{\max} = \int_{A_c} (\mu p r \sin \gamma) r \, d\gamma \, dr = 4\mu p c r^2 \quad (3.52)$$

where

- A_c = Area of sleeve to shaft interface
- μ = Coefficient of friction
- p = Shrink-fit pressure
- r = Radius of interface
- γ = Circumferential coordinate

Using the same nomenclature as in Section 3.1.1, where the rotor slope components are (α, β) in a rotating frame (fixed on the rotor) and (θ, ϕ) in a nonrotating fixed frame, the components of the instantaneous moment transmitted across the joint are then given by

$$\begin{aligned} -M_x &= K_a \Delta\theta \\ -M_y &= K_a \Delta\phi \end{aligned} \quad \text{if } \chi=0 \text{ and } |M_e| < M_{\max} \quad (3.53a)$$

$$\begin{aligned} -M_x &= M_{\max} (\Delta\dot{\theta} + \Omega\Delta\phi) / \dot{\chi} \\ -M_y &= M_{\max} (\Delta\dot{\phi} - \Omega\Delta\theta) / \dot{\chi} \end{aligned} \quad \text{if } \chi > 0 \text{ or } |M_e| > M_{\max} \quad (3.53b)$$

where

$$M_e = K_a (\Delta\theta^2 + \Delta\phi^2)^{1/2} \quad (3.54a)$$

$$\dot{\chi}^2 = \Delta\dot{\alpha}^2 + \Delta\dot{\beta}^2 = (\Delta\dot{\theta} + \Omega\Delta\phi)^2 + (\Delta\dot{\phi} - \Omega\Delta\theta)^2 \quad (3.54b)$$

$$\Delta\alpha = \alpha_2 - \alpha_1 - \Delta\alpha_s \quad (3.54c)$$

$$\Delta\beta = \beta_2 - \beta_1 - \Delta\beta_s \quad (3.54d)$$

M_e is the elastic moment. The subscripts 1 and 2 denote the two sides of the joint while Δ is used to denote the difference in any quantity across the joint. $\Delta\alpha_s$ and $\Delta\beta_s$ are the components of the cumulative amount of angular slip that has occurred between the shaft and the sleeve since initial loading and are calculated by integration versus time of

$$\dot{\Delta\alpha}_s = \begin{cases} 0 & \text{if } \dot{\chi}=0 \text{ and } |M_e| < M_{\max} \\ \dot{\Delta\alpha} & \text{if } \dot{\chi}>0 \text{ or } |M_e| > M_{\max} \end{cases} \quad (3.55a)$$

$$\dot{\Delta\beta}_s = \begin{cases} 0 & \text{if } \dot{\chi}=0 \text{ and } |M_e| < M_{\max} \\ \dot{\Delta\beta} & \text{if } \dot{\chi}>0 \text{ or } |M_e| > M_{\max} \end{cases} \quad (3.55b)$$

When $d\alpha_1/dt = d\alpha_2/dt$ and $d\beta_1/dt = d\beta_2/dt$, $d\chi/dt = 0$, the joint is locked and the moment transmitted is elastic (M_e) until it exceeds the maximum friction moment (M_{\max}). The energy dissipated in the joint can be calculated by integrating the product of the relative displacements and the shear stress over the slipping interfaces. It can be found by integration versus time of

$$\frac{dE}{dt} = M_x \dot{\Delta\theta} + M_y \dot{\Delta\phi} \quad (3.56)$$

When the joint is locked, the relative angular velocity across the joint is zero and no energy is dissipated.

This mathematical model differs from that of the spline only in that the joint may be locked during some parts of the transient simulation. When the joint is slipping, the friction moment transmitted across the joint is constant in magnitude (M_{\max}) and opposite to the relative angular velocity in direction, just like the spline model discussed in Section 3.1.1, which transmits a friction moment equal to $\mu T/\pi$.

The phenomenon of joint reattachment introduces great numerical difficulties, since the discontinuity in joint stiffness associated with the stick/slip phenomenon introduces a very high natural frequency for which the time integration of the governing equations must use a very small time step. In order to circumvent this numerical difficulty, the time integration was performed at every time step assuming that no reattachment had occurred. After each step, a check was performed to see if during the time step

- The relative velocity was small in magnitude
- Both components of relative velocity switched sign.

If both conditions were met, interpolation was performed for the time within the time step when the relative velocity across the joint became zero, at which time the simulation was continued assuming that the joint was stuck. Among the rotor model simulations that were performed with this "macroslip" type of interference joint, reattachment occurred rarely if at all (one or two times out of 30,000 time steps) and did not appear to have any significant effect on rotor behavior or stability.

3.1.3 Curvic Coupling

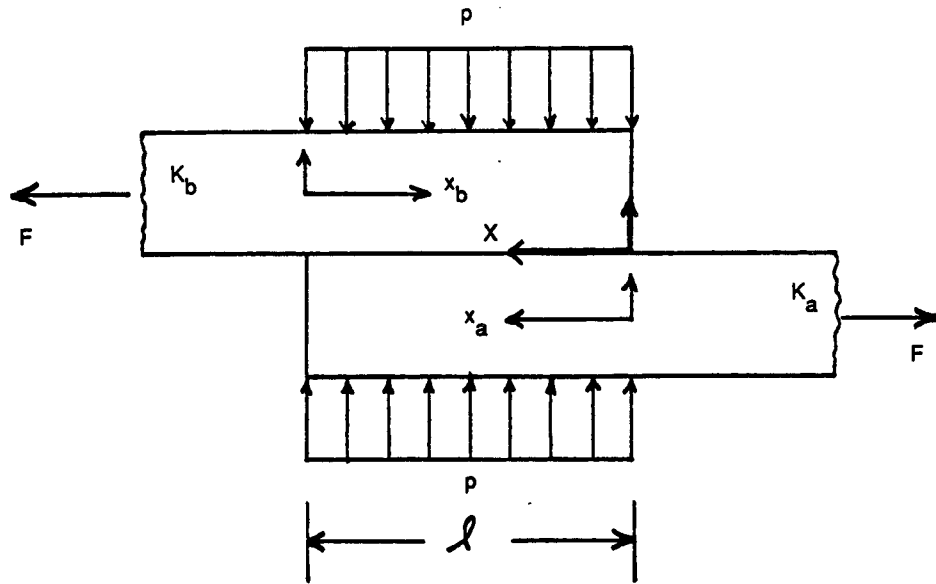
The HPOTP Curvic coupling consists of two rows of 36 teeth that protrude axially from the two structural members and mesh with each other. The two members of the coupling are bolted together by axial bolts at a bolt circle that lies between the inner and outer rows of teeth. The Curvic model developed here consists of a discrete number of lap joints evenly distributed around the circumference to represent each of the tooth pairs, as well as radial and angular elastic stiffnesses (in parallel to the teeth) to represent the bolt forces. The pressure acting to press the teeth together is assumed to be constant and independent of transmitted torque or bending moment. This is the case when the bolt prestress is relatively high and is the largest contributor to the normal tooth contact forces. Each of the tooth interfaces may have any number of slip regions that must be kept track of as functions of time.

Lap joints have been analyzed previously by a number of researchers. However, the solution of the governing equations for an arbitrary load history had to be developed as part of the present work, as described below.

Figure 3-10 illustrates the lap joint geometry. It consists of two stiffness members that

- Are of constant cross-sectional area
- Are pressed against each other under a constant pressure, p
- Overlap by an amount ℓ .

Only displacements along the length of the members (axial direction) are considered, and these are only functions of the coordinate (x) along this direction (i.e., there is no bending). For the i -th member (where $i = a$ for the lower member and $i = b$ for the top



90570

Figure 3-10. Lap Joint Geometry

member), the relationship between the local axial force, f_i , and displacement, u_i , is given by the differential equation

$$\frac{du_i}{dx} = \frac{f_i}{K_i} \quad (3.57a)$$

$$K_i = A_i E_i \quad (3.57b)$$

where K_i is the longitudinal stiffness, A_i is the cross-sectional area, and E_i is Young's modulus. A force balance on member i about a differential element of length, dx , gives the relationship between the axial force and the applied shear stress at the surface:

$$\frac{df_i}{dx} = -T w \quad (3.58)$$

where T is the shear stress applied by the other member in the positive x direction and w is the width of the contact.

The governing equations can be consolidated if we now define coordinates x_i measured along the length, starting at the end of the other member ($x_i = 0$) toward the end of the i -th member ($x_i = l$):

$$x_a = x \quad (3.59a)$$

$$x_b = l - x \quad (3.59b)$$

$$x_a + x_b = l \quad (3.59c)$$

Then, the equation governing the force and its boundary conditions can be written:

$$\frac{df_i}{dx_i} = -T_i w \quad (3.60)$$

$$f_i(x_i=0) = f \quad (3.61a)$$

$$f_i(x_i=l) = 0 \quad (3.61b)$$

where T_i is the shear stress applied to the i -th member in the positive x_i direction and f is the total force transmitted across the joint.

As the total displacement across the joint is changed, one of two things happen:

1. Under initial loading or if the time rate of change of the displacement is of the opposite sign from the previous time that the displacement changed, a new region of slip develops from each of the ends of the two members.
2. If the time rate of change of the displacement is of the same sign as the previous time that the displacement changed, the extent of the outermost region of slip increases with increasing (or decreases with decreasing) displacement.

The shear stress within the growing (outer) slip region has the same sign as the time rate of change of the displacement. As this region expands, it is continuously reversing the direction of the shear stress at its border, while outside of this region, the state of shear stress remains unaffected.

The total displacement across the joint is related to the applied force by the following integral equations:

$$U = \frac{u K}{l f_{\max}} = (C_1 F + C_3 \int_0^1 \zeta s(\zeta) d\zeta) \quad (3.62a)$$

$$= \int_0^1 (C_1 + C_3 \zeta) s(\zeta) d\zeta$$

$$F = \frac{f}{f_{\max}} = \int_0^1 s(\zeta) d\zeta \quad (3.62b)$$

where

$$f_{\max} = \mu p w l \quad (3.63)$$

$$C_1 = C_2 - C_3 \quad (3.64a)$$

$$C_2 = \frac{K_a^2 + K_b^2}{K_a K_b} \quad (3.64b)$$

$$C_3 = \frac{K_a^3 + K_b^3}{K K_a K_b} \quad (3.64c)$$

$$K = K_a + K_b \quad (3.65)$$

The maximum friction force, f_{\max} , and the friction coefficient, μ , can be transmitted across a tooth pair. The function $s(\zeta)$ represents the sign of the shear stress in each slip region. It is either zero where slip has not occurred or ± 1 where it has. If the sign of (du/dt) when the j -th slip region is formed is denoted by s_j and n is the number of slip regions present, the function s may be written as

$$\begin{aligned} s(\zeta) &= 0 && \text{for } \zeta_1 < \zeta < 1 \\ &= s_1 && \text{for } \zeta_2 < \zeta < \zeta_1 \\ & && \dots \\ &= s_{n-1} && \text{for } \zeta_n < \zeta < \zeta_{n-1} \\ &= s_n && \text{for } 0 < \zeta < \zeta_n \end{aligned} \quad (3.66)$$

where

$$s_j = -s_{j-1} \quad \text{for } j > 1 \quad (3.67)$$

and

$$\zeta = \frac{K x_i}{K_i \ell} \quad (3.68)$$

is the dimensionless coordinate along any of the members, and the values ζ_j are the dimensionless extents of the slip regions, in order of decreasing size:

$$0 < \zeta_n < \dots < \zeta_2 < \zeta_1 \leq 1. \quad (3.69)$$

When the displacement across the lap joint equals u_{\max} , the friction force equals the maximum allowed (f_{\max}) and macro slip begins. At this point, there is only one slip zone that extends the whole length (ℓ) of the contact, and the shear stress is only in one direction:

$$\begin{aligned} u &= u_{\max}, \quad F=1, \quad n=1, \quad s_1=1, \quad \zeta_1=1 \\ U_{\max} &= \frac{u_{\max} K}{\ell f_{\max}} = (C_1 + C_3/2)/K = (C_2 - C_3/2)/K \quad (3.70) \\ &= \left(1 + \frac{K_a^3 + K_b^3}{2 K K_a K_b} \right) \end{aligned}$$

Beyond this point, any further increase (if it had been increasing or decrease if it had been decreasing) in displacement across the lap joint results in no additional transmitted force. Thus the forward stiffness of the joint is zero and continues to be so until (du/dt) reverses in sign.

When both members have the same stiffness, ($K_a = K_b = K/2$),

$$U_{\max} = 3/2 \quad (3.71a)$$

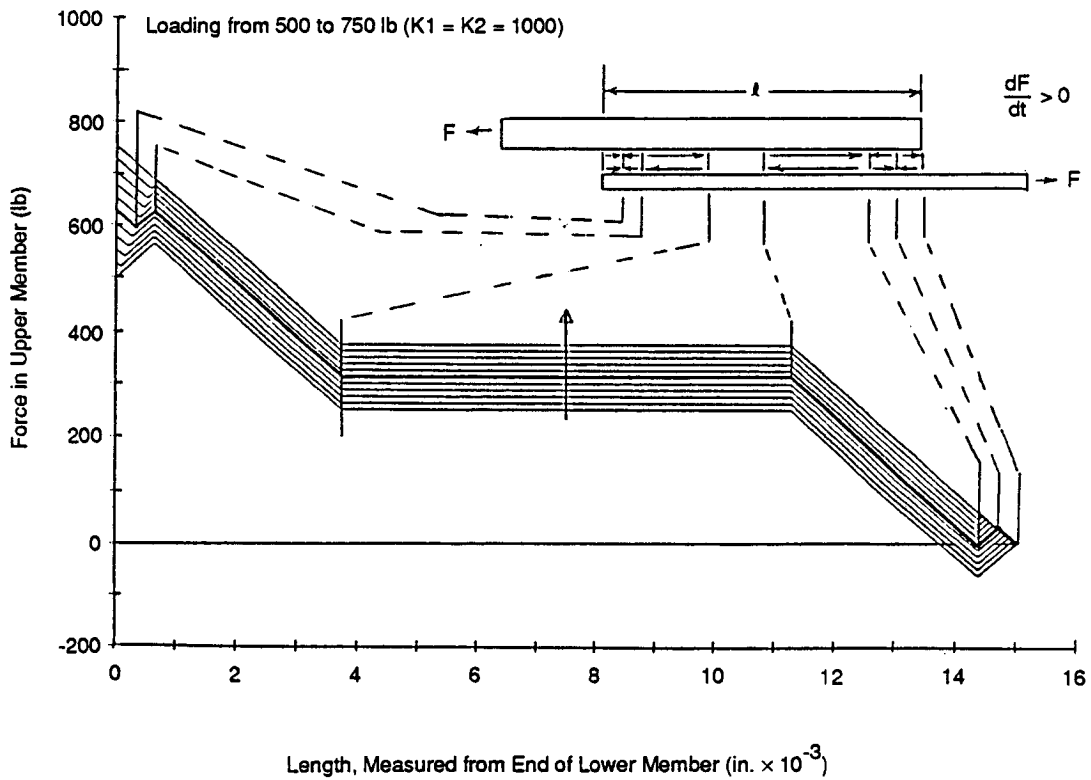
$$u_{\max} = 3\ell f_{\max}/2K \quad (3.71b)$$

Equation 3.62 may be solved for F as a function of U by searching for the position of the newest slip zone, ζ^* , within each of the intervals: $(\zeta_1, 1)$, (ζ_2, ζ_1) , ..., $(0, \zeta_n)$, until the error in satisfying Equation 3.62a changes sign. When the correct interval is found, Equation 3.62a yields a quadratic in ζ^* , the positive root of which is the extent of the new slip zone. Any smaller zones that were previously present ($\zeta_j < \zeta^*$) are eliminated, and the size and sign (ζ_n and s_n) of the new zone are thus established. F is then readily calculated from Equation 3.62b. The inverse problem, calculation of the load for an arbitrary displacement history, is easily performed using a similar approach with Equation 3.62b.

The force in one of the members of a lap joint versus distance along the joint during sample loading and unloading paths is illustrated in Figures 3-11 and 3-12, respectively. Note that within any one slip region, the force varies linearly with distance, so that the displacement varies quadratically. Of course, the sum of the forces on both members is constant and equal to f . Figure 3-13 shows the force transmitted by the joint versus the displacement across the joint length, for a sample load history: initial loading to 750 lb, unloading to -1000 lb, and reloading to 1000 lb. Note that as loading increases or decreases, the stiffness is decreasing continuously (i.e., paths OA, AB, BC) while at points of load reversal (points A, B, C) the stiffness changes discontinuously. The behavior of the lap joint is not only a function of the geometry and the applied load, but also of the load history: during a loading or unloading path, the response of the joint depends strongly on the maximum and minimum forces to which it has been subjected.

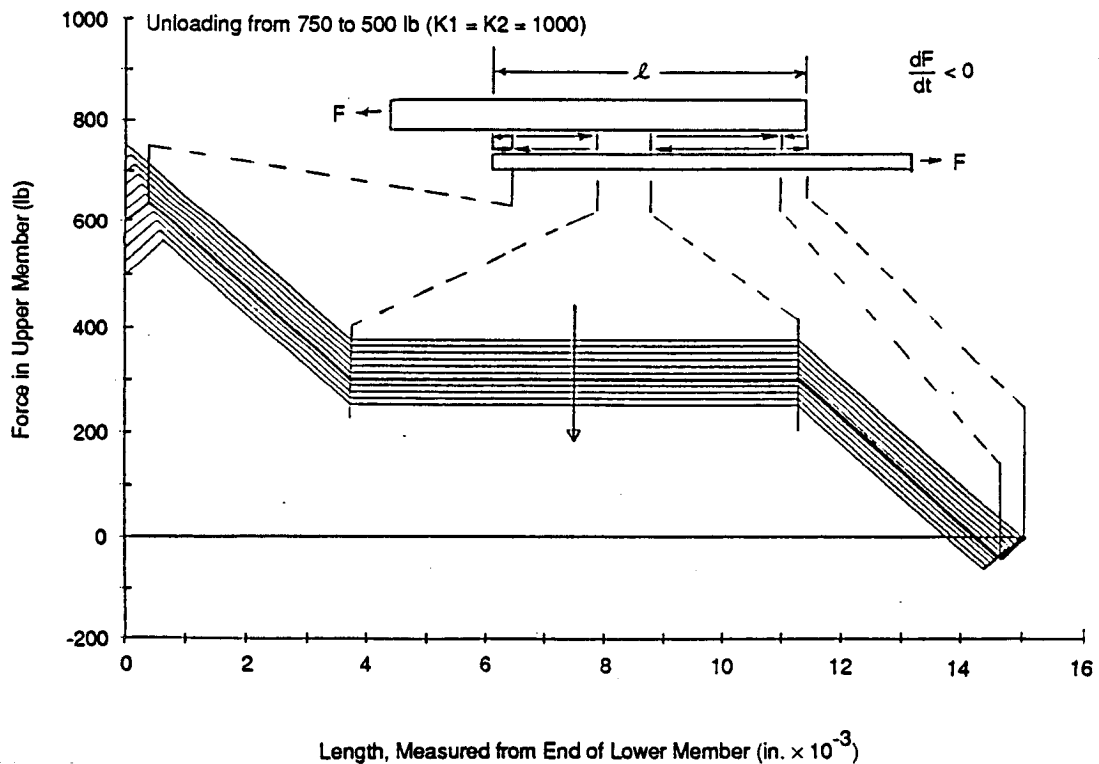
Figure 3-14 is a plot of the dimensionless frictional tooth force versus circumferential position of each tooth pair, as the dimensionless friction moment transmitted across the joint (M^*) is increased. For $0 < M^* < 1.5$, all of the teeth are undergoing microslip and the force that each of them transmits is less than the maximum friction force. As the angular deflection is increased beyond this point, the teeth with the largest moment arms and subsequently the ones next to them undergo macroslip, with the transmitted force constant in magnitude but opposite to the relative velocity. Note, however, that even when $M^* = 4$, the teeth pair with the smallest moment arms is still undergoing microslip.

The energy dissipated in a lap joint that is undergoing an applied load between $-f_0$ and f_0 can be calculated by integrating the area of the hysteresis loop in the displacement versus force plane. Assuming that the reduction in stiffness is small due to friction, we obtain



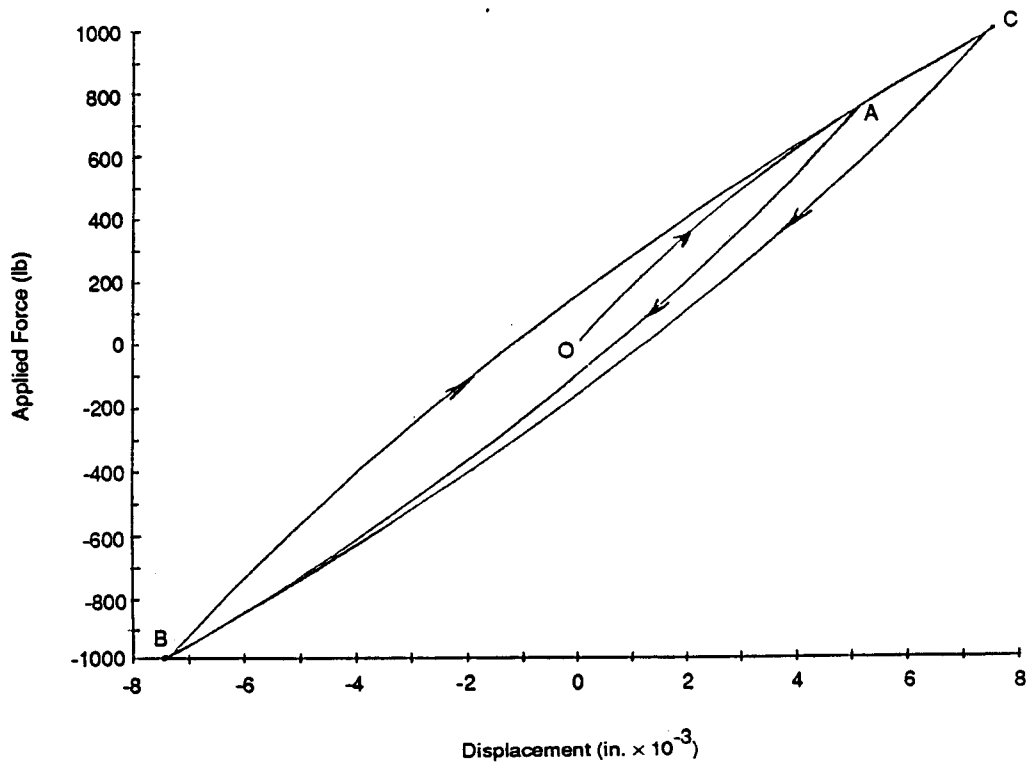
90571

Figure 3-11. Force Distribution along Length of Lap Joint Interface (Upper Member)



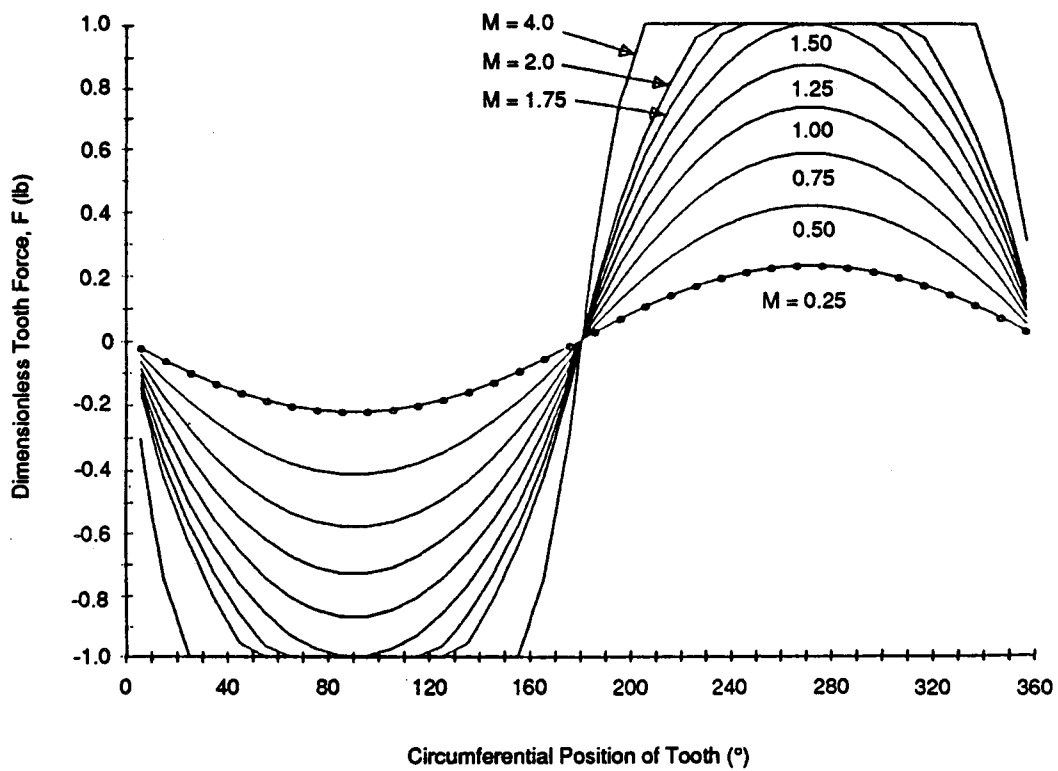
90572

Figure 3-12. Force Distribution along Length of Lap Joint Interface (Lower Member)



90573

Figure 3-13. Plot of Force versus Displacement Hysteresis Loop for Lap Joint



90574

Figure 3-14. Plot of Tooth Force versus Circumferential Position and Applied Moments

$$E = \int_{-f_0}^{f_0} u \, df = C_4 f_0^3 \quad (3.72)$$

Thus, the energy dissipated under oscillatory conditions is independent of frequency but proportional to the cube of the amplitude.

In parallel to the connection brought about by the teeth, there is another structural connection brought about by the axial bolts. These are represented by angular and radial stiffnesses (K_a and K_r) across the coupling joint.

Using the same nomenclature used in Section 3.1.1 for the spline analysis, the bending moment transmitted across the two structural members of the Curvic coupling (expressed in a frame fixed on the rotor) can now be calculated simply by adding all the contributions from all the teeth, as well as that due to the bolts:

$$-M_\zeta = K_A \Delta\alpha + \sum_k^n F_k(u_k) R \cos\gamma_k \quad (3.73a)$$

$$-M_\eta = K_A \Delta\beta + \sum_k^n F_k(u_k) R \sin\gamma_k \quad (3.73b)$$

where $F_k(u_k)$ is the force transmitted across the j -th tooth pair as a function of the relative axial displacement across the tooth pair as given by

$$u_k = R (\Delta\alpha \cos \gamma_j + \Delta\gamma_j) \quad (3.74)$$

As done previously for the spline and interference fit joints, the components of moments transmitted across the coupling may be expressed in the stationary coordinates by Equation 3.45 of Section 3.1.1.

3.2 Integrated Analysis and Parametric Evaluations

After their development, the models of the internal friction components were integrated into a multilevel rotordynamics model and evaluated to study the effects of the rotor-bearing system parameters on stability. This section contains first a brief discussion of the integration procedure and its limitations, the initial conditions, and the rotor model,

followed by the results of an extensive parametric evaluation of the stability of a rotor-bearing system with spline couplings as the internal-friction components. The parameters studied included the friction coefficient, torque, external damping, imbalance, and side force, as well as asymmetric bearing stiffness coefficients.

3.2.1 Numerical Approach

The stability of rotor-bearing systems containing internal friction components was analyzed using a fourth-order Runge-Kutta method to perform the numerical integration of the governing nonlinear equations of motion versus time. Compared to other methods, the Runge-Kutta method was found to be much more accurate in integrating the highly nonlinear equations involved. Two numerical limitations had to be dealt with: first, the time step had to be small enough to preserve numerical stability, and second, the operating conditions and initial conditions had to be such that the frictional joint would continue to slip.

The rotor was modeled with the finite element computer program FEATURE (Finite Element Analytic Tool for Utility Rotordynamic Evaluation), which was developed in a joint effort between MTI and the Electric Power Research Institute (EPRI). This computer program represents the rotor by a number of linear beam elements, which include shear deformations as well as gyroscopic inertia terms. Each of the stations along the length of the rotor contain four degrees of freedom, two lateral and two angular displacements. Active stations are selected where either external forces (such as bearings, imbalance forces, or lateral aerodynamic forces) or internal forces (forces resulting from any interconnection between levels such as from internal friction components) are to be applied. The mass, stiffness, damping, and gyroscopic matrices are then assembled and reduced to eliminate the nonactive degrees of freedom. These matrices, which describe the linear part of the rotordynamic model, are downloaded to a mini-computer where time integration of the nonlinear equations of motion is then performed. The nonlinearities are included in the right-hand-side force vector, which, with the Runge-Kutta integration method, must be evaluated four times within every time step.

3.2.1.1 Time Step Size. The time integration method used in this analysis was the fourth-order Runge-Kutta with a fixed time step. This is an explicit method, whereby the time rates of change of the variables being integrated (the displacements and velocities associated with each degree of freedom) are only a function of the instantaneous values

of these variables. The Runge-Kutta method is accurate even for highly nonlinear problems, provided a small-enough time step is used; the integration error being proportional to the fifth power of the time step size.

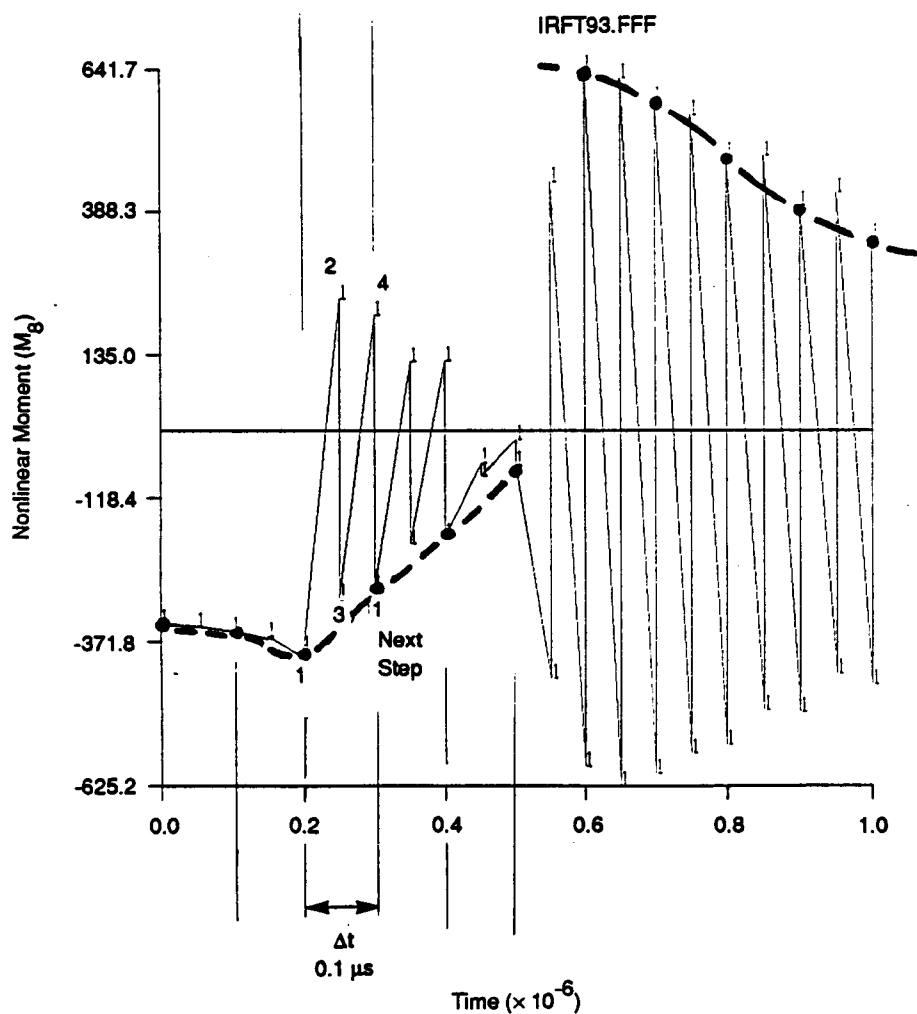
When too coarse a time step is used, the integration becomes numerically unstable. In a numerical instability the variables being integrated become erratic and very large within a very few time steps (increasing exponentially). A numerical instability may be readily identified as such and is easily distinguished from a rotordynamic instability. The time step required for a numerically stable integration usually follows the highest characteristic frequency of the system being simulated. An integration time step equal to about 1/10 of the period of the largest natural frequency is usually adequate for stability. Since the higher frequency modes might not be of interest, "tuning" of the model may be performed in order to lower or eliminate these modes without affecting the modes of interest. This is done by eliminating relatively small masses and/or relatively high element stiffnesses.

The accuracy of this integration method was checked by repeating several simulations with half of the step size (which reduces the integration error by a factor of 32). Good repeatability in the solutions with decreasing time step size was achieved, demonstrating that the subsynchronous vibration and self-excited instabilities obtained were due to the rotor internal friction phenomena.

3.2.1.2 Continuously Slipping Friction Model. A Coulomb friction joint model that assumes a continuously slipping interface will encounter numerical difficulties under near-sticking conditions. As the magnitude of the relative velocity across the joint interface approaches zero, the sign of the friction force in the joint will alternate back and forth every time step.

This can easily be illustrated by numerically integrating the motion of a one-degree-of-freedom system (such as that of a block on top of a table) with a simple tangent-line Euler method. After the initial conditions have decayed, the velocity of the block will become a saw-tooth wave versus time, with an amplitude equal to the maximum friction force (i.e., the coefficient of friction times the weight of the block) times the integration time-step divided by the inertia of the block. In reality, the block will stick to the table the first time that its velocity reaches zero, and the motion will stop.

A more accurate integration method, such as the fourth order Runge-Kutta, does not solve the intrinsic numerical difficulty; rather, because the method involves an average of four evaluations, it tends to camouflage the alternating of the sign of the friction force every time step. This is illustrated in Figure 3-15, which is a plot of a component of the moment across a spline joint near sticking conditions. In this figure, the four evaluations within each time step are connected by a solid line while a dotted line connects only the end points of each time step, which are normally saved for plotting. (A time step of $0.1 \mu\text{sec}$ was used in this illustration.)



90586

Figure 3-15. Moment across Spline versus Time near Sticking Conditions

In order to numerically integrate the behavior of a Coulomb friction joint accurately when it is in near-sticking conditions, the integration procedure must be specifically modified to catch the point of slip or stick. That is, during slipping it is necessary to "freeze" the sign (or direction) of the frictional forces within each time step and then go back and interpolate for the time when the sticking actually took place. After the two degrees of freedom are stuck, they must be treated as one, although the frictional force must subsequently be monitored to catch and similarly interpolate for the incipience of slipping.

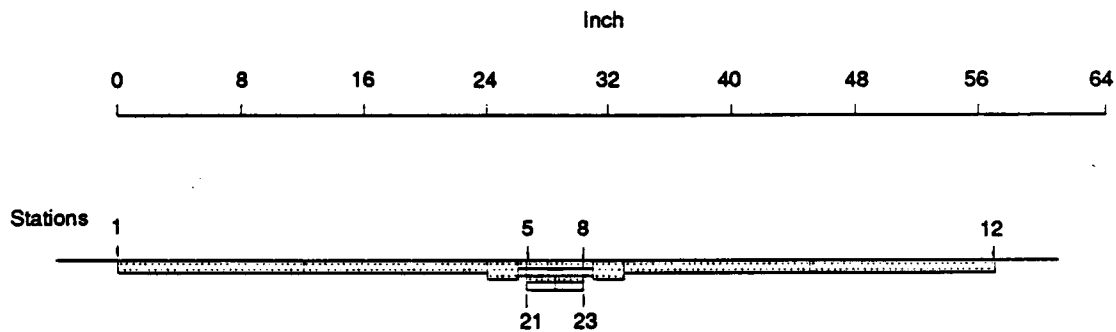
However, the grey zone or boundary separating whether a Coulomb friction joint is stuck or slipping is not of much importance. Some mechanism is usually present (such as the initial transient, an external side load, unbalance forces, or the energy produced by the friction mechanism itself) that will cause the joint to slip. If these conditions are such that the joint is always slipping, the continuously slipping Coulomb friction joint model may be integrated versus time without numerical difficulties. On the other hand, if the joint approaches a condition of stick (as is the case, for example, when the spin speed is below the first bending critical or when sufficiently large external damping is present), the analysis may be stopped before the difficulties with the alternating sign of the frictional force are encountered, since the transitional phenomenon from a slipping to a sticking interface is not relevant to the rotor-bearing stability. After the joint sticks, the model will become linear, and the motion of the rotor will be stable.

In summary, after a careful review, it was concluded that the analysis and integration approach is valid in spite of the limitations associated with continuously slipping friction joint models.

3.2.2 Rotor Model and Initial Conditions

This section presents a discussion of the rotor model that was used to study the spline friction joint model as well as the initial conditions for the parametric study.

3.2.2.1 Rotor Model. A two-level, rotordynamic, finite element model with an axial coupling as the friction-producing joint was prepared in order to evaluate the destabilizing effects of this joint. The model, shown in Figure 3-16, uses one level to describe the main shaft and bearing support structure and a second level to describe the spline sleeve. The two levels are interconnected by the force and moment of the nonlinear spline joint



90587

Figure 3-16. Rotor Model Used to Study Spline Friction Joint

model. The drive shaft (level 1) contains four active stations. Static condensation (Guyan reduction) was used by the finite element rotordynamic code (FEATURE) to remove the degrees of freedom between the active stations, reducing the size of the matrices describing the rotor system. This reduction minimizes both computer memory requirements and program execution time.

The shaft model is connected to ground by the bearings located at each end (stations 1 and 12). Isotropic radial stiffnesses of 100,000 lb/in. and zero angular stiffnesses were used at the bearing locations. The shaft is also connected to the axial spline sleeve (the second level) through one active station near each end of the sleeve. The data describing the rotor dimensions and its mass/elastic properties are given in Table 3-1.

A radial stiffness of 71.5×10^6 lb/in. was calculated for each spline interconnection. The torque transmitted across the spline teeth due to the circumferential offset (18 min) was 5,000 lb-in. Since these joints were lubricated with a dry film, a coefficient of friction of 0.2 was assumed in the rotor joint model. This resulted in a friction moment of $2\mu T/\pi = 636.6$ lb-in. across the joint being used in the time transient simulations. In the parametric study that follows, a reference friction moment coefficient of 500 lb-in. was used, although the value was varied from 0 to 1000 lb-in.

The lowest 5 out of the 24 damped natural frequencies of the linear (zero friction at spline teeth) model with external damping at the sleeve of $B_s = 1$ lb-sec/in. are given in Table 3-2, showing that the first critical speed has both forward and backward whirling modes at 1246.2 and 1248.7 rpm, respectively. The first of these mode shapes is plotted

Table 3-1. Rotordynamic Model for Parametric Study

	Rotor Segment between Stations	Segment Length (in.)	Stiffness Diameter (in.)	Mass Diameter (in.)	Inner Diameter (in.)
Level 1	1 and 2	12.0000	1.6800	1.6800	0.0000
	2 and 3	12.0000	1.6800	1.6800	0.0000
	3 and 4	2.0000	2.5000	2.5000	0.0000
	4 and 5	0.6250	1.0000	2.0000	0.0000
	5 and 6	1.3750	1.0000	2.0000	0.0000
	6 and 7	1.0000	1.0000	1.2000	0.0000
	7 and 8	1.3750	1.0000	2.0000	0.0000
	8 and 9	0.6250	1.0000	2.0000	0.0000
	9 and 10	2.0000	2.5000	2.5000	0.0000
	10 and 11	12.0000	1.6800	1.6800	0.0000
	11 and 12	12.0000	1.6800	1.6800	0.0000
Level 1 Total		57.0000			
Level 2	21 and 22	1.8750	3.0000	3.9002	2.0500
	22 and 23	1.8750	3.0000	3.9002	2.0500
Level 2 Total		3.7500			

Material Number	Modulus of Elasticity (lb/in. ²)	Density (lb/in. ³)	Shear Modulus (lb/in. ²)	Poisson's Ratio
1	0.3000E+08	2.830	0.1100E+08	0.3000

Table 3-2. Five Lowest Natural Frequencies of the Linear Model ($B_s = 1$ lb-sec/in.)

Level	Natural Frequencies		
	rpm	rps	rad/s
1	1246.2	20.770	130.50
2	1248.7	20.811	130.76
3	9883.9	164.73	1035.0
4	9951.5	165.86	1042.1
5	15870.0	246.50	1661.9

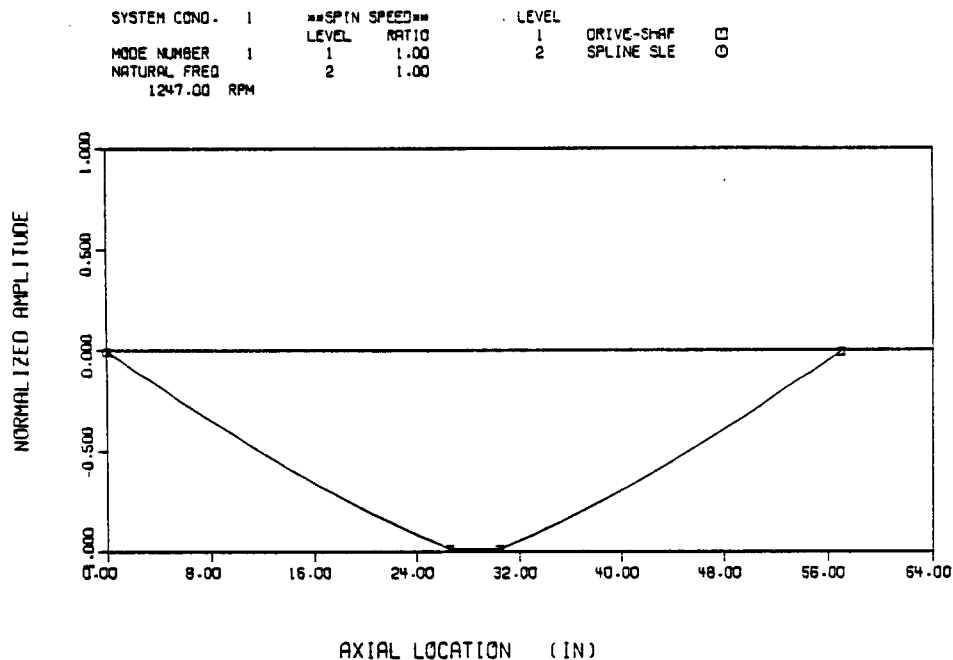
in Figure 3-17. Station 5 on the shaft, at the point of connection to the spline sleeve, is the location on the rotor model that is plotted in the figures of rotor transient orbits in the sections below.

Equation 3.46 (from Section 3.1) expressed the components of the friction moment transmitted across the spline-joint interface as

$$-M_x = K_A \Delta\theta + \frac{2\mu T}{\pi \cos\psi} (\Delta\dot{\theta} + \Omega\Delta\phi) / (\Delta\dot{\alpha}^2 + \Delta\dot{\beta}^2)^{1/2}$$

$$-M_y = K_A \Delta\phi + \frac{2\mu T}{\pi \cos\psi} (\Delta\dot{\phi} - \Omega\Delta\theta) / (\Delta\dot{\alpha}^2 + \Delta\dot{\beta}^2)^{1/2}$$

3.2.2.2 Initial Conditions. In order to excite a transient motion to investigate the stability of the orbit, some nonzero initial conditions must be used. Two sets of initial conditions were generated for this study by applying



90588

Figure 3-17. Mode Shape Corresponding to First Natural Frequency of Model without Friction

- a. An imbalance force of 400 lb for 1 sec to the rotor starting from rest (rotating at 3500 rpm but with all lateral and angular displacements and velocities equal to zero)
- b. A static side force of 400 lb for 1 sec to the rotor starting from rest.

The states of displacements and velocities that resulted at the end of each of the above two simulations were used as initial conditions in the studies to be discussed below. (These will subsequently be referred to as the imbalance initial conditions and the side force initial conditions, respectively.) As will be discussed in Section 3.2.3.1, under symmetric operating conditions, both of these initial conditions resulted in transient orbits that eventually reached the same circular limit cycle. Since this parametric study is mostly concerned with the effect of the parameters on the final motion, starting from this limit cycle was found to be the best choice of initial conditions. These will subsequently be referred to as the limit cycle initial conditions.

Under some operating conditions, such as with a static side load, the eventual motion had two different solutions, depending on the magnitude of the initial conditions that were used. In order to study the threshold that divided one solution from the other, a factor (SI) was implemented in the program in order to scale the set of initial displacement and velocity conditions used.

3.2.3 Numerical Results

The parametric study that was performed to exercise the rotor model with the spline joint is discussed in this section. Transient simulation of the rotor model with the spline component was performed for a number of different conditions, such as amount of external damping, running speed, product of friction coefficient and torque (μT), side force, imbalance force, and initial conditions. The simulations performed are discussed below.

3.2.3.1 Symmetric Conditions. It was shown in Section 3.1.1.3 that under symmetric conditions (no side force and $K_{xx}=K_{yy}$ at the bearings), when the rotor is spinning at frequency Ω and its whirl motion is circular at frequency ω , the energy added to the rotor-bearing system by the spline friction forces in one cycle is

$$U_f = \text{sgn}(\omega - \Omega) 4\mu T r_1 / (\cos \psi) \quad (3.75)$$

where r_1 is the amplitude of the relative angular displacement across the joint and ψ is the contact pressure angle. On the other hand, the energy contribution from a viscous damper is given by

$$U_V = -2\pi\omega Br_2^2 \quad (3.76)$$

where r_2 is the radius of the circular whirl orbit at the damper location. The negative sign means that the energy is dissipated by the damper. After the initial transient has died out and the motion has reached the limit cycle, the net energy added to the rotor-bearing system is zero. If the sum of the above two energies are set to zero, one obtains:

$$r_1 = 0, \quad \text{if } \Omega < \omega$$

$$r_1 = 2\mu T (r_1/r_2)^2 / (\omega\pi B \cos\psi), \quad \text{if } \Omega > \omega \quad (3.77)$$

Below the first bending natural frequency, both energy contributions are negative, resulting in zero motion. Above the first bending natural frequency, the radius of the limit cycle orbit is proportional to the product of the friction coefficient and the spline torque (μT) and inversely proportional to the external viscous damping. The ratio r_1/r_2 is obtained from the mode shape of the motion.

Figures 3-18 and 3-19 show the transient response orbits for three initial conditions:

Case D1: Imbalance initial conditions.

Case D2: Imbalance initial conditions but displacements and velocities scaled by a factor of SI = 0.60.

Case D3: Side force initial conditions

Figure 3-18 plots the first two cycles ($0 < t < 0.1$ sec) while Figure 3-19 plots the remaining cycles ($0.1 < t < 1$ sec) of the motion. It is noticed that for cases D1 and D3 the rotor motion approaches a circular orbit from the outside, while for case D2 it approaches the same circle from the inside.

3.2.3.2 External Damping and Friction Torque. Several runs were made with different values of external damping (from sleeve to ground) in order to verify that the numerical model produced the inverse relationship of the size of the circular orbit with external damping. Figure 3-20 is a plot of the inverse of the orbit radius versus damping coefficient.

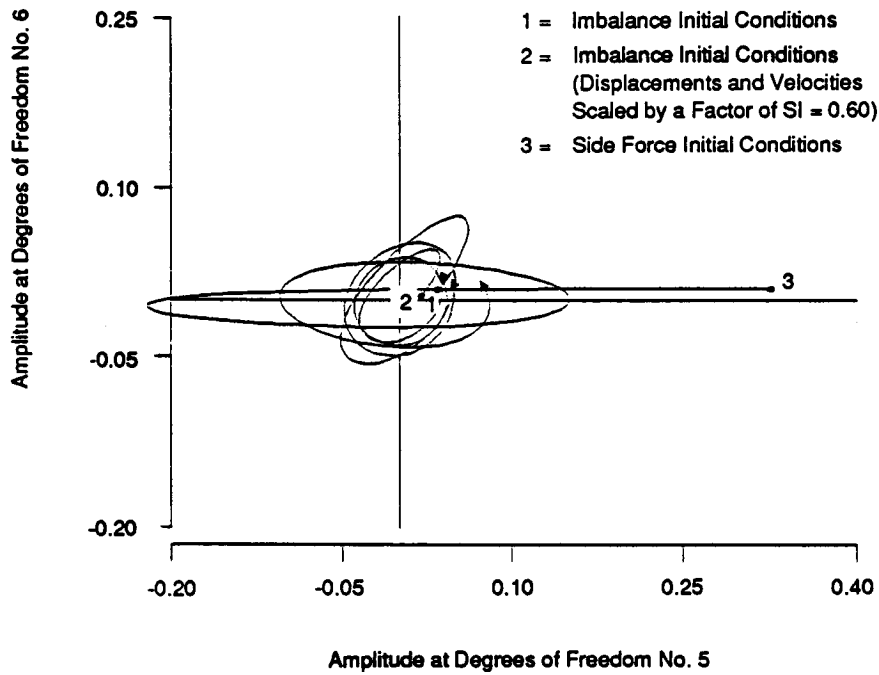


Figure 3-18. Transient Response to Different Initial Conditions ($0 < t < 0.1$ sec)

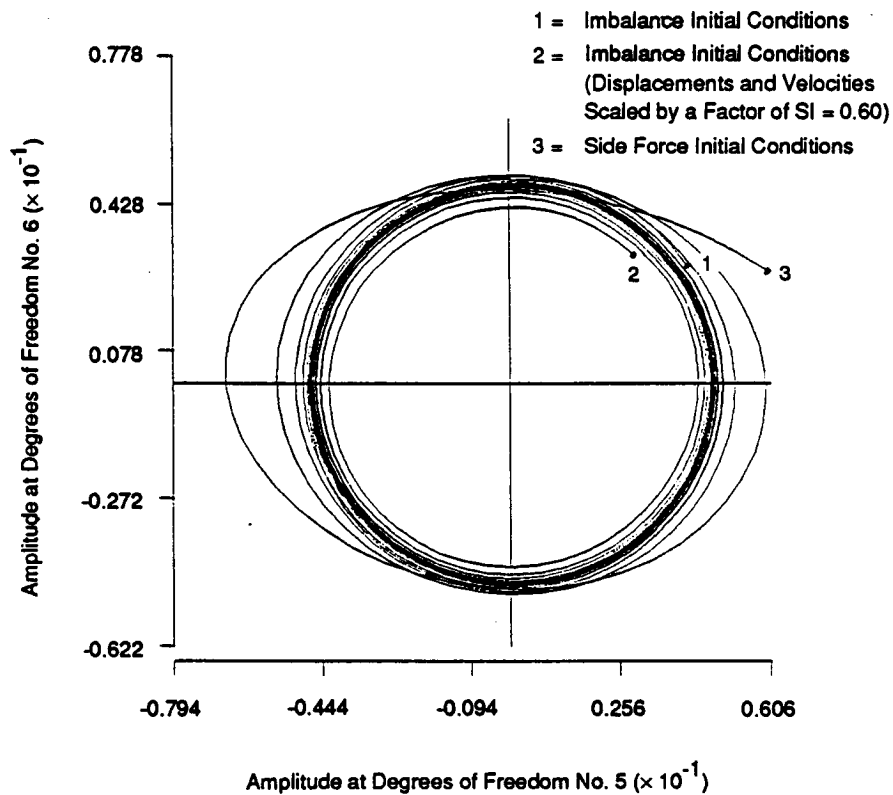
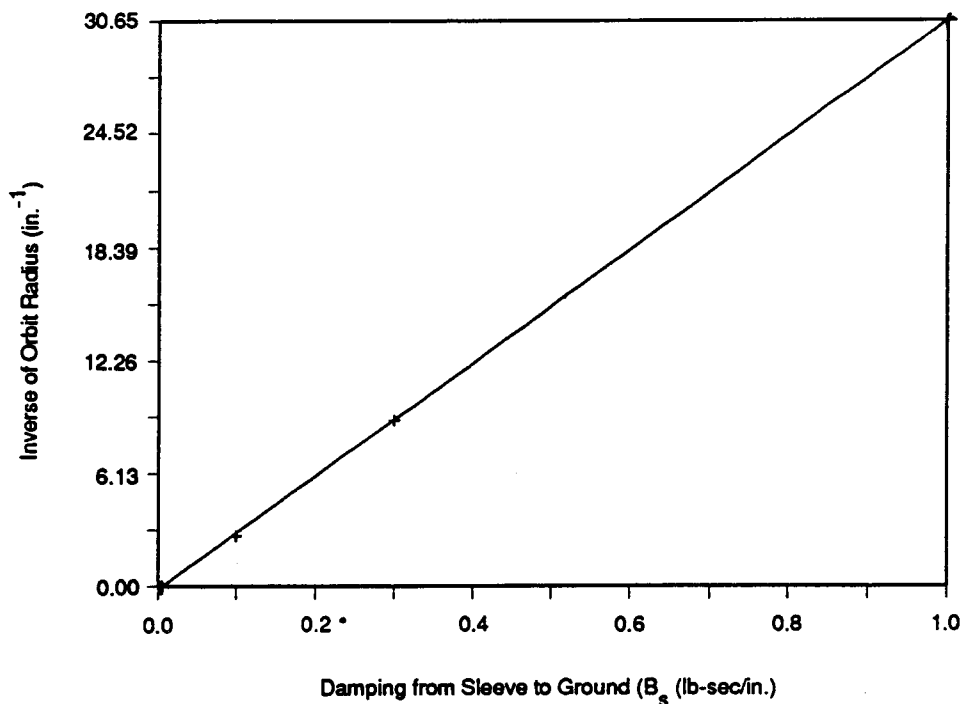


Figure 3-19. Transient Response to Different Initial Conditions ($0.1 < t < 1.0$ sec)



90590

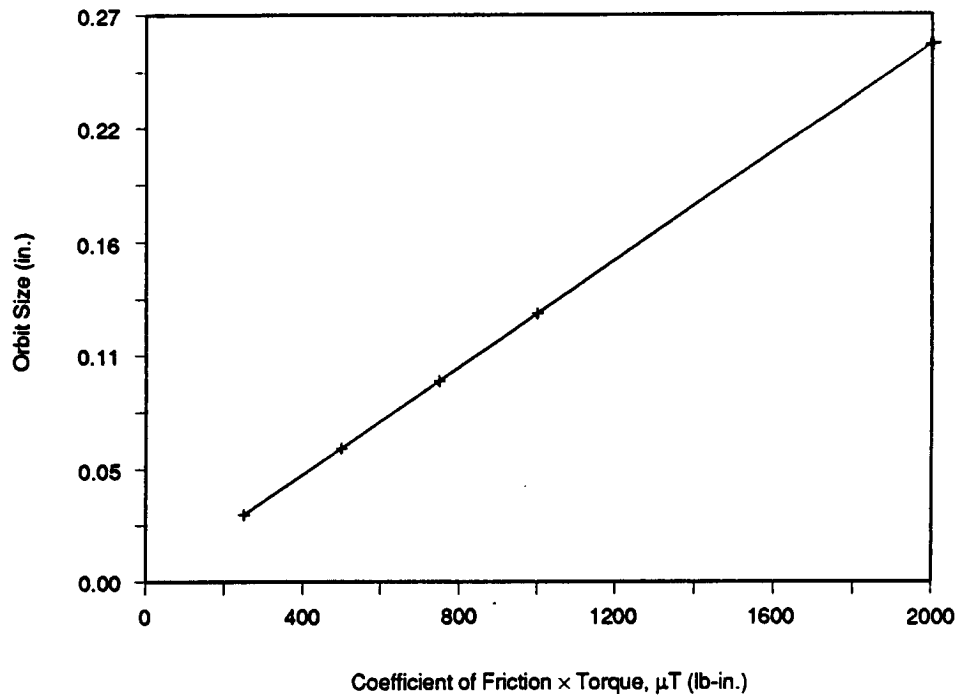
Figure 3-20. Dependence of Limit Cycle on Damping

Several runs were also made with different values of the product of the friction coefficient and the spline torque in order to verify the expected proportional relationship to the size of the circular orbit. Figure 3-21 is a plot of the orbit radius versus μT . The slope of this curve was also verified to agree with Equation 3.77 above.

3.2.3.3 Imbalance. Figure 3-22 is a plot of three different limit cycle orbits showing combined effects of friction and imbalance:

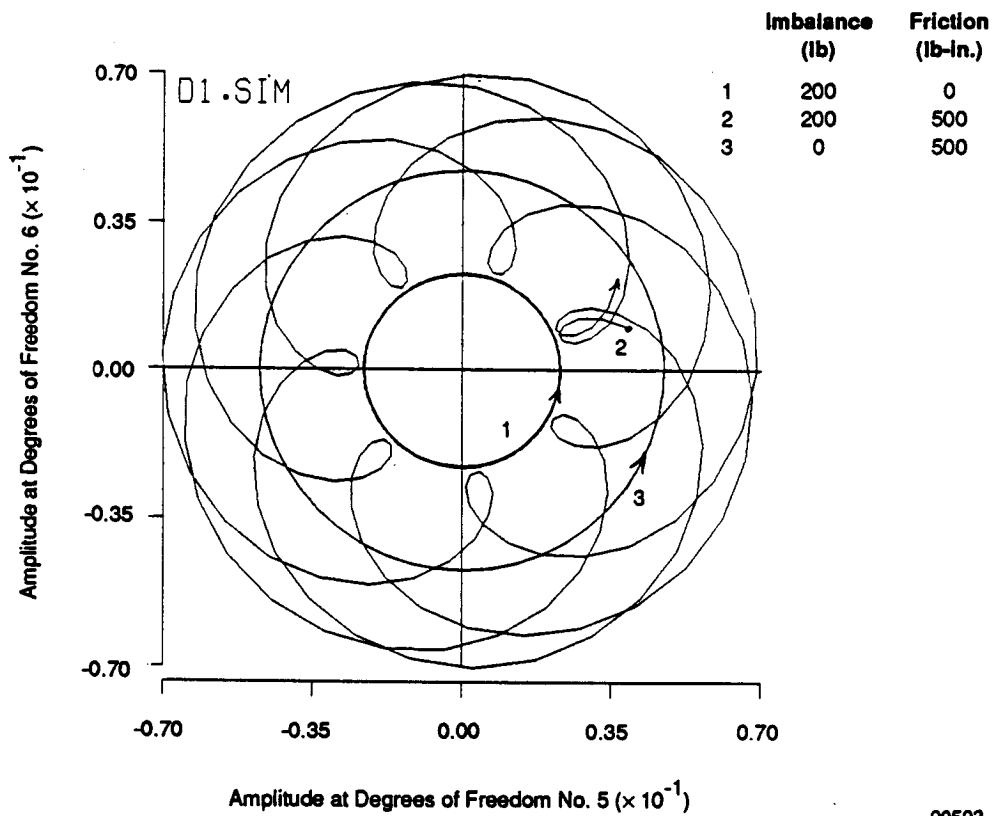
1. $F_u = 200$ lb, $\mu T = 0$ lb-in. (Case DUNF)
2. $F_u = 200$ lb, $\mu T = 500$ lb-in. (Case D10)
3. $F_u = 0$ lb, $\mu T = 500$ lb-in. (Case D1)

Figure 3-23 shows a comparison of the FFT of the x displacement for the last 0.8 sec of these three cases. Clearly, the case with imbalance only has purely synchronous motion while the case with friction only has motion purely at the first bending critical frequency. The case with both imbalance and friction shows a combined motion beating between the two frequencies. Figure 3-24 shows the FFT of the x displacement with $\mu T = 500$ as the imbalance force is increased from 0 to 200 lb. Clearly, the synchronous



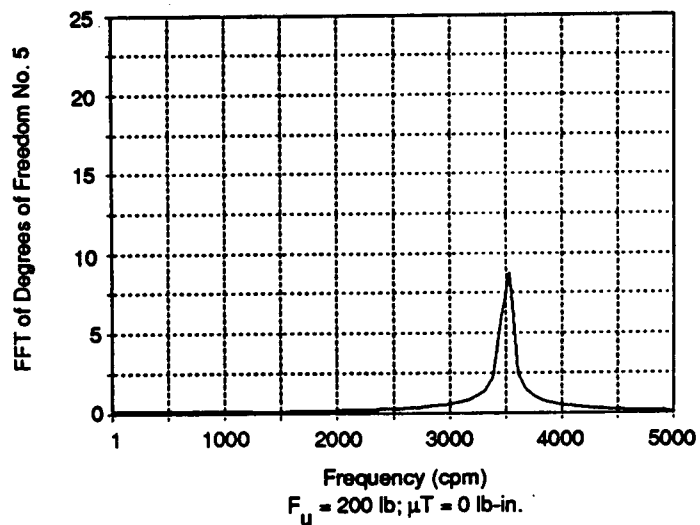
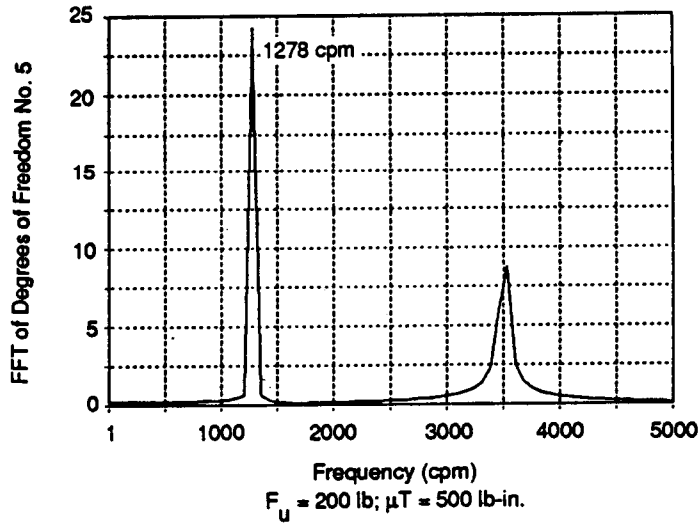
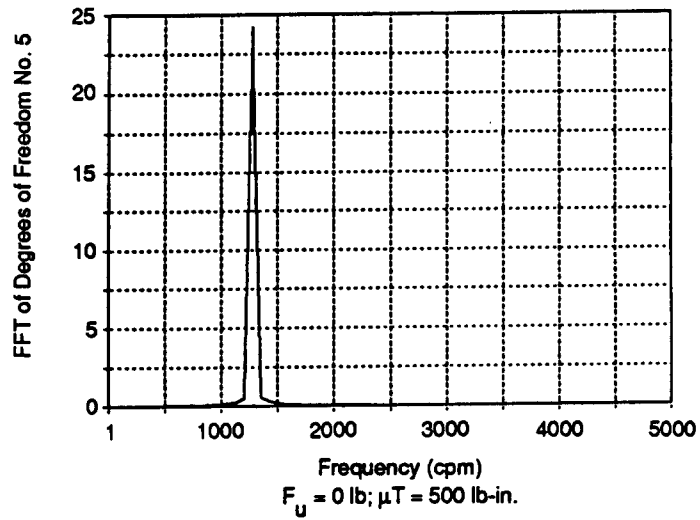
90591

Figure 3-21. Dependence of Limit Cycle on Friction-Torque Product



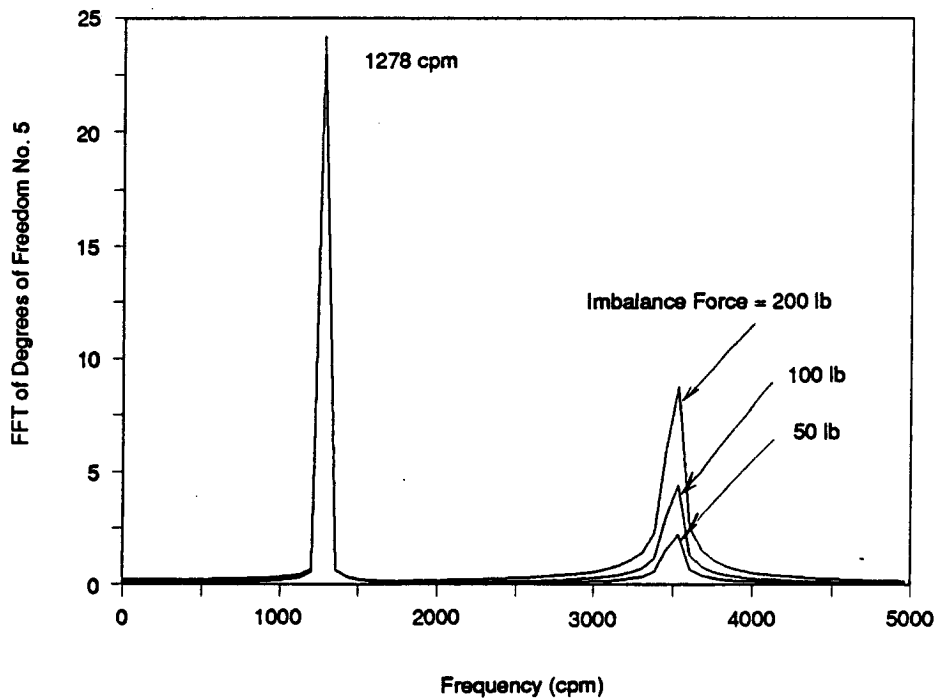
90592

Figure 3-22. Limit Cycle Orbits for Different Combinations of Imbalance and Friction-Torque Product



90593

Figure 3-23. Comparison FFT of Lateral Motion for Different Combinations of Imbalance and Friction-Torque Product



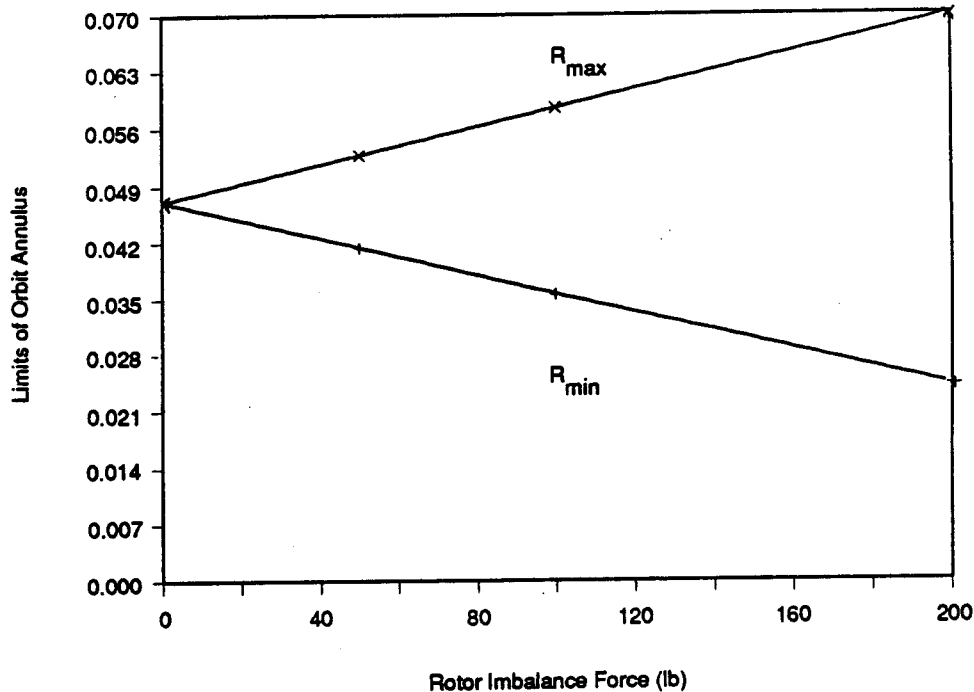
90594

Figure 3-24. FFT of Lateral Motion for Different Amounts of Imbalance

motion increases in proportion to the imbalance force while the subsynchronous component is unaffected.

Figure 3-25 is a plot of the inner and outer radii bounding the limit cycle orbit versus the magnitude of the imbalance force. With imbalance, the limits of the orbit widen from a circle to an annular region. The motion contains two components at two frequencies: a subsynchronous component (at the first bending critical) and the synchronous component. The subsynchronous component is proportional to the product of the friction coefficient and the spline torque. The synchronous component is proportional to the imbalance force and is responsible for the width of the annular region. Both components appear to be fairly uncoupled from each other.

3.2.3.4 Side Load. A static side load applied to the rotor will cause a moment to be transmitted through the spline connections between the sleeve and the rotor. There exists a threshold for this side load beyond which the rotor-bearing system is stable and all motions decay to a point. Below the threshold, the transient motion will approach one



90595

Figure 3-25. Effect of Imbalance on Limits of Orbit Annulus

of two solutions as $t \rightarrow \infty$, depending on the initial conditions, as discussed below. In this study of side load, the limit cycle initial conditions were used, scaled by a factor (SI). Also, a value of 0.1 lb-sec/in. external damping at the sleeve ends and $\mu T = 500$ lb-in. were used.

In the study of the stability of nonlinear systems, a limit cycle is defined as an isolated closed phase path,* which corresponds to a periodic mode of operation in the system. If all neighboring phase paths approach this cycle (from both the inside and outside) asymptotically as $t \rightarrow \infty$, it is called a stable limit cycle. On the other hand, if there exists at least one neighboring phase path that does not approach this cycle as $t \rightarrow \infty$, it is called an unstable limit cycle. Similarly, a stable or unstable node is a singular point toward or away from which all neighboring phase paths move as $t \rightarrow \infty$. For more information on this subject, see Andronov [27].

*"Phase path" is the term given to the path of a representative point in the phase plane, while "phase" is used to describe the state of the system, i.e., the set of displacements and velocities of the system at a given time.

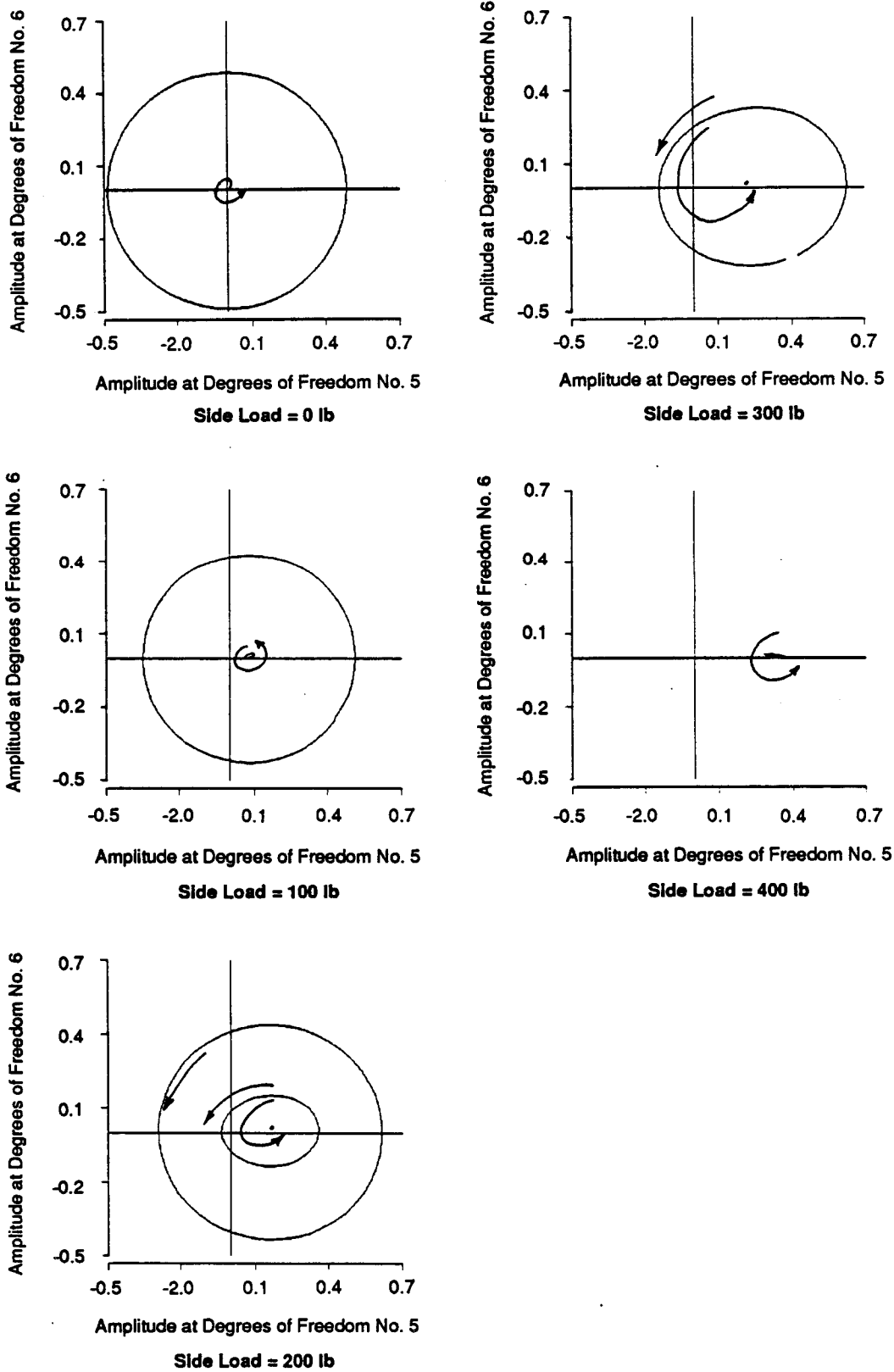
When the rotor is operating above the first bending critical and at zero side load, there is an orbitally stable circular limit cycle for the motion at a whirl frequency equal to the first bending critical, regardless of the initial conditions. The center of this circle is an unstable node.

As the side load is applied, the center of the orbitally stable limit cycle moves in the direction of the load. This unstable node grows into an orbitally unstable limit cycle. Figure 3-26 is a comparative plot of the two limit cycles as the side load is progressively increased from 0 to 400 lb. The arrows indicate the stability status of the different cycles and nodes.

The unstable limit cycle is elliptical and has its major axis inclined a few degrees from the direction of the applied load, as can be determined by looking in more detail at the case of 200-lb side load at different initial conditions. Figure 3-27 shows part of the orbit of the rotor near this cycle for three values of initial conditions ($SI = 3.5, 3.875, \text{ and } 4.25$) between $t = 0.55$ and $t = 0.60$ sec. Figure 3-28 shows the complete orbits (from $t = 0$ to 1 sec) for these three conditions. As seen, the orbit decays to a point for $SI = 3.5$ while it grows to the stable limit cycle for $SI = 4.25$. For $SI = 3.875$, on the other hand, the orbit does not depart drastically from the cycle in Figure 3-27 even after time has reached a full second. The criteria that determines the final orbit is not simply whether the rotor displacement is inside or outside this unstable limit cycle but is a function of all of the displacements and velocities of the system.

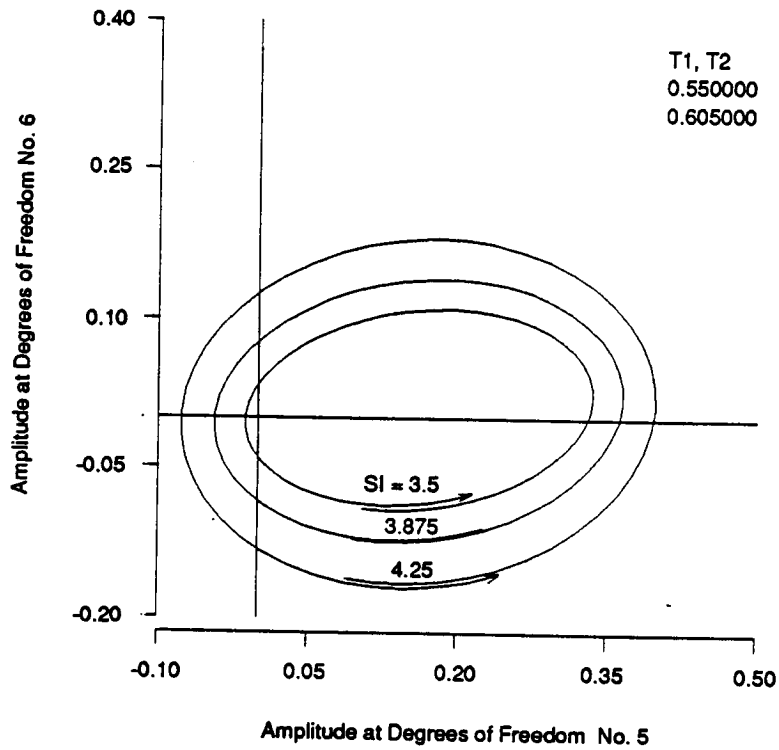
Thus, the unstable limit cycle represents a threshold for the initial conditions of the rotor-bearing system to eventually reach the nonzero orbitally stable limit cycle, which is manifested as a subsynchronous vibration. For small initial conditions, the transient orbit will decay in an elliptically shaped spiral toward a point at its center, which is now a stable node. Figure 3-29 illustrates the transient orbits for three different values of small initial conditions ($SI = 3.5, 2 \text{ and } 1$). On the other hand, for large enough initial conditions, the orbit grows towards the larger, more-circular stable limit cycle, from either the inside or the outside. Figure 3-30 illustrates the transient orbits for three different values of large initial conditions ($SI = 5, 10, \text{ and } 20$).

As the side load is increased, the orbitally unstable limit cycle grows very rapidly toward the larger limit cycle. This larger cycle, on the other hand, decreases and gradually becomes elliptical with increasing side load. The principal axis of this larger cycle is



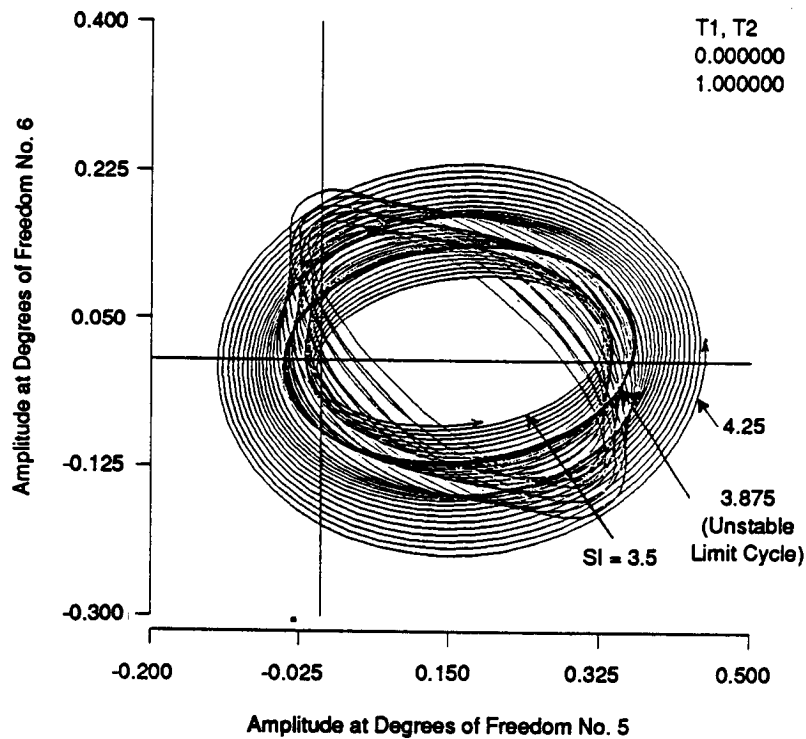
90609

Figure 3-26. Comparison of Orbitally Stable (Larger) and Unstable (Smaller) Limit Cycles at Different Side Loads ($T = 500$ lb-in. and External Damping = 0.1 lb-sec/in.)



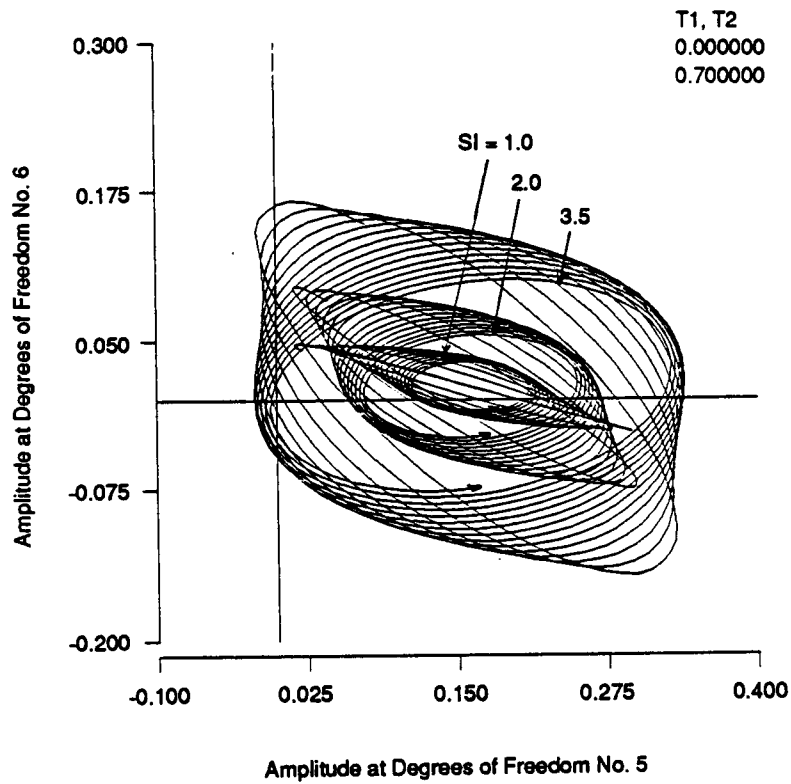
90596

Figure 3-27. Transient Orbit for Three Different Initial Conditions near the Unstable Limit Cycle between $t = 0.55$ sec and $t = 0.65$ sec



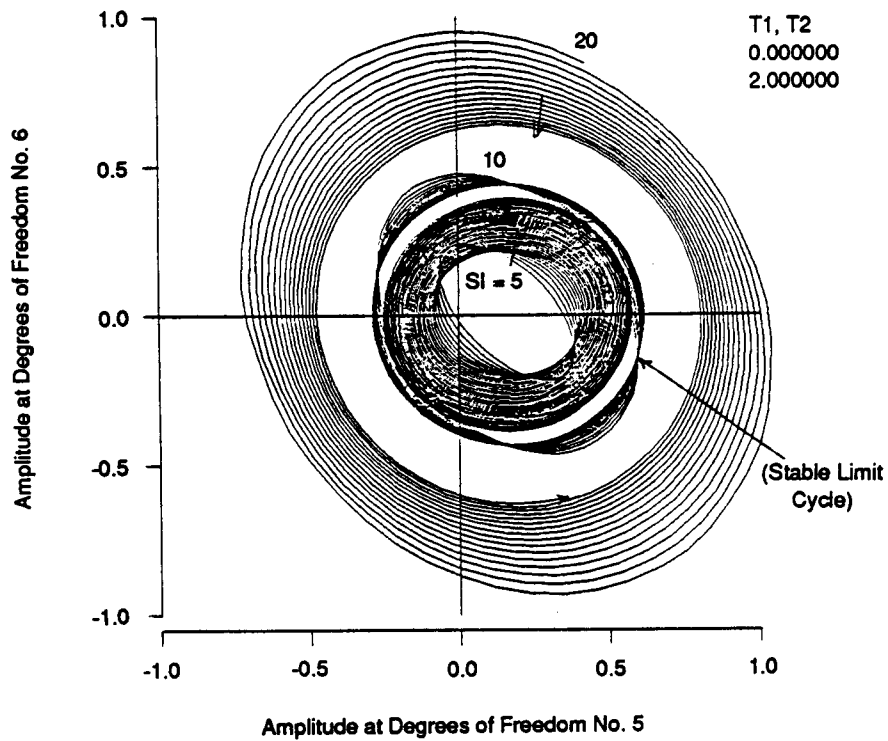
90597

Figure 3-28. Transient Orbit for Three Different Initial Conditions near the Unstable Limit Cycle between $t = 0.0$ sec and $t = 1.0$ sec



90598

Figure 3-29. Transient Orbit for Small Initial Conditions Showing Decay to Stable Mode



90599

Figure 3-30. Transient Orbit for Large Initial Conditions Showing Approach to Stable Limit Cycle

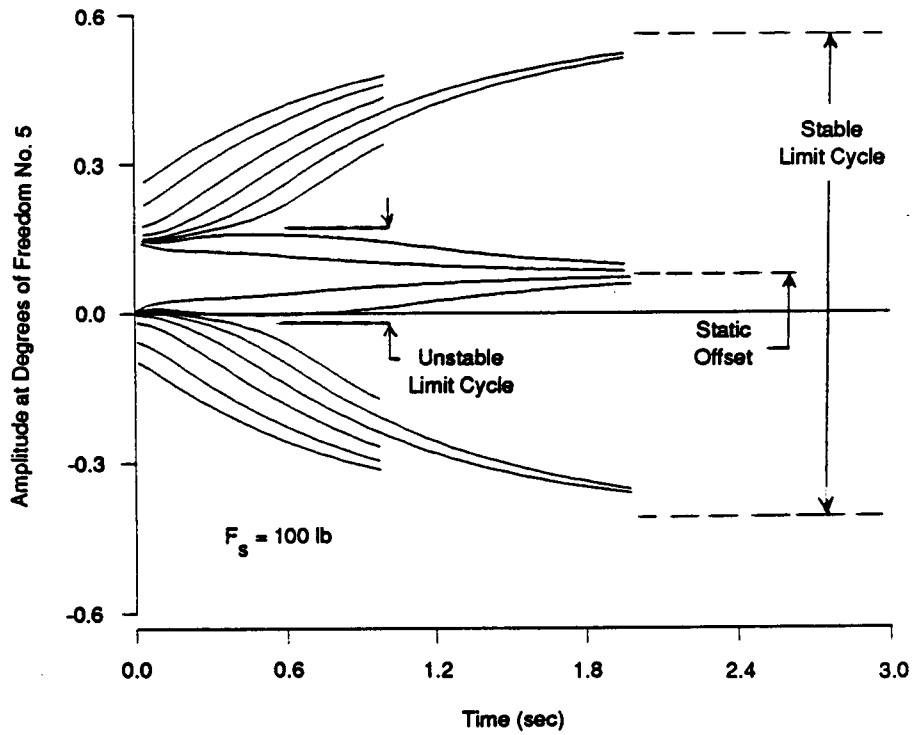
along the direction of load. Both limit cycles merge into one another at the threshold of side load (about 300 lb for this case) to form what is called a "semistable" or double cycle [27]. Although motions with large initial conditions approach this cycle asymptotically from the outside, any disturbance will cause the motion to decay toward the stable node at its center.

Figure 3-31 contains superimposed plots of the envelopes of the x-component of motion versus time for numerous values of the initial condition scale factor (SI) and a side load of 100 lb. Figures 3-32, 3-33, and 3-34 are similar plots for side loads of 200, 300, and 400 lb, respectively, except the scale of the abscissa scale goes from -1.2 to 1.2 in. instead of -0.6 to 0.6 in.. These four figures and the envelope for the zero side load case are combined in Figure 3-35 with the same abscissa scales for comparison. It is noticed that, at large orbit amplitudes (near the limit cycles), the decay rate with time is fairly slow and as the orbit size decreases, the decay rate rapidly increases.

Further increase in side load beyond the threshold increases the rate of decay of the motion toward the stable node at the static offset. This is shown in the plots of the envelopes for the case of 400 lb side load (Figure 3-34), which do not show any evidence of a limit cycle. Figure 3-36 is a plot of the size of the larger (stable) limit angle ellipse as well as its ellipticity versus side load.

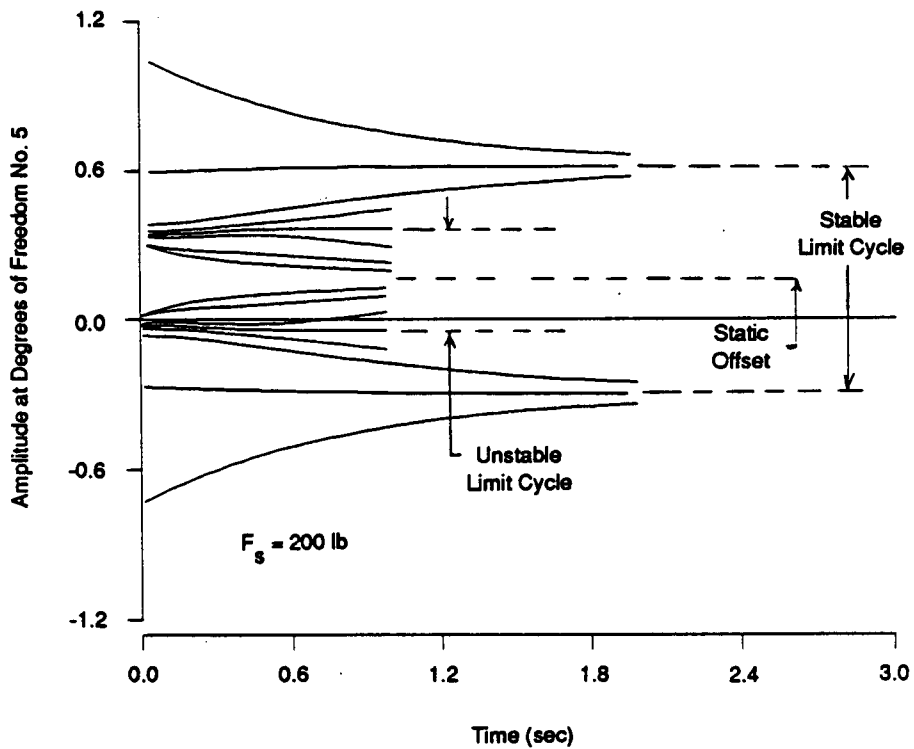
At a value of external sleeve damping 10 times larger (1.0 lb-sec/in.) with no side load, the circular limit cycle orbit was reduced to 1/10, as expected. However, with all the side load values previously applied, the transient orbits spiraled to the static offset stable node as shown in Figure 3-37. These spirals show a backward whirl, while all the orbits previously presented for the smaller external damping showed a forward whirl.

3.2.3.5 Asymmetric Bearing Coefficients. Figure 3-38 shows the effect of decreasing one of the components of direct bearing stiffness (K_{yy}) on the limit cycle orbit. As K_{yy} is decreased from 100,000 to 10,000 lb/in., the orbit becomes elliptical with the major axis inclined about 135° from the x-axis and increasing to about 110% of the radius of the original circular orbit. Further decrease in K_{yy} decreases the size of the orbit without much further effect on its ellipticity. Figure 3-39 is a plot of the major and minor axes of the limit cycle ellipse.



90600

Figure 3-31. Envelopes of Lateral Motion vs Time for Different Initial Conditions at 100-lb Side Load



90601

Figure 3-32. Envelopes of Lateral Motion vs Time for Different Initial Conditions at 200-lb Side Load

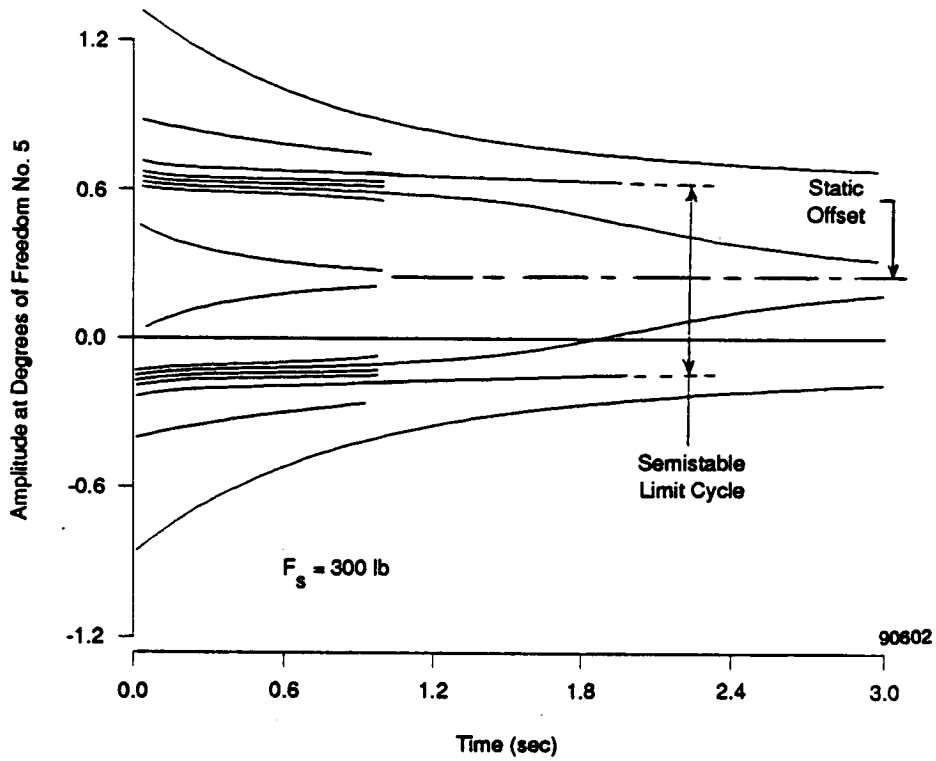


Figure 3-33. Envelopes of Lateral Motion vs Time for Different Initial Conditions at 300-lb Side Load

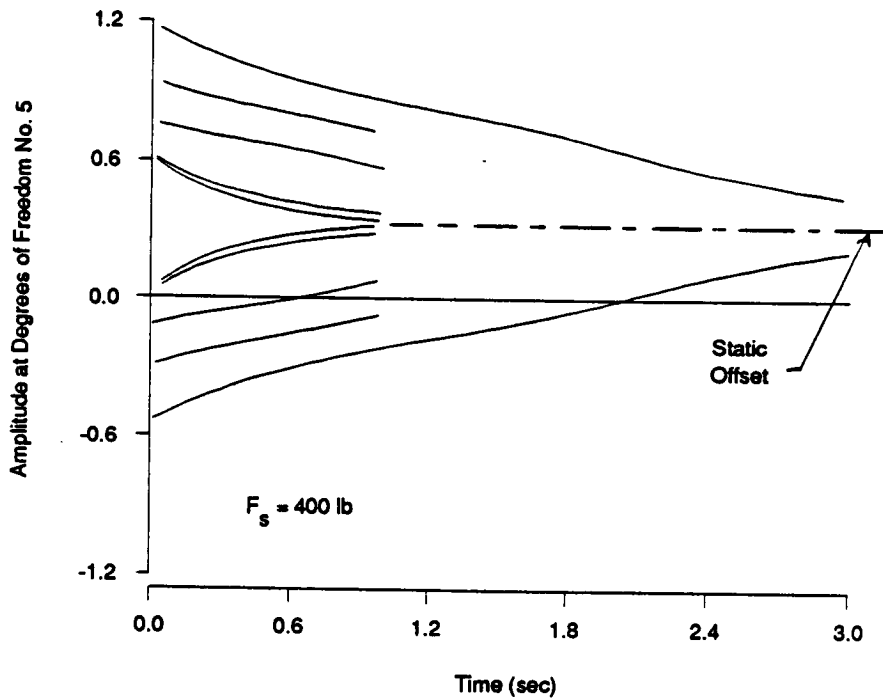
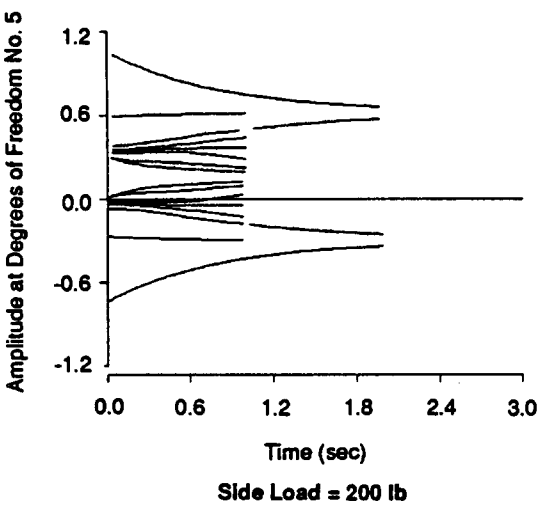
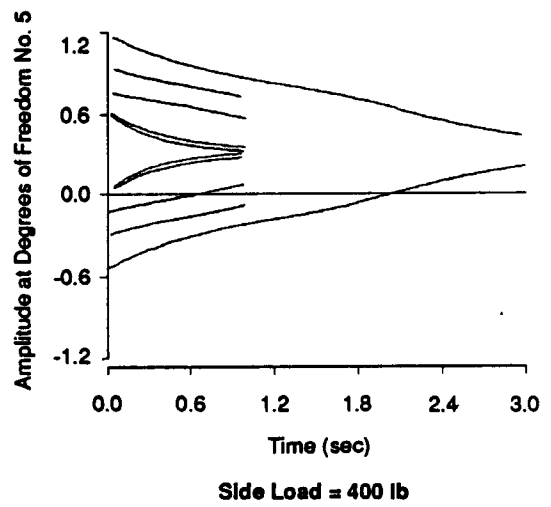
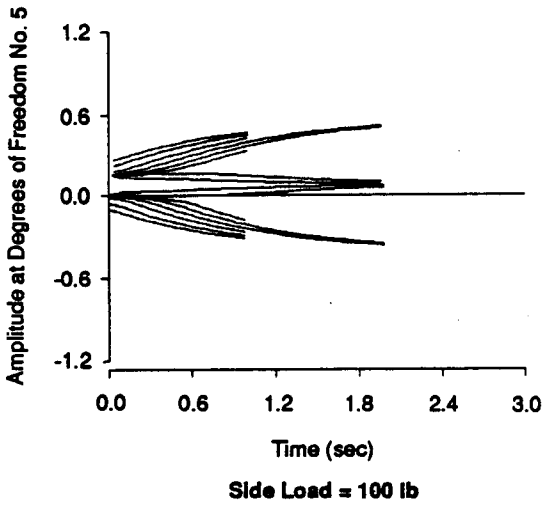
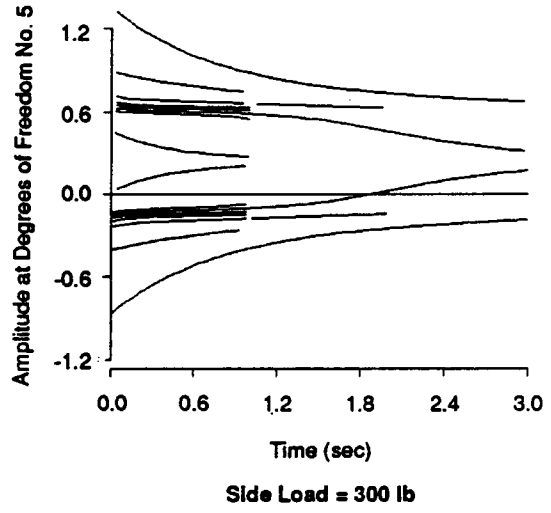
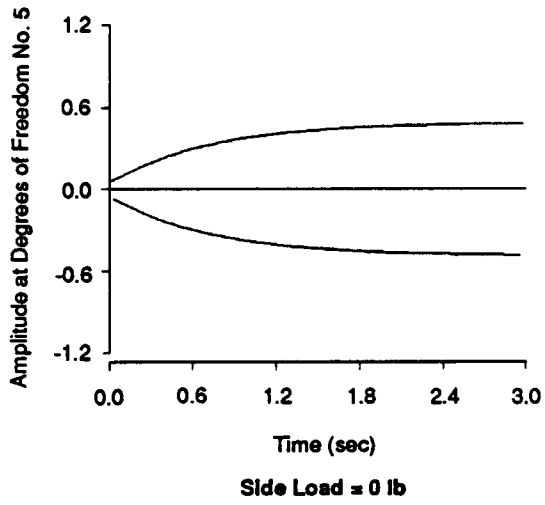
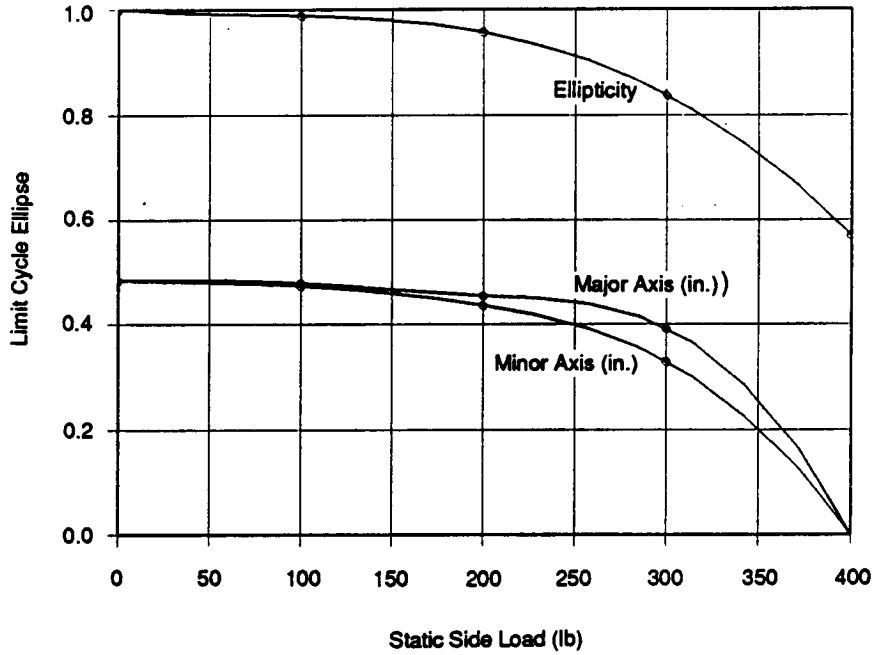


Figure 3-34. Envelopes of Lateral Motion vs Time for Different Initial Conditions at 400-lb Side Load



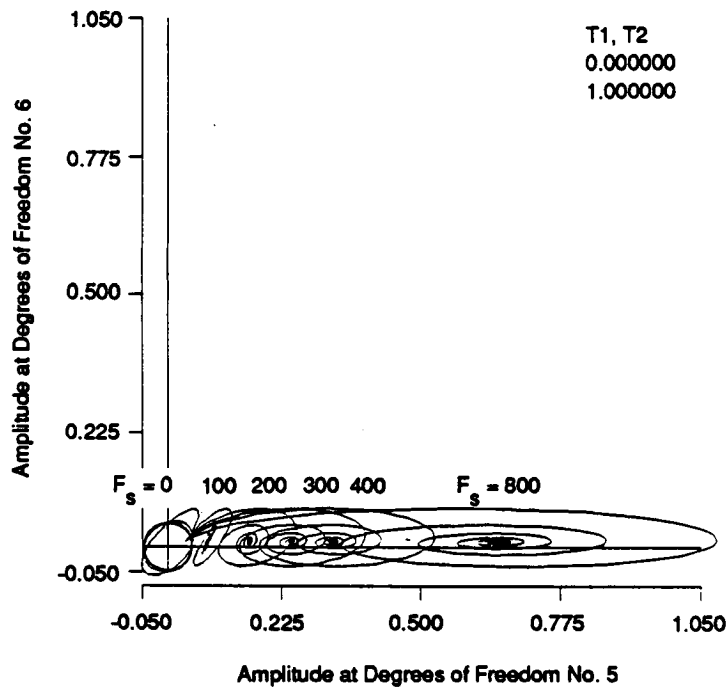
90604

Figure 3-35. Comparison of Envelopes of Lateral Motion vs Time for Different Initial Conditions and Side Loads



90638

Figure 3-36. Effect of Side Load on Limit Cycle



90605

Figure 3-37. Transient Orbit for Six Different Side Loads and Larger (1 lb-sec/in.) External Damping

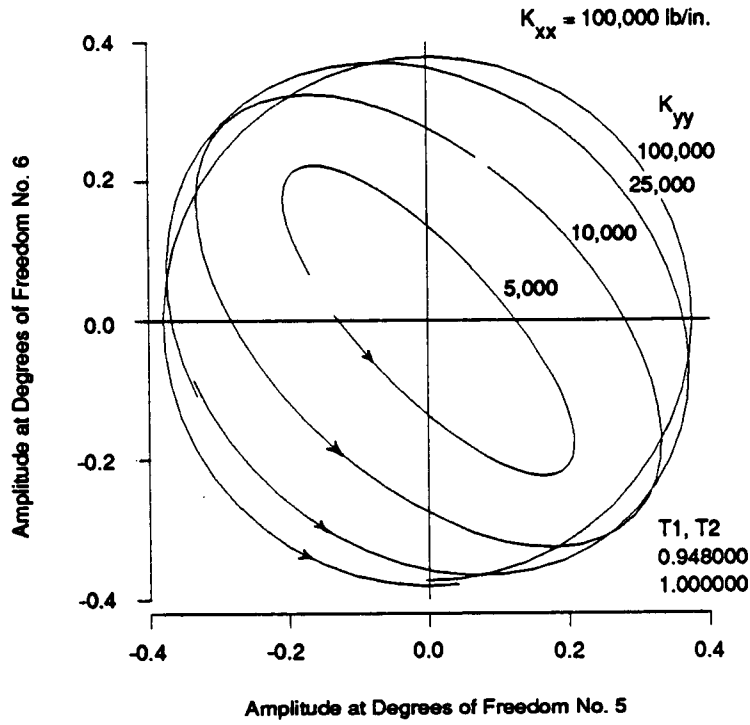


Figure 3-38. Limit Cycle Orbits at Different Degrees of Bearing Asymmetry.

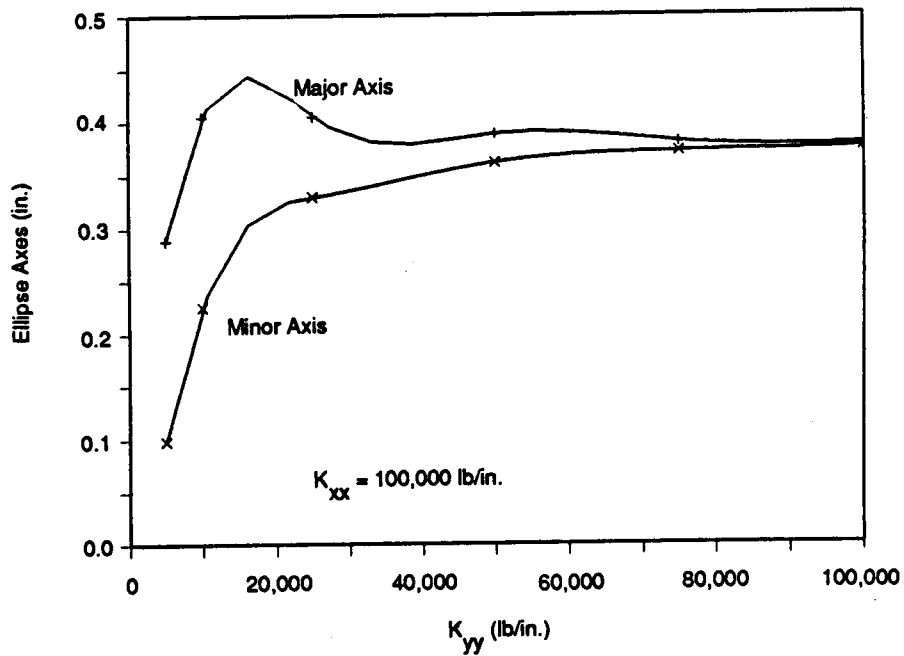


Figure 3-39. Limit Cycle Ellipse Size vs K_{yy} Stiffness Coefficient

In the case of this rotor model, no reduction in the major axis is noticed until K_{yy}/K_{xx} is less than 10%. However, as shown by the mode shape in Figure 3-16, the rotor model utilized here to exercise the spline joint is fairly flexible compared to the bearing stiffnesses. A stiffer rotor would involve more participation of the bearings in the first bending mode. Therefore, it is expected that for relatively stiffer rotors, asymmetric bearing stiffnesses should have a more beneficial effect in controlling rotor instability.

3.2.3.6 Rotating Speed. As mentioned previously, for the case of symmetric conditions, the rotor will be stable or unstable depending on whether the rotating speed is lower or higher than the first bending critical speed of the rotor-bearing system. Several runs at a fixed side load (200 lb) were made showing no noticeable effect of speed. Other than determining whether the bending critical speed is exceeded, the rotating speed has no effect on the size of the orbit and practically no effect on the transient motion to reach it. The only effect is through the small influence that the gyroscopic effects have on the first bending critical speed and mode shape.

3.2.4 Conclusions

For symmetric operating conditions (symmetric bearing coefficients and no side load):

1. There is only one asymptotic solution (as $t \rightarrow \infty$) independent of the initial conditions.
2. If the spin speed is less than the first bending critical speed, the energy contribution from the friction in the spline is negative, resulting in zero subsynchronous motion and a stable rotor.
3. If the spin speed is greater than the first bending critical speed, the rotor is unstable and its motion is a circular limit cycle whirling at a frequency equal to the first rotor bending critical. The radius of this limit cycle orbit is proportional to the product of the friction coefficient and the spline torque and is inversely proportional to the external viscous damping. Transient motions proceed in spiral paths, from either the inside or the outside, toward the limit cycle circle. The center of the circle is an unstable node.

4. Other than determining whether instability is present or not, there is very little effect of spin speed on the size of the subsynchronous motion, only the small influence that the gyroscopic effects have on the first bending critical speed and mode shape.
5. With rotor imbalance the limits of the rotor orbit widen from a circle to an annulus. The motion within this annulus contains two components at two frequencies: a subsynchronous component (at the first bending critical) and the synchronous component. The subsynchronous component is proportional to the product of the friction coefficient and the spline torque. The synchronous component is proportional to the imbalance force and is responsible for the width of the annular region. Both components are fairly uncoupled from each other.

For nonsymmetric operating conditions (asymmetry bearing coefficients and side load):

6. Asymmetry in rotor-bearing stiffness coefficients reduces the size of the subsynchronous whirl orbit brought about by internal friction.
7. A static side load applied to the rotor will cause a moment to be transmitted through the spline connections between the sleeve and the rotor. There exists a threshold for this side load beyond which the rotor-bearing system is stable and all motions decay to a point. Below the threshold, the transient motion will approach one of two asymptotic solutions depending on the initial conditions.
8. As the side load is applied, the unstable node at the center of the orbitally stable limit cycle moves in the direction of the load and grows into an orbitally unstable limit cycle. For small initial conditions, the transient orbit will decay in an elliptically shaped spiral toward a point at its center, which is now a stable node. On the other hand, for large-enough initial conditions, the orbit grows toward the larger, more circular stable limit cycle, from either the inside or the outside.
9. As the side load is increased, the orbitally unstable limit cycle grows very rapidly toward the larger limit cycle. This larger cycle, on the other hand, decreases and gradually becomes elliptical with increasing side load. Both limit cycles merge into one another at the threshold of side load to form a semistable or double cycle. Although motions with large initial conditions approach this cycle asymptotically

from the outside, any disturbance will cause the motion to decay toward the stable node at its center.

10. Further increase in side load beyond the threshold increases the rate of decay of the motion toward the stable node at the static offset.

3.3 Analysis of SSME High Pressure Oxidizer Turbopump

In this section of the report, results from a series of analytic simulations evaluating the impact of internal friction on the SSME LOX turbopump stability are presented. The rotor model, the linear rotordynamic analysis, the results of the nonlinear, time-transient analytic simulations, and the conclusions drawn from the simulations are presented in order.

3.3.1 Turbopump Rotordynamic Model and Linear Analysis

A three-level finite element rotor-bearing system model of the Phase I SSME LOX turbopump was prepared for use in evaluating the impact of internal rotor friction on HPOTP rotor system stability. As shown in Figures 3-40 and 3-41, this model included one level each for the main shaft, the preburner pump and the main impeller. Two sets of rolling element bearings, a turbine interstage seal, and provision for up to five friction producing interconnections (two at the preburner pump and three at the main impeller) were also included. Table 3-3 is the computer listing of the rotor geometric model showing the lengths and diameters of the finite elements making up each of the three rotor system levels. The bearing and interstage seal properties for this model are defined in Table 3-4, and the baseline parameters used for the test cases evaluated (joint angular and radial stiffness, joint friction torque value, rotor spin speed, and imbalance and side load conditions) are presented in Table 3-5. Since the numerical integration method used requires that the time step be approximately one order of magnitude smaller than the highest natural frequency for numerical stability, the rotor system model was tuned to keep its highest natural frequency as low as possible. During the tuning process, the integrity of the lowest modes were maintained so as not to adversely affect the simulation results.

The system critical speeds that were calculated for the linear model are given in Table 3-6. The first two flexible bending critical speeds occur at 11,771 rpm and 27,818 rpm

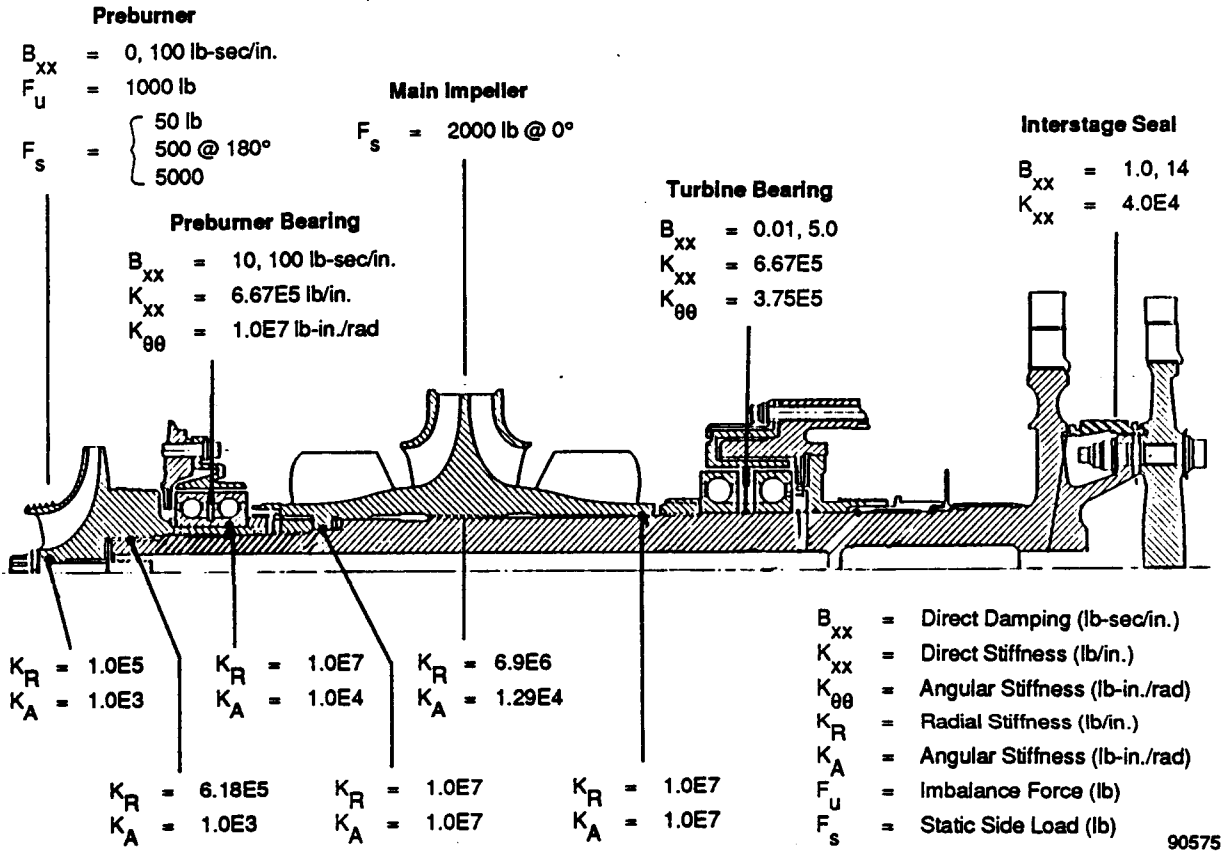


Figure 3-40. HPOTP Cross Section Showing Bearing and Shaft Interconnections

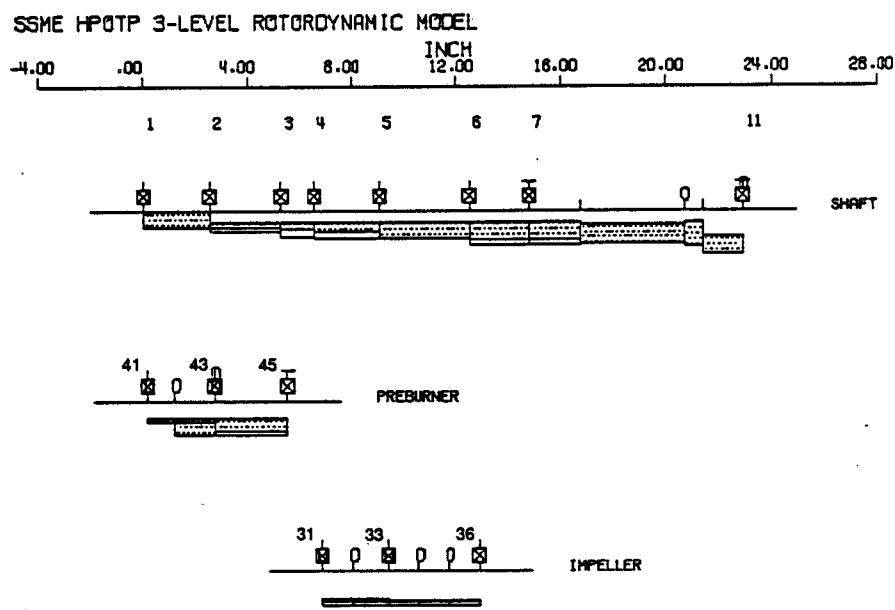


Figure 3-41. HPOTP Three-Level Geometry Model Plot

Table 3-3. HPOTP Three-Level Rotordynamic Model

	Rotor Segment between Stations	Segment Length (in.)	Stiffness Diameter (in.)	Mass Diameter (in.)	Inner Diameter (in.)
Level 1	1 and 2	2.5313	1.25	1.25	0.00
	2 and 3	2.7437	1.25	1.50	0.75
	3 and 4	1.2500	1.35	2.00	0.75
	4 and 5	2.5000	1.50	2.10	0.75
	5 and 6	3.4500	2.10	2.10	0.75
	6 and 7	2.3250	2.15	2.60	0.75
	7 and 8	1.9050	2.15	2.60	0.75
	8 and 9	3.9650	2.50	2.50	1.00
	9 and 10	0.7200	2.70	2.70	0.75
	10 and 11	1.4900	3.30	3.30	2.00
Level 1 Total Length		22.8800			
Level 2	41 and 42	1.0000	1.500	1.50	1.25
	42 and 43	1.5313	2.500	1.50	1.25
	43 and 44	2.7437	2.125	2.50	1.25
Level 2 Total Length		5.2750			
Level 3	31 and 32	1.2000	2.25	2.55	2.10
	32 and 33	1.3000	2.25	2.55	2.10
	33 and 34	1.1500	2.25	2.55	2.15
	34 and 35	1.1500	2.25	2.55	2.15
	35 and 36	1.1500	2.25	2.55	2.15
Level 3 Total Length		5.9500			

Level	Station	Lumped Mass Data			Eccentricity (in.)
		Mass (lb)	IT (lb-in. ²)	IP (lb-in. ²)	
1	9	11.000	59.80	118.70	0.00
2	41	0.870	0.82	1.60	0.00
2	42	3.770	4.79	7.89	0.00
2	43	0.870	0.82	1.60	0.00
3	31	1.875	2.50	3.75	0.00
3	32	3.750	5.00	7.50	0.00
3	33	3.750	5.00	7.50	0.00
3	34	3.750	5.00	7.50	0.00
3	35	1.875	2.50	3.75	0.00

Table 3-4. Bearing and Joint Stiffness

LATERAL COEFFICIENTS				
Station Number	K_{xx} (lb/in.)	K_{xy} (lb/in.)	K_{yx} (lb/in.)	K_{yy} (lb/in.)
41 and 1	0.1000E+06	0.0000E+00	0.0000E+00	0.1000E+06
2 and 43	0.6176E+06	0.0000E+00	0.0000E+00	0.6176E+06
44 and 0	0.6670E+06	0.0000E+00	0.0000E+00	0.6670E+06
3 and 44	0.1000E+08	0.0000E+00	0.0000E+00	0.1000E+08
4 and 31	0.1000E+08	0.0000E+00	0.0000E+00	0.1000E+08
5 and 33	0.6897E+07	0.0000E+00	0.0000E+00	0.6897E+07
6 and 36	0.1000E+08	0.0000E+00	0.0000E+00	0.1000E+08
7 and 0	0.6670E+06	0.0000E+00	0.0000E+00	0.6670E+06
11 and 0	0.4000E+05	0.0000E+00	0.0000E+00	0.4000E+05

ANGULAR COEFFICIENTS				
Station Number	K_{bb} (in.-lb/rad)	K_{bt} (in.-lb/rad)	K_{tb} (in.-lb/rad)	K_{tt} (in.-lb/rad)
41 and 1	1000	0.0000E+00	0.0000E+00	1000
2 and 43	1000	0.0000E+00	0.0000E+00	1000
44 and 0	0.1000E+08	0.0000E+00	0.0000E+00	0.1000E+08
3 and 44	0.1000E+05	0.0000E+00	0.0000E+00	0.1000E+05
4 and 31	0.1000E+08	0.0000E+00	0.0000E+00	0.1000E+08
5 and 33	0.1293E+05	0.0000E+00	0.0000E+00	0.1293E+05
6 and 36	0.1000E+08	0.0000E+00	0.0000E+00	0.1000E+08
7 and 0	0.3750E+06	0.0000E+00	0.0000E+00	0.3750E+06

Table 3-5. SSME Turbopump Spline Coupling Parameters

Lateral Stiffness (K_L):	0.6176×10^6 lb/in.
Angular Stiffness (K_A):	1000 in.-lb/rad
Imbalance (M_g):	1000 lb
Speed:	30,000 rpm
Preburner Spline Friction Torque:	500 in.-lb
Preburner Side Load:	50 lb
Main Impeller Side Load:	2000 lb

Table 3-6. SSME HPOTP Critical Speeds

	rpm	rps	rad/s
1	11,771	196.18	1,232.6
2	27,818	463.64	2,913.1
3	38,601	643.35	4,042.3
4	95,870	1,597.80	10,040.0
5	0.13760E+06	2,293.40	14,410.0
6	0.16053E+06	2,675.60	16,811.0
7	0.24143E+06	4,023.90	25,283.0
8	0.31916E+06	5,319.40	33,423.0
9	0.37478E+06	6,246.40	39,247.0
10	0.43484E+06	7,247.40	45,537.0
11	0.46983E+06	7,830.60	49,201.0
12	0.57727E+06	9,621.10	60,451.0
13	0.79405E+06	13,234.00	83,152.0
14	0.10126E+07	16,877.00	0.10604E+06
15	0.13345E+07	22,242.00	0.13975E+06
16	0.18477E+07	30,795.00	0.19349E+06
17	0.26061E+07	43,436.00	0.27292E+06

and thus fall below the expected operating speed of 30,000 rpm. The highest critical speed was calculated to occur at 2,606,100 rpm. Since the period of this critical speed is approximately 23 μ sec, the time step selected for the time transient analysis was 2 μ sec to insure that numerical stability would not be compromised.

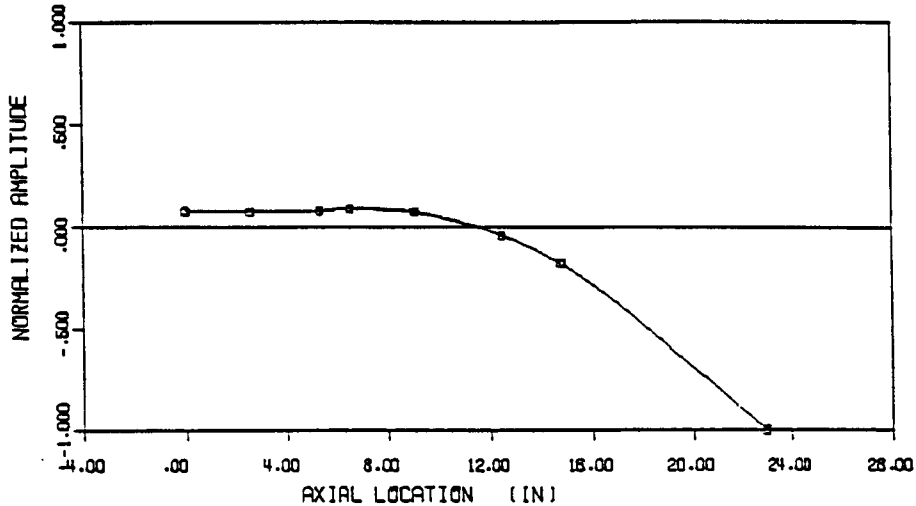
Figure 3-42 shows the mode shapes corresponding to the first two HPOTP rotor system critical speeds. Since the first mode shaft bending does not occur at any of the spline joints, internal rotor friction induced instability would not be expected for this mode. The second mode, on the other hand, produces bending at both the preburner and main impeller splines. Therefore, self excited internal friction instability may be expected when the rotor spin speed exceeds the second critical speed. The results of a linear stability analysis supports this contention. The logarithmic decrement for the first and second natural frequencies at a spin speed of 30,000 rpm are 0.52 and 0.09, respectively. As can be seen, the HPOTP is marginally stable at the second natural frequency, even though it was assumed that the damping at the preburner bearings, turbine end bearings, and turbine interstage seals was 10.0, 5.0, and 14 lb-sec/in., respectively.

While most previous analytic models of the HPOTP predict that the second critical speed occurs at approximately 34,500 rpm, it is not unexpected that this critical speed could fall below 30,000 rpm under actual operating conditions. Phenomena that may affect the

SSME HPOTP 3-LEVEL ROTORDYNAMIC MODEL

FEATURE/COLOUR
CRITICAL SPD

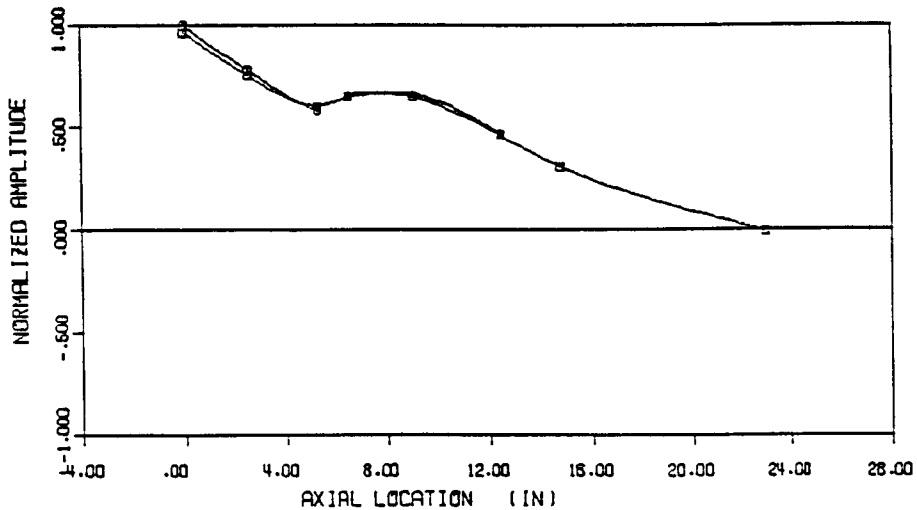
SYSTEM COND.	1	%SPIN SPEED		LEVEL	SHAFT	CRITICAL SPD
MODE NUMBER	1	LEVEL	RATIO	1	PREBURNER	□
NATURAL FREQ	2	1.00	1.00	2	IMPELLER	○
11770.00 RPH	3	1.00	1.00	3		△



SSME HPOTP 3-LEVEL ROTORDYNAMIC MODEL

FEATURE/COLOUR
CRITICAL SPD

SYSTEM COND.	1	%SPIN SPEED		LEVEL	SHAFT	CRITICAL SPD
MODE NUMBER	2	LEVEL	RATIO	1	PREBURNER	□
NATURAL FREQ	2	1.00	1.00	2	IMPELLER	○
27820.00 RPH	3	1.00	1.00	3		△



90577

Figure 3-42. HPOTP Mode Shape Plots

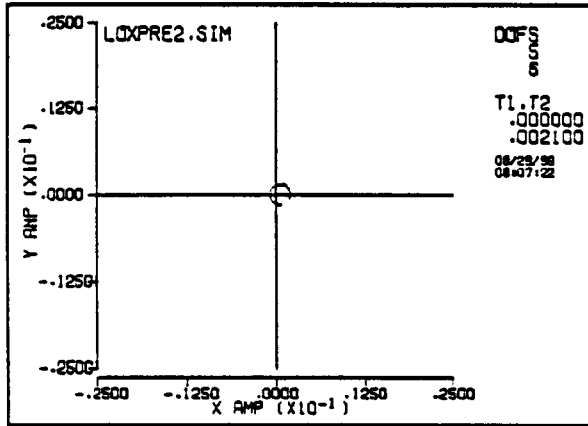
critical speeds include reduced bearing stiffnesses, increased rotor mass, a more flexible rotor, or the presence of aero/fluid forces that manifest themselves as either negative stiffness or an apparent increased mass. Both Childs (28) and Adkins and Brennan (29) have reported measurements of negative stiffness coefficients for centrifugal pump impellers. While most of the interest has been directed toward the determination of the cross-coupled stiffness terms for stability analysis, the negative stiffness values resulting from the hydrodynamic forces on impellers can cause lower rotor systems natural frequencies. For example, the HPOTP second critical speed can drop from 34,513 rpm to 27,830 rpm if a negative stiffness of 100,000 lb-in. is applied at the main impeller.

Reduced bearing stiffness is another possibility for a lower second critical speed. Post-run turbopump bearing inspections have revealed bearing ball diameters that have been reduced by as much as 0.0067 in. Changes such as this reduce predicted bearing stiffnesses, which in turn affect rotor system natural frequencies. With any combination of these factors occurring simultaneously in the turbopump, it is possible that the second critical speed may indeed fall below the operating speed. Consequently, under low levels of external damping, subsynchronous self-excited vibrations due to internal friction may be experienced by the HPOTP.

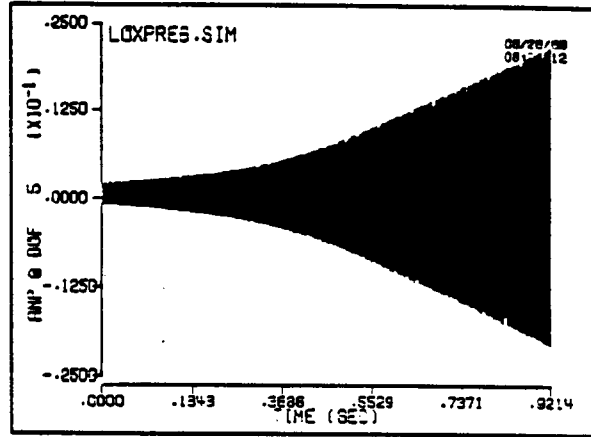
3.3.2 HPOTP Rotordynamic Time Transient Simulations

Using the developed rotordynamic model, a series of time transient simulations of the SSME HPOTP rotating at constant speed of 30,000 rpm were completed. These simulations investigated the effect of external damping and imbalance on the stability of the HPOTP. Figures 3-43 through 3-47 summarize the results of these simulations.

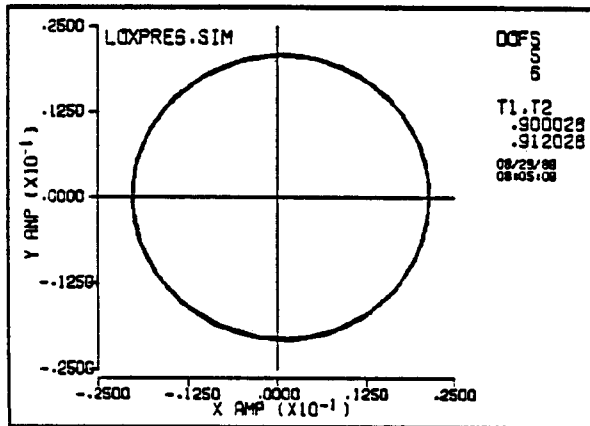
Figure 3-43 shows the results of a 1.0-sec simulation that was completed. In this first simulation, damping at the preburner bearing and turbine interstage seal were 10.0 and 1.0 lb-sec/in each. Further, the rotor was initially spinning at 30,000 rpm, but without any initial lateral displacements or velocities, when side loads of 2000 and 5000 lb at the main impeller and preburner were applied. As seen, the orbit grows to almost 0.025 in. during the 1.0-sec simulation. The dominant frequency for this simulation is the second natural frequency at approximately 25,600 rpm as opposed to the spin speed at 30,000 rpm. From this it is concluded that the presence of the internal joint friction caused the self-excited vibrations observed.



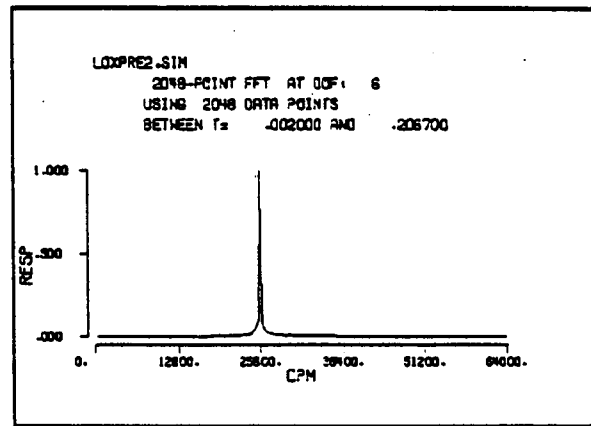
a) HPOTP Orbit After 2 msec Simulation



b) HPOTP Horizontal Displacement During Simulation



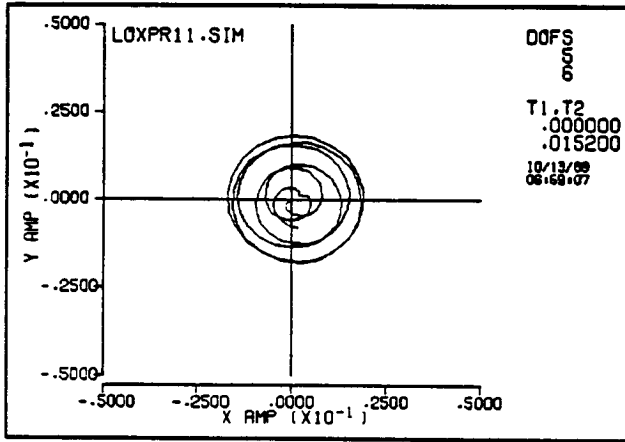
c) HPOTP Orbit After 0.9 sec of Simulation



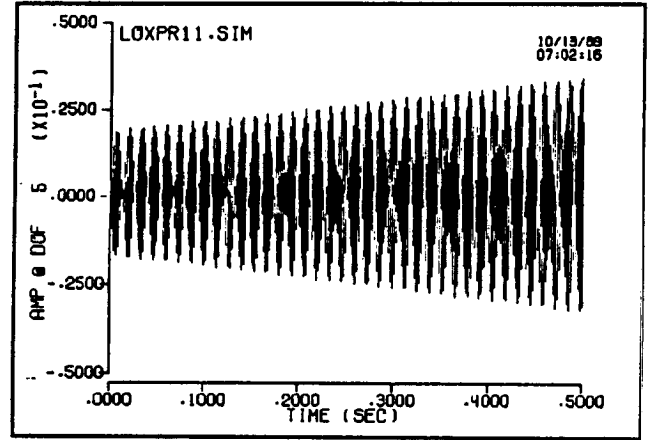
d) FFT of HPOTP

90578

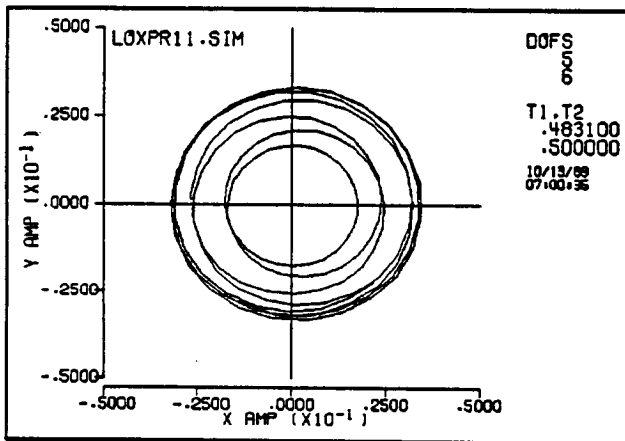
Figure 3-43. Time Transient Simulation of HPOTP at 30,000 rpm



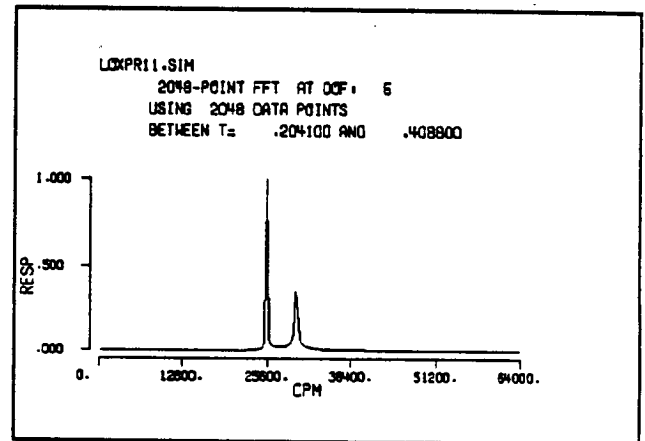
a) Preburner Orbit During First 15 msec



b) Preburner Displacement vs. Time



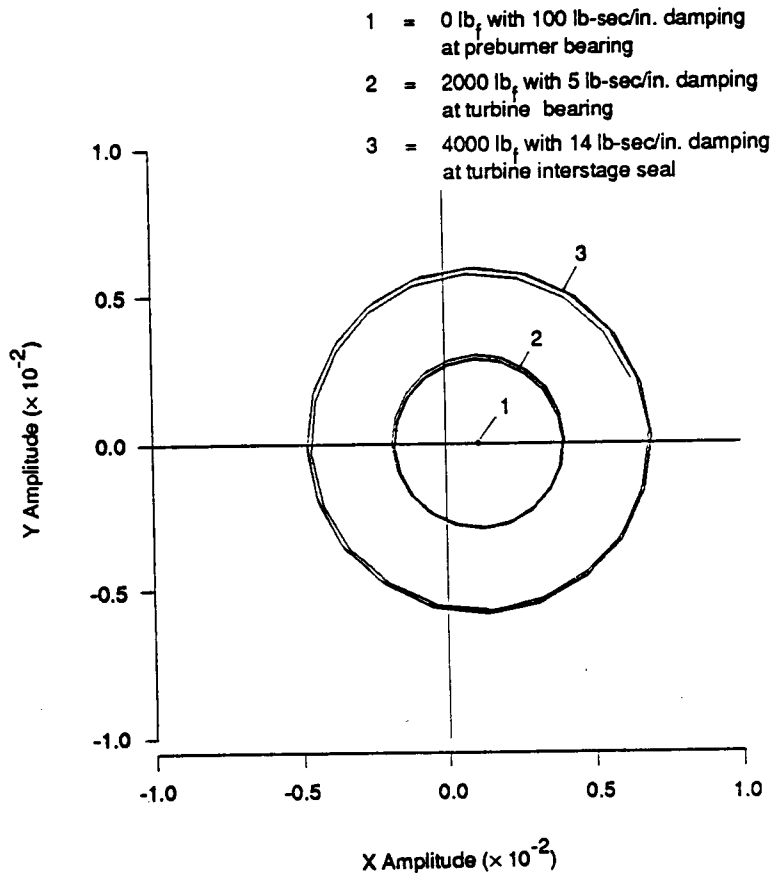
c) Preburner Orbit During Last 17 msec



d) FFT of Preburner Vibrations

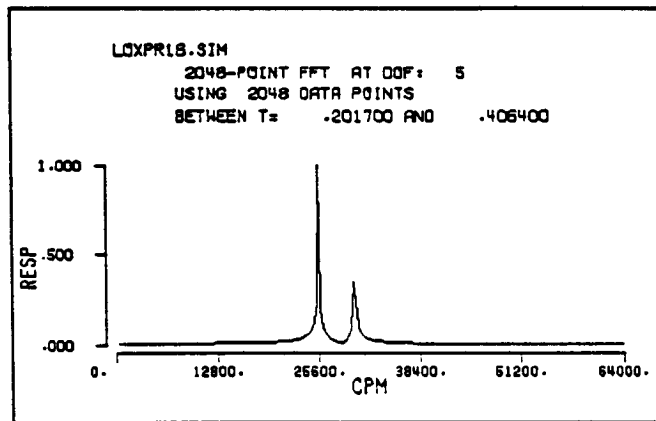
Figure 3-44. Effect of Main Impeller Imbalance on HPOTP Vibrations at the Preburner

90579

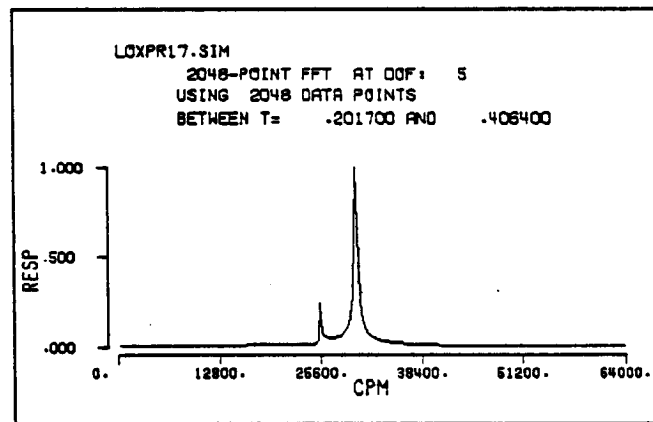


90580

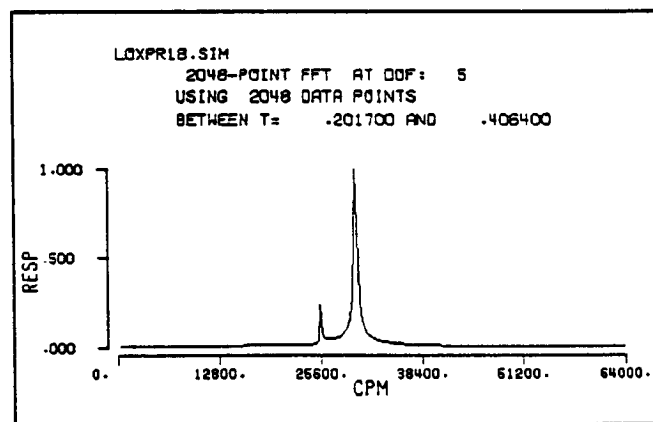
Figure 3-45. Effect of Main Impeller Imbalance on HPOTP Orbit at Preburner Spline



a) FFT for 0.0 lb_f Imbalance Force



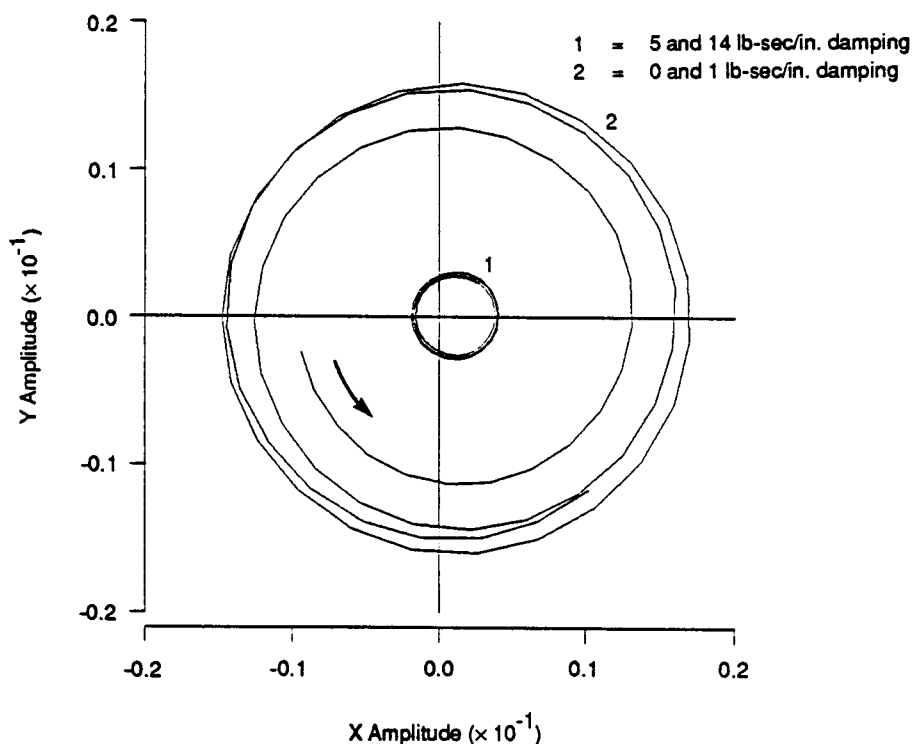
b) FFT for 2000 lb_f Imbalance Force



c) FFT for 4000 lb_f Imbalance Force

90581

Figure 3-46. Normalized FFT Plots for Preburner Vibration under Various Imbalance Forces



90582

Figure 3-47. Effect of Turbine Bearing and Interstage Seal Damping on HPOTP Orbit at Preburner Spline

Subsequent simulations were run to confirm the presence of the instability shown in Figure 3-43. As seen in Figure 3-44, when 6000 lb of imbalance forces are applied at the main impeller and realistic preburner and main impeller side loads of 50 and 2000 lb are included, both the subsynchronous second natural frequency and the synchronous imbalance vibrations are present. Further, even for the large imbalance forces assumed (equivalent to 0.013 in mass c.g. offset), it should be noted that the subsynchronous vibrations are significantly larger than the synchronous vibrations. As expected, beating between the two frequencies is evident in the orbit and displacement plots.

Figures 3-45 and 3-47 demonstrate that, with enough external damping, the self-excited subsynchronous vibration in the HPOTP can be controlled. In Figure 3-45, orbit plots of three separate time transient runs for different imbalance conditions are compared between 0.496 and 0.5 sec after the start of each simulation. During these three simulations, external damping at the preburner was 100 lb-sec/in., a level that may be expected if a damping seal were installed. Imbalance forces applied during these simulations included 2000 lb_f at the impeller and 0, 2000, and 4000 lb_f at the preburner. When no imbalance force is applied to the preburner rotor, the rotor orbit at the

preburner is essentially zero, but is displaced from the origin due to the static side load applied to both the preburner and main impeller. As preburner imbalance forces increase, the size of the orbit also increases. As seen in the frequency spectrums of Figure 3-46, both synchronous and subsynchronous vibrations are present in each case. However, with the introduction of imbalance forces at the preburner, the vibrations become dominated by the imbalance forces as opposed to the internal friction self-excited forces.

An additional two simulations were run to assess the impact of turbine end bearing and interstage seal external damping on the HPOTP subsynchronous vibrations. Figure 3-47 shows that the introduction of 5.0 and 14.0 lb-sec/in. at the turbine bearing and interstage seal, respectively, can reduce the magnitude of the vibrations experienced at the preburner.

3.3.3 Conclusions

Based on the above simulations, the following conclusions are drawn with regard to the SSME HPOTP:

1. Internal rotor friction at the preburner spline joint can cause self-excited subsynchronous vibrations in the HPOTP.
2. The self-excited vibrations occur at the HPOTP second critical speed or approximately 86% of the assumed operating speed.
3. External damping at the turbine interstage seal or turbine end bearings can be used to control the instability caused by internal rotor friction. The most effective means of controlling the internal rotor friction induced vibrations, however, is achieved by applying damping at the preburner, as could be accomplished with a damping seal.

These conclusions should be tempered by the fact that the friction torque parameter assumed in all simulations remained constant at 500 in.-lb. For the expected preburner torque load of 5000 in.-lb, the material coefficient of friction would have to be 0.1. If, however, the coefficient of friction were higher or increased with amplitude, higher levels of damping would be required to control the resulting vibrations.

4.0 TRACTION TESTING

In this section of the report, the test item description, method of test, and results of the traction tests are presented. The objective of the traction testing was to confirm the coefficient of friction for the materials and conditions identified in the Propulsion Hardware Review task and to assess the applicability of using a constant coefficient of friction in the rotordynamic internal rotor friction joint models.

4.1 Test Rig and Specimen Description

Figures 4-1 and 4-2 show the test specimens and the test setup used to determine the coefficients of friction under small amplitude oscillatory motions for material combinations found in the SSME turbopumps. To simulate the SSME turbopump joint interface conditions, the test specimen pairs (static and dynamic) were designed and manufactured so that representative contact stresses, surface finishes, flatness, and machining marks were achieved. The static specimen crown radius provided Hertzian contact stresses ranging from approximately 15,000 to 65,000 psi for loads ranging from 5 to 100 lb.

Each test specimen also had provision for internally mounted thermocouples and was designed so that two test points could be acquired from each specimen. Test specimens were fabricated from Waspaloy, Inconel 718, titanium (5 Al- 2.5 Sn ELI) and 4340 steel. The steel specimens were fabricated to provide data for use in the component and rotor-dynamic testing since those tests would use steel test specimens.

The coefficient of friction test rig (Figure 4-2) measures the friction forces that result from small amplitude oscillatory motion between two mating surfaces under a controlled normal load. Under this program, the test rig was operated over a frequency range of 10 to 1000 Hz, temperatures from -320 to 1000°F and at peak-to-peak amplitudes to 0.002 in. The major components used to achieve the required operating characteristics and to acquire the test data included the Ling Electronics Model 335a electrodynamic shaker, test specimen holders, chill cup assembly, high temperature oven, normal load device, and instrumentation including thermocouples, load cells, accelerometers, and displacement probes.

The stationary specimen holder permits both the application of the normal load and measurement of the friction forces. As seen in Figure 4-2, the load arm is connected to

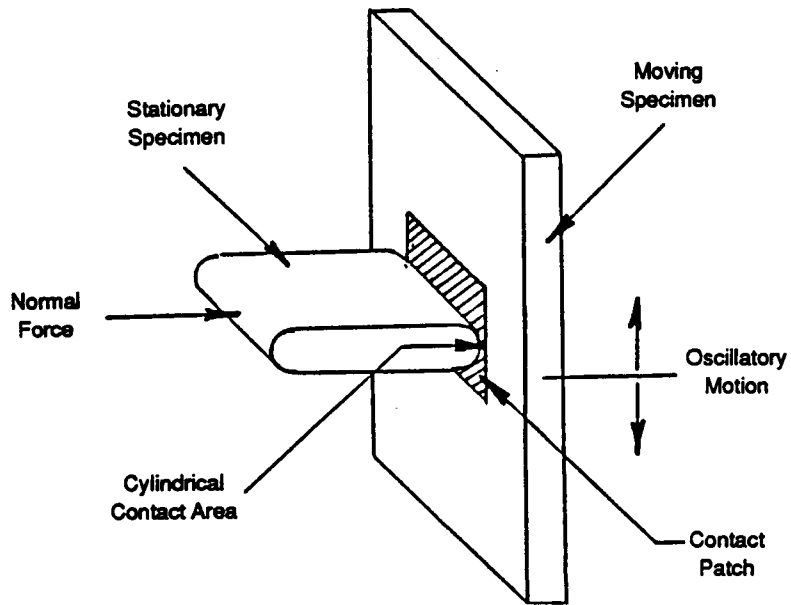


Figure 4-1. Coefficient of Friction Test Configuration

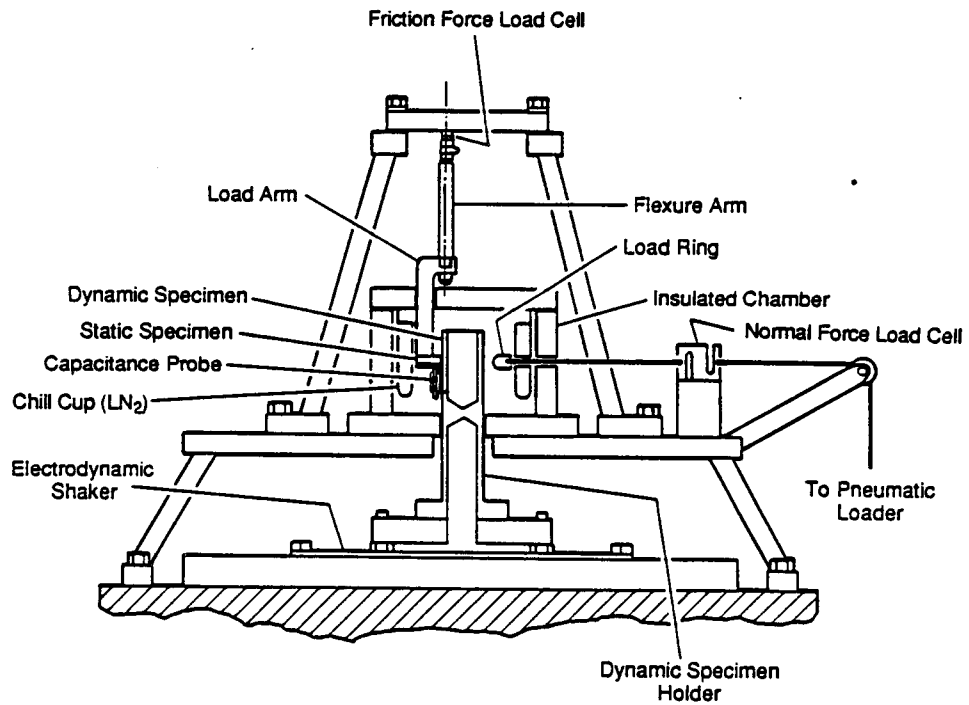


Figure 4-2. Traction Test Rig with Chill Cup

a friction force load cell through a flexure element that aligns the friction force load cell with the contact zone. To assure alignment of the static and dynamic test specimens over the wide temperature ranges expected, while accurately transmitting the friction force, the flexure arm assembly is stiff in the friction force direction and torsionally "soft" in the normal load plane. Once the test specimens are aligned, the desired normal load is applied through the load ring by a pneumatic load cylinder.

The dynamic specimen holder is a partially hollowed-out post that is bolted to the Ling shaker table. The lower portion of the support post is hollowed out to minimize conduction between the shaker table and the post during the elevated and cryogenic temperature tests. The top of the post is also hollowed out so that it can be filled with a cryogenic fluid during low-temperature testing.

For cryogenic and elevated-temperature testing, an insulated chamber and either a chill cup assembly or a high-temperature oven surrounds the test specimens. The chill cup assembly, which is filled with liquid nitrogen during testing, is of split construction to facilitate assembly and allow the normal loading cable to be attached to the load ring. Provision was also made to introduce a dry, inert cover gas into the test region before cooling and during testing to displace the air present in the chamber and prevent frosting of the test surfaces.

For elevated-temperature tests, the chill cup assembly is replaced with an electric resistance heating oven. Heat shields are located above and below the test region to protect both the load cell and flexure arm above and the Ling shaker below. Ceramic insulation is also used to isolate the shaker from the test chamber during both the elevated and cryogenic tests.

Test instrumentation to measure and monitor pertinent test parameters include a high-sensitivity, piezoelectric, Kistler Model 9312A load cell to measure the friction forces, an Omega LCB-100 load cell and a DP2000S-2 panel meter to measure normal load, and both B&K 4333 accelerometers and MTI Accumeasure™ System 1000 capacitance probes to measure relative motions between the static and dynamic test specimens. The capacitance probes were used to measure the relative motion between the static and dynamic specimens in the vertical, normal, and transverse directions, and the accelerometers were used to measure the macromotions of the dynamic specimen post in the vertical direction and the static specimen in the normal load direction. A separate

accelerometer, mounted on the shaker table, was also used to measure and control the shaker input motions. Temperatures of both the static and dynamic test specimens were measured with internally mounted thermocouples.

4.2 Method of Test

The matrix of conditions and material combinations used in determining the coefficients of friction are presented in Table 4-1. During testing, the following parameters were varied:

- Normal load
- Frequency
- Slip Amplitude
- Surface condition
- Lubricant
- Temperature

Table 4-1. Traction Test Matrix

Test	Materials				Temperature (°F)			Lubricant		Surface Finish				
	Waspaloy/ Waspaloy	Waspaloy/ Inconel	Titanium/ Titanium	Steel/ Steel	70	1000	-320	None	Dry	8 rms	16 rms	32 rms	New	Worn
1	•				•			•			•		•	•
2		•			•			•			•		•	•
3			•		•			•			•		•	•
4				•	•			•			•		•	•
5	•				•				•		•		•	
6		•			•				•		•		•	
7			•		•				•		•		•	
8				•	•				•		•		•	
9	•				•			•		•			•	
10	•				•			•				•	•	
11		•			•			•		•			•	
12		•			•			•				•	•	
13				•	•			•		•			•	
14				•	•			•				•	•	
15	•					•		•			•		•	•
16	•					•			•		•		•	
17		•					•	•			•		•	
18		•					•		•		•		•	
19	•						•	•			•		•	•
20	•						•		•		•		•	

Normal loads of approximately 11 and 56 lb were used during the testing so that contact stresses ranging from approximately 20,000 to 50,000 psi were achieved. Three frequencies (43, 155, and 391 Hz) and five amplitudes including 0.1, 0.2, 0.5, 1.0, and 2.0 mil provided the test conditions representative of the SSME environment being simulated. Surface finishes used were 8, 16 and 32 μ in rms. The three temperatures evaluated included -300, 1000^oF, and room temperature. Materials were also tested under both unlubricated and lubricated conditions. Lubricated specimens were treated with MoS₂ according to Rocketdyne SSME specification RB140-007. Finally, an assessment of the effect of wear was also attempted. Specimens used to determine the coefficient of friction from worn interfaces were those that had been used for the various other tests.

The test sequence was established at room temperature and then followed for the remainder of the elevated and cryogenic tests. The test sequence was as follows:

- Set the lowest normal force and test frequency
- Acquire data starting with the lowest test slip amplitude
- Increase slip amplitude and repeat tests until highest desired amplitude is achieved
- Go to the next test frequency and repeat the amplitude sweep
- After highest frequency data was acquired increase the normal load and repeat the amplitude sweeps at each of the three test frequencies
- At the conclusion of the test sequence repeat the initial test sequence (i.e. low amplitude, frequency and load) as a repeatability check.

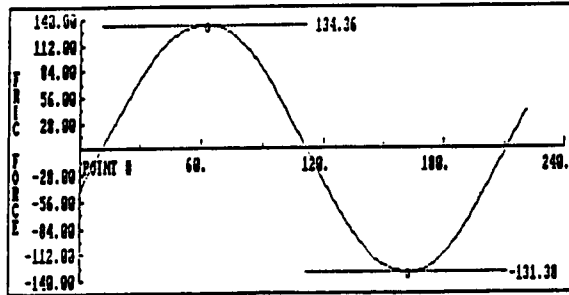
Once the tests using the nominal or baseline test specimens were completed, the effects of dry film lubrication, surface finish, and service conditions as outlined in Table 4-1 were evaluated. Baseline test conditions were conducted at room temperature, under an 11-lb normal load and with unlubricated surfaces having a 16- μ in rms finish. The tested surface finishes were selected to simulate those conditions experienced in the assembled HPOTP and HPFTP rotors. In addition to matching the specified material surface finishes, the test specimens were oriented so that the machining marks were in the same direction as experienced in the assembled rotors.

4.3 Results

Representative results from the coefficient of friction testing are presented in this section. Figure 4-3 presents profiles of the measured friction force for four of the five different amplitudes of motion for steel against steel at an 11-lb load, 43 Hz frequency,

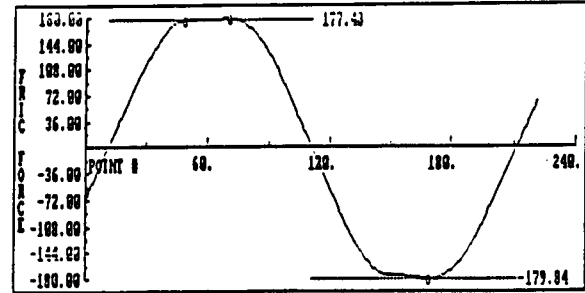
Normal Load = 50 N; Frequency = 43 Hz; Temperature = 70°F; Nonlubricated

5.0 Micron P.P. — Slip Amplitude



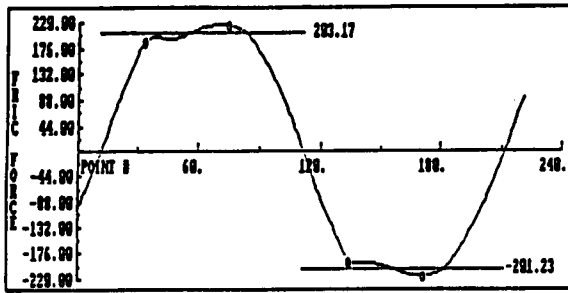
COEFFICIENT OF FRICTION: .531

12.6 Micron P.P. — Slip Amplitude



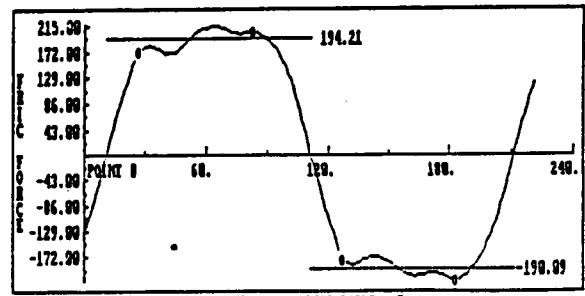
COEFFICIENT OF FRICTION: .715

28.0 Micron P.P. — Slip Amplitude



COEFFICIENT OF FRICTION: .889

56.0 Micron P.P. — Slip Amplitude



COEFFICIENT OF FRICTION: .769

Figure 4-3. Friction Force Wave Form

90585

70°F unlubricated condition. The 0.1-mil and 0.2-mil amplitude tests resulted in forces that were predominantly the result of elastic motions of the load train. As seen in Figure 4-3, the force waveform for the two low amplitude tests is almost sinusoidal as opposed to a square wave, as would be expected under the oscillatory motions imposed. Upon review, it was determined that the measured sinusoidal forces resulted since the applied motions were inadequate to overcome the static coefficient of friction. However, when test specimen dynamic motions were in the range of 0.4 to 0.8 mil, a transition between elastic deformation and sliding motions was encountered. At the higher amplitudes (0.8 mil or more), slippage occurred more readily though some small effect of elastic motion was still observed. The larger amplitudes produced waveforms that became more like the expected square wave as seen in the 0.5, 1.0, and 2.0 mil slip amplitude tests.

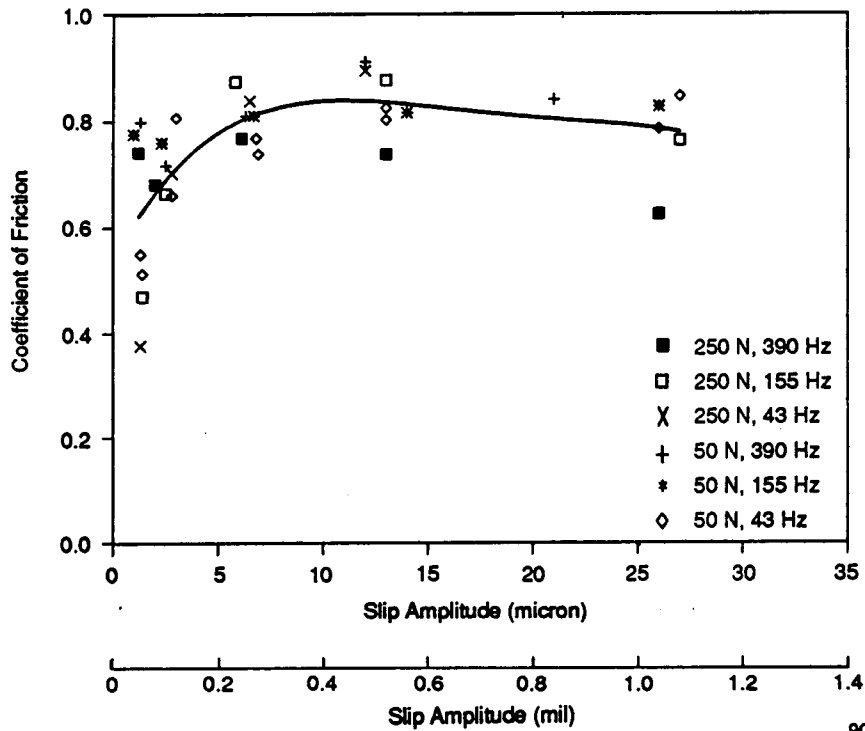
Using the measured wave forms, the coefficient of friction was determined by first establishing the average friction force and then dividing this value by the measured normal force. Figures 4-4 through 4-9 and Tables 4-2 and 4-3 summarize the test results. For each curve plotted, the friction data at all of the tested normal loads and frequencies were used. From Figure 4-4, it is seen that while there is scatter in the coefficient of friction data, the trends for each of the loads and frequencies tested are very similar. Since there was little variation in friction data as a function of load and frequency, the data analysis and subsequent plots used the composite data set consisting of all loads and frequencies for each temperature and lubrication condition.

In addition to the lack of variation in friction coefficient due to load and frequency, there was no significant change in the coefficient of friction as a function of the prepared surface finish (Table 4-2). The lack of significant change in the coefficient of friction due to surface conditions is most likely due to the immediate surface wear that occurs in the test sequence. After the first few cycles, the surfaces become effectively the same, regardless of the initial prepared surface condition. As a result these test data were also incorporated into the composite data sets for presentation of the friction coefficient as a function of amplitude.

Figure 4-5 shows the friction data for steel at both lubricated and unlubricated conditions and the curve that was drawn through the test points. As seen, the coefficient of friction for the lubricated tests remains fairly constant and linear regardless of the amplitude of motion. On the other hand, the unlubricated coefficient of friction increases with increases in amplitude for approximately the first 0.2 to 0.4 mil (5 to 10 micron) and then remains fairly constant for further increases in amplitude. These two trends are evident for almost all tests conducted as evidenced by the test results shown in Figures 4-5 through 4-9.

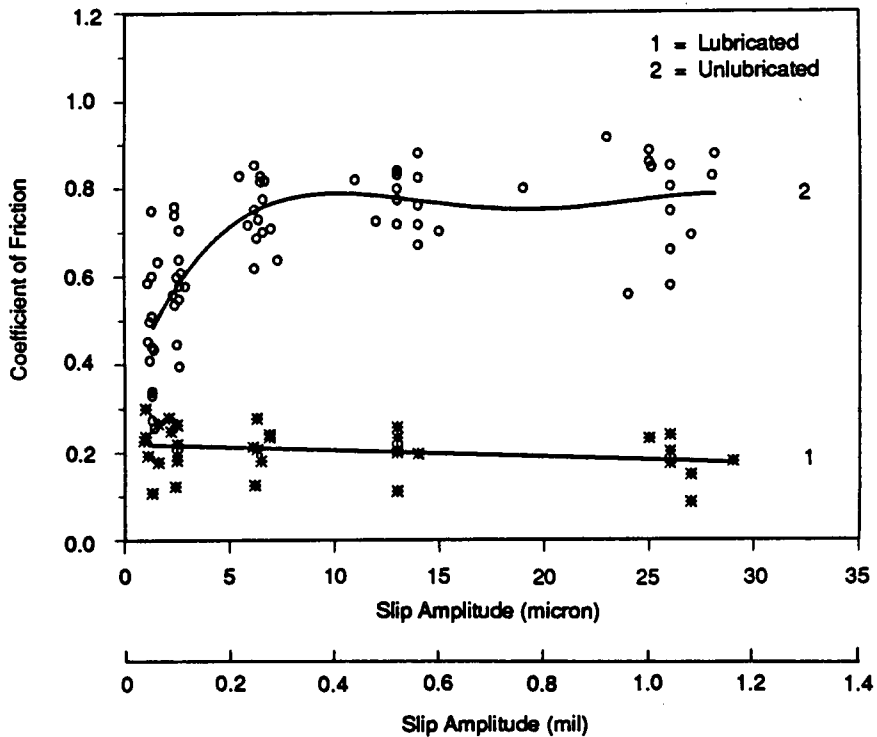
The observed variation in the coefficient of friction with amplitude as seen in the unlubricated test results may be explained either by an increase in sliding speed or by relative motion between the two test specimens that is smaller than the contact area, permitting wear debris to remain in the contact area and act as a third body lubricant. Both of these phenomena are known to affect dry contacts in the way observed.

In addition to these general trends, it should also be noted that, in all cases, the unlubricated, room temperature tests resulted in the highest coefficients of friction.



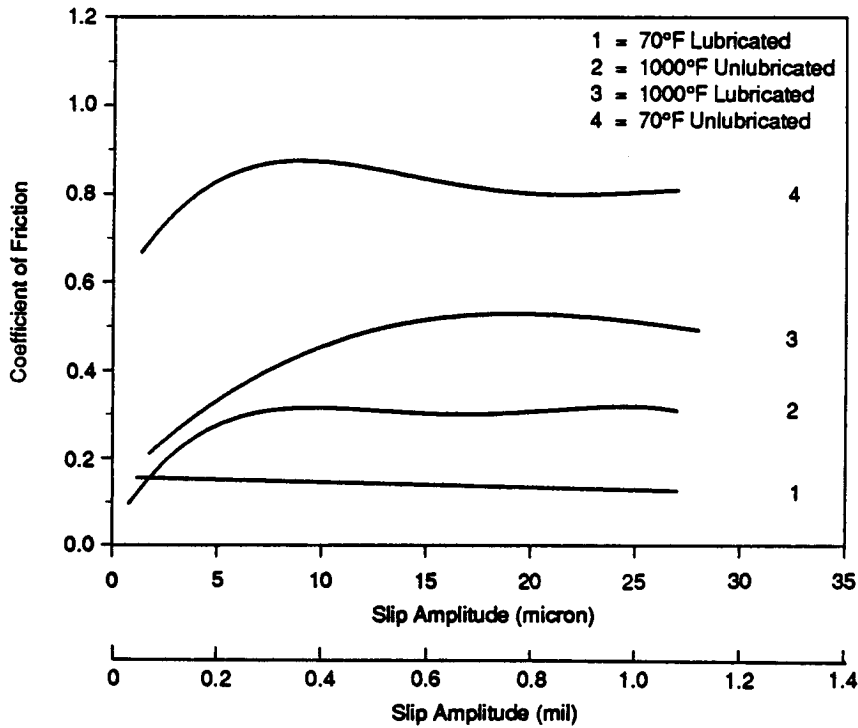
90636A

Figure 4-4. Friction Coefficient for Unlubricated Inconel vs Waspaloy at 70°F, Two Normal Loads and Three Frequencies



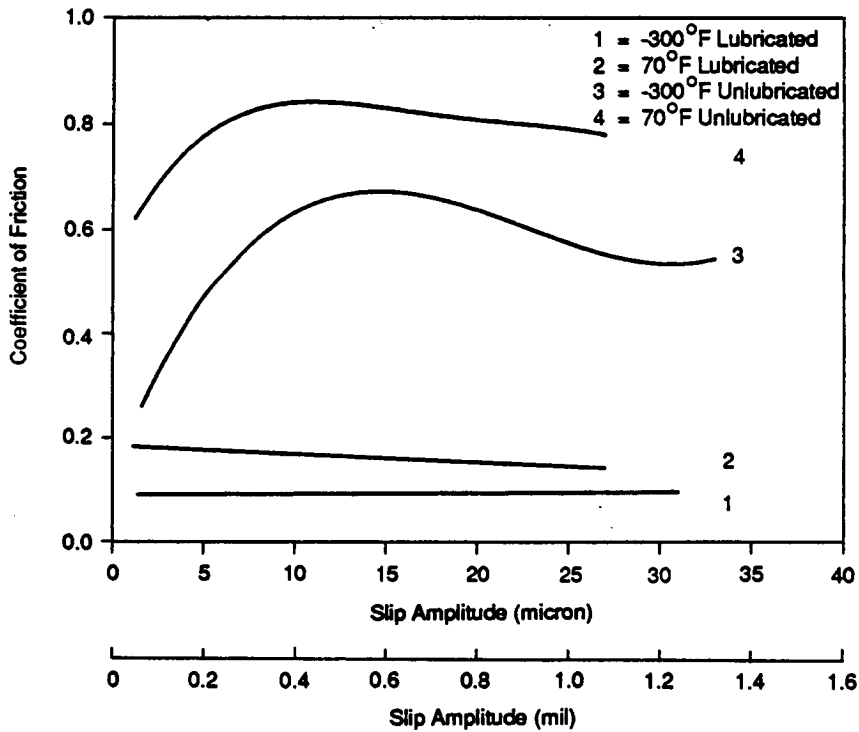
90636B

Figure 4-5. Steel vs Steel Friction Coefficient at 70°F under Lubricated and Unlubricated Conditions



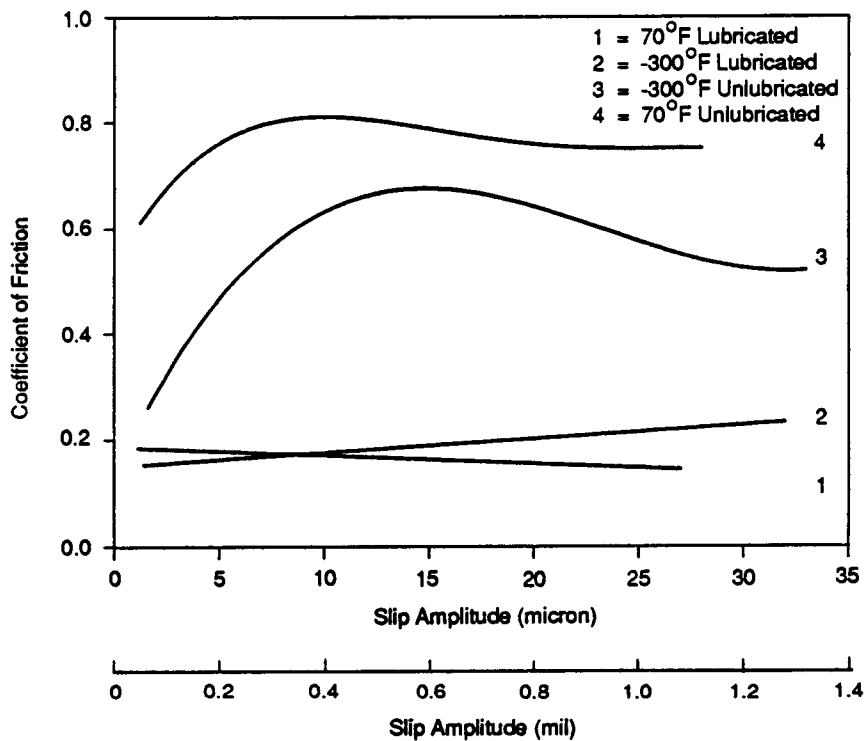
90634A

Figure 4-6. Waspaloy vs Waspaloy Friction Coefficient at 70 and 1000°F Temperatures under Lubricated and Unlubricated Conditions



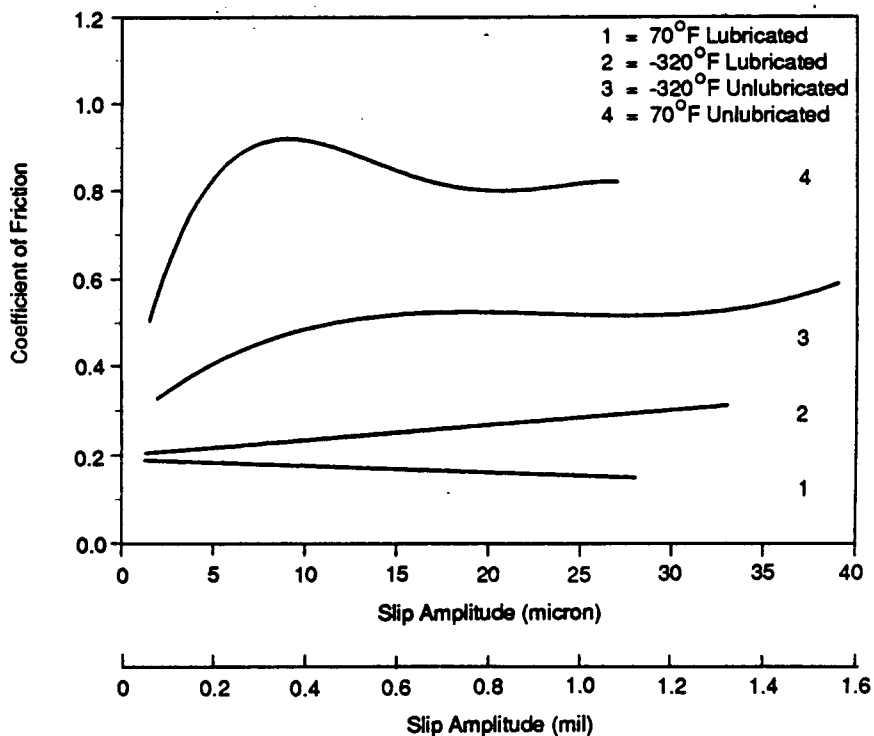
90634B

Figure 4-7. Inconel vs Waspaloy Friction Coefficient at 70 and -300°F Temperatures under Lubricated and Unlubricated Conditions



90635A

Figure 4-8. Inconel vs Inconel Friction Coefficient at 70 and -300°F Temperatures under Lubricated and Unlubricated Conditions



90635B

Figure 4-9. Titanium Friction Coefficient at 70 and -320°F Temperatures under Lubricated and Unlubricated Conditions

Table 4-2. Coefficient of Friction (Unlubricated)

Test Condition	Waspaloy/ Waspaloy	Inconel/ Waspaloy	Titanium/ Titanium	Steel/ Steel
70°F/16 rms	0.7 to 0.9	0.8 to 0.9	0.7 to 0.92	0.75 to 0.91
70°F/8 rms	0.8 to 1.0	0.7 to 0.9	--	0.72 to 0.90
70°F/32 rms	0.7 to 0.92	0.6 to 0.85	--	0.65 to 0.90
1000°F	0.25 to 0.42	--	--	--
-300°F	--	0.6 to 0.85	0.5 to 0.65	--

Table 4-3. Coefficient of Friction (Lubricated)

Test Condition	Waspaloy/ Waspaloy	Inconel/ Waspaloy	Titanium/ Titanium	Steel/ Steel
70°F	0.09 to 0.22	0.12 to 0.25	0.17 to 0.25	0.15 to 0.30
1000°F	0.35 to 0.62	--	--	--
-300°F	--	0.07 to 0.20	0.15 to 0.46	--

Further, regardless of material combination, the coefficients of friction for the unlubricated tests were found to fall between 0.7 and 0.9 once amplitudes exceeded approximately 0.4 mil (10 microns).

The lower unlubricated coefficients of friction for the elevated and cryogenic tests are most likely due to oxidation and increased material hardness. Specifically, the Waspaloy high-temperature tests (Figure 4-6) showed a lower coefficient of friction at 1000°F than at room temperature. The lower coefficient of friction may be attributed to oxidation of the material surfaces at the temperatures, which in turn provided interface lubrication.

Cryogenic testing of both the titanium/titanium and Inconel/Waspaloy unlubricated material combinations showed lower coefficients of friction than the baseline room temperature tests. It is not believed that the reduction in the measured coefficient of friction is due to condensation on the surfaces since care was taken to purge the test

chamber with an inert gas prior to testing. However, simple friction coefficient theories state that the coefficient of friction is inversely proportional to material hardness that may be increased under the cryogenic test conditions.

In only one case did the coefficient of friction for the lubricated condition exceed an unlubricated test condition. Figure 4-6 shows that the coefficient of friction for lubricated Waspaloy at 1000°F exceeded that for the unlubricated condition at 1000°F. The increase in the coefficient of friction for the high-temperature lubricated test is not unexpected however, since the MoS₂ dry film lubricant is known to break down at temperatures in excess of 750°F and lose its lubricating properties. At the same time the oxides formed on the uncoated test specimens tend to act as interface lubrication.

In summary, the effects of normal load, amplitude, frequency, surface condition, lubrication, and temperature on the coefficient of friction for material combinations found in the SSME turbopumps were studied. These tests revealed that estimates of the coefficient of friction in the neighborhood of 0.1 to 0.3 and 0.7 to 0.9 for lubricated and unlubricated conditions, respectively, are reasonable when motion in excess of 20 micron (0.8 mils) are expected. At elevated temperatures the coefficient of friction was seen to increase to approximately 0.5 for the lubricated condition and decrease to approximately 0.4 for the unlubricated condition. In several cases (see Figures 4-5 through 4-9), the coefficient of friction was observed to decrease slightly for increases in amplitude. This decrease may be due to the increased sliding velocities experienced. As the sliding velocity increases the surface temperature may rise, resulting in increased oxidation of the materials, which would effectively lubricate the contact zone.

Based on these results it has become evident that the simplified assumptions made in the analysis of the friction-producing joints need to be reevaluated. The basic assumption made and used in the analytic development was that the coefficient of friction would remain constant for the motions experienced. This assumption appears valid for the lubricated condition, which constitutes the majority of conditions experienced in the SSME hardware. However, for those cases where the joint interfaces may not be lubricated, the assumed constant coefficient of friction does not appear valid. This is especially true when these joints undergo very small relative motions as may be expected for the SSME LOX turbopump preburner and main impeller axial splines. However, before a variable coefficient of friction model should be incorporated in the internal rotor friction joint models, a better understanding of the relationship between the

coefficient of friction and amplitude of motion is required. Further, since most of the SSME Lox turbopump joints are dry-film lubricated, the present analysis using a constant coefficient of friction appears be valid.

5.0 COMPONENT TESTING

In this section of the report, the test item description, method of test, and results will be presented for the component damping tests. The objective of the component testing was to identify the form and quantity of damping present in three SSME turbopump friction-producing joints. The three joints selected for component testing were the HPOTP pre-burner axial spline, Curvic coupling, and main impeller interference fit joints.

5.1 Test Item Description

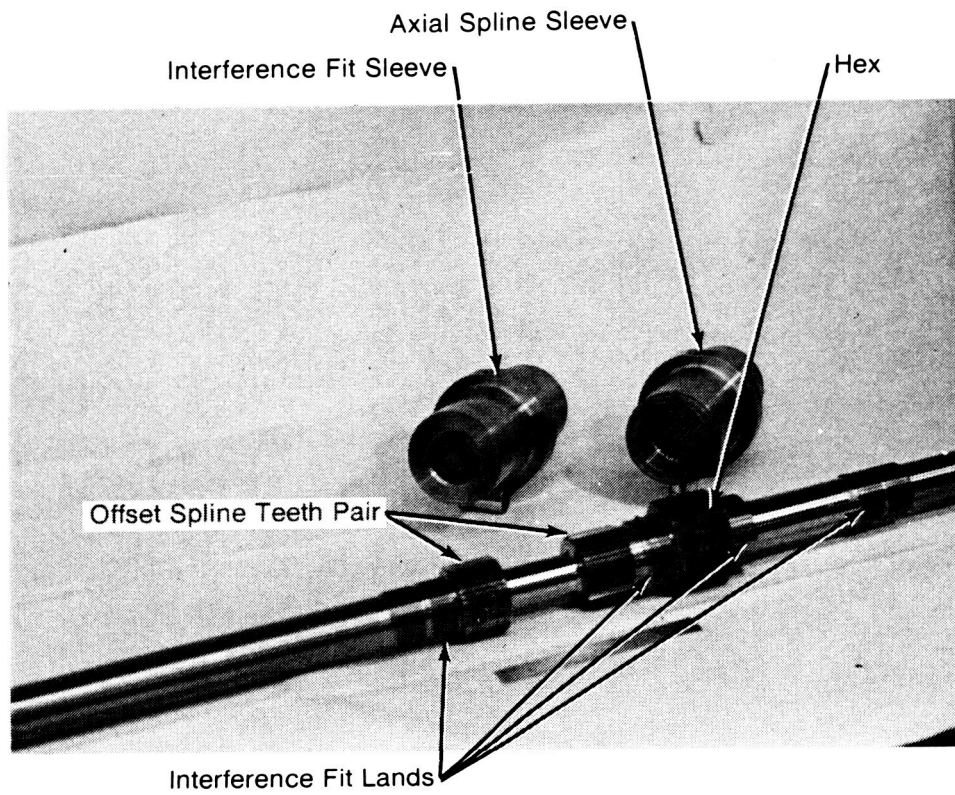
Two series of test articles were fabricated for dynamic testing. The first series of shafts were solid, but they were machined to the same external dimensions as the final test configurations with friction-producing joints to ensure dynamic similarity for evaluation of material hysteresis effects. Two of these solid shafts were then machined to the final SSME HPOTP configurations as shown in Figure 5-1.

To ensure that the test joints would be exercised during the swept sine forced excitation testing, each joint was placed near the center of the shaft where maximum bending stresses would occur when excited at the first natural frequency. The Curvic coupling joint used 12 bolts, torqued/stretched to two different values to provide contact pressures similar to the projected operating conditions of the HPOTP. The bolt load levels selected to simulate the range of operating conditions were 3130 and 2000 lb.

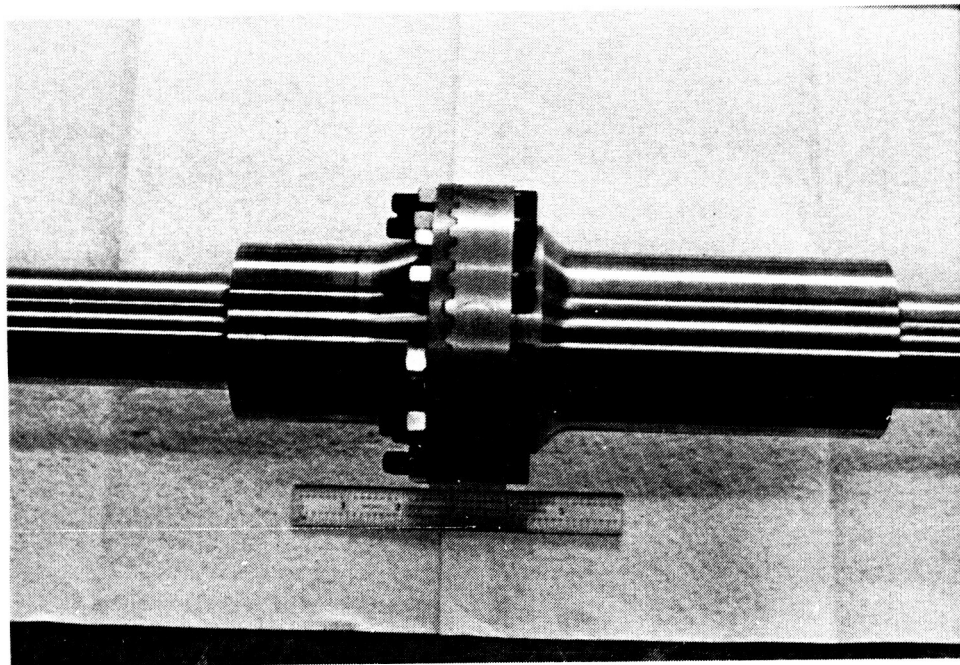
The axial spline and interference fit test articles were fabricated in such a way that the same basic shaft could be used with each joint independently. Additionally, the component test shaft was designed so that it could also be used for the rotordynamic testing. As seen in Figures 5-1 and 5-2, the spline/shrink shaft used two different collars or sleeves, one to introduce a spline joint and one to introduce an interference fit joint. To ensure that each of the test joints were exercised during the dynamic shaker testing, the joints were placed near the center of the shaft at the antinode of the first bending mode.

The interference fit joints were similar to those found on the HPOTP main impeller and had approximately one mil radial interference. Selection of the interference fit level was accomplished by developing a finite element model of the component test shaft and assessing the moment transmitted across the joint interface for given applied excitation

ORIGINAL PAGE
BLACK AND WHITE PHOTOGRAPH



Offset Spline and Interference Test Joint Shaft



Curvic Component Joint Test Shaft

Figure 5-1. Component Test Specimens As Fabricated

ORIGINAL PAGE
BLACK AND WHITE PHOTOGRAPH

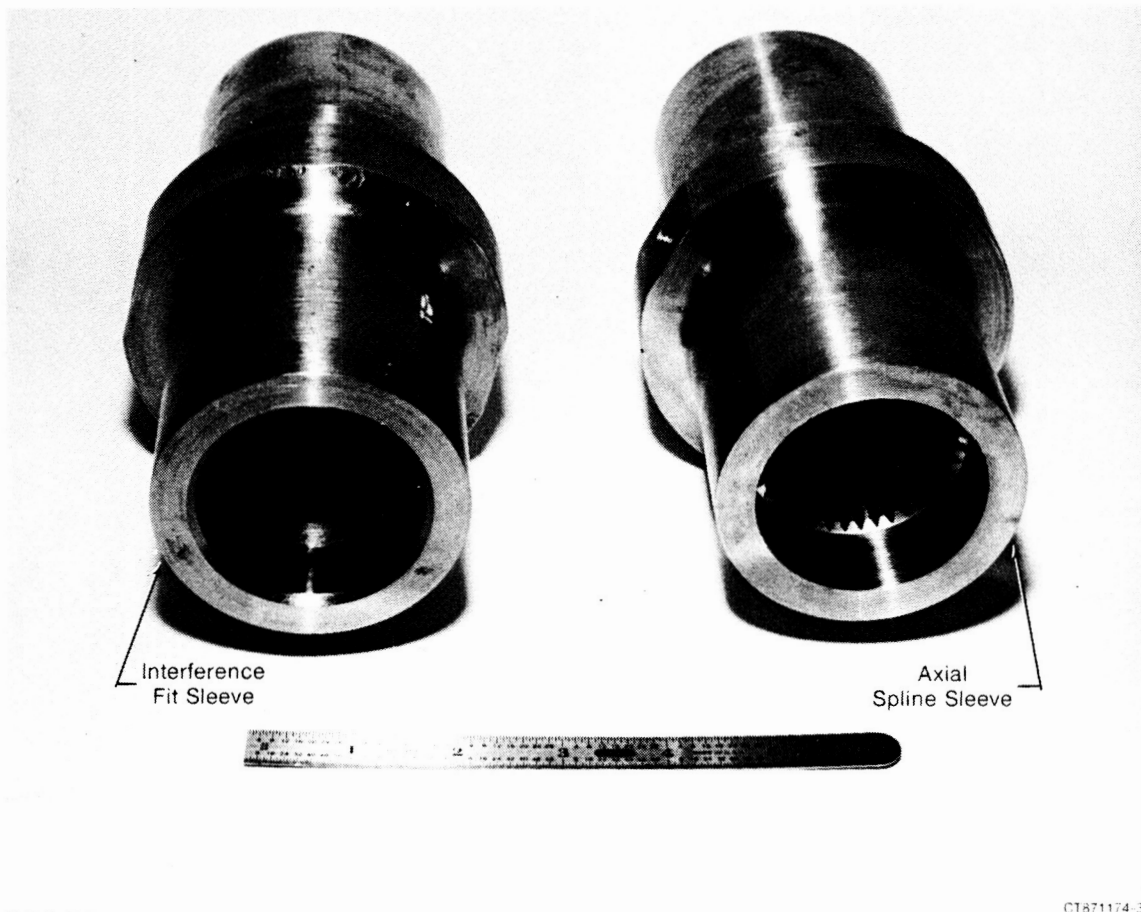


Figure 5-2. Interference Fit and Axial Spline Sleeves As Manufactured

forcing levels. By comparing the moment transmitted across the interference fit joint against the calculated maximum moment before slippage was predicted to occur, using Equation 3.52 of Section 3.1, the interference fit level was selected.

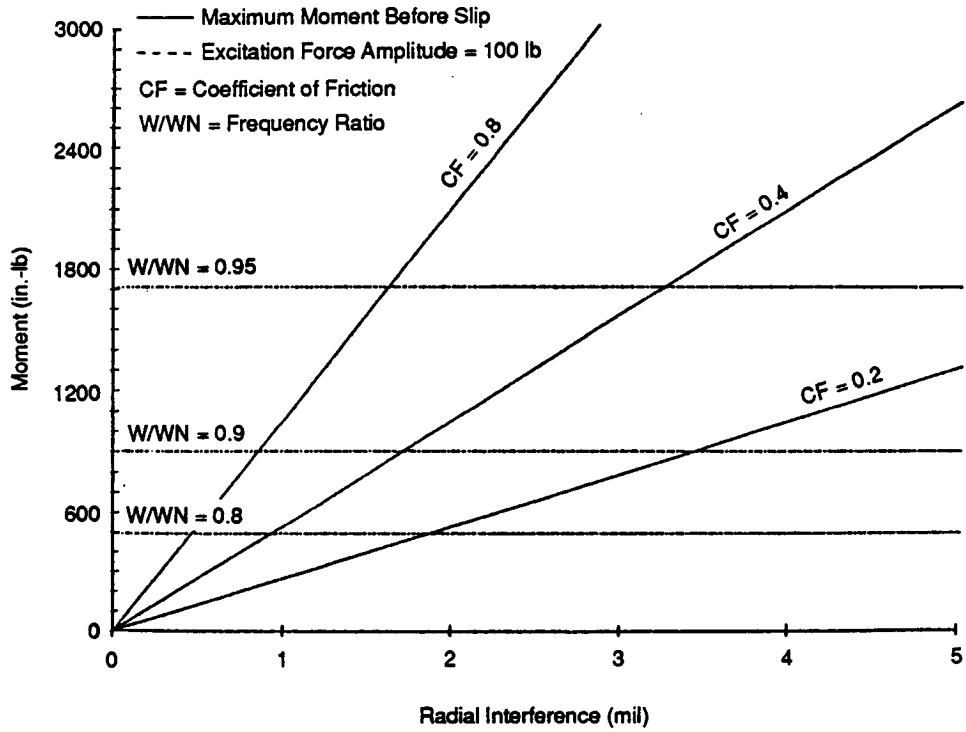
The transmitted moment per unit applied side load force for each of the two interference fit joints on the test shaft are summarized in Table 5-1. As with the HPOTP, the two interference fit lands have different diameters (2.15 and 1.65 in.). The data presented in the table include the frequency ratio (excitation frequency/natural frequency) and the maximum bending moment that can be transmitted across each interference fit land per unit applied side load force.

Table 5-1. Component Test Shaft with Interference Sleeve

Frequency Ratio (W/W_n)	Maximum Transmitted Bending Moment Per Unit Side Load for 1 mil Interference at Each Joint	
	Joint 1 2.155 in. Diameter	Joint 2 1.65 in. Diameter
0.80	±4.9	±5.1
0.90	±9.0	±9.3
0.95	±17.1	±17.8

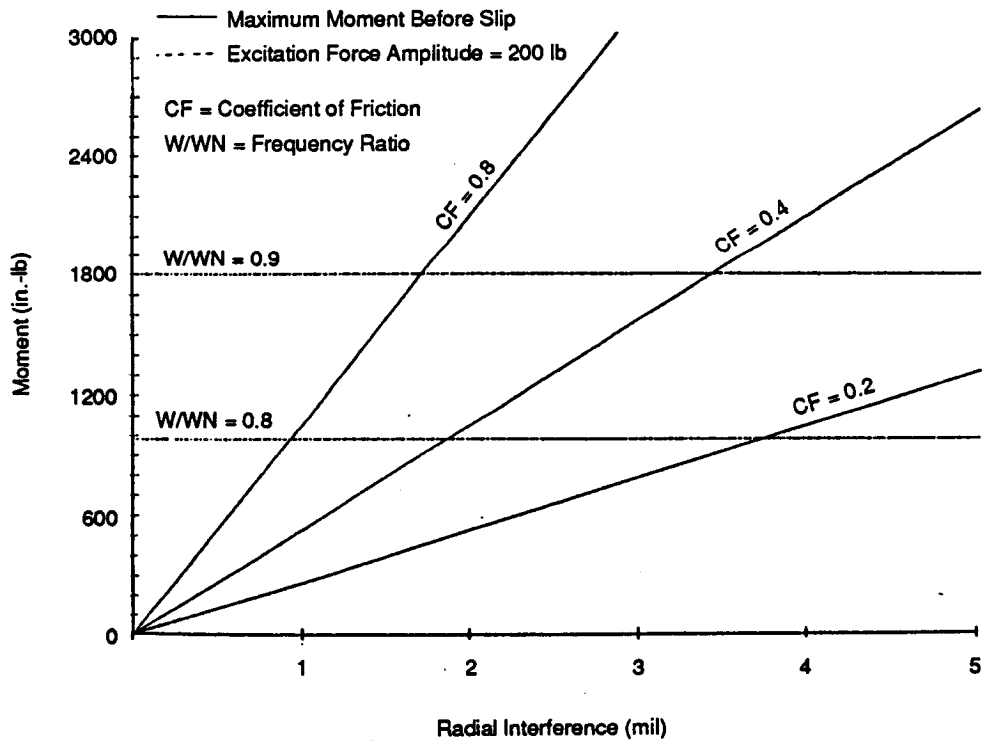
Figures 5-3 through 5-6 show the maximum moment before slippage as a function of the radial interference for different values of coefficient of friction. In addition, the force transmitted through the joint at different ratios of excitation frequency to the natural frequency is shown as a dashed horizontal line. Thus, by selecting an interference fit level, it was possible to assess the potential for slippage within the joint for different values of coefficient of friction and as a function of the excitation frequency. Based on this analysis, the interference fit levels were chosen to be one mil of radial interference for each end of the interference fit test sleeve.

The axial spline test portion of the shaft was designed to permit the static torque loading of the spline at approximately 5000 in.-lb, the level expected in the preburner spline during operation. To achieve the applied static torque, two sets of spline teeth, offset by 18 min from each other, were machined onto the test shaft. The diameter of the shaft



90608

Figure 5-3. Moment Transmitted across 2.15-in. Diameter Joint before Slip As a Function of Interference (100-lb Excitation)



90610

Figure 5-4. Moment Transmitted across 2.15-in. Diameter Joint before Slip As a Function of Interference (200-lb Excitation)

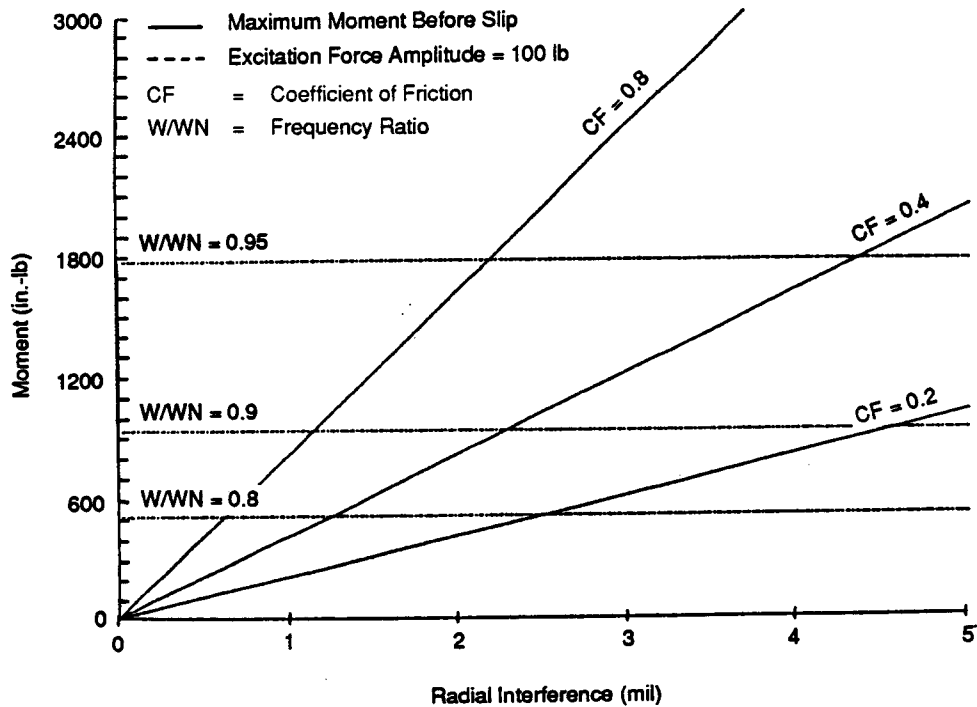


Figure 5-5. Moment Transmitted across 1.65-in. Diameter Joint before Slip As a Function of Interference (100-lb Excitation)

90611

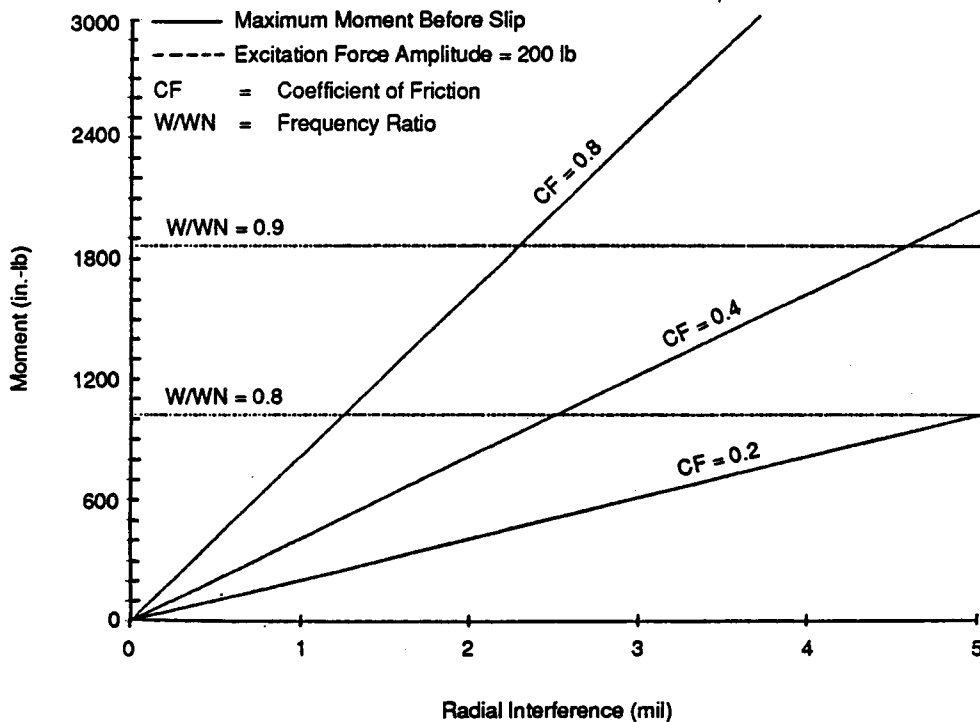


Figure 5-6. Moment Transmitted across 1.65-in. Diameter Joint before Slip As a Function of Interference (200-lb Excitation)

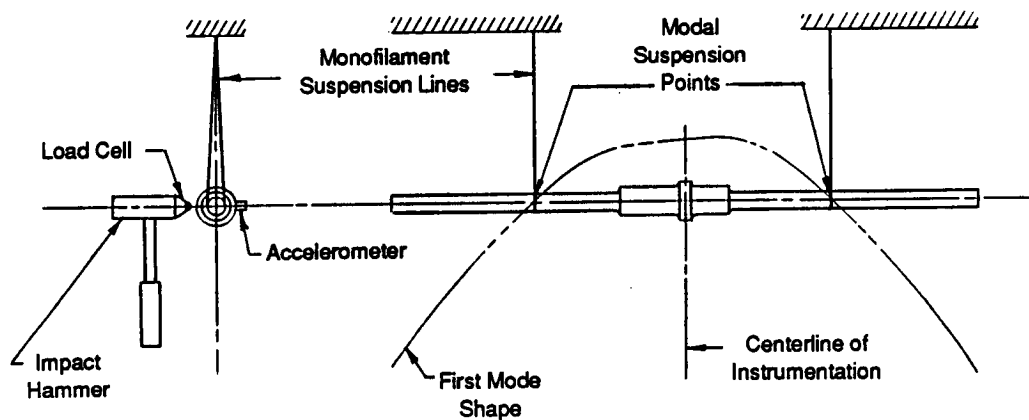
90612

between the two sets of spline teeth was 1.16 in. This diameter combined with the spline offset was selected to provide the desired 5000 in.-lb of static torque, while at the same time being evaluated for slip potential in a manner similar to that used for the interference fit joint.

5.2 Method of Test

To ensure that material hysteresis was accounted for during the component testing, three solid test shaft configurations were tested. Figure 5-7 shows the test setup used to assess the test shaft material hysteresis. Each shaft was hung at the predicted first mode nodal point by monofilament line. The instrumentation used included a calibrated impact hammer, an accelerometer mounted on the shaft at its antinode, and a two-channel spectrum analyzer. Shaft natural frequencies and node points were determined first. Once the nodal points were established, transient/impact free decay testing of each shaft was accomplished. Impact testing was conducted at both the first and second natural frequencies.

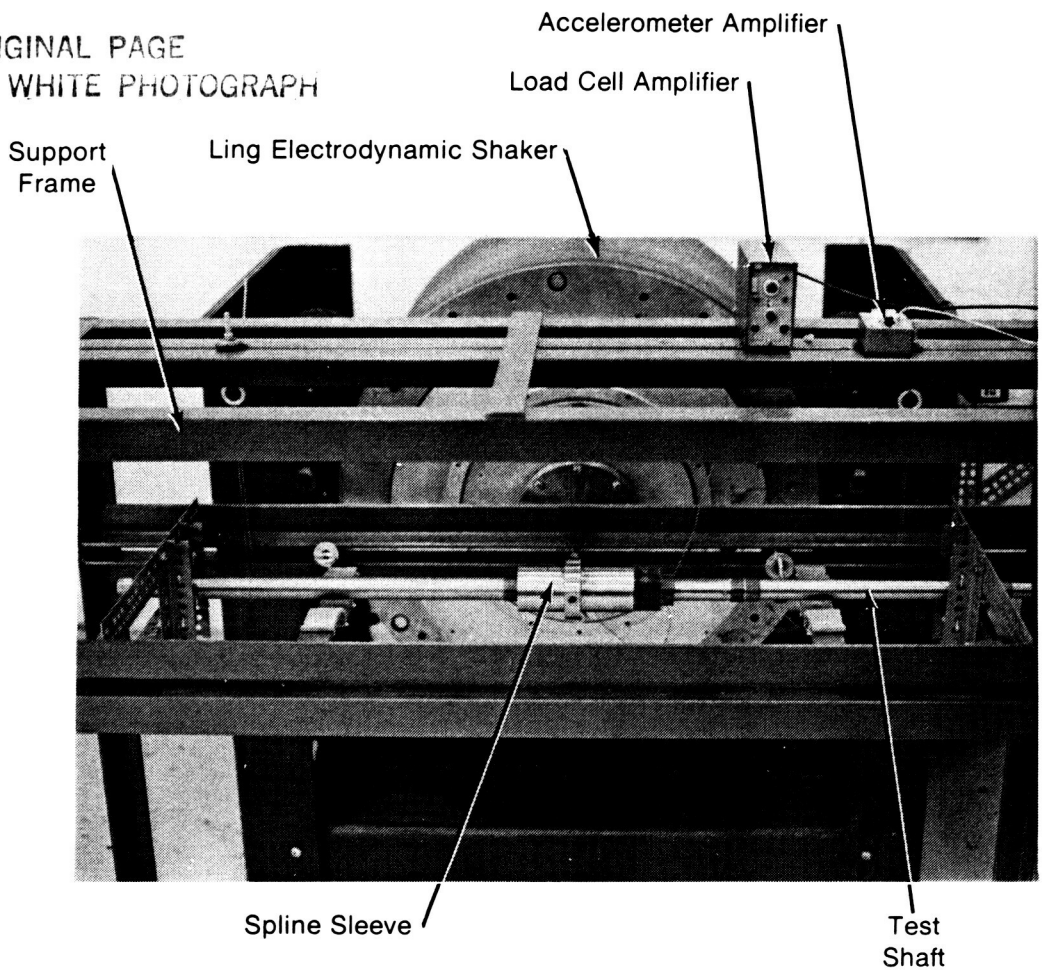
After the magnitude of the material hysteresis had been quantified, the two 60-in.-long shafts were machined to the final test configurations shown in Figure 5-1 and readied for the forced excitation testing. Figure 5-8 shows the test setup used. As seen, each shaft was suspended in air, attached to a shaker through a stinger, and included a force cell in



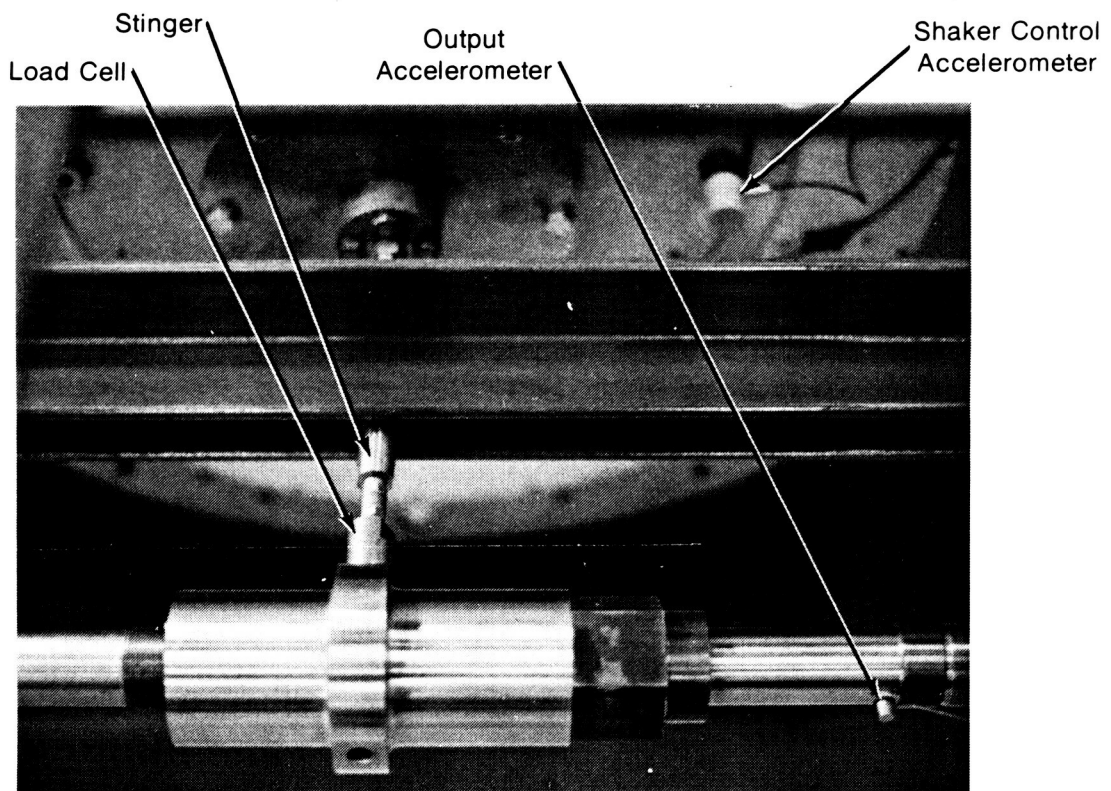
90613

Figure 5-7. Solid Shaft Impact Testing Setup

ORIGINAL PAGE
BLACK AND WHITE PHOTOGRAPH



Component Shaft Test Setup



Component Shaft Test Instrumentation

Figure 5-8. Component Damping Test Setup and Instrumentation
5-8

the stinger and an accelerometer mounted at the antinode for the mode being evaluated. The damping ratios were measured by exciting each shaft through a range of frequencies from just below to just above the natural frequency under constant amplitude. Measurements were made of the shaft motions and excitation forces using the shaft-mounted accelerometer and load cell.

An example of the measured test data and the plotted transfer function is shown in Figure 5-9. These data were then analyzed to assess the form and quantity of damping present in the joint to determine if the constant coefficient of friction assumed in the analytical joint models was appropriate.

5.3 Component Test Results and Data Reduction

In this section the test data acquired from the component testing are reduced to investigate the form of damping present in each of three different component joints: the axial offset spline, the interference fit collar, and the Curvic coupling. Preliminary impact testing of the solid shafts showed material hysteresis loss factors to be in the range of 1.1 to 1.6×10^{-5} for both the first and second modes. These values, which compared favorably with published data, were used as a benchmark for the joint testing. Preliminary tests with the friction-producing joints revealed at least an order of magnitude higher loss factor. Following this preliminary assessment, the forced excitation tests were conducted.

As described in Section 5.1, each of the test joint sleeves were mounted on the shaft, which was suspended by wires attached at the two nodes of the first natural frequency. For each test, the acceleration amplitude was maintained constant while the frequency was varied about the first natural frequency. Evaluation of the form of damping for data taken at the second natural frequency was not performed as damping of the second mode was minimal. The transfer function, the ratio of the measured acceleration to the applied input force, was measured versus frequency at fixed acceleration amplitude levels.

Four sets of data were selected for reduction, as follows:

- Axial spline
- Interference fit joint
- Curvic coupling at 3130 lb contact load
- Curvic coupling at 2000 lb contact load.

SHAKER TEST 17 IRF 80" CURVIC 3130# BOLT FORCE
 200Hz A1 AC/ 5V B1 AC/ 10V S. SVP 114/8 DUAL 1k

AVERAGE
 SP SWEP
 MASS MEM
 BL: 0
 RE: 0

WINDOW
 FLAT
 OVERLAP
 MAX
 Ch DELAY
 OF 0

TRIGGER
 ChA
 SLOPE: +
 LEVEL:
 19.3%
 POSITION
 -OF 9/84
 UNIT
 X: Hz
 Y: EU
 COH BLINK
 OFF

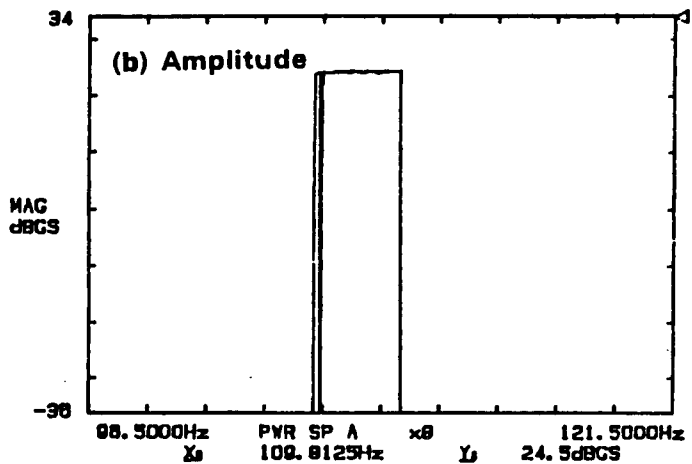
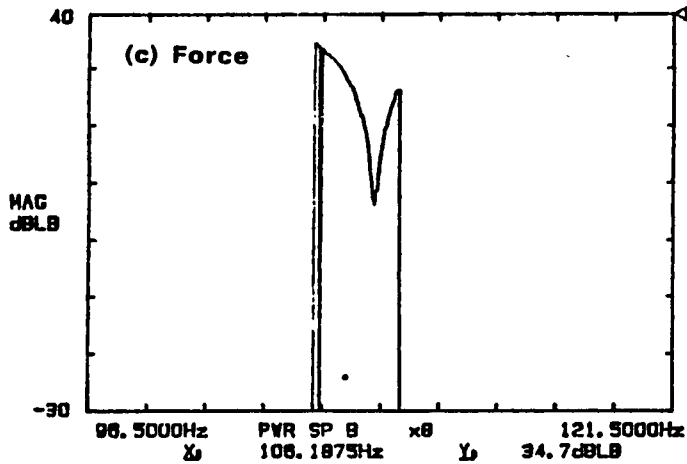
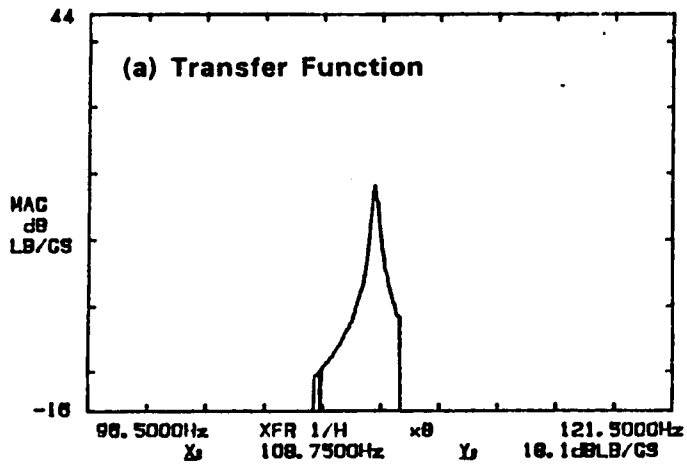


Figure 5-9. Curvic Test Joint Swept Sine Test Data

90614

Test data for each of these components were selected at four separate amplitude levels. The first data point to be used in the data reduction was selected at that excitation amplitude level where material hysteresis damping was still dominant (i.e., minimal joint damping present). The other selected test points are at increasing amplitude levels with observed increases in component damping over the material hysteresis levels characterized for the solid baseline shafts.

5.3.1 Data Reduction Algorithm

The data reduction algorithm implemented to extract the joint damping ratios is discussed in this section. For a linearly damped structure, the transfer function in the vicinity of any of the resonances is given by

$$Y = \frac{a}{F} = \frac{x \omega^2}{F} = \frac{A \omega^2}{\left(\left\{ 1 - (\omega/\omega_0) \right\}^2 + (2\zeta\omega/\omega_0)^2 \right)^{1/2}} \quad (5.1)$$

where

- A is a scale factor
- a is the acceleration
- F is the applied force
- x is the displacement
- ω is the frequency of the applied force
- ω_0 is the undamped natural frequency
- ζ is the damping ratio for that mode.

The above formula was fitted to the test data using a least squares fit, where the three parameters (A, ζ , and ω_0) were found such that the sum of the squares of the deviations of the curve from the data points would be minimized. Results of the data reduction efforts are presented in Table 5-2. It should be noted that while the amplitude data are presented as g levels, frequency variations are very small and as such the variation in g level is representative of the displacements measured on the shaft.

Table 5-2. Results of Component Test Data Reduction

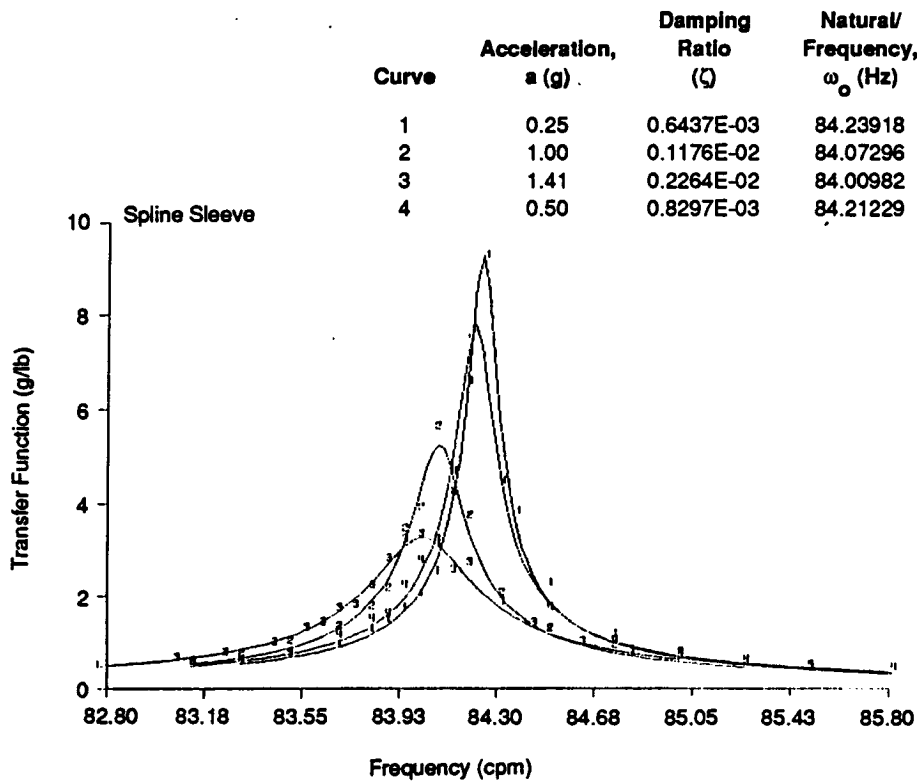
	Acceleration, (g)	Damping Ratio ζ	Natural Frequency, ω_0 (Hz)	Scale Factor (A)	Bolt Load (lb)
Spline	0.25	0.6437E-03	84.23918	0.1681E-05	
	0.50	0.8297E-03	84.21229	0.1822E-05	
	1.00	0.1176E-02	84.07296	0.1739E-05	
	1.41	0.2264E-02	84.00982	0.2087E-05	
Interference Sleeve	4.00	0.4076E-03	87.24855	0.1317E-05	
	8.00	0.9202E-03	87.17637	0.1551E-05	
	11.30	0.1601E-02	87.17140	0.1735E-05	
	16.00	0.4693E-02	86.94593	0.1892E-05	
Curvic	8.00	0.6025E-03	108.8483	0.8785E-06	3130
	11.40	0.1044E-02	108.7511	0.9966E-06	
	16.00	0.1369E-02	108.6337	0.9314E-06	
	1.41	—	108.9375	—	2000
	2.42	0.1221E-03	108.9210	0.8049E-06	
	5.67	0.5671E-03	108.8494	0.8905E-06	
	11.35	0.1291E-02	108.7067	0.8803E-06	

5.3.2 Axial Spline Data Reduction Results

Figure 5-10 is a plot of the axial spline test points (numerals) and of the fitted curves (solid lines) at each of four acceleration levels. (The actual test point in the graph is located at the lower left corner of each of the numerals 1, 2, 3, or 4). It is noticed that a fairly good fit is provided by the above formula. Further, as the acceleration amplitude increases, the curve peak broadens with a corresponding increase in damping ratio as well as a slight decrease in frequency. The most notable increase in damping occurred when the shaker excitation level increased from 1.00 to 1.41 g. During this change in excitation, the damping ratio almost doubled, increasing from 0.00118 to 0.00226. The estimated natural frequency was approximately 84.2 Hz for the lower two acceleration levels and 84.0 Hz for the higher two acceleration levels. While this variation (about 0.2%) in natural frequency is very small and is probably within the tolerance of the experimental errors, there does appear to be a dependence of damping on amplitude.

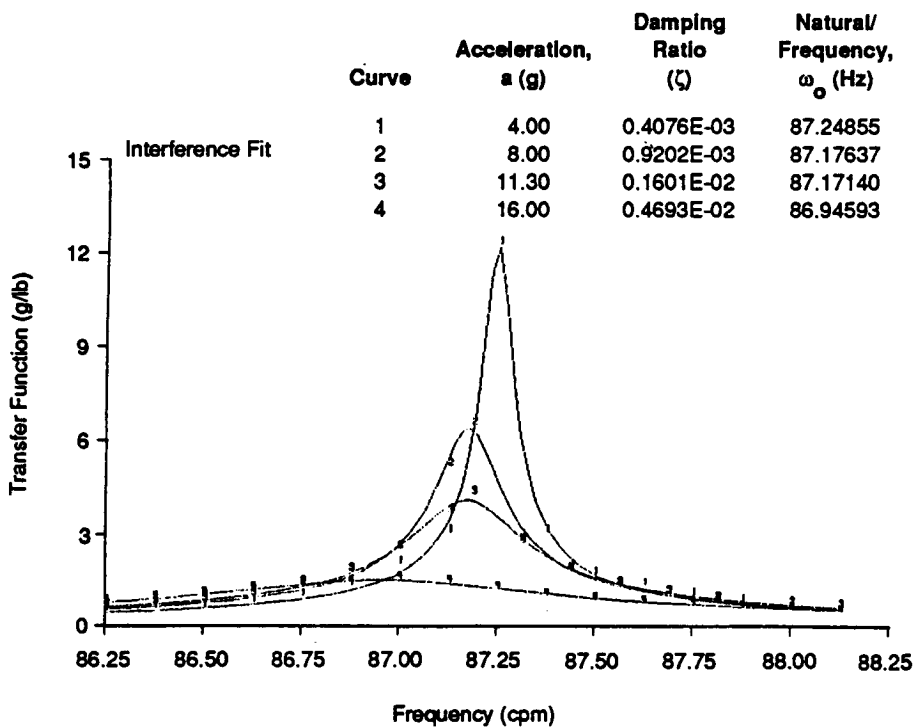
5.3.3 Interference Fit Data Reduction Results

Figure 5-11 is a plot of the test points of the interference fit component as well as the curve fitted to each acceleration level. Much larger acceleration levels had to be run for



90615

Figure 5-10. Spline Component Data: Transfer Function versus Frequency



90616

Figure 5-11. Interference Fit Component Data: Transfer Function versus Frequency

this component than for the spline in order to start producing significant changes in the damping ratio (from 4 to 16 g). Again, as the acceleration amplitude increases the curve peak broadens with a corresponding increase in damping ratio and a slight decrease in frequency. The most notable increase in damping occurred when the acceleration increased from 11 to 16 g, again more than doubling the damping ratio, increasing it from 0.0016 to 0.0047. The largest change in the fitted natural frequency (a 0.3% decrease) occurs between these two largest acceleration levels, while almost no change was noticed between the three lower levels.

5.3.4 Curvic Spline Data Reduction Results

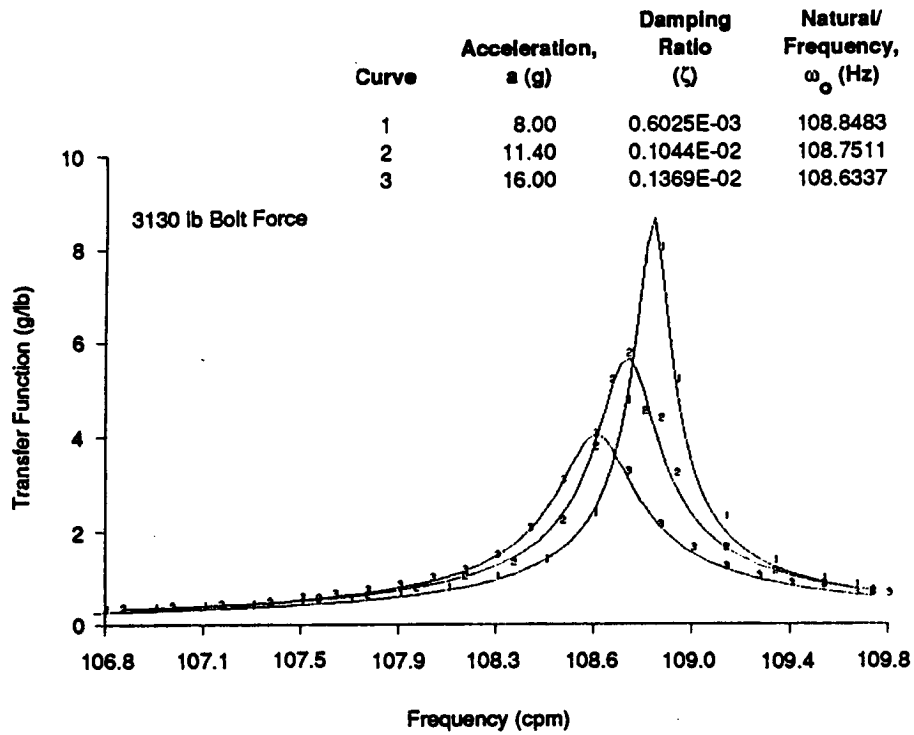
The test points of the Curvic component are plotted in Figures 5-12 and 5-13. Figure 5-12 is for a curvic bolt load of 3130 lb while Figure 5-13 is for a bolt load of 2000 lb. Larger acceleration levels were also needed for this component than for the spline to start producing any significant effect on the damping. The total acceleration for these tests varied from 1.41 to 16 g. At the larger bolt torque, the fitted damping ratio increases from 0.00060 to 0.00137 as the acceleration level is increased from 8 to 16 g, while at the lower bolt torque the damping ratio increases from 0.00056 to 0.00130 as the acceleration level is increased from 5.7 to 11.35 g. There is no significant change in natural frequency observed due to either bolt torque or acceleration level.

At the lower Curvic bolt torque, the formula for the transfer function could not be successfully fitted to the test data at the lowest acceleration level (1.41 g) because the peak was very sharp and not enough points were taken near the resonance. Figure 5-13 shows the test points for this case, connected by straight line segments. It is noticed that the maximum point is much larger than the corresponding curves at higher excitation levels, which is evidence that the damping was smaller at this amplitude.

5.3.5 Dependence of Damping on Amplitude

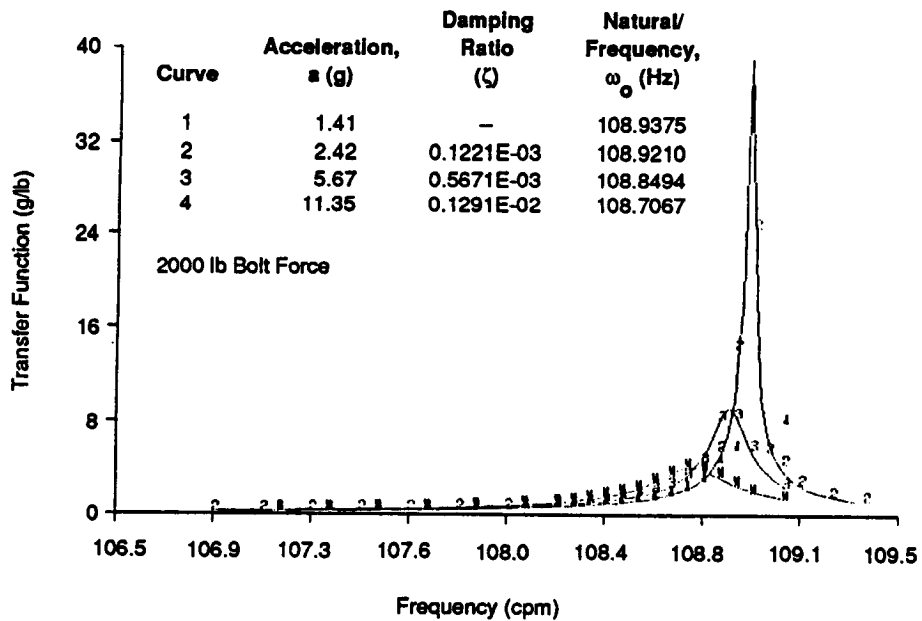
In a structure with internal damping that is undergoing a forced oscillation, the energy dissipated during one cycle by the damping mechanism is given by:

$$E = \int_0^T f v dt \quad (5.2)$$



90617

Figure 5-12. Curvic Component Data (3130 lb Bolt Force): Transfer Function versus Frequency



90618

Figure 5-13. Curvic Component Data (2000 lb Bolt Force): Transfer Function versus Frequency

where

f is the damper force,

v is the velocity difference across the damper,

$T = 2\pi/\omega$ is the period of the oscillations.

For a linear damper,

$$f = -cv \quad (5.3)$$

$$E_1 = c v_0^2 T/2 = \pi c v_0^2 / \omega \quad (5.4)$$

where

E_1 is the energy dissipated by the linear damper,

c is the damping coefficient,

v_0 is the amplitude of v

ω is the frequency of the oscillations.

On the other hand, for a Coulomb damper, the energy dissipated during one cycle (E_C) can be calculated assuming that the velocity difference across the sliding surfaces behaves sinusoidally:

$$f = -\text{sign}(v) \mu N \quad (5.5)$$

$$\begin{aligned} E_C &= \int_0^T f v dt \\ &= \mu N \int_0^T |v| dt \\ &= 4 \mu N v_0 / \omega \end{aligned} \quad (5.6)$$

where

μ is the friction coefficient

N is the normal force across the joint.

Of course, this last formula is only valid if no sticking occurs between the sliding surfaces during the motion.

A careful study of a one-degree-of-freedom system with both viscous and Coulomb damping (macroslip) under forced oscillation was made in order to understand the effect of amplitude on damping. This analysis showed that

- While the Coulomb friction joint is stuck during part of the oscillation and slipping during the rest, the effective damping coefficient increases
- As the amplitude continues to increase, the approximation of a sinusoidal velocity in calculating the energy dissipation becomes more accurate.

Thus, the energy dissipated is proportional to the square of the velocity amplitude in the linear damper and proportional to the velocity amplitude in the Coulomb friction damper, while in both cases it is inversely proportional to the frequency. If both linear and Coulomb damping are present in the joints, the energy dissipated can then be added:

$$E = \pi c v_0^2 / \omega + 4r\mu N v_0 / \omega \quad (5.7)$$

where the factor r has been included in the second term to account for different relative velocity amplitudes when the Coulomb and linear dampers are not located across the same joint. For small enough amplitudes, however, the friction joints are undergoing microslip, not macroslip. In this case, the second term in the above equation should be replaced by a term proportional to v_0^3 , since, as discussed in Section 3.1.3, the energy dissipated in a lap joint under microslip is proportional to the cube of the amplitude.

If this energy is now equated to that dissipated by an equivalent linear damper, the equivalent damping coefficient is obtained:

$$c_e = \begin{cases} c + c\mu v_0, & v_0 < v_{01} \\ c + \frac{4r\mu N}{\pi v_0}, & v_0 > v_{02} \end{cases} \quad (5-8)$$

where v_{O1} represents a threshold velocity amplitude below which the joint only undergoes microslip during the cycle, while v_{O2} represents a threshold velocity amplitude above which the joint only undergoes macroslip. In the transition region ($v_{O1} < v_O < v_{O2}$) where the joint is sticking for part of the cycle (microslip) and slipping (macroslip) during the remaining part, this last equation cannot be used and numerical integration is necessary.

The fitted damping ratio is plotted versus acceleration amplitude in Figure 5-14 for all four component tests. The fitted damping ratios of all components are observed to increase with amplitude:

- Both the spline and interference fit components display nearly linear behavior of damping with amplitude except for the last (largest amplitude) data point, which in both cases shows a substantial increase above linear. A curve fit through all of the data points shows more of a cubic dependence with amplitude.
- The Curvic component test data show a fairly linear dependence with amplitude. At the larger bolt load, the curve shows a slight convexity.

The only analytical model considered here that shows an increase in damping with amplitude is that of microslip at a lap joint, where the energy dissipated is proportional to the cube of the displacement amplitude. The effective damping produced by this joint is proportional to the amplitude.

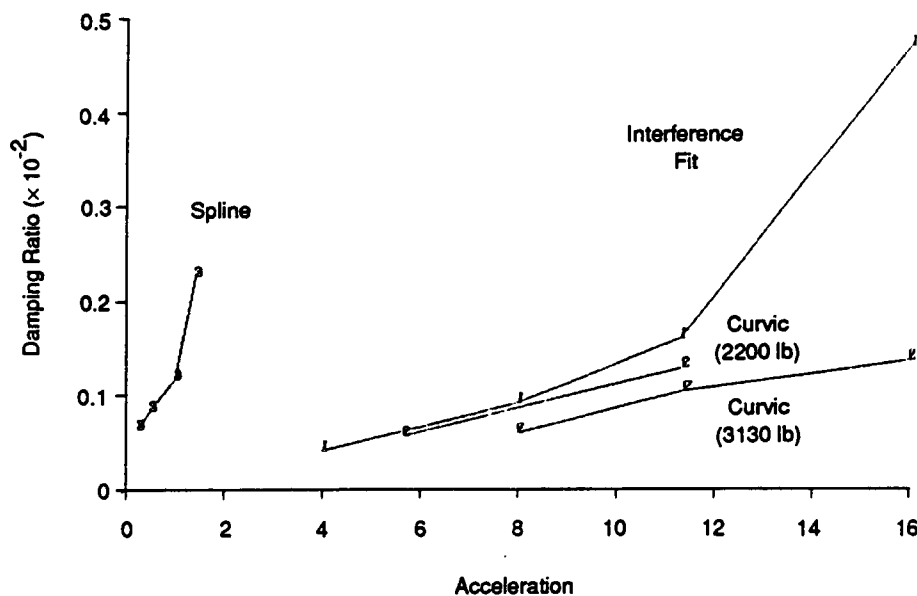


Figure 5-14. Component Data: Damping Ratio versus Amplitude

90641

In conclusion, the form of damping observed in the component tests does not behave with amplitude like a linear damper or like a Coulomb friction joint undergoing macroslip. Of the analytical models studied, only the friction joints (such as lap joints) undergoing microslip can explain the linear increase in effective damping coefficient with amplitude. Stronger dependence on amplitude, such as the cubic behavior of the spline and interference fit joints when the largest acceleration test data point is included, could perhaps be explained analytically by including the dependence of the normal force across the joint on amplitude. This analysis, however, was not pursued.

6.0 ROTORDYNAMIC TESTING

In this section of the report, the test item description, method of test, and test results will be presented for the rotordynamic tests. The objective of the rotordynamic testing was to assess the rotor instabilities due to damping present in two of the SSME HPOTP friction-producing joints. The two joints selected for rotordynamic testing were the axial spline and interference fit joints. This selection was made based on a review of the component test data (Figure 5-14), which shows that both the axial spline and the interference fit joints had higher damping ratios than did the Curvic coupling. Additionally, the Curvic joint in the HPOTP is located between the two turbine stages where there is little if any bending experienced across the joint. Both the interference fit and axial spline joints, on the other hand, do undergo bending within the operating speed range. Since the interference fit and axial spline joint had the highest damping ratios and are located in regions where they can be expected to produce destabilizing friction forces in the HPOTP, they were selected for the rotordynamic testing.

6.1 Test Item Description

The axial spline and interference fit test shaft used for the component testing was also used for the rotordynamic testing. As seen in Figure 5-1, both an interference fit and an axial spline joint could be installed on the shaft either simultaneously or independently. Modifications to permit bearing installation were accomplished prior to rotordynamic testing. The test rig with the shaft system, instrumentation, and side-loading mechanism is shown in Figures 6-1 and 6-2. The shaft system was supported at each end by a single, preloaded, oil-lubricated, angular contact bearing. The rotor was driven by a 100-hp electric motor through a vari-drive and speed increaser gearbox. The final configuration incorporating the side-loading mechanism, as shown in Figures 6-1 and 6-2, used rubber straps to introduce the nonrotating side load to the shaft in simulation of the side load experienced in the SSME turbopumps. The rubber straps were attached to the outside of a deep-groove ball bearing, which was mounted on the outside of the axial spline sleeve and provided antirotation for the bearing as well as introducing the side load.

In the design and fabrication of the test rig, care was taken to minimize the introduction of any external damping that might mask the presence of the subsynchronous vibrations expected from the internal friction-producing joints. As such, bumpers, made of Rulon (a high-temperature, glass-filled Teflon) and lubricated with oil, were used to limit orbits.

ORIGINAL PAGE
BLACK AND WHITE PHOTOGRAPH

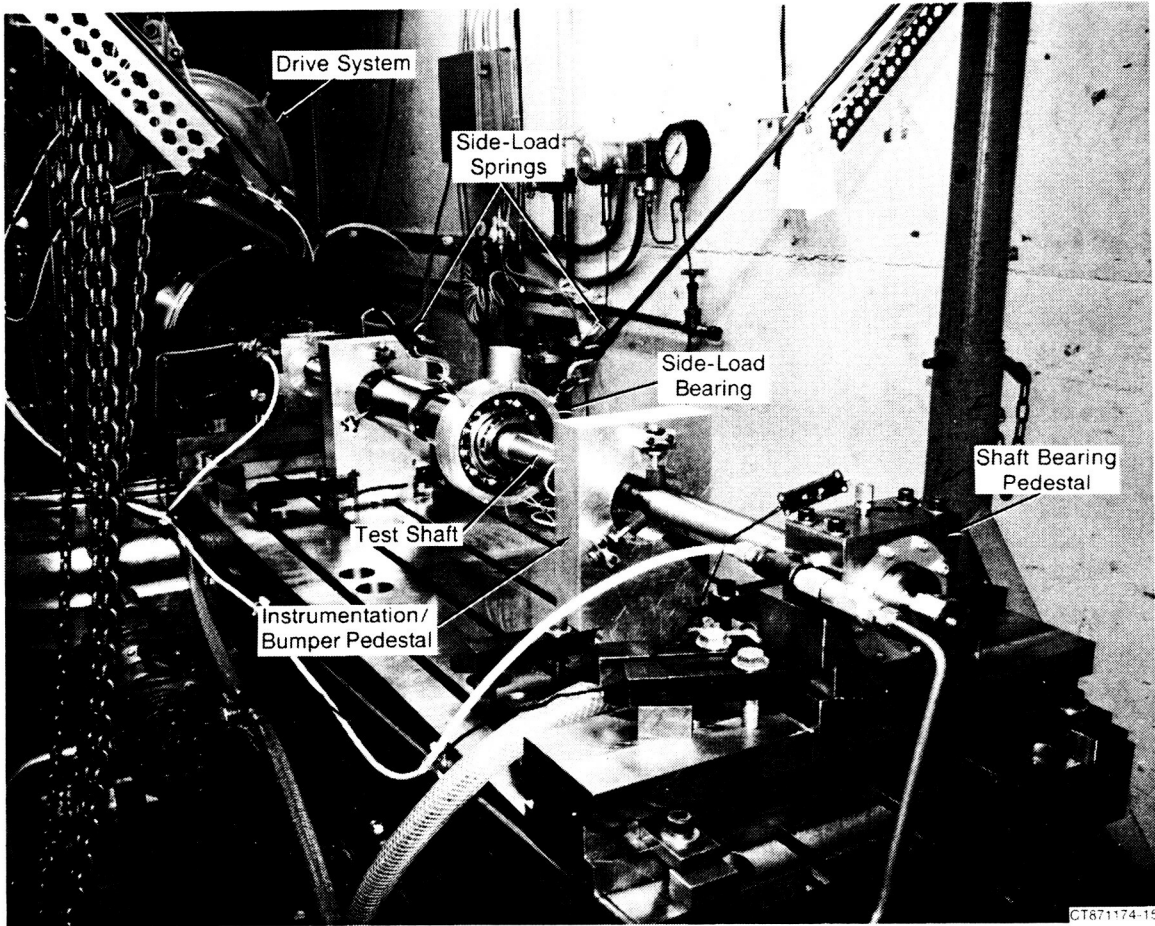


Figure 6-1. Rotordynamic Test Rig

ORIGINAL PAGE
BLACK AND WHITE PHOTOGRAPH

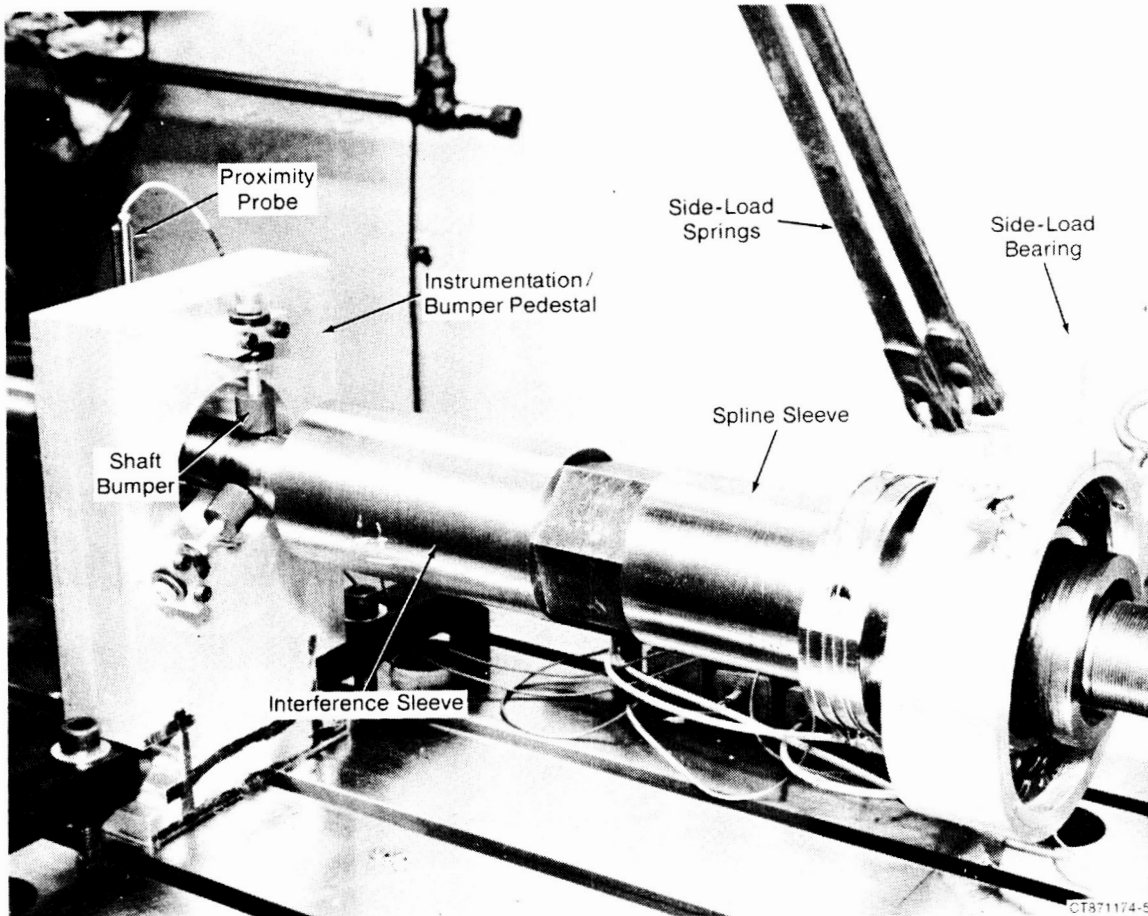


Figure 6-2. Close-up of Rotordynamic Test Rig

The bumpers were mounted on the instrumentation pedestals with elastomer washers to provide a low spring rate should they be contacted. The gap was set at 25 mils so that they acted only as protective devices to limit the orbits and prevent the shaft from being deformed due to bending stresses.

Four displacement probes and a light-sensitive speed probe were used to measure the shaft dynamic performance. Each pair of displacement probes was placed 90° apart so that rotor orbits could be observed during the tests. Data from each test run were recorded as well as evaluated through the use of a real-time frequency spectrum analyzer. Additional monitoring sensors used included bearing-mounted thermocouples and accelerometers.

6.2 Method of Test

To evaluate the effect of internal rotor friction, tests were run with the axial spline alone, the interference fit alone, and both joints together. In each case, the rotor systems were run without any side load. For the combined tests, side loads of 28 and 70 lb were also evaluated.

The rotordynamic testing plan called for balancing the rotor to as fine a degree as possible and then running the rotor above the first critical speed. For each run, data were acquired on magnetic tape and reviewed on a spectrum analyzer to assess the presence and strength of the subsynchronous vibrations. Variations in the rotor imbalance and side load were attempted.

6.3 Rotordynamics Test Rig Analysis

The rotordynamics test rig analysis was performed to correlate the predicted supercritical test rig behavior with experimental results. The rotor-bearing model, analysis procedures, and initial conditions used are presented first, followed by the analytic results obtained.

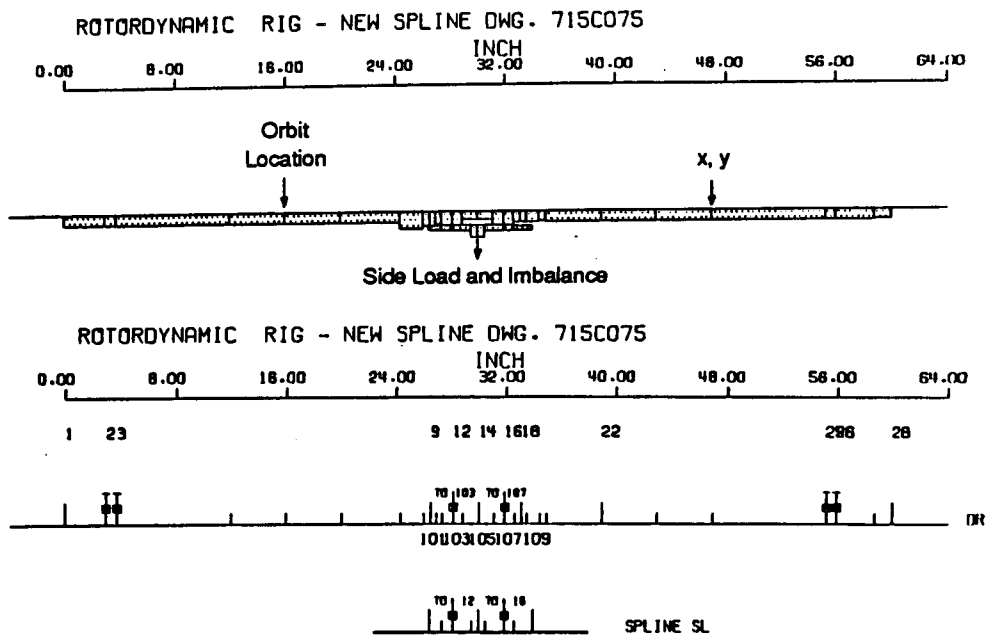
6.3.1 Dynamic Test Rig Model

A two-level, rotordynamic, finite element model of the experimental test rig with a friction-producing joint (e.g., axial spline or interference fit joint) was prepared in order

to assess the rotor's supercritical, time-transient behavior. The developed model of the rotordynamic test shaft with the spline sleeve is shown in Figure 6-3. This model uses one level to describe the main shaft and bearing support structure and a second level to describe the spline or interference fit sleeve. Once each level has been defined, they are connected through the joint interface with assumed lateral and angular coupling stiffnesses. The joint interface friction parameters are defined separately and incorporated on the right-hand side of the system equations of motion for use in the time-transient analysis. In this way the effects of the joint stiffness on rotor system critical speeds may be assessed prior to performing the time-transient analysis. Further, the first series of time-transient analyses may be performed without the destabilizing internal friction coefficients to assess both the numerical and system stability prior to full system evaluation.

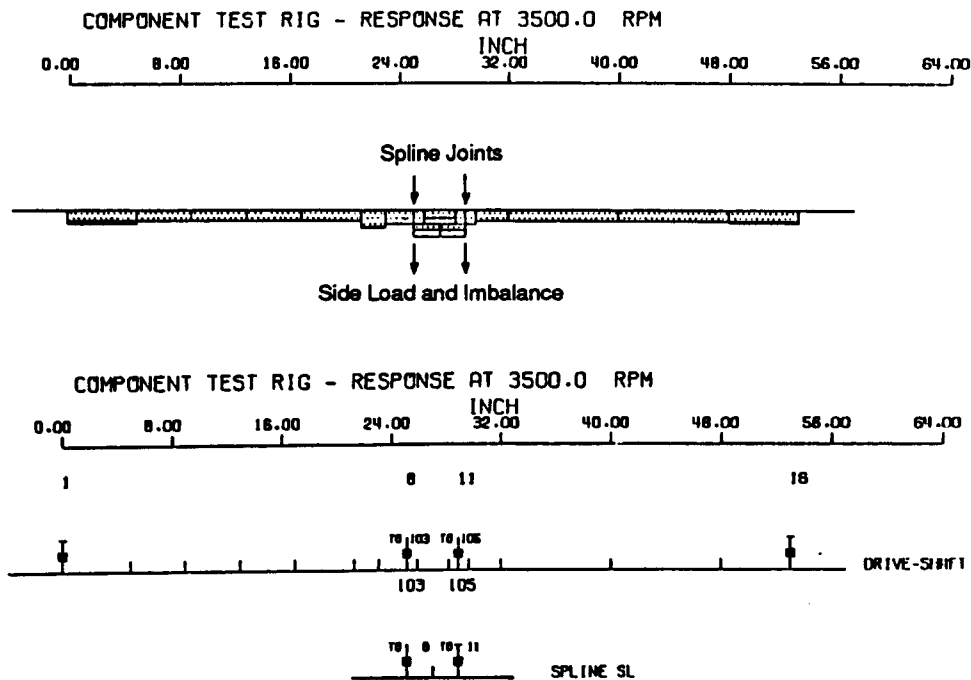
When compared to the experimental test results for the test rig, this model accurately represented the first bending natural frequency. The model was then modified to remove the very high natural frequencies that normally result in a structural model due to relatively small or concentrated masses and/or relatively high element stiffnesses. Care was taken in the tuning and preparation of the model for the time-transient analysis not to adversely influence the frequency and mode shapes of the lower modes. The final time-transient rotordynamic test rig model is shown in Figure 6-4. The drive shaft (level 1) contains four active stations. Active stations are those rotor stations where imbalances, external forces, bearings, or level interconnections can be located. To minimize computer memory requirements and run time, "static condensation" (Guyan reduction) is used by MTI's finite element rotordynamic code to reduce the size of the matrices describing the rotor system. The computer program automatically uses the static condensation technique to remove degrees of freedom between each active station, creating one large finite element to substitute for elements between the active stations. After calculations are completed, deflections at condensed stations can then be determined.

The shaft model is connected to ground by ball bearings located at each end. The shaft is also connected to the axial spline sleeve (the second level) through one active station for each set of spline teeth. Isotropic radial stiffnesses of 100,000 lb/in. and zero angular stiffnesses were used at the ball bearing locations. Radial stiffnesses of 71.5×10^6 lb/in. and angular stiffnesses of 9.32×10^6 lb-in./rad were calculated for each spline interconnection. The torque transmitted across the spline teeth due to the circumferential



90619

Figure 6-3. Rotordynamic Test Rig Model with Spline Sleeve



90620

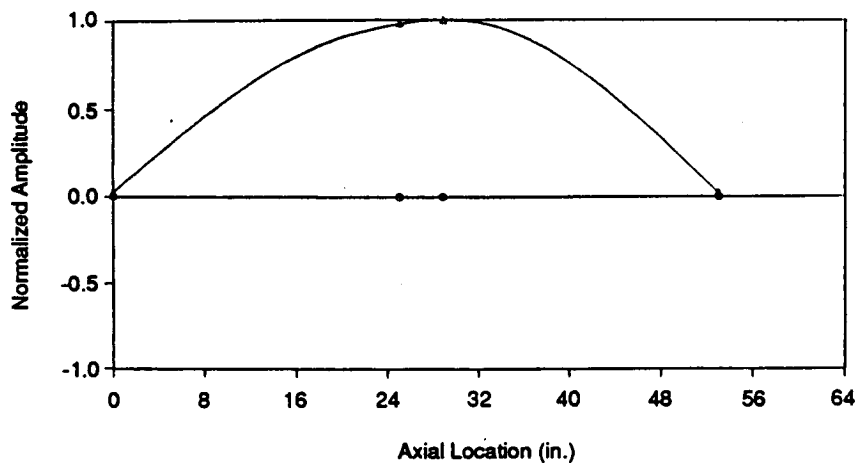
Figure 6-4. Rotordynamic Test Rig Model with Spline Sleeve As Simplified for Time-Transient Analysis

offset (18 min) was 5,000 lb-in. Since these joints were lubricated with dry film, a coefficient of friction of 0.2 was assumed in the rotor joint model. This resulted in a friction moment of 636.6 lb-in. across the joint being used in the time-transient simulations.

Table 6-1 gives the damped natural frequencies of the linear model (zero friction at spline teeth and 1% of critical damping to ground) showing that the first critical speed has both forward and backward whirling modes at 2282 and 2279 rpm, respectively, with a corresponding log decrement of 0.0631. The first of these mode shapes is given in Figure 6-5.

Table 6-1. Damped Natural Frequencies of Rotordynamic Test Rig with Spline

	Natural Frequencies			Log Decrement
	rpm	rps	rad/s	
1	2,278.8	37.979	238.63	0.63124E-01
2	2,281.5	38.025	238.92	0.63121E-01
3	10,638.0	177.300	1,114.00	0.20224E-02
4	10,684.0	178.070	1,118.90	0.20178E-02
5	21,942.0	365.700	2,297.80	0.15142E-02



90621

Figure 6-5. Rotordynamic Test Rig First Mode Shape with Spline Sleeve

6.3.2 Results of Test Rig Transient Analysis

Transient simulation of the rotordynamic test rig with the spline sleeve component was performed to assess the ability of the analysis to accurately predict the presence of the internal friction instability. The external damping in the test rig (as determined from experiment) was included in the rotor system model as a linear radial damping coefficient to ground and was applied at the active station on the spline sleeve near the side load bearing.

The response of the rotordynamic test rig to imbalance at the spline sleeve was first calculated for several levels of damping to assess test rig system damping when compared with test results. In order for the test rig to cross the first critical speed, a minimum peak-to-peak response of about 30 mils was observed and imbalance correction weights of 6 g were typically used. From these data, it was concluded that an external bearing damping of at least 0.063 lb-sec/in. was present in the test rig (corresponding to a damping ratio of 0.18%). This damping was so minimal, however, that it would take approximately 10 sec, or about 467 revolutions at 2800 rpm, for the initial perturbation conditions to analytically decay to 1.0% of their starting value. With an integrating time step of 5×10^{-6} sec, (which was required due to the high natural frequencies inherent in the simplified model), up to 2,000,000 time steps would be required before the initial condition transient would die out. To make the time integration more manageable, therefore, 1% of critical damping was used, corresponding to a radial damping coefficient of 0.340 lb-sec/in. as opposed to the measured 0.18% test rig damping ratio. Since radial damping to ground is known to make a rotor more stable, any instabilities shown in the transient analyses of the rotordynamics test rig should therefore be considered significant.

Equation 3.46 in Section 3.1 gives the bending moment transmitted across a spline joint as a function of the differences in angular displacements across the joint, as well as the time rate of change of these differences. From these equations, one can calculate the instantaneous angular cross-coupling coefficients that are acting across the joint:

$$\frac{\partial M_x}{\partial \Delta \phi} = \frac{2\mu T \Omega}{\pi \Delta V} \left\{ \frac{(\dot{\Delta \phi} + \Omega \Delta \theta)^2}{\Delta V^2} \right\} \quad (6-1a)$$

$$\frac{\partial M_y}{\partial \Delta \theta} = - \frac{2\mu T \Omega}{\pi \Delta V} \left\{ \frac{(\dot{\Delta \theta} - \Omega \Delta \phi)^2}{\Delta V^2} \right\} \quad (6-1b)$$

where,

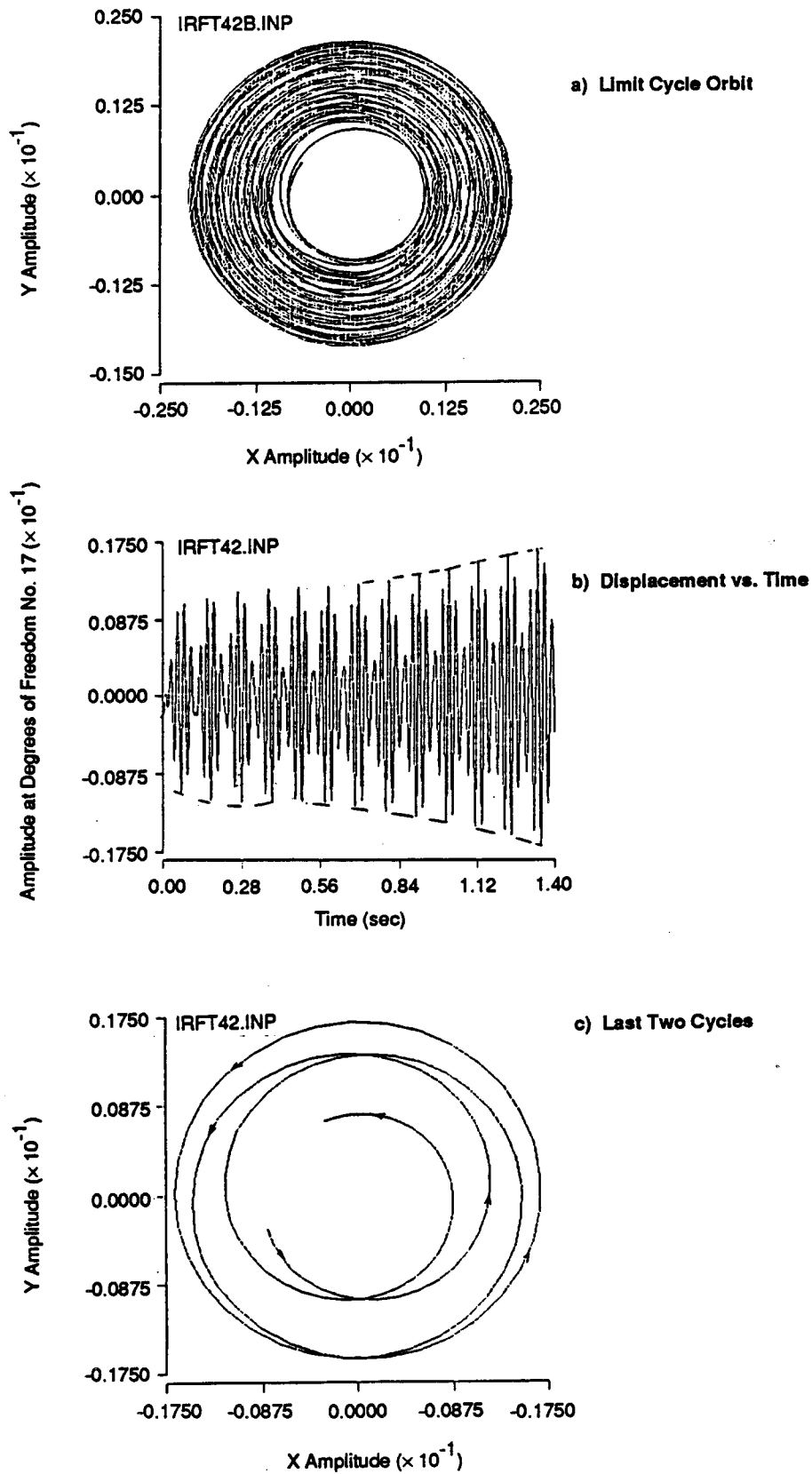
$$\Delta V = \left\{ (\dot{\Delta \theta} + \Omega \Delta \phi)^2 + (\dot{\Delta \phi} - \Omega \Delta \theta)^2 \right\}^{1/2} \quad (6-2)$$

is the magnitude of the relative angular velocity vector across the joint. Note that the quantities inside the brackets in Equation 6.1 are always less than or equal to unity. The above equations show that the angular cross-coupling coefficients

- Are inversely proportional to the magnitude of the relative angular velocity across the joint
- Are always opposite in sign
- Are equal to each other in magnitude when the orbit is circular.

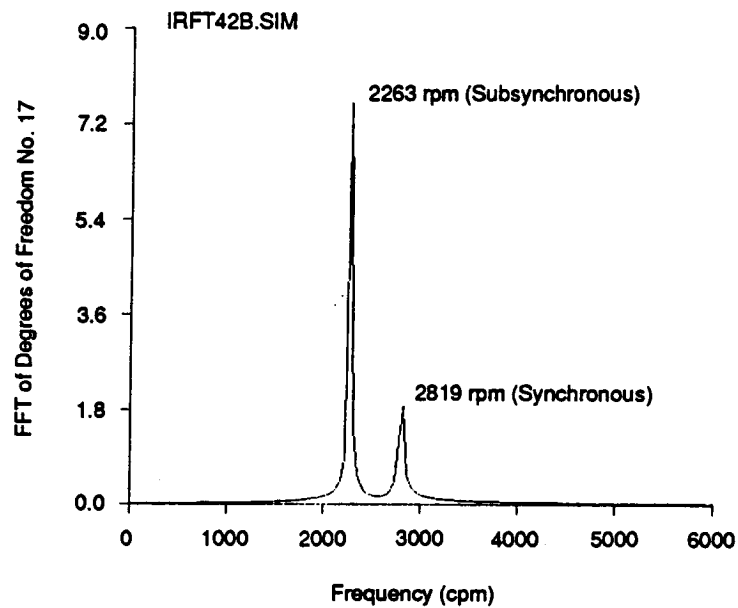
In general, cross-coupling coefficients that are opposite in sign act to destabilize rotors operating above natural frequencies. In the developed analysis, a Coulomb friction model is used, and it is assumed that the spline interfaces are always slipping. As a result, the friction moment transmitted across the spline is constant in magnitude and time varying in direction, depending upon the values of the relative displacements and velocities as given by Equation 3.46. The angular cross-coupling coefficients given by Equation 6.1 are a measure of the relative importance of the destabilizing friction moment as compared to the other system forces and moments. Thus, since the cross-coupling coefficients are inversely proportional to the relative angular velocity across the joint, it can be seen that the use of small initial conditions (i.e., velocities) may result in the instability, and the use of large initial conditions may not. These analytical results and conclusions, while consistent with the models developed, seem to contradict the experimental results obtained from the component shaker tests (Section 5.0), where increased internal friction damping coefficient was observed with an increase in excitation amplitude and may point to a limitation in the Coulomb friction model used in the analysis.

Regardless, the analysis does predict internal friction instability as shown in Figures 6-6 and 6-7. As seen in Figure 6-6, the rotor response settled into a limit cycle orbit alternating between an inner and an outer circle as it precessed. Figures 6-6a and 6-6b show the transient response of this run, while Figure 6-6c shows only the last two revolutions of the orbit. Figure 6-7 is an FFT plot of the displacement of this orbit, showing two



90622

Figure 6-6. Rotordynamic Test Rig Predicted Time-Transient Response



90623

Figure 6-7. FFT Plot of Rotordynamic Rig Analytic Predictions

peaks corresponding to the first bending natural frequency (2263 rpm) and to the synchronous speed (2819 rpm).

6.4 Experimental Rotordynamic Test Results

Figures 6-8 through 6-17 present the experimental results of the rotordynamic testing. Tests of the shaft with spline alone, interference fit alone, and of both the spline and interference fit joints together were conducted. Initial test plans called for an evaluation of the effects of different values of imbalance on the strength of the instability. However, the spline would shift every time the critical speed was approached, changing the imbalance level and causing orbits to grow to levels that prevented passage through the critical speed. While bumpers were installed to limit the orbits so that passage through the critical speed was possible, an evaluation of imbalance effects was not possible due to the continued spline shifts.

6.4.1 Axial Spline Rotordynamic Testing

As seen in Figures 6-8 and 6-9, once supercritical operation was achieved, the rotor system experienced extremely high subsynchronous vibrations at the first natural frequency. The location of the first critical speed was analytically predicted to occur between 2200 and 2300 rpm and was experimentally identified by observing the two-per-rev component of the vibrations when passing through 1100 to 1200 rpm. Figure 6-8 is a series of FFT spectrum plots showing rotor vibrations as speed was increased from 2010 rpm (below the critical speed) to 2630 rpm. Figure 6-8a shows that, even when operating below the first critical speed, the rotor first natural frequency was excited supersynchronously.

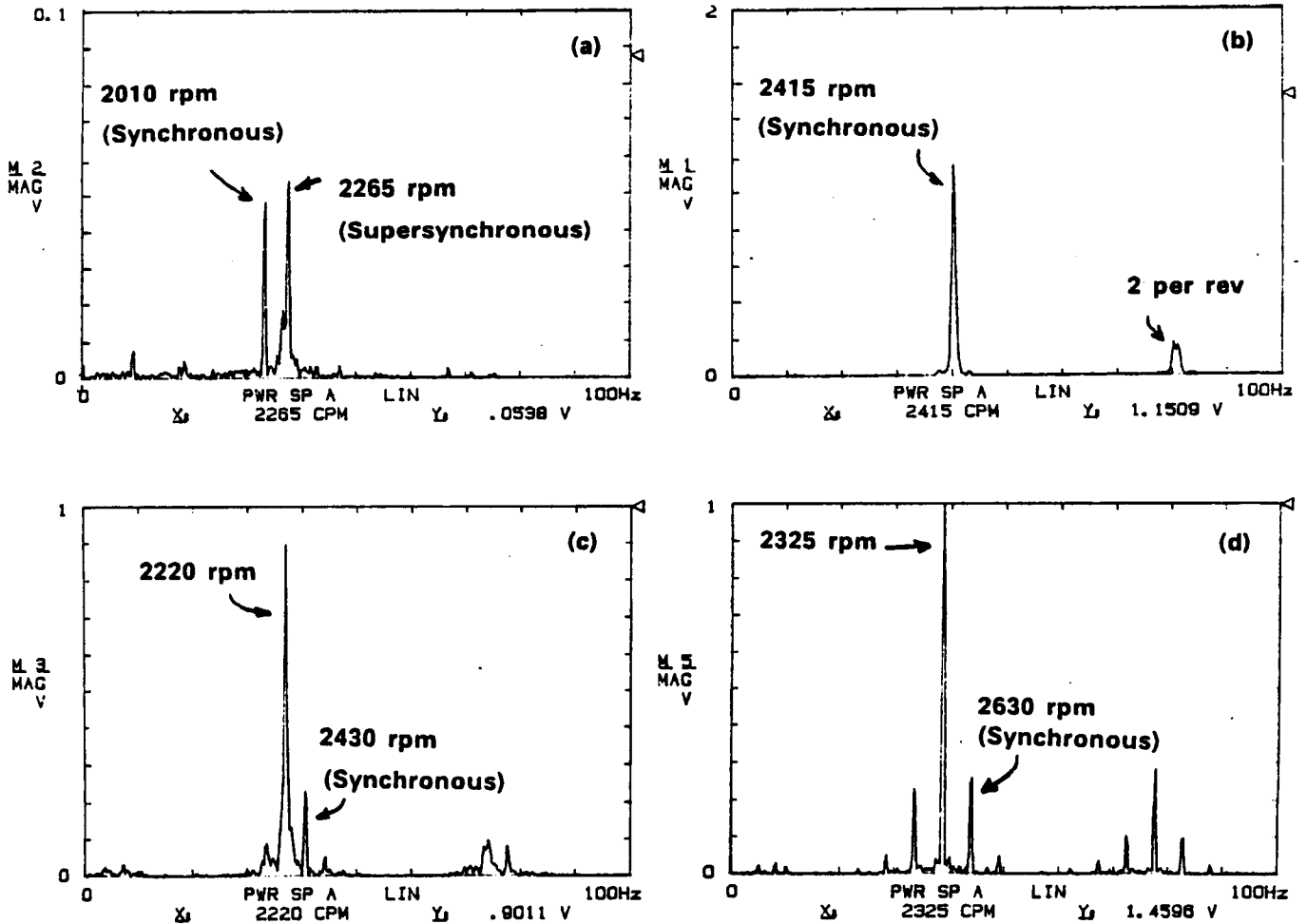
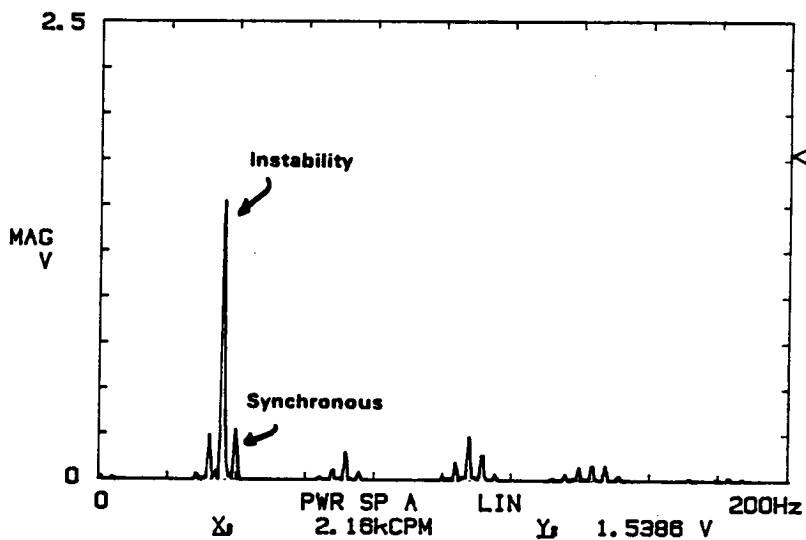


Figure 6-8. FFT Plots Showing Sub and Supercritical Operation of Rotordynamic Test Rig with Axial Spline

90624

IRF OFFSET SPLINE SLEEVE 0# LOAD (after 100# load) AVERAGE
 200Hz A: AC/ 5V B: AC/ 50V INST 0/18 DUAL 1k SP SUM

MASS MEM
 BL: 7
 RE: 0



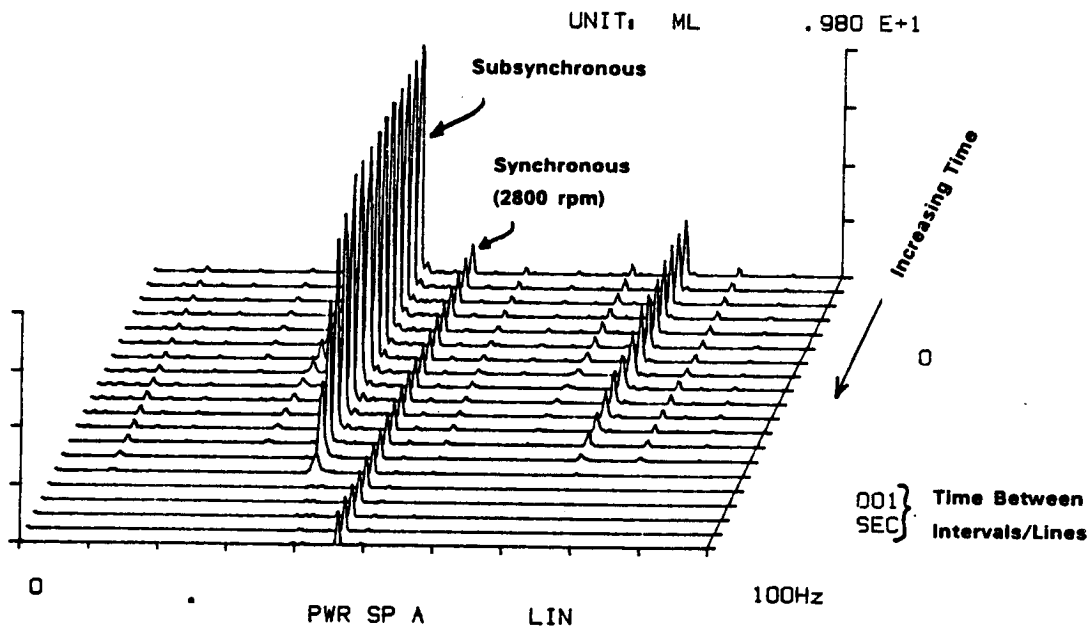
WINDOW
 HANNING

OVERLAP
 MAX
 Ch DELAY
 OF 0

TRIGGER
 ChA
 SLOPE: +
 LEVEL:
 0.0%
 POSITION
 -OF 8/64
 UNIT
 X: CPM
 Y: V
 COH BLNK
 OFF

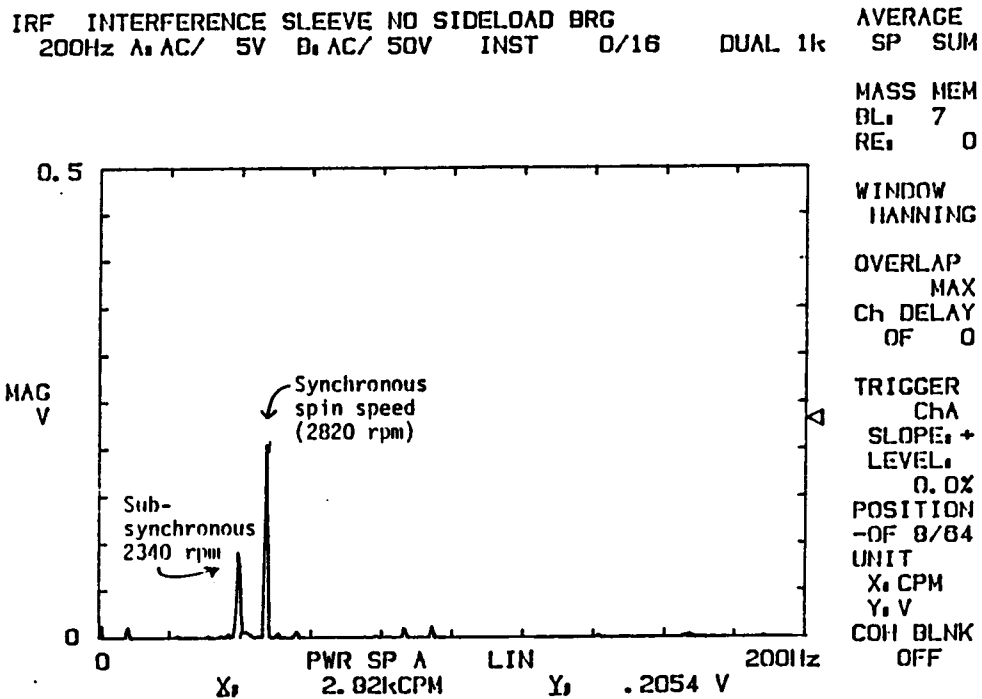
90625

Figure 6-9. FFT Plot of Axial Spline Subsynchronous Instability



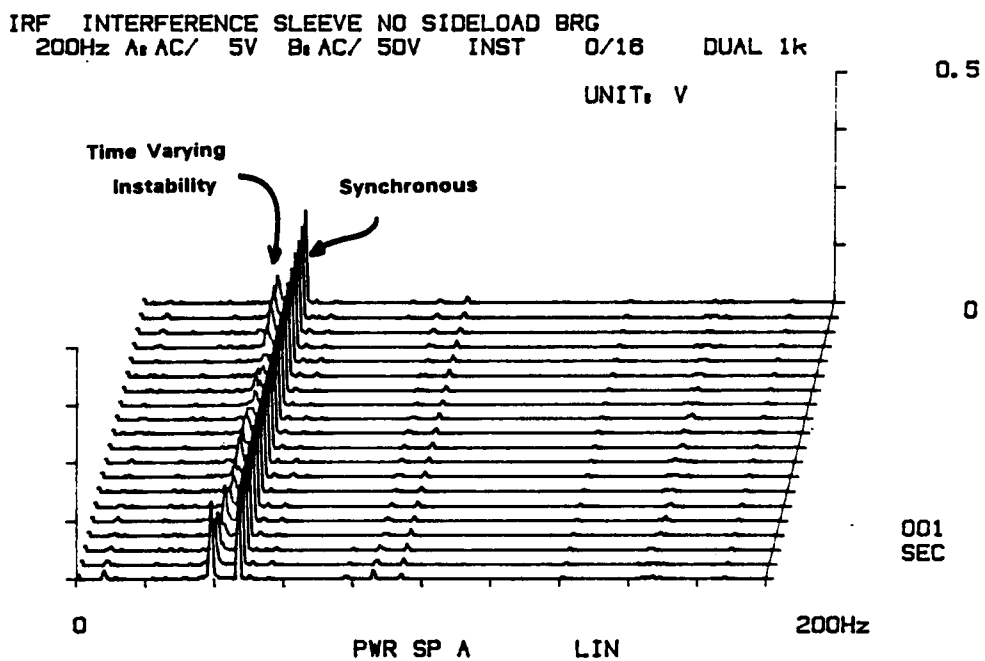
90626

Figure 6-10. FFT Waterfall Plot Showing Loss of Spline Friction Instability



90627

Figure 6-11. FFT Plot of Experimentally Observed Interference Fit Induced Subsynchronous Vibrations



90628

Figure 6-12. FFT Waterfall Plot Showing Time Varying Nature of Interference Fit Induced Subsynchronous Vibrations

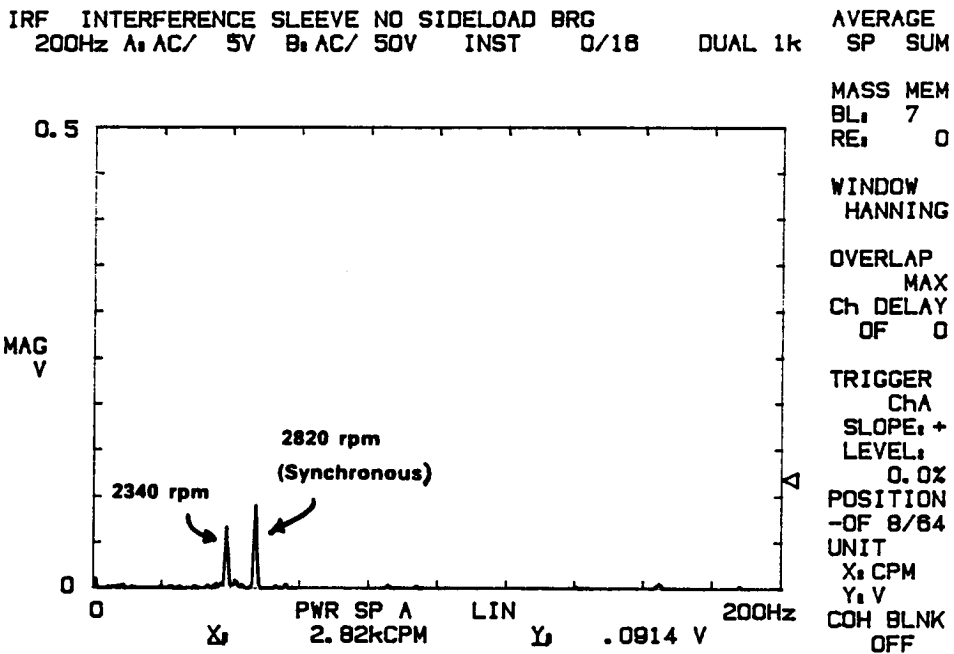


Figure 6-13. FFT Plot for Interference Fit Joint with 5-gram Change in Imbalance at Sleeve

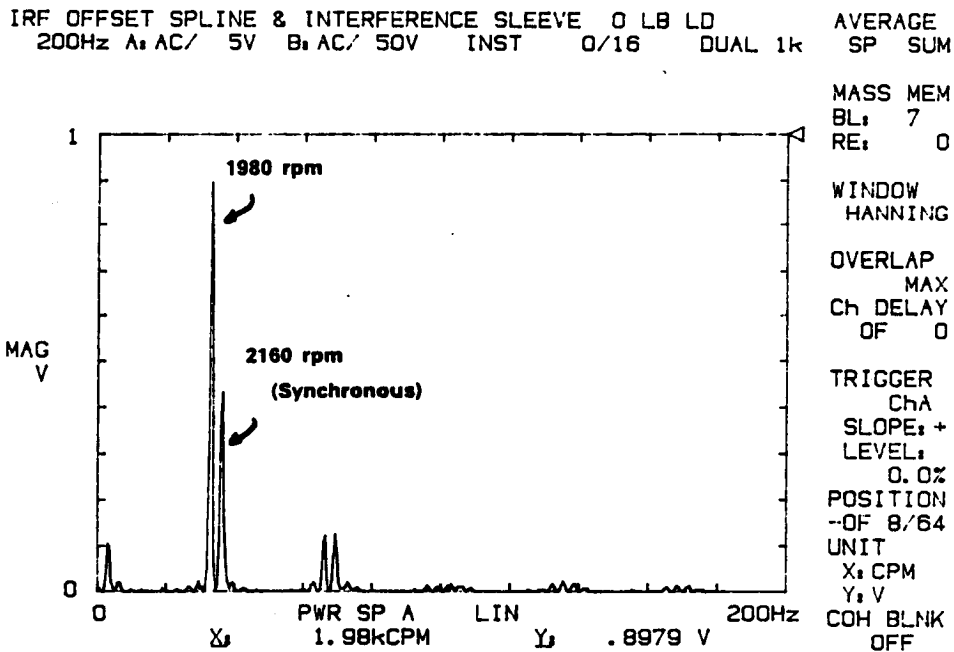
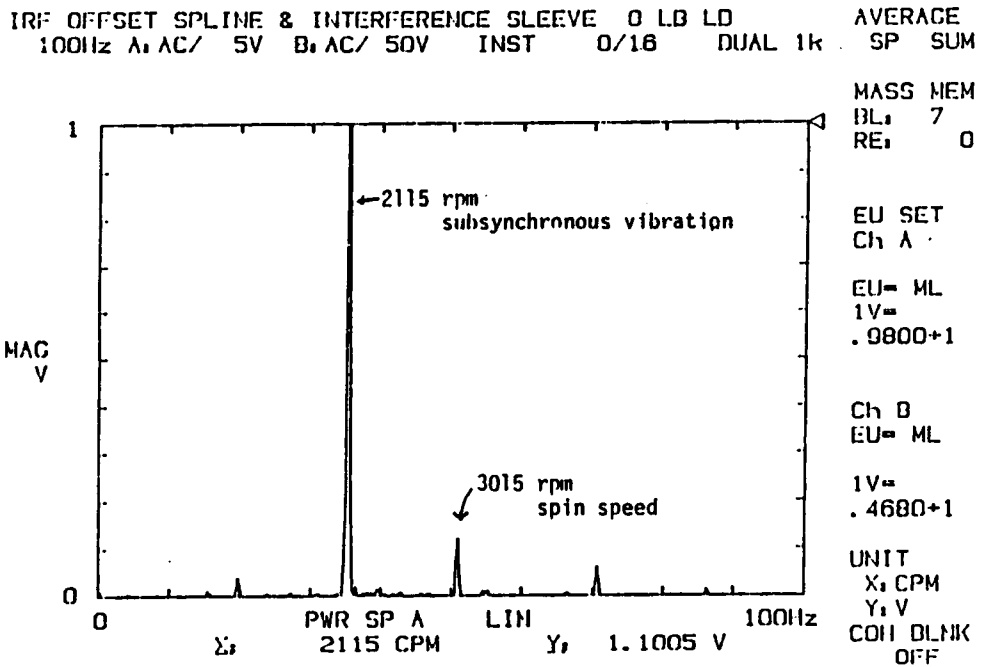


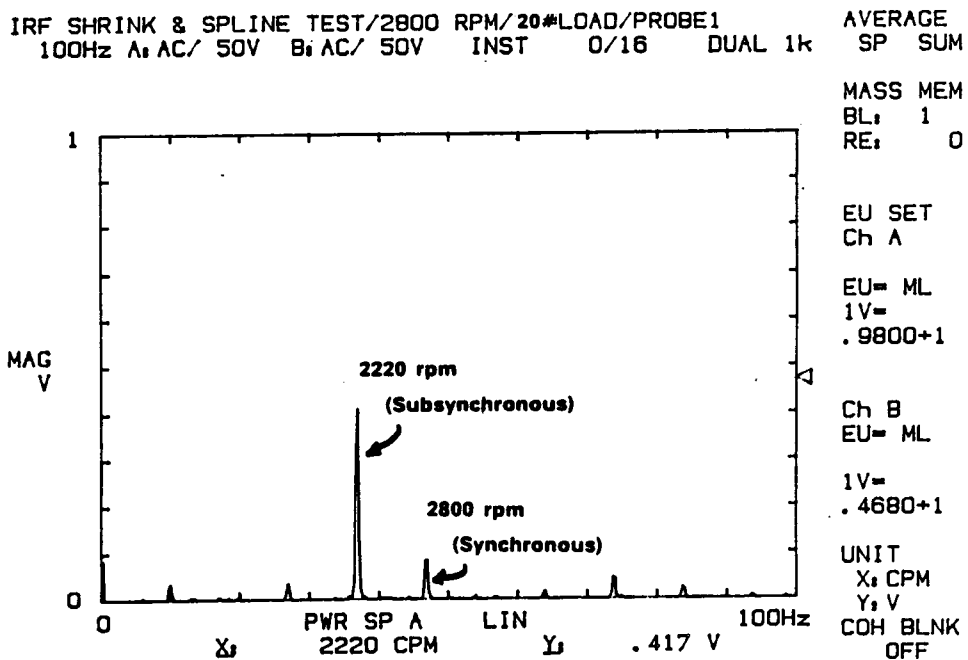
Figure 6-14. FFT Plot Showing Instability for Shaft with Both Interference Fit and Axial Spline Joints

90630



90631

Figure 6-15. Experimentally Observed Internal Friction-Induced Instability for Combined Interference Fit and Spline Joints

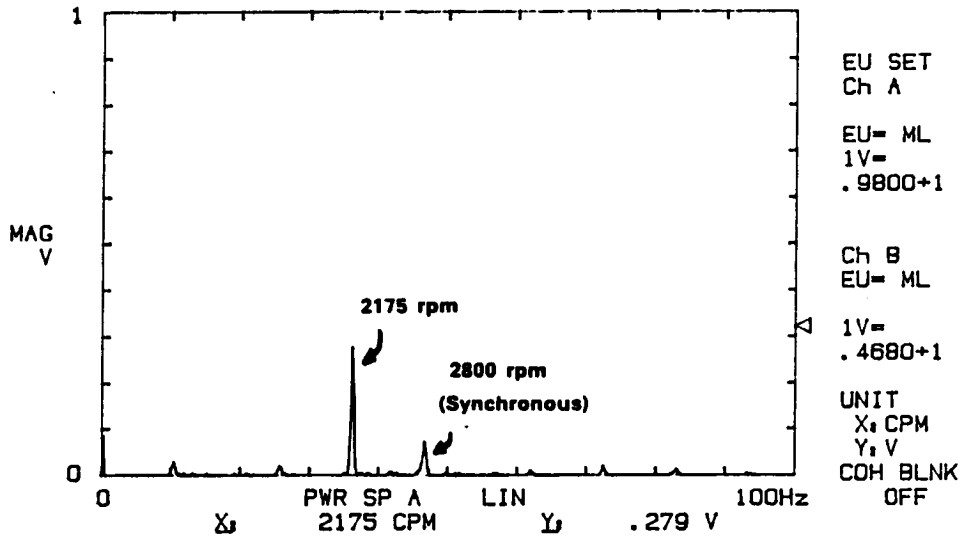


90632

Figure 6-16. FFT Plot Showing Subsynchronous Instability for 20-lb Side Load at Axial Spline Joint

IRF SHRINK & SPLINE TEST/2800 RPM/70#LOAD/PROBE1
 100Hz A: AC/ 50V B: AC/ 50V INST 0/16 DUAL 1k AVERAGE SP SUM

MASS MEM
 BL: 1
 RE: 0



90633

Figure 6-17. FFT Plot Showing Instability for 70-lb Side Load at Axial Spline

The extreme sensitivity of the rotor system's first natural frequency can be attributed to the low level of external damping present in the rig. The excitation of the first natural frequency, when the rotor was spinning between 1100 and 1200 rpm, can be explained as resulting from the effects of rotor gravity sag, which produces a two-per-rev excitation and thus excites the first natural frequency. However, the continued presence of the supersynchronous excitation of the first natural frequency at speeds all the way up to the critical speed is most likely due to spline joint movement. Small movements within the spline in an intermittent stick-slip fashion would result in low-amplitude broadband noise that could then excite the first natural frequency. The presence of the spline joint motions, while not measured directly, was indicated during the balancing attempts.

Balancing of the rotor was attempted to reduce the synchronous vibration amplitudes near the critical speed and to eliminate the large imbalance shifts that were observed below the critical speed. The shifts in synchronous vibrations were attributed to shifts of the spline sleeve on the shaft. Large shifts in the synchronous vibrations were observed at increasing speeds after each balance operation. After each shift, decelerating the rotor and rerunning it resulted in an entirely new synchronous response profile and a new

imbalance condition. To increase the speed at which the shift occurred, multispeed balancing was used. The rotor would be balanced at speeds where rotor vibrations were large but below where a large shift was experienced. This would permit a higher speed to be reached and an additional improvement to the rotor balance.

While this approach did permit higher speeds to be achieved before the spline shifted, at no time was the rotor first critical speed traversed without the spline shifting. The highest speed achieved without a spline shift was approximately 1800 rpm. Once this speed was achieved, each subsequent spline shift resulted in an imbalance condition which required an approximate 6-gram correction weight to rebalance the rotor. The spline shifts likely occurred because the dry-film lubricant reduced the static coefficient of friction and thereby permitted small amplitude stick-slip motion between the spline joint teeth prior to the shift.

In an effort to restrict the orbits without introducing external damping, which might have masked the internal friction instability, two sets of shaft bumpers were installed. These bumpers were positioned to restrict the shaft center orbits to less than 100 mils peak-to-peak. With the bumpers installed, supercritical operation was achieved. As rotor speed reached approximately 2260 rpm (the first critical speed), the rotor vibrations became almost exclusively synchronous and remained so to 2430 rpm. The FFT plot presented in Figure 6-8b, for a rotor speed of 2415 rpm, shows that the rotor response is predominantly synchronous. From these data, it appeared that the first critical speed had not been traversed as was predicted analytically. However, when rotor speed was increased to 2430 rpm, the synchronous component of the vibrations decreased and subsynchronous vibrations at 2265 rpm increased dramatically. The subsynchronous vibrations remained extremely large for all speeds tested above the critical speed once they were excited.

One potential explanation for the delay in the onset of the first natural frequency subsynchronous vibrations is that as the rotor approached the first critical speed and the orbits increased in size, the relative motions between the spline joint teeth ceased. This then resulted in a stiffer rotor system with a subsequent increase in the rotor system critical speed. In addition, once the rotor began contacting the orbit limiting bumpers, they would act as additional bearings in the system and raise the rotor critical speed. It was initially thought that the critical speed was being increased solely due to the

increased system stiffness introduced by the bumpers. However, as seen in Figure 6-8c, the subsynchronous vibrations occurred at 2265 rpm, which was near the expected first natural frequency.

It therefore appears that the apparent increase in the critical speed, as the rotor speed was increased from 2260 to 2430 rpm, resulted from something other than just the bumpers. It appears that, as the orbits grew, the relative motion between the shaft and sleeve spline teeth could have ceased because the rotor whirl became synchronous (no reverse or oscillatory bending of the joint) and the deflected rotor shape was dominated by the first mode content. This condition may have resulted in a stiffer rotor system. Then, as speed was further increased and the modified critical speed exceeded, it is likely that the spline joint again began to slip, since the shaft mode shape would have included other mode components resulting in some degree of reverse bending through the joint. Having overcome the static friction, the joint stiffness was most likely reduced (the critical speed dropped to 2265 rpm) and the first natural frequency could then have been excited due to the joint friction.

In a review of the data shown in Figure 6-8, it was found that the synchronous vibrations were on the order of 10 mil peak-to-peak, whereas the subsynchronous vibrations were on the order of 60 mil peak-to-peak. The rotor orbits were restricted throughout the testing by the softly mounted Rulon bumpers. Efforts to have the rotor run without contacting the bumpers were made by moving the bumpers further from the center of the rotor and closer to the bearing pedestals. For test runs with the bumpers relocated, orbits increased until the bumpers were again contacted. Further increases in orbit were not attempted for fear of permanently deforming the shaft.

On at least one occasion during the course of the spline testing, the instability was observed to decay and disappear, as shown in Figure 6-10. Upon disassembly and examination of the spline joints, it was found that the lubricant coating (MoS_2) was worn off the sides of the spline teeth. It is postulated that the loss of lubricant caused the coefficient of friction to increase and become large enough to "lock" the spline with a subsequent loss of the subsynchronous vibrations. After the spline teeth were cleaned and recoated with the dry film lubricant, the instability was again observed.

Additional testing with the axial spline also resulted in several cases of the spline locking and the disappearance of the instability. In these cases, stopping the rotor and rerunning

it through the critical speed reintroduced the subsynchronous vibrations. In each of these cases, it is likely that the orbits approaching and passing through the critical speed were such that the spline shift that occurred was substantial enough to free the spline and allow the spline teeth to undergo relative sliding either because dry lubricant was pulled into the contact area during the large spline positional shift or, more likely, that the contact zone was moved to an area with dry film lubricant.

In evaluating the spline friction induced subsynchronous vibrations, a review of the work reported by Marmol [23] was completed. That report appears to be at odds with the spline testing accomplished under this program. The conclusion reached by Marmol (23) was that rotors that are coupled with unlubricated splines are prone to internal friction instability and that lubricating the spline had a stabilizing effect on the rotor response. In the tests conducted under this effort, the opposite appears to be true. The discrepancy could be related to the differences between the two test series.

In the Pratt and Whitney testing, the side-fit spline had 36 teeth, a pressure angle of 30° , a 3.0-in. pitch diameter and an applied torque level of 2000 in.-lb. The HPOTP-simulated spline used under MTI's program was also a side fit spline but it had 42 teeth, a 30° pressure angle, a 2.1-in. pitch diameter, and an applied torque level of 5000 in.-lb. The other major difference between the two test series was that Pratt and Whitney used oil to lubricate the spline while MTI used dry-film lubricant. From the traction tests reported in Section 4.0, coefficients of friction of approximately 0.1 to 0.2 are likely for dry-film-lubricated contacts. Oil-lubricated contacts, on the other hand, would be expected to yield coefficients of friction of approximately 0.01 to 0.02. Based on the analysis developed under this effort, the magnitude of the destabilizing forces is a function of the coefficient of friction and the applied torque.

Thus with lower levels of torque and coefficients of friction for an oil-lubricated spline, the magnitude of the destabilizing forces would be smaller than for a solid-lubricated joint with a higher torque level. Correspondingly, the lower torque level applied to the Pratt and Whitney spline would not be as likely to cause an unlubricated spline to "lock up." This points out that there may be an internal friction instability threshold based on the spline parameters, applied torque, and lubricated condition (coefficient of friction).

Another factor, which should be considered in assessing the results of the axial spline tests, relates to the observed increase in the joint damping ratio as a function of

amplitude (see the component shaker test results, Figure 5-14). The change in damping ratio with increasing amplitude increases the magnitude of the destabilizing internal friction forces and may have been one reason for the inability to complete any of the spline tests without the use of the orbit limiting bumpers.

6.4.2 Interference Fit Rotordynamic Testing

Interference fit joint testing was accomplished after the spline testing and is summarized in Figures 6-11 through 6-13. As seen from these figures, the subsynchronous vibrations caused by the interference fit joint were not as large as the vibrations observed for the axial spline tests. In each of the interference fit joint tests, it was possible to operate the test rig at supercritical conditions without contacting the orbit limiting bumpers.

Figure 6-12 is a waterfall spectrum plot of rotor supercritical response showing the amplitude of the subsynchronous vibrations occurring at the first natural frequency. As can be seen, the amplitude of the subsynchronous vibrations vary with time. The oscillations in the subsynchronous vibration levels may be due to changes in the interference fit contact area that affect the microslip-based internal friction forces. For example, it may be that the maximum bending moment necessary to cause macroslippage in the joint is not being reached, but that the bending moments are large enough to introduce microslip. Further, as the joint goes through reverse bending, the microslip region may decrease to zero and then increase to a maximum, establishing a time-varying hysteresis loop similar to that shown in Figure 3-13. Thus the magnitude of the microslip-induced destabilizing forces may vary with time, going from zero to some maximum value. Alternatively, the changes in the contact area may be due to wear or burnishing of the dry lubricant in the interference fit joint contact zone, which could also affect the magnitude of the internal friction forces.

A comparison of rotor response with the interference fit joint for a different level of imbalance was also made. Figure 6-13 shows rotor response with a 5-gram change in the state of balance. Comparing this to Figure 6-11 shows a reduction in the synchronous vibrations by a factor of two. Subsynchronous vibrations also decrease, but not to the same level. The reduced level of subsynchronous vibrations in this case is most likely due to the reduced synchronous amplitudes, which in turn corresponds to smaller relative motions between the shaft and the interference fit joint.

6.4.3 Combined Spline/Interference Fit Joint Testing

Testing of the interference fit and axial spline joints mounted on the test shaft simultaneously (see Figure 6-2) demonstrated conditions observed during both of the previous tests sequences. In most cases, however, the response of the rig appeared to be dominated by the axial spline internal friction forces. As seen in Figure 6-2, both the interference fit and the spline sleeves are mounted near the hex nut in the center of the shaft. The internal friction test joints were installed near the center of the shaft to ensure that they would experience bending moments and consequently slippage in the joint during testing. As with the individual axial spline joint tests, the subsynchronous vibrations were significantly larger than the synchronous imbalance induced vibrations.

Figure 6-14 presents a representative spectrum plot of responses observed for the combined joint rotor tests. As with the axial spline tests, each run of the combined joint shaft was run above the first critical speed. Orbits were limited only by the installed bumpers. Similarly, a test case was completed where the large amplitude subsynchronous vibrations disappeared. In this test a small oscillating subsynchronous vibration, like the interference fit joint alone, was observed. To reinitiate the presence of the large amplitude instability, a side load was applied to the shaft, and the shaft was run above its critical speed. After removal of the side load and rerunning the shaft above the first critical speed, the instability returned. It is believed that the axial spline instability was initially lost due to a "locking" of the spline as occurred during the axial spline joint alone. The application of a static side load worked to free the joint and permit relative motions in subsequent tests.

The final series of tests were conducted by varying the magnitude of the applied side load to the axial spline sleeve (see Figure 6-2). Two side load force levels (20 and 70 lb) were used. Figures 6-15 through 6-17 show the results of the side load tests. The three figures show that the magnitude of the subsynchronous vibrations decrease with increasing side load. The observed vibration decrease is consistent with the parametric evaluations completed, as discussed in Section 3.2. It is possible that the application of the side load reduced the gap between the shaft and the bumpers, resulting in the lower-than-expected vibrations. Thus with the increased side loads, the orbits may have been restricted more than when the shaft was centered between all three bumpers. While the rubber straps used to apply the side load introduced some external damping, it is not believed that their damping was the cause of the reduced orbits since the bumpers were

still required to prevent the rotor orbits from increasing to the destruction of the rotor. Therefore, it more likely that the reduced bumper clearance and the magnitude of the side load, as shown in Section 3.2, are the causes for the reduction in subsynchronous vibrations.

From this test series it has been shown that the instability introduced by the axial spline is more severe than that caused by an interference fit joint. These results are consistent with the results of the component tests, which showed that the damping in the axial spline was larger than measured in the interference fit joint. An in-depth assessment of the effects of both imbalance and side load was restricted, however, due to the severe instability encountered and the need to continually use orbit-restricting bumpers.

7.0 CONCLUSIONS AND RECOMMENDATIONS

This section presents a summary of the conclusions reached during the conduct of this program.

7.1 Conclusions

Three nonlinear analytical Coulomb friction models of interference fit, axial spline, and Curvic coupling joints have been developed for use with a finite element rotordynamic analysis tool. Each of the three models may be used to predict rotor system stability through time-transient simulations. Using the axial spline model, an in-depth parametric assessment was completed under both symmetric (isotropic bearings and no side load) and nonsymmetric conditions. This assessment showed that, under symmetric operating conditions,

1. Operation above a bending critical speed, with bending across the joint, results in the presence of a subsynchronous instability at the bending critical speed.
2. The radius of the limit cycle orbit for symmetric rotor conditions is proportional to the product of the friction coefficient and torque and is inversely proportional to the external damping. Transient motions spiral toward the limit cycle when excited either from inside or outside the limit cycle circle.
3. Spin speed has little effect on the instability once the critical speed has been traversed.
4. With the introduction of imbalance, beating between the excited subsynchronous natural frequency and the synchronous operating speed occurs. The size of the subsynchronous component of the orbit is proportional to the product of the friction torque, while the synchronous component is proportional to the magnitude of the imbalance.

Under nonsymmetric operating conditions, the following was found:

1. Asymmetry in the bearing coefficients reduces the size of the internal friction-induced subsynchronous whirl orbit.

2. There is a threshold for the side load beyond which the rotor-bearing system is stable and all motions decay to a point.
3. Below the threshold, the transient motion will approach one of two asymptotic solutions depending on the initial conditions. As the side load is applied, the unstable node at the center of the orbitally stable limit cycle grows into an orbitally unstable limit cycle. For small initial conditions, the transient orbit will decay in an elliptically shaped spiral toward a point at its center resulting in a stable rotor, while for large initial conditions, the orbit grows toward the larger, more circular, stable limit cycle, from either the inside or the outside, resulting in subsynchronous whirl motion.
4. As the side load is increased, the orbitally unstable limit cycle grows very rapidly toward the larger limit cycle. This larger cycle, on the other hand, decreases and very gradually becomes elliptical with increasing side load. Both limit cycles merge into one at the threshold of side load to form a "semistable" or double cycle. Further increase in side load beyond the threshold increases the rate of decay of the motion toward the stable node.

An analytic assessment of the HPOTP stability in the presence of internal friction due to an axial spline at the preburner pump was also completed. For the model and initial conditions used, the results of this assessment showed that internal rotor friction adversely affects HPOTP stability. As discussed in Section 3.3, the subsynchronous instability occurs at the second natural frequency, which is approximately 86% of the 30,000 rpm operating speed. This analytically predicted instability was shown to be controllable with external damping at either the turbine end of the rotor or with a damping seal located at the preburner.

Predictions of internal friction-induced instability for the rotordynamic test rig were confirmed during testing. As predicted, the instability occurred at the first bending critical speed. Based on the confirmation of the instability, it is concluded that the developed analytic models are useful in identifying the presence of internal friction instability. However, while the appropriate frequency was identified, the magnitude of the orbit was not correctly predicted, indicating the need for further enhancements to the analytic models. The direction for these enhancements is seen in the discussion on the measured damping ratio for spline and interference fit joints.

Coefficient of friction testing was accomplished for material combinations present in both the HPOTP and the HPFTP. The measured friction forces under small amplitude oscillatory motion, when coupled with the applied normal force, resulted in coefficients of friction in the expected ranges. Coefficients of friction of approximately 0.2 and 0.8 for lubricated and unlubricated surfaces, respectively, were measured for amplitudes of motion above approximately 0.8 mil. Below this amplitude, the unlubricated material interfaces demonstrated rapidly increasing coefficients of friction with increases in amplitude. Thus the analytically assumed constant coefficient of friction in friction joints should be reexamined. The motion is expected to be small and no lubricant is to be applied at the material interface. However, for cases where motions are expected to be above 0.8 mil or solid-film lubricants are to be applied, the assumption of a constant coefficient appears valid.

Measured component joint damping, however, was not as expected. Difficulties were encountered in interpreting the variation of equivalent damping ratio as a function of amplitude. For all three component joints tested, the equivalent damping ratio appeared to increase with increasing amplitude. On a theoretical basis, it is hard to conceive of a situation where the damping coefficient would increase with amplitude without bound. Ultimately a limit would have to be reached if the shaft did not fail first. It may be that in the tests conducted, the small amplitudes applied were in a region of increasing damping ratio as a function of amplitude, but that there is a region where the damping ratio behaves more like Coulomb friction damping. It may be that as the vibration amplitude and consequently the joint bending increases, a larger portion of the joint begins to experience slip. As more of the joint participates, an increase in the joint damping would be expected.

Additionally, since the joints were not disassembled, cleaned, and recoated with new lubricant or had the surfaces redressed after each test point, it is possible that the observed variation in the damping ratio could be due to degradation of joint interface with time. Since the analytic joint model of the axial spline assumes Coulomb friction without stick-slip and is evenly distributed within the joint, additional effort to determine the cause for the increasing joint damping with amplitude is required.

Rotordynamic testing was conducted using the axial spline and interference joints both independently and together. In every test conducted, the onset of instability, or at least the presence of subsynchronous vibrations at the natural frequency, occurred above the

critical speed. The axial spline produced the most severe instability requiring orbit-limiting stops to complete the tests without damaging the shaft. A "locked-up" spline, however, did not exhibit subsynchronous instability. The effects of variation in imbalance for the axial spline were not discernible due to the severity of the instability encountered.

Tests of the interference fit joint also demonstrated subsynchronous vibrations at the first natural frequency. However, the subsynchronous vibrations were generally smaller than the synchronous vibration levels. Limited imbalance response testing with the interference fit joint showed a small decrease in the magnitude of the subsynchronous vibrations with a decrease in the synchronous vibrations. The decrease in subsynchronous vibrations may be due to the reduced amplitudes experienced and subsequently smaller relative motions within the joint to produce destabilizing forces. Results from the component tests indicate that the internal friction forces may be proportional with amplitude. Thus, smaller shaft orbits would result in smaller motions within a joint and, consequently, smaller destabilizing forces.

The final series of rotordynamic tests varied the level of side load applied to the center of the rotor (at the axial spline). In these tests, the instability was always present and at a level that required the bumpers to prevent shaft damage. As such, attempts to assess the impact of side load and imbalance were restricted. The tests that were run with the side load showed a decrease in the subsynchronous vibrations with increasing side load. However, since the clearance between the rotor and the bumpers was reduced when the load was applied, it cannot be stated with confidence that the increases in side load were completely responsible for the reduced subsynchronous vibrations, even though analytic evaluations indicate this may be true.

7.2 Recommendations

Based on the results of this experimental and analytical program, the following recommendations are made:

1. In the area of design practices, it appears that there is a band or threshold region where axial or side fit splines may cause internal friction instability. Conclusions based on prior experimental work [23] indicated that lubricating splines eliminated internal friction instability caused by side fit splines and that unlubricated splines

caused internal friction instability. This effort, at first, glance would have appeared to have found the exact opposite, but in reality concurs with the results of the earlier work upon a detailed review. Due to the differences between the two test programs and the test splines, it is concluded that the threshold conditions affecting the internal friction instability may be governed by the interface coefficient of friction, the contact pressures on the spline teeth (torque), the magnitude of the shaft deflections (i.e., the bending moment across the joint), and the amount of external damping available to dissipate the internal friction destabilizing forces.

2. The use of liquid lubricants in the spline joint is recommended since the friction torque product and, hence, the destabilizing force are likely to be small. However, if it is not possible to liquid lubricate the spline then it is recommended that the spline be assembled unlubricated, or with a piloting surface to limit the relative spline motions. Dry film lubricants should not be used since they yield coefficients of friction in the range of 0.1 to 0.2, which, when combined with the applied torque, may produce internal friction forces large enough to cause instability.
3. In the design and fabrication of a rotor system that requires the use of side fit splines, the designer needs to assess the operating conditions, spline design, tooth interface contact region, and their impact on the spline internal friction. Design approaches that restrict the motions at internal friction-producing joints or that result in very low coefficients of friction (liquid lubricated) should be pursued when operation above a bending critical speed is expected.
4. Based on the experimental test results, it is recommended that additional testing be performed. Specifically, the presence of a joint damping ratio that increases with amplitude needs to be further examined. Testing to either confirm or explain away this phenomena needs to be completed. Based on the results of these additional component damping assessment tests, the analytical component models of the interference fit, axial spline, and the curvic spline joints could then be revised to reflect the experimentally measured performance of the joints. Additionally, to gain a better understanding of the strength of the internal friction instabilities and to further confirm the analytical models developed, testing with external dampers replacing the bumper stops needs to be conducted.

8.0 REFERENCES

1. Kimball, A. L. "Internal Friction Theory of Shaft Whirling." General Electric Review 27 (1924): 244.
2. Robertson, D. "Hysteretic Influence on Whirling of Rotors." Proc. Inst. Mech. Engineers 131 (1935): 513-37.
3. Timoshenko, S., Vibration Problems in Engineering. Princeton, New Jersey: D. Van Nostrand Co., 1959.
4. Dimentberg, F. M. Flexural Vibrations of Rotating Shafts. London: Butterworth, 1961.
5. Tondl, A. Some Problems of Rotor Dynamics, Prague: Publishing House of the Czechoslovak Academy of Science, 1965.
6. Gunter, E. J. "The Influence of Internal Friction on the Stability of High Speed Rotors." Journal of Engineering for Industry, ASME Transactions, (November 1967): 683-88.
7. Ehrich, F. F. "Shaft Whirl Induced by Rotor Internal Damping." Journal of Applied Mechanics 31 (1969): 279-82.
8. Ehrich, F. F. "The Dynamic Stability of Rotor/Stator Radial Rubs in Rotating Machinery." Journal of Engineering for Industry, ASME Transactions 91 (1969): 1025-28.
9. Black, H. F. "Interaction of a Whirling Rotor with a Vibrating Stator Across a Clearance Annulus." Journal of Mechanical Engineering Science 10, no. 1 (1968): 1-12.
10. Bolotin, V. V. Nonconservative Problem of the Theory of Elastic Stability. New York: Pergamon Press, 1963.
11. Childs, D. W. "Fractional-Frequency Rotor Motion Due to Nonsymmetric Clearance Effects." Journal of Engineering for Power, ASME Transactions, presented at International Gas Turbine Conference, March 1981.
12. Black, H. F. "The Stability Capacity of Bearings for Flexible Rotors with Hysteresis." Journal of Engineering for Industry, ASME Transactions (February 1976): 87-91.
13. Williams, R., and R. Trent. "The Effect of Nonlinear Asymmetric Supports on Turbine Engine Rotor Stability." SAE 700320.
14. Lund, J. W. "Stability and Damped Critical Speeds of a Flexible Rotor in Fluid Film Bearings." Journal of Engineering for Industry, ASME Transactions 96 (1974): 509-17.
15. Dimarogonas, A. D. "A General Method for Stability Analysis of Rotating Shafts," Ingenieur-Archiv 44 (1975): 9-20.

16. Zorzi, E. S., and H. D. Nelson. "Finite Element Simulation of Rotor-Bearing Systems with Internal Damping." Journal of Engineering for Power, ASME Transactions 99, no. 1 (1977): 71-76.
17. Lazan, B. J. Damping of Materials and Members in Structural Mechanics, New York: Pergamon Press, 1968.
18. Pisarenko, G. S. "Vibration of Elastic Systems Taking Account of Energy Dissipation in the Material." AD-274-743, February 1962.
19. Pisarenko, G. S. "Vibration Absorbing Properties of Structural Materials: A Handbook." AD-784 925, April 1974.
20. Davidenkov, N. V. "In Energy Dissipation in Vibration." Journal of Technical Physics 3, no. 6 (1938): 983.
21. Krylov, N. M., and N. N. Bogolyubov. On Some Formal Series Expansions in Nonlinear Mechanics, Ukrainian SSR, 1934.
22. Marmol, R. A., A. J. Smalley, J. A. and Tecza. "Spline Coupling Induced Nonsynchronous Rotor Vibrations." Journal of Mechanical Design, ASME Transactions 102 (1980): 168-76.
23. Marmol, R. A. "Engine Rotor Dynamics, Synchronous and Nonsynchronous Whirl Control." Report No. USARTL-TR-79-2, prepared for Applied Technology Laboratory, U.S. Army Research and Technology Laboratories, Fort Eustis, VA 23604, by Pratt & Whitney Aircraft Group, West Palm Beach, Florida, 1979.
24. Murakani, H. "A Laminated Beam Theory with Interlayer Slip." Journal of Applied Mechanics 51 (1984): 551.
25. Lund, J. "Destabilization of Rotors from Friction in Internal Joints with Micro-slip." International Conference on Rotordynamics, JSME, Tokyo, September 1986.
26. Nelson, H. D., and J. M. McVaugh. "The Dynamics of Rotor-Bearing Systems using Finite Elements." Transactions ASME, Journal of Engineering for Industry, Paper No. 75-WA/DE-19 (1976): 593.
27. Andronov, A.A., A. A. Vitt, and S. E. Khaikin. Theory of Acillators, p 289. New York: Dover Publications, 1966.
28. Childs, D. W. "Force and Moment Rotordynamic Coefficients for Pump Impeller Shroud Surfaces." NASA CP 2436, Vol. I, 1986, pp 296-326
29. Adkins, D. R., and C. E. Brennan. "Analyses of Hydrodynamic Radial Forces on Centrifugal Pump Impellers." Journal of Fluids Engineering, Transactions ASME, 110 (1988): 20-28.

APPENDIX A

ANALYSIS OF A SLEEVE SHRUNK ON A SHAFT UNDER BENDING PRIOR TO SLIP

No known analytical solution exists for a section of shaft with a shrunk-on sleeve under a pure bending moment, even when a welded contact is assumed at the shaft/sleeve interface. In order to understand the state of stress distribution in the shaft/sleeve joint, a finite element model of the joint was constructed, as shown in Figure A-1. If the origin of Cartesian coordinates is located at the center of the shaft and at the midlength of the sleeve, a plane of symmetry exists at $z = 0$. Furthermore, when the coordinate system is chosen so that the applied moment is about the x-axis, there is another plane of symmetry at $x = 0$. These two symmetries allow modeling only 1/4 of the full joint, as shown in the figure. This finite element model was run in the ADINA program at MTI, treating the interface as being welded and without any prestress from the fit, in order to determine the normal and shear stresses at the interface. Under these assumptions, these stresses are linearly proportional to the applied moment. Figure A-2 shows a view of the model distorted by the displacements greatly exaggerated in magnitude.

Figure A-3 is a plot of the normal stress versus the circumferential coordinate at different axial positions along the sleeve, from the axial centerline ($z = 0$) to the sleeve end ($z = 0.6$ in.). It is noted that the stress is antisymmetric about the $y = 0$ plane ($\theta = 0$). Near the sleeve end, the stress is tensile at the top and compressive at the bottom while this order is reversed and the stress is much less in magnitude toward the axial midplane. Figure A-4 is a similar plot of the magnitude of the shear stress. These figures indicate that

- At the sleeve ends, slip will start at the top, where the normal stress increases with moment most rapidly.
- Toward the axial midplane, slip will start near the bottom, if it occurs at all.

Figure A-5 is a plot of the angle that the shear traction vector makes with the z-axis. It is seen that, particularly near the sleeve end, the shear stress is nearly axial (since the plotted angle is near 0 or 180°), and the antisymmetry about $\theta = 0^\circ$ follows the sign of the applied forces. Figures A-6 and A-7 plot the axial and circumferential components, respectively, of the shear traction stress. It is noted that the circumferential component is relatively small.

Figures A-8 and A-9 are plots of the normal stress and magnitude of the shear stress versus the axial coordinate at the different circumferential positions. Due to the anti-symmetry about $\theta = 0^\circ$, the top and bottom curves of the shear stress magnitude coincide exactly with each other. Figures A-10 and A-11 are plots of the angle that the shear stress makes with the z-axis and the axial component of the shear stress, respectively. These figures point out how the stress is mostly axial in direction, and how it varies from near zero at the axial midplane to about equal to the normal stress at the sleeve ends.

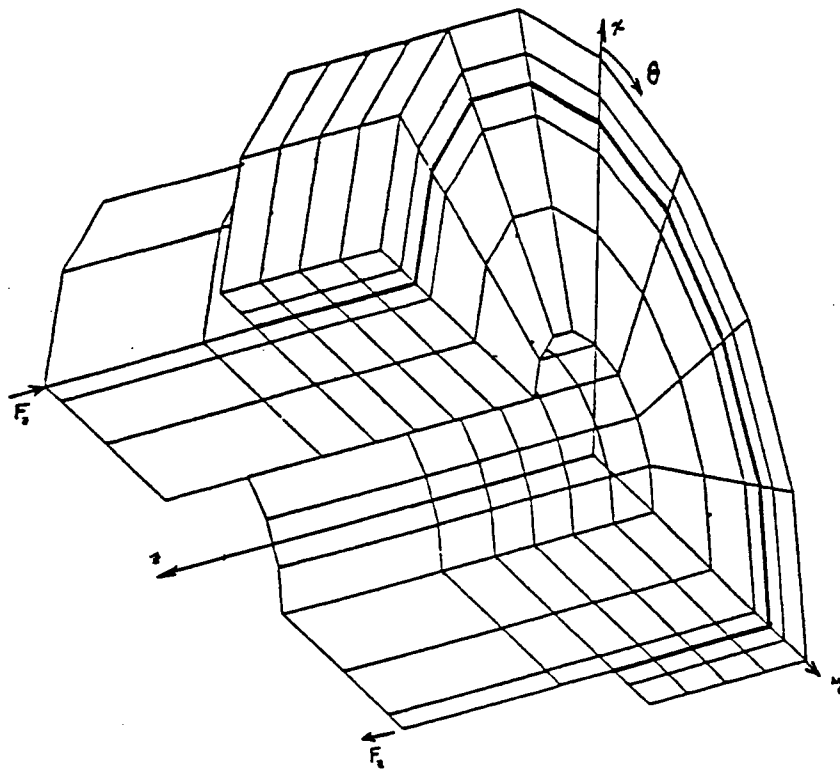


Figure A-1. Undistorted Finite Element Model of Interference Fit Joint

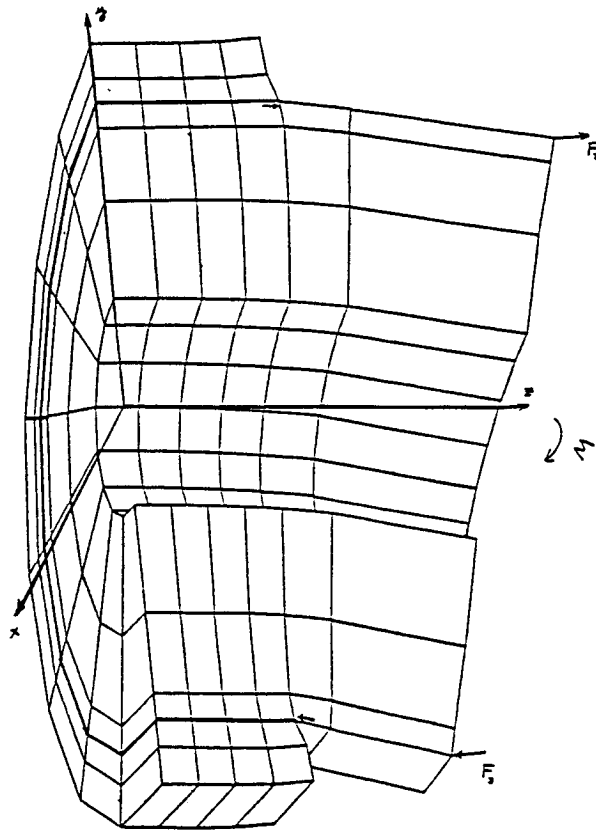


Figure A-2. Distorted Finite Element Model of Interference Fit Joint

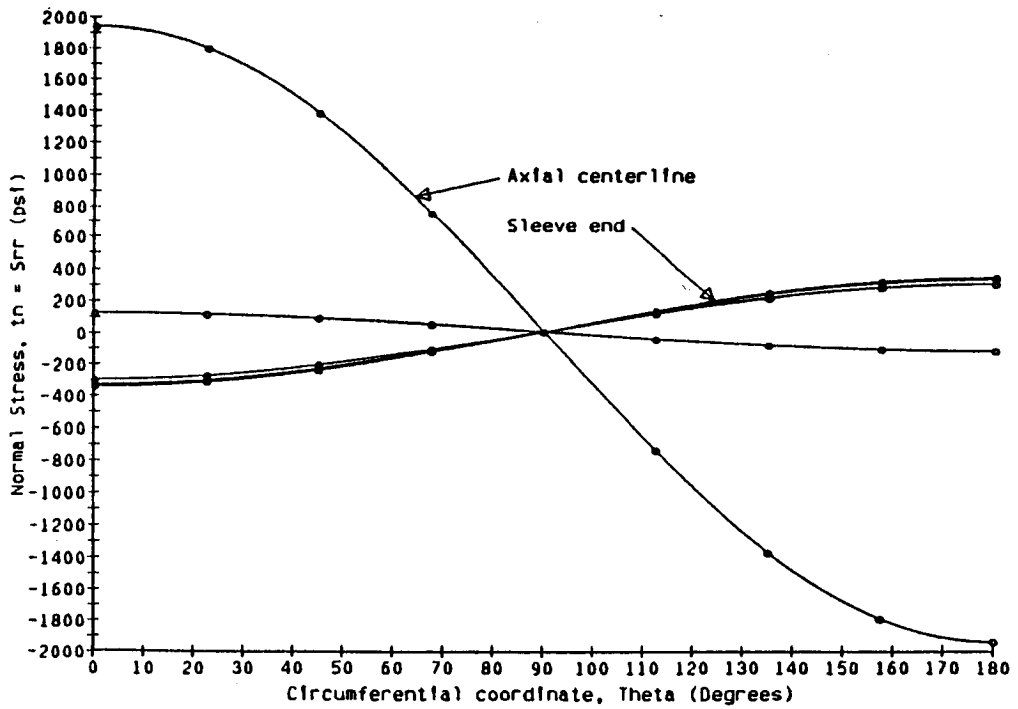


Figure A-3. Plot of Normal Stress vs Circumferential Position for Interference Fit Joint

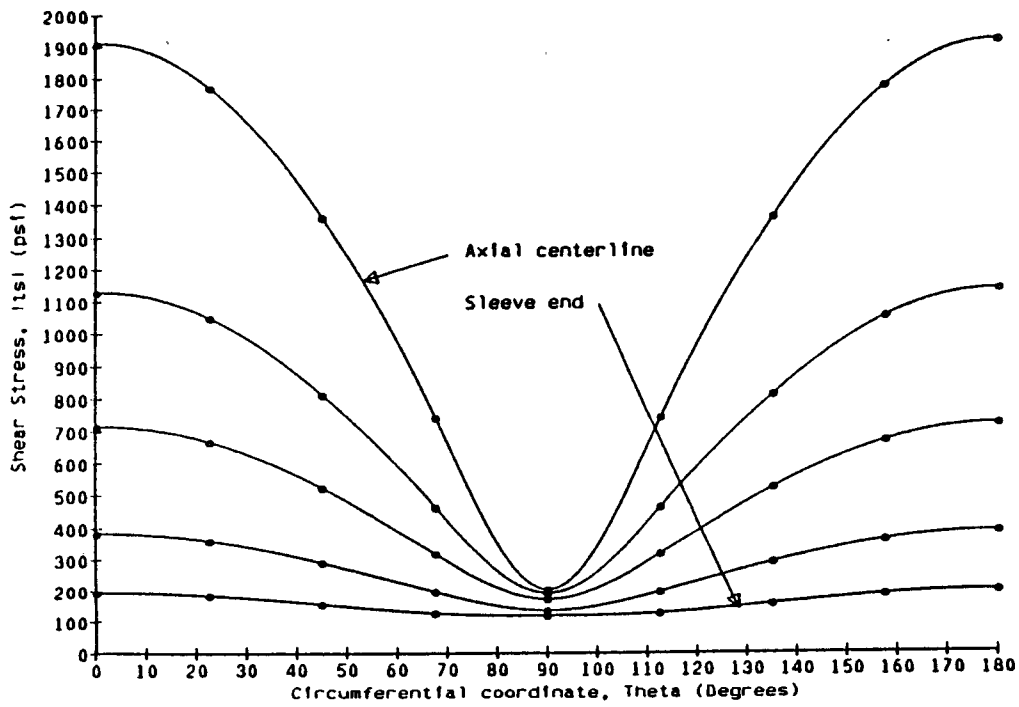


Figure A-4. Plot of Shear Stress vs Circumferential Position for Interference Fit Joint

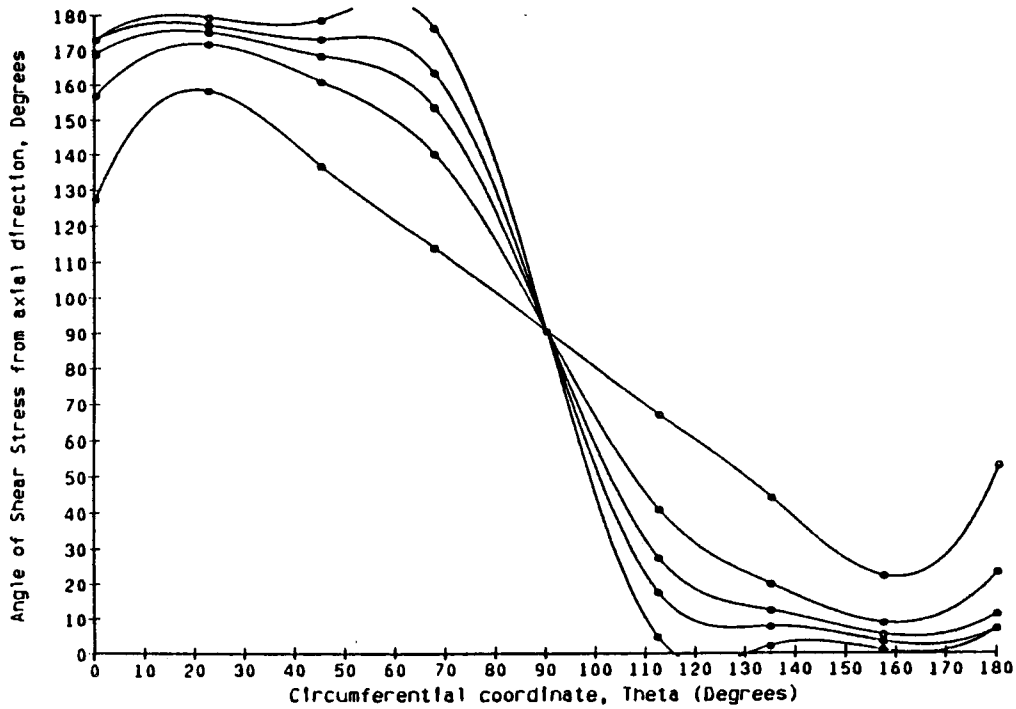


Figure A-5. Plot of Shear Traction Vector Angle as a Function of Circumferential Position Due to Pure Bending Moment

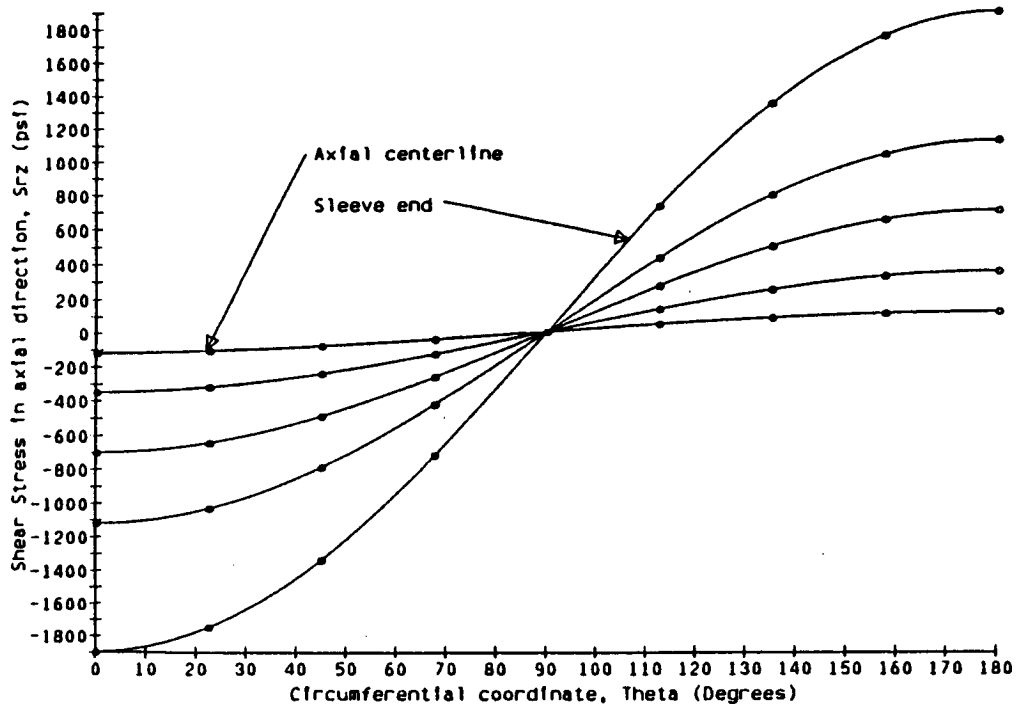


Figure A-6. Axial Shear Traction Stress

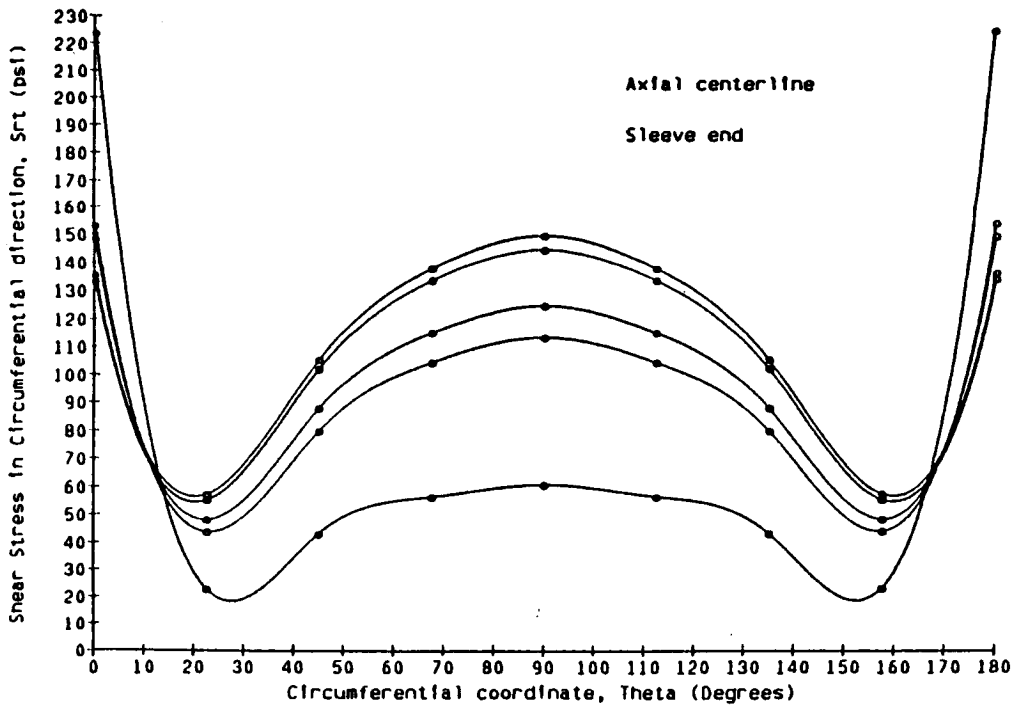


Figure A-7/ Circumferential Shear Traction Stress

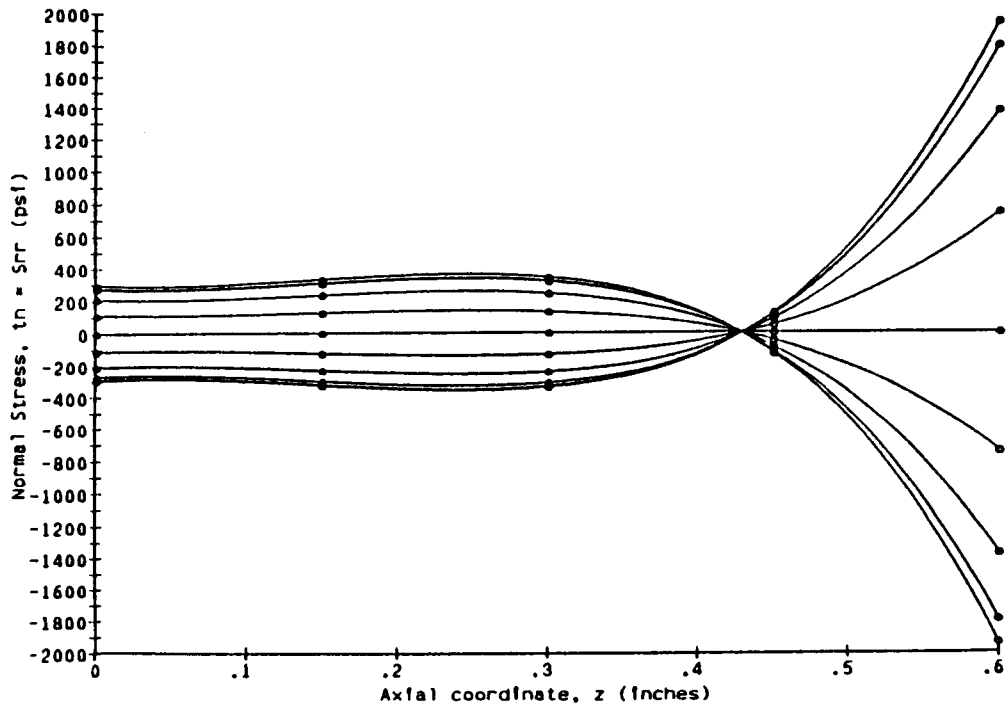


Figure A-8. Interference Fit Joint Normal Stresses along Axial Coordinate

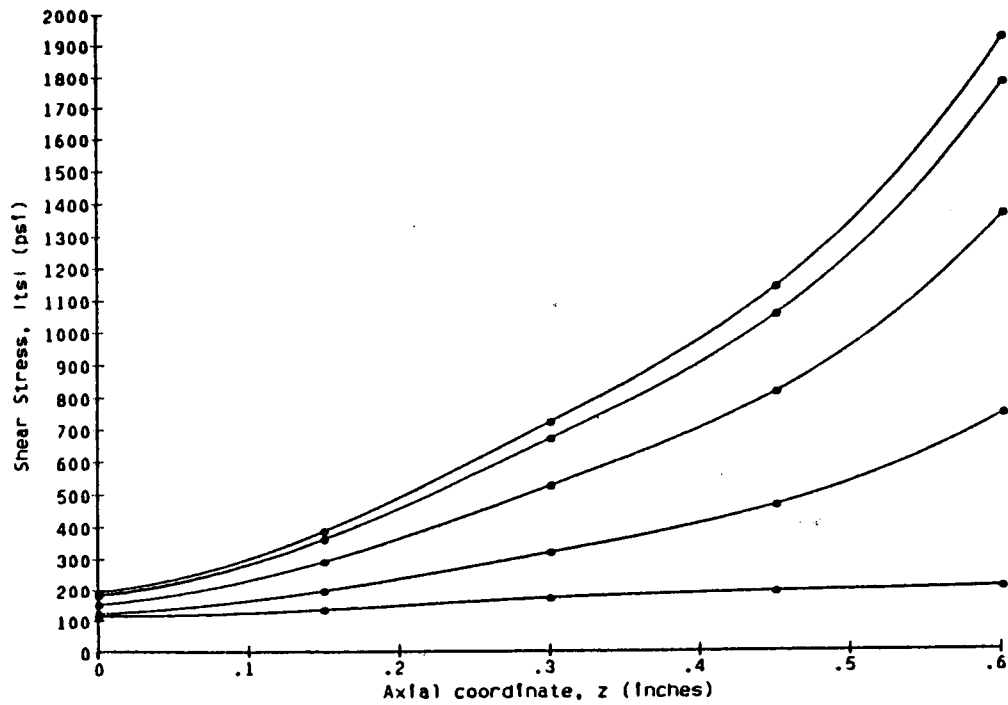


Figure A-9. Interference Fit Joint Shear Stresses along Axial Coordinate

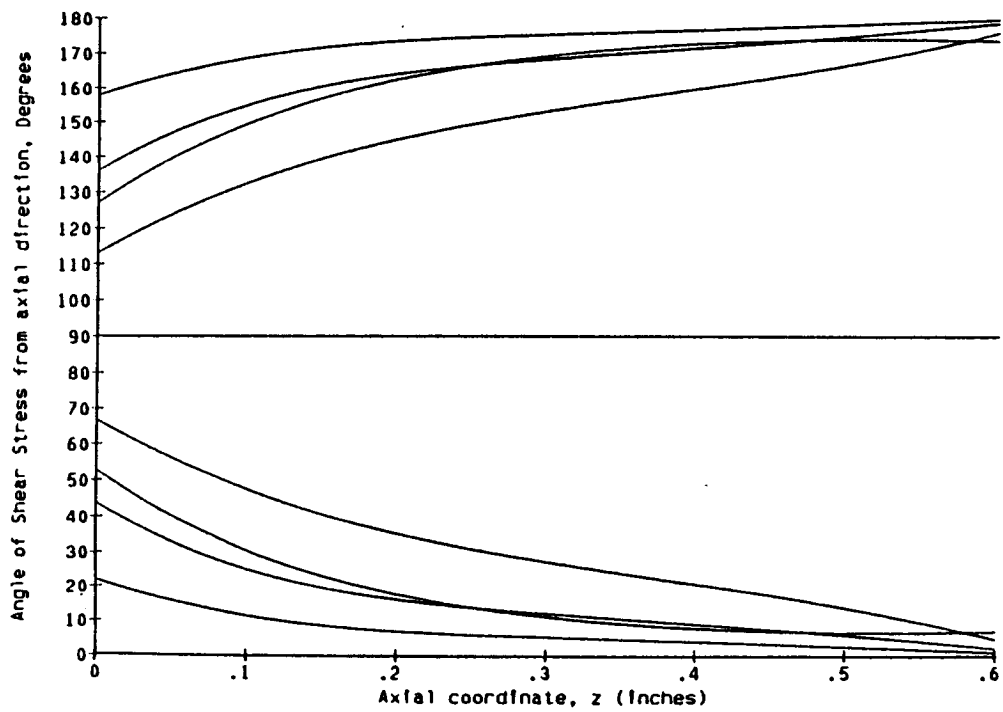


Figure A-10. Plot of Shear Stress Angle with Respect to Axial Direction

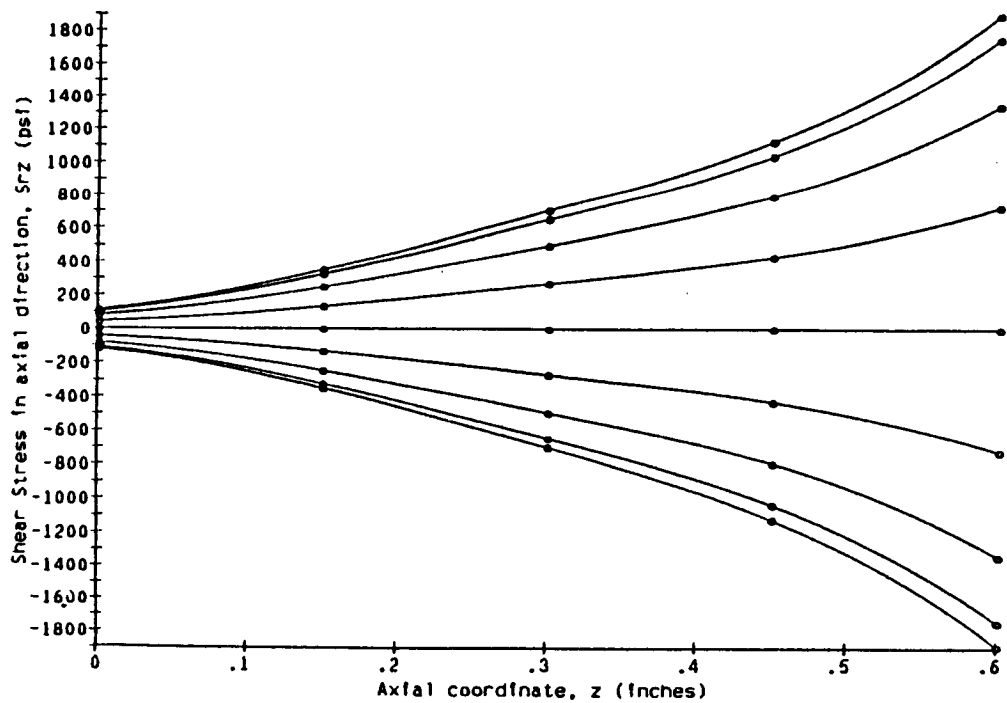


Figure A-11. Interference Fit Joint Shear Stress Axial Direction Component

APPENDIX B

RELIEVED SHRUNK-ON SLEEVE

Figure B-1 shows a shrunk-on sleeve of length, L , which has been relieved, making contact with the shaft only for a relatively short extent, c , at its ends. When a bending moment, M , is applied to the shaft ends, part of the moment is transmitted by the shaft (M_1) and the rest by the sleeve (M_2). The displacement of the ends of the shaft and sleeve must match. Assuming that c is small compared to $L/2$, there is a maximum moment that can be transmitted to the sleeve before slip begins to occur, given by:

$$M_{2\max} = \iint_{A_c} y\mu p \, dA = 4\mu p c R^2 \quad (\text{B-1})$$

where

- A_c = Area of sleeve to shaft contact
- μ = Coefficient of friction
- p = Shrink-fit pressure
- c = Axial Extent of A_c
- R = Radius of A_c

Let k_1 and k_2 denote the angular stiffnesses of the shaft and sleeve, respectively; that is, the moment supported by each member divided by the relative rotation of that member across its ends (γ). For an annular cylinder, beam theory gives:

$$k = M/\gamma = 2EI/L = \pi E(R_o^4 - R_i^4)/2L \quad (\text{B-2})$$

The moment applied is the sum of the moments carried by each member:

$$M = M_1 + M_2 \quad (\text{B-3})$$

The moment through the shaft is always given by:

$$M_1 = k_1 \gamma \quad (\text{B-4})$$

while that carried by the sleeve depends on the history as well as the sign of the time-rate-of-change of the motion:

$$M_2 = \begin{cases} k_2(\gamma - \gamma_s) & \text{if } |k_2(\gamma - \gamma_s)| \leq M_{2\max} \\ \text{sgn}(d\gamma/dt) M_{2\max} & \text{if } |k_2(\gamma - \gamma_s)| > M_{2\max} \end{cases} \quad (\text{B-5})$$

where γ_s is the cumulative amount of angular slip that has occurred between the shaft and the sleeve since initial loading and is given by integration versus time of:

$$d\gamma_s/dt = \begin{cases} 0 & \text{if } |k_2(\gamma - \gamma_s)| \leq M_{2\max} \\ d\gamma/dt & \text{if } |k_2(\gamma - \gamma_s)| > M_{2\max} \end{cases} \quad (\text{B-6})$$

Figure B-2 shows the total moment versus rotation curve for the prescribed joint rotation versus time shown in Figure B-3. Under initial loading (OAB), the joint responds with the combined stiffness ($k_1 + k_2$) until the maximum moment to the sleeve is exceeded, where it only has the stiffness of the shaft, k , from A to B. Upon unloading at B, the greater stiffness is regained and γ_s now has a value equal to the slip that occurred between A and B. It is noted that under conditions of slip, the stiffness of the joint is discontinuous with load direction, or $d\gamma/dt$.

As unloading proceeds from B to D, the moment decreases with the greater stiffness ($k_1 + k_2$) until M_2 becomes less than $-M_{2\max}$ at C; at which point slip occurs, the stiffness is k_1 , and γ_s decreases until the minimum load is reached at D. Further loadings (DEF) and unloadings (FGH) proceed in a similar fashion.

The energy dissipated in the joint can be calculated by integrating the product of the relative displacements and the shear stress over the slipping interfaces:

$$\Delta E = 4\mu pcR^2 |\Delta\gamma| = M_{2\max} |\Delta\gamma| \quad (\text{B-7})$$

It can be found by integrating:

$$dE/dt = \begin{cases} 0 & \text{if } |k_2(\gamma - \gamma_s)| \leq M_{2\max} \\ M_{2\max} |d\gamma/dt| & \text{if } |k_2(\gamma - \gamma_s)| > M_{2\max} \end{cases} \quad (\text{B-8})$$

The energy dissipated in the joint due to the applied rotation history of Figure B-3 is illustrated in Figure B-4. Note that no energy increase occurs when the joint is stuck (OA, BC, DE, FG, and HI).

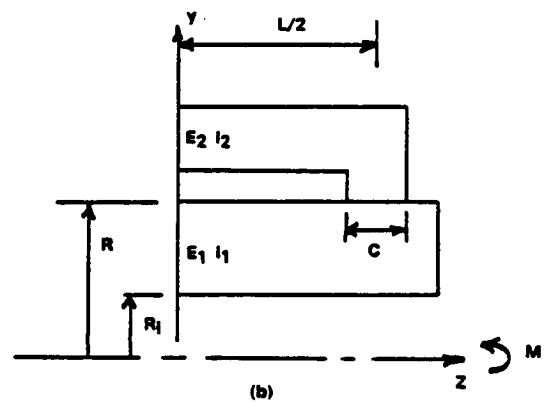
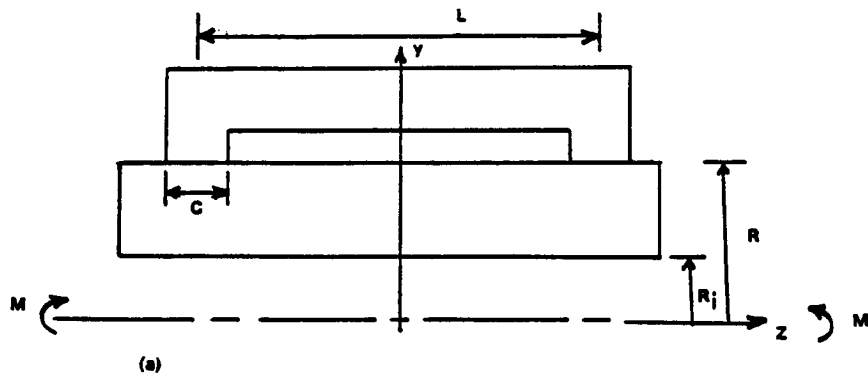


Figure B-1. Sketch of Relieved Shrunk-on Sleeve

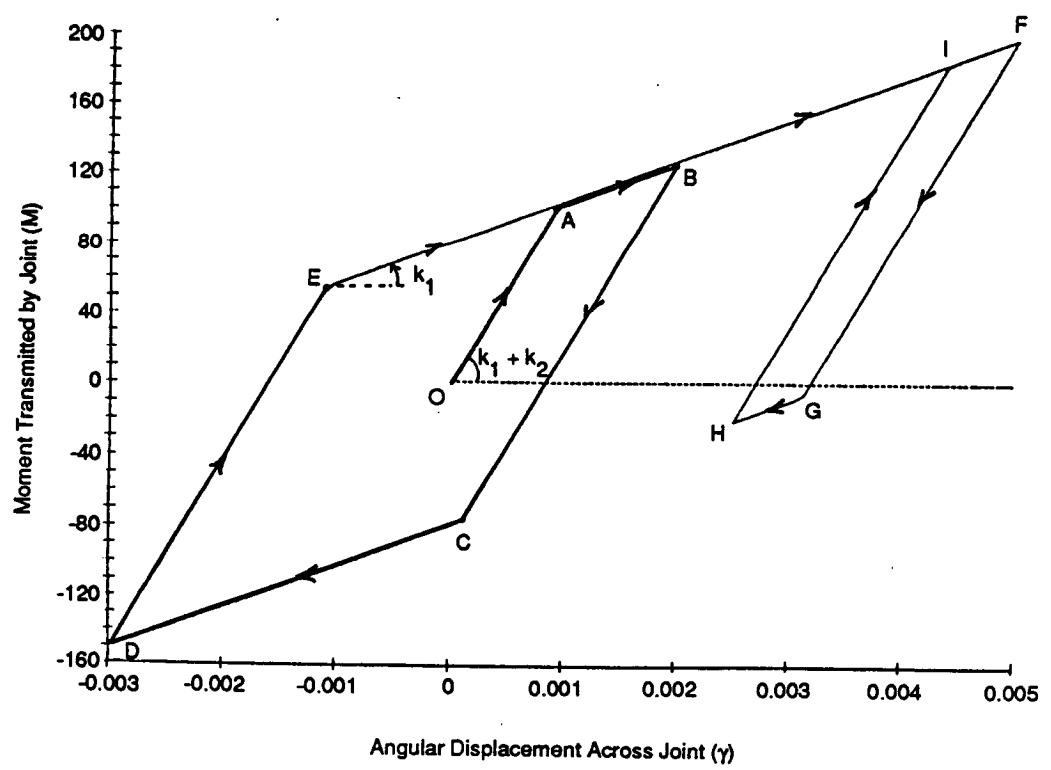


Figure B-2. Moment/Displacement Relationship for a Relieved Shrunk-on Sleeve

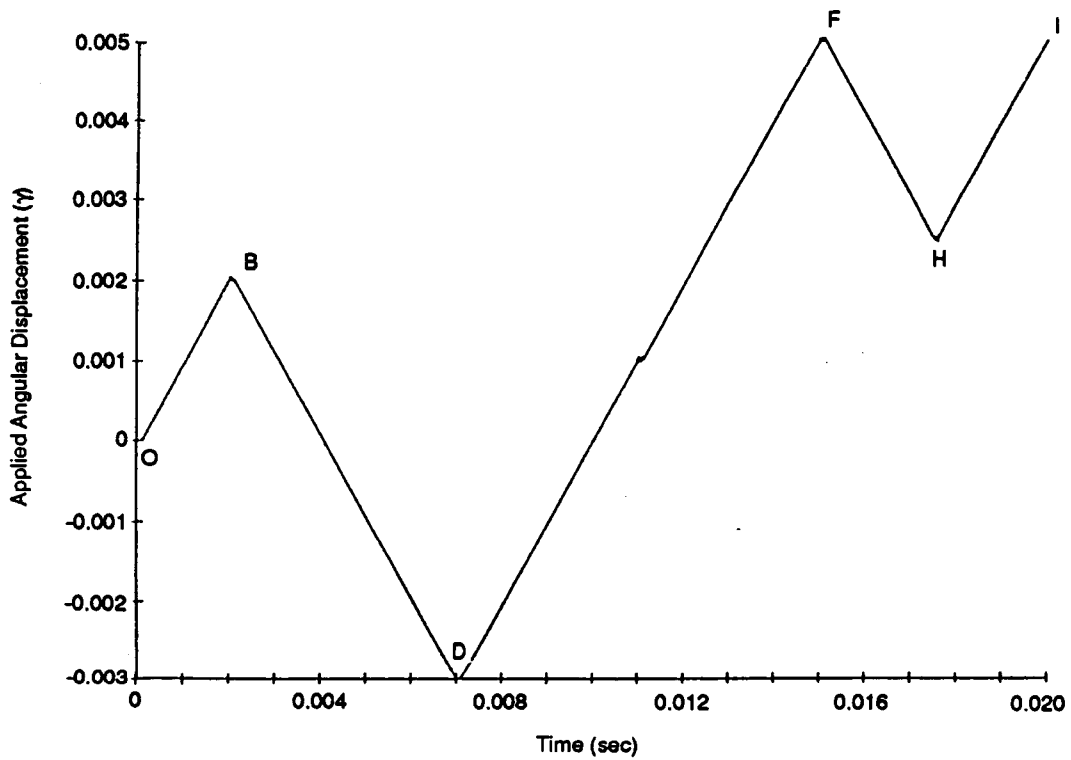


Figure B-3. History of Angular Displacement for Moment Applied at Shaft Ends

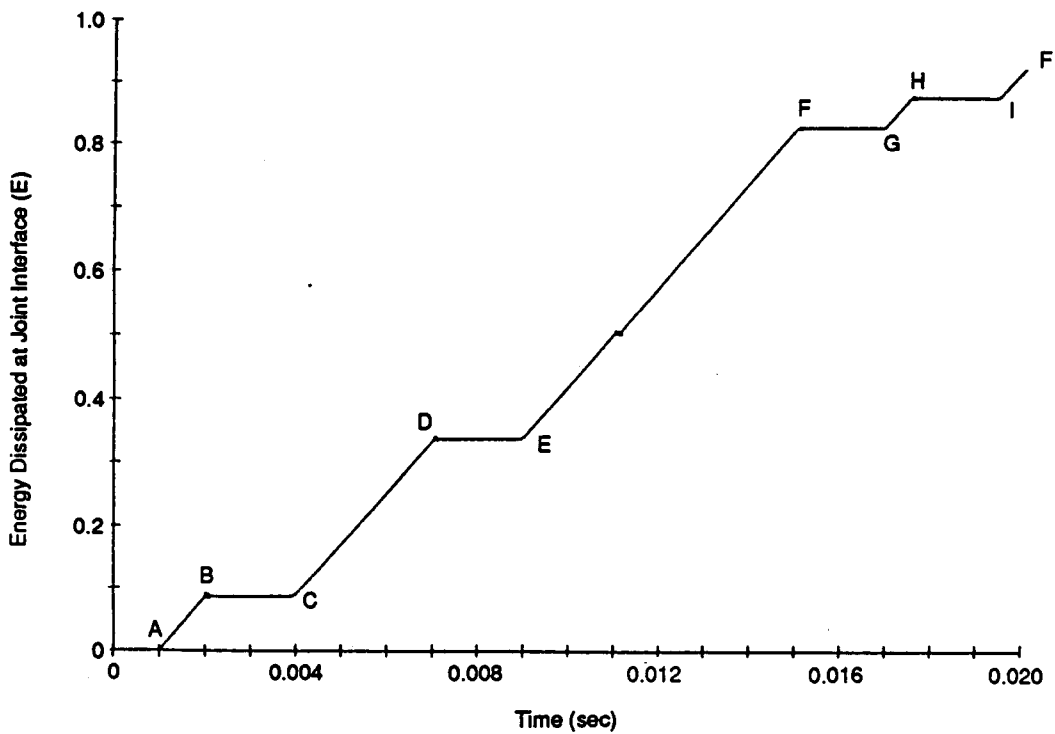


Figure B-4. History of Energy Dissipated at Interference Fit Joint Interface

16. Abstract (continued)

model developed under this program. Corresponding rotordynamic testing of a shaft with an interference fit joint demonstrated the presence of subsynchronous vibrations at the first natural frequency. While subsynchronous vibrations were observed, they were bounded and significantly lower in amplitude than the synchronous vibrations.

1. Report No.		2. Government Accession No.		3. Recipient's Catalog No.	
4. Title and Subtitle Internal Rotor Friction Instability				5. Report Date February 1990	
				6. Performing Organization Code	
7. Author(s) J. Walton, A. Artiles, J. Lund, J. Dill, and E. Zorzi				8. Performing Organization Report No. MTI 89TR39	
				10. Work Unit No.	
9. Performing Organization Name and Address Mechanical Technology Incorporated 968 Albany-Shaker Road Latham, New York 12110				11. Contract or Grant No. NAS8-35601	
				13. Type of Report and Period Covered Contractor Report: Final	
12. Sponsoring Agency Name and Address NASA/George C. Marshall Space Flight Center Marshall Space Flight Center Alabama 35812				14. Sponsoring Agency Code	
15. Supplementary Notes Project Manager: George von Pragenau NASA/MSFC, Huntsville, Alabama					
16. Abstract This report documents the analytical developments and experimental investigations performed in assessing the affect of internal friction on rotor systems dynamic performance. Analytical component models for axial splines, Curvic™ splines, and interference fit joints commonly found in modern high-speed turbomachinery were developed. Rotor systems operating above a bending critical speed were shown to exhibit unstable subsynchronous vibrations at the first natural frequency. The effect of speed, bearing stiffness, joint stiffness, external damping, torque, and coefficient of friction, was evaluated. Testing included material coefficient of friction evaluations, component joint quantity and form of damping determinations, and rotordynamic stability assessments. Under conditions similar to those in the SSME turbopumps, material interfaces experienced a coefficient of friction of approximately 0.2 for lubricated and 0.8 for unlubricated conditions. The damping observed in the component joints displayed nearly linear behavior with increasing amplitude. Thus, the measured damping, as a function of amplitude, is not represented by either linear or Coulomb friction damper models. Rotordynamic testing of an axial spline joint under 5000 in.-lb of static torque, demonstrated the presence of an extremely severe instability when the rotor was operated above its first flexible natural frequency. The presence of this instability was predicted by nonlinear rotordynamic time-transient analysis using the nonlinear component (over)					
17. Key Words (Suggested by Author(s)) Internal Friction Instability Rotordynamics			18. Distribution Statement Subsynchronous Whirl Spline Curvic™ Spline		
19. Security Classif. (of this report)		20. Security Classif. (of this page)		21. No of pages 182	22. Price*